Controlled Microfluidic Synthesis of Biological Stimuli-Responsive Polymer Nanoparticles for Drug Delivery Applications

by

Yuhang Huang
B.Eng., Wuhan University of Technology, 2018

A Thesis Submitted in Partial Fulfillment
of the Requirements for the Degree of

MASTER OF SCIENCE

in the Department of Chemistry

Supervisory Committee

Controlled Microfluidic Synthesis of Biological Stimuli-Responsive Polymer Nanoparticles for Drug Delivery Applications

by

Yuhang Huang
B.Eng., Wuhan University of Technology, 2018

Supervisory Committee

Dr. Matthew Moffitt, Department of Chemistry
Supervisor

Dr. Fraser Hof, Department of Chemistry
Departmental Member

Abstract

Supervisory Committee
Dr. Matthew Moffitt, Department of Chemistry
Supervisor
Dr. Fraser Hof, Department of Chemistry
Departmental Member

Polymer nanoparticles (PNPs) that exhibit selective stimuli-responsive degradation and drug release at tumor sites are promising candidates in the development of smart nanomedicines. In this thesis, we demonstrate a microfluidic approach to manufacturing biological stimuli-responsive PNPs with flow-tunable physicochemical and pharmacological properties. The investigated PNPs contain cleavable disulfide linkages in two different locations (core and interface, DualM PNPs) exhibiting responsivity to elevated levels of glutathione (GSH), such as those found within cancerous cells.

First, we conduct a mechanistic study on the microfluidic formation of DualM PNPs without encapsulated drug. We show that physicochemical properties, including size, morphology, and internal structure, of DualM PNPs are tunable with manufacturing flow rate. Microfluidic formation of DualM PNPs is explained by the interplay of shear-induced coalescence, shear-induced breakup, and intraparticle chain rearrangements. In addition, we demonstrate that rates of GSH-triggered changes in size and internal structure are linearly correlated with initial PNP sizes and internal structures, respectively.

Next, we expand our study to focus on microfluidic control of pharmacological properties of DualM PNPs containing either an anticancer drug (paclitaxel, PAX-PNPs) or a fluorescent drug surrogate (DiI-PNPs). Microfluidic PAX-PNPs and DiI-PNPs show similar sizes and morphologies with their non-drug-loaded counterparts under the same flow conditions. We then show that pharmacological properties of DualM PNPs, including encapsulation efficiency, GSH-triggered release rate, cell uptake, cytotoxicity against MCF-7 (cancerous) and HaCaT (healthy), and relative difference in MCF-7 and HaCaT cytotoxicity, all increase linearly as flow-directed PNP size decreases, providing remarkably simple process-structure-property relationships. In addition, we show that microfluidic manufacturing improves encapsulation homogeneities within PNPs relative to bulk nanoprecipitation. These results highlight the potential of flow-directed shear

processing in microfluidics for providing controlled manufacturing routes to biological stimuli-responsive nanomedicines optimized for specific therapeutic applications.

Finally, we summarize various design strategies of biological stimuli-responsive PNPs. We show that the location and density of disulfide linkages within PNPs determines stimulus-triggered degradation mechanism and kinetics. In addition, we show various bottom-up approaches to tune PNP responsivities that involves chemical processing, including formulation chemistry and intramolecular forces. Along with the top-down microfluidic approach that we demonstrate experimentally, this chapter provides a more comprehensive understanding of process-structure-property relations opening up vast possibilities for manufacturing smarter nanomedicines.

Table of Contents

List of Tables

List of Figures

Acknowledgments

First and foremost, I would like to express my most sincere gratitude to my supervisor, Dr. Matthew Moffitt, for his constant support and encouragement, endless patience, and profound knowledge of science. I am truly thankful for all of the things he has taught me. Without his guidance and advice, this thesis would not be possible.

I would also give my thanks to my co-supervisor, Dr. John Oh, and PoND (Polymer Nanoparticle for Drug Delivery) collaborative training program for the amazing opportunity to work on such a fascinating project.

My sincere thanks go to my mom and dad, for their love, companion, understanding, and support through my academic journey and all other endeavors.

Thanks to everyone in Moffitt group past and present: Liza Silverman, for her friendship and the guidance through my training on almost every aspect in the lab; Elliot Howell, for his hard work as a part that cannot be lost in my research; Sun Kly, for his helpful discussion and assistance on my experiments; Dr. Jiying Men, for her insightful suggestions on my research; Gitika Bhatti, Riddhi Baddhwar, Talita de Francesco, and Anup Singh, for making the lab a wonderful place to spend so many hours for so many days.

I would also acknowledge Arman Moini Jazani for providing me with the polymer sample; Dr. Jeremy Wulff for his invaluable help on experimental design and data evaluation on cell studies; Dr. Lisa Reynolds for her guidance and assistance on flow cytometry experiments; Rebecca Hof for passing on her tissue-culture expertise; Dr. Patrick Nahirney and Brent Gowen for the continued use of their electron microscope.

Last and definitely not least, all the faculty and staff in Chemistry Department – thank you for your help and continued support on academic and administrative issues towards my degree completion. Thank you all for making the two years of my M.Sc. studies a truly great experience!

Chapter 1 Introduction

1.1 Background and Motivation

As human understanding of the quantitative structure-activity relationship of chemical therapeutics continues to deepen, more and more drugs based on small molecules have been discovered and marketed.[1-2] However, the research and development challenges of drug discovery has increased year by year. Many newly discovered small molecule drugs are classified in the biopharmaceutical classification system as class II or IV, which are found to have low solubility, poor *in vivo* stability, and low bioavailability. These properties greatly diminishes positive pharmacological effects and lead to challenges in clinical use.[3] Another issue for many small molecule drugs, particularly chemotherapeutics, is the non-specific biodistribution, causing severe side effects to healthy tissues. For example, anticancer drug paclitaxel tends to interrupt the normal function of microtubule in the cells with fast growth cycles. When the drugs distribute throughout the body in a non-specific fashion, both cancerous cells and healthy cells that are also fast-growing would be affected. Side effects of taking paclitaxel thus include bone marrow suppression, since the drug would kill blood-forming cells in the bone marrow.[2]

Recent developments in material science, including the advent of smart biomaterials for encapsulating class II or IV therapeutics, have responded to the above challenges.[4-5] Several "vehicles" for drug encapsulation and delivery have been well studied and commercialized, including liposomes,[6-8] nanoemulsions,[9-10] and polymer nanoparticles (PNPs) self-assembled from amphiphilic block copolymers.[11-16] Unlike lipid-based carriers, which act on tissues solely *via* their own chemotactic properties,[6-10] PNPs exhibit ease of functionalization and broad diversity in chemico-physiological properties, which

provides potentials for better performances in terms of drug encapsulation, targeting and controlled release.[11-16]

For example, the self-assembly of poly(ethylene oxide)-*block*-poly(caprolactone) (PEO-*b*-PCL) in aqueous media would give rise to PNPs consisting of hydrophilic PEO-forming coronae and hydrophobic PCL-forming cores. A wide range of hydrophobic drugs can be encapsulated within the PCL cores enhancing bioavailability, while the PEO coronae protects the PNPs from the reticular endothelial system (RES) and prevents renal clearance, improving performance of biodistribution. PNPs that are solely assembled from block copolymers without functionalization are usually passive delivery systems, meaning that the target delivery to a particular site depends on the physico-chemical factors of the PNPs and anatomical/physiological factors of the target site, including size,[17] morphology,[18-19] and surface (corona) properties.[19-20] On the one hand, PNP size plays a crucial role in the drug delivery to cancerous site; it has been found that PNP on the colloidal scale (~10–100 nm) are favorably retained in tumor tissues throughout the distribution.[20-23] On the other hand, PNP morphology is shown to strongly affect the cellular uptake process.[18-19]

However, although rational design of PNPs with certain size and morphology increases the chance of delivery to the target site and of uptake by target cells, it could not eliminate the possibility of PNPs up-taken by non-target cells during the biodistribution thus still causing side effects.[16-17] Since PNP size and morphology generally plays a less important role in the intracellular release process than PNP internal structure (i.e., core-forming chain composition, core-forming chain conformation, and core-forming chain

crystallinity), a mechanism of "double protection" should be established so that drug release would only occur within the target cells.[24-25]

Recently, stimuli-responsive degradation (SRD) strategies have been applied to design smart PNP platforms that enable more controlled and selective intracellular release of drugs.[24-25] For applications in chemotherapy in particular, SRD strategies consider the specific biological characteristics of cancerous tissues in order to develop mechanisms of enhanced release that are specific to the environment of the cancerous cell.[26] This is in contrast to passive release relying solely on the diffusion mechanism, in which drug is released at the same rate within cancerous and non-cancerous cells. SRD involves cleavable covalent bonds within the copolymer structure which are cleaved in response to intracellular stimuli, thus causing PNP degradation and concomitant release of encapsulated drug.[24-25] For cancer chemotherapy, the elevated levels of glutathione (GSH, a cysteine-contained tripeptide) found in cancer cells is of particular interest as an external stimulus.[27] Disulfide linkages (-S-S-) introduced into the structure of a block copolymer can be cleaved to the corresponding thiols in the presence of GSH or other reducing agents, providing an active release mechanism for GSH-responsive polymeric nanomedicines.[28-29]

Conventional manufacturing approaches for PNPs generally relies on some element of chemical control to modulate the structural and therapeutic properties of the nanomedicine. For example, in SRD PNPs specifically, changes in the composition, concentration and location of cleavable linkages *via* polymer synthesis can be used to tune the PNP size, morphology, and responsivity.[30-32] On the other hand, microfluidics provides a fascinating manufacturing method for controlling PNP structure and drug delivery characteristics without changes in the formulation chemistry or the structure and

composition of constituent block copolymers.[33-34] In our group, we have applied a two-phase liquid–gas microfluidic reactor to manipulate PNP formation using various block copolymers.[35-47] Briefly, the localized high-shear "hot spots" within the corners of the gas–liquid plugs have been shown to affect PNP shear processing, enabling control of PNP size, structure, and drug delivery properties by simple changes in the microfluidic flow rate.[40, 42, 44-47] To our knowledge, prior to this thesis research, there had been no investigations into the potential of microfluidic shear processing for controlling the structure and properties of biological responsive PNPs for drug delivery.

In this thesis, we demonstrate microfluidic shear processing control over the structure and drug delivery properties of PNPs consisting of a GSH-responsive amphiphilic block copolymer with dual-location of disulfides at the hydrophobic/hydrophilic junctions and within the hydrophobic chains. Specifically we show that microfluidic manufacturing control can be applied to direct PNP sizes, morphologies, internal structure, GSH responsivity, drug loading, GSH-triggered drug release, cell uptake, cytotoxicity, and selectivity. The particular block copolymer used in this work was synthesized by Arman Moini Jazani in the group of our collaborator Prof. John Oh (Department of Chemistry and Biochemistry, Concordia University). Prof. Oh's group has previously published on the drug delivery properties of PNPs manufactured from similar block copolymers using conventional bulk methods.[32] The results of this thesis should provide some fundamental insights into the formation of PNPs under high shear in microfluidic channels, along with shedding a light on the potential for future commercial applications of manufacturing biological responsive PNPs using microfluidics.

1.2 Block Copolymers and Their Self-Assembly

1.2.1 Basic Concepts of Polymers

A *polymer* is a compound with a high molecular weight, which consists of repeating structural units (*repeat units*) linked by covalent bonds.[48-50] The repeat units are derived from the structure of the molecules (*monomers*) that react to form the polymer through polymerization. The structural formula for a polymer describes the composition and number of the constituent repeat units. For example, the structure of a polyethylene (PE) sample consisting of an average of *n* ethylene repeat units can be drawn as Figure 1-1, in which the repeat unit is included in the bracket, while the average number of repeat units, *n*, is shown as a subscript. The mean number of the repeat units, *n*, is also referred to as degree of polymerization (DP).[48-50] The molecular weight of a polymer, *M*, can be calculated based on DP and the molecular weight of the repeat units, M_0: $M = M_0 \bullet \mathrm{DP}$.

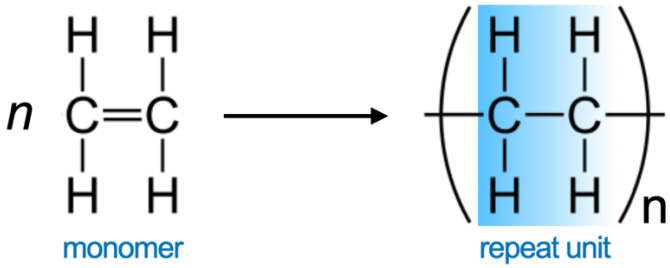

Figure 1-1. Structural formula of polyethylene formed by ethylene (monomer) *via* polymerization.

When the macromolecule consists of only one type of monomer, it is called a *homopolymer* (Figure 1-2A). If the polymer chain is composed of two types of repeat unit, it is called *copolymer* (Figure 1-2B to E).

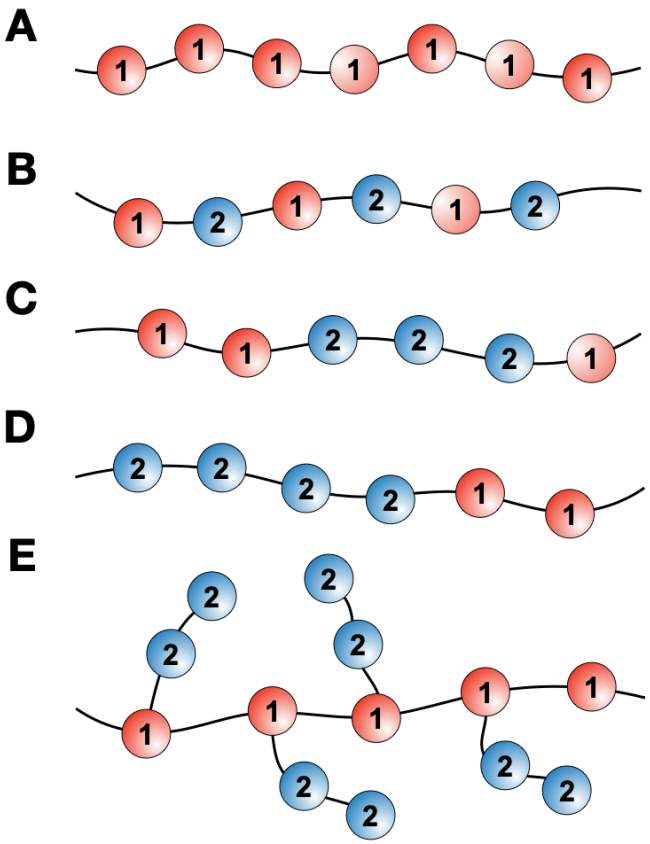

Figure 1-2. Schematic illustrations of (A) homopolymers, (B) alternating copolymers, (C) random copolymers, (D) block copolymers, and (E) grafted copolymers.

Since a copolymer contains at least two different repeat units, it can be categorized according to the organization of its repeat units.[48-50] Figure 1-2B to E shows four possible architectures arising from two different repeat units labeled 1 and 2. In summary, *alternating copolymers* (Figure 1-2B) refer to copolymers with two repeat units distributed in an alternating fashion along the polymer chain such that the mole fraction of both in the copolymer is ~50%. While *random copolymers* (Figure 1-2C) are copolymers in which the two repeat units are distributed randomly along the chain. *Block copolymers* (Figure 1-2D) are copolymers with each repeat unit clustered together and forming "blocks" of repeat units. *Graft copolymers* (Figure 1-2E) are branched polymers, in which the branches and backbone consist of different repeat units.

Polymer samples generally contain a distribution of chains of varying molecular weights.[50] The molecular weight of a polymer therefore refers to the *average* molecular weight of the distribution. There are two main ways for representing the polymer molecular weight average: namely, the number-average molecular weight (M_n), and the weight-average molecular weight (M_w).[50] M_n is calculated from the total weight of all the polymer molecules in a sample divided by the total number of polymer chains: $M_n = \frac{\sum_i N_i M_i}{\sum_i N_i}$. Colligative methods, such as osmotic pressure can be used to determine M_n since number of molecules can be effectively counted using these method. While M_w depends not only on the number of polymer chains, but also the weight of each polymer chain. In fact, bigger polymer chains contain more of the total mass of the mixture. When considering the weight factor, N_i is replaced with w_i where w_i is the total weight of chains in fraction i: $w_i = N_i W_i$ so that $M_w = \frac{\sum_i w_i M_i}{\sum_i w_i} = \frac{\sum_i N_i M_i^2}{\sum_i N_i M_i}$. Light scattering technique which depends on the size rather than number of molecules can be used to determine M_w.

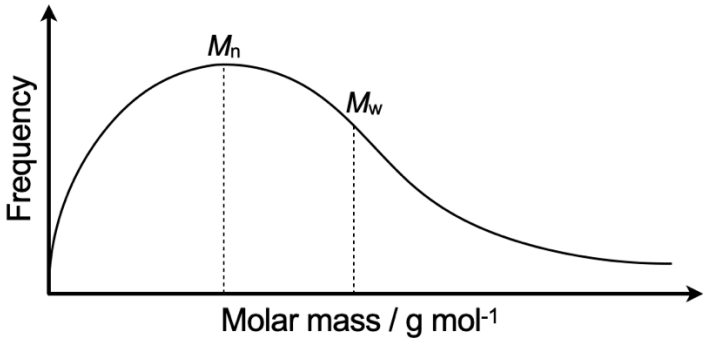

Figure 1-3. Molecular weight distribution of a polymer mixture. Reprinted and adapted from ref. 50. Copyright 2007 CRC Press.

The molecular weight distribution of a polymer mixture can be illustrated by plotting the number of polymer chains versus molecular weight, as shown in Figure 1-3. For a monomodal distribution, M_w is larger than M_n as polymer chains with higher M contribute

more to M_w than M_n. In general, it is more appropriate to use M_w to characterize polymers than M_n, because the performance of polymers is usually more dependent on molecules with larger molecular weights.

There is a numerical way representing the breadth of the molecular-weight distribution of a polymer mixture. The term molar-mass dispersity is defined as $Đ = \frac{M_w}{M_n}$.[50] It is clear that $Đ = 1$ when $M_w = M_n$, i.e., all polymer chains are with the same molecular weight and thus the sample is *monodisperse*. However, a monodisperse sample is a theoretical limit that cannot be experimentally achieved by current polymerization techniques.

1.2.2 Self-Assembly of Block Copolymers

The spontaneous self-assembly of block copolymers with thermodynamically incompatible blocks in a selective solvent into various micellar colloids termed polymer nanoparticles (PNPs) has been studied both theoretically and experimentally since the 1990s.[48-52] Understanding the mechanisms of the block copolymer self-assembly and the variability of PNP size and morphology as functions of experimental parameters, including block copolymer composition, concentration, solvent, and water content, is of immense importance for applications in numerous areas including cosmetics,[53] medical sensors,[54] and drug delivery.[11-16]

The amphiphilic copolymers consisting of both hydrophilic and hydrophobic blocks self-assembly under aqueous conditions would result in PNPs with hydrophobic-block forming core and hydrophilic-block forming coronae. In such case, PNP are referred as *regular* PNPs. On the other hand, if such amphiphilic copolymer self-assembly occurs in organic solvents, the resulting PNPs would consists of hydrophilic cores and hydrophobic

coronae, and such formation is referred as *reverse* PNPs. For either regular or reverse cases, "*crew-cut*" PNPs are referred to those with relatively long core-forming blocks and short coronae-forming blocks, while "*star-like*" PNPs are referred to those with relatively short core-forming blocks and long coronae-forming blocks.[51] A schematic of PNPs with different formations is shown below in Figure 1-4.

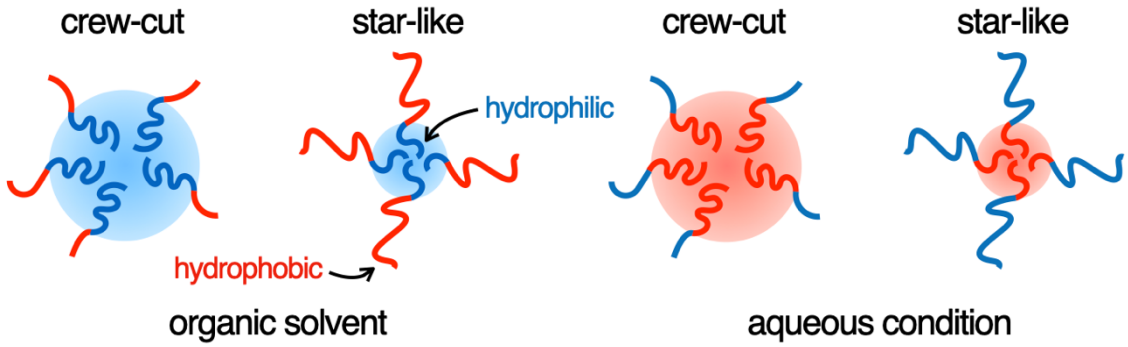

Figure 1-4. Schematic illustrations of the block copolymer self-assembly in various solvents.

In general, the block copolymer self-assembly upon appropriate solvent conditions is a spontaneous process; microphase separation allows the system to achieve minimum Gibbs free energy, G, based upon the equilibrium between the copolymer aggregates (micelles) and molecularly dispersed copolymer chains. At a fixed temperature T, the fundamental thermodynamic equation relating the change in system G and changes in system enthalpy H and entropy S is:[51-52]

$$\Delta G = \Delta H - T\Delta S$$

Self-assembly at a fixed temperature and pressure would only spontaneously occur when $\Delta G < 0$, which depends on the signs and magnitudes of the corresponding enthalpy and entropy changes. The thermodynamics of self-assembly in organic solvents have been investigated for several copolymer systems, including polystyrene-*block*-poly(acrylic acid) (PS-*b*-PAA),[55] polyethylene-*block*-polypropylene oxide-*block*-polyethelene (PEO-*b*-PPO-

b-PEO),[56] and polystyrene-*block*-polyisoprene (PS-*b*-PI),[57] and found to be enthalpically driven. In organic solvent, an entropic penalty ($\Delta S < 0$) would occur because of the localization of block junctions at the core/coronae interface (loss of translational entropy) and the chain stretching within the core- and coronae-forming blocks (loss of conformational entropy). On the other hand, an enthalpic loss ($\Delta H < 0$) would also occur due to its transformation from high energy polymer−solvent interactions low energy interactions between core-forming blocks. In fact, $\Delta H < -T\Delta S$ so that $\Delta G < 0$, i.e., the such self-assembly process remains spontaneous.

In contrast to organic conditions, the copolymer self-assembly under aqueous conditions is an entropically driven process; the hydrophobic effect raised by water molecules around the block copolymers drives the self-assembly process.[55] Specifically, introducing hydrophobic polymer blocks into water leads to the reconstruction of hydrogen bonds between water molecules and formation of water "cages" around the blocks. Such process induces an entropy loss of the water molecules. While the hydrophobic blocks are encapsulated within the cores and removed from the water, the entropy of the water thus increases ($\Delta S > 0$) promoting self-assembly.

In this thesis, we used a mixture of polar organic solvent (DMF) and water as the media driving the self-assembly of dissolved block copolymers. Eisenberg group have studied the thermodynamics of PS-*b*-PAA self-assembly in DMF/water mixture with varying water content.[60-63] Based on these studies, the PS-*b*-PAA self-assembly in DMF/water mixture appeared to be both an enthalpically and entropically driven process; the determining factor is the water content. At low water contents (< 5 wt%), the transformation of unfavorable polymer−solvent interactions to favorable polymer−

polymer and solvent−solvent interactions would lead to a negative enthalpy change, which would drive the self-assembly. However, at higher water contents (> 15 wt%), the strong hydrophobic effect raised by water molecules around the hydrophobic polymer chains would cause a positive enthalpy change. The recovery of free water molecules would also cause a positive entropy change, thus overwhelming the enthalpic penalty and driving the self-assembly.

During the PNP formation, three sources of the system Gibbs free energy determine the PNP morphologies, namely core-forming chain stretching, interfacial forces, and corona-forming chain interaction.[60] For example, Eisenberg and coworkers investigated the effect of copolymer concentration on the resulting PNP morphologies using PS-*b*-PAA (Figure 1-5).[61] When increasing the PS-*b*-PAA concentration in the solvent/water mixture at a fixed water content, the observed morphologies changed from monodispersed spheres to the mixture of spheres and short rods. With further increasing of the copolymer concentration, only long cylinders could be observed. Since the increase of the copolymer concentration would lead to higher aggregation number of the resulting PNPs, the core density of the PNPs would increase and PS would undergo chain-stretching. The system would have the tendency to lower the free energy *via* lowering the curvature, which leads to formation of the cylinders (Figure 1-5F).

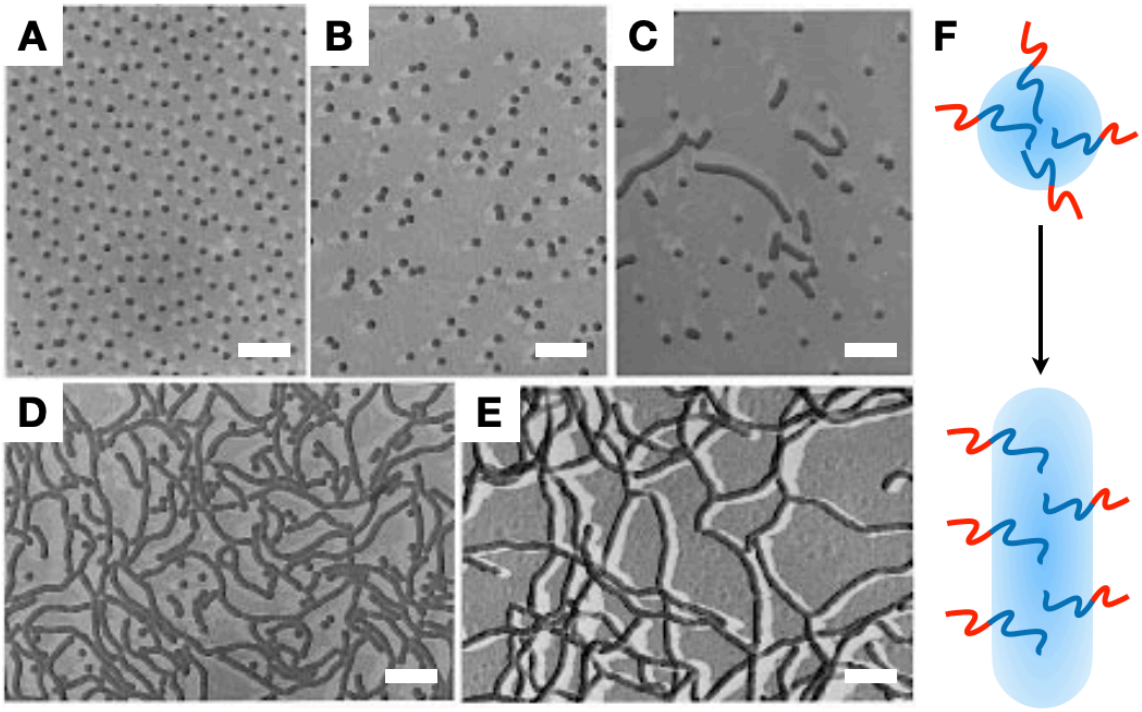

Figure 1-5. Aggregates made by dissolution of PS_{190}-*b*-PAA_{20} in a 94.5/5.5 (w/w) DMF/water mixture to different final copolymer concentrations at (A) 1.0, (B) 2.0, (C) 2.5, (D) 3.0, and (E) 3.5 wt %. (F) Schematic of morphological transition from spheres to cylinders. Reprinted and adapted from ref. 61. Copyright 1999 American Chemical Society.

In the same study, the effect of water content in the solvent mixture was also investigated.[61] As shown in Table 1-1, in the case of low water content, PNP morphology was observed to have high curvature, while PNPs tended to have lower curvature when the initial water content was higher. This transition is understandable, since the aggregation number of the resulting PNPs would increase with the water content increasing, which would trigger a morphological transition to lower curvature in order to reduce PS chain stretching.

Table 1-1. Morphologies[a] of PS_{190}-*b*-PAA_{20} formed at different polymer concentration and water content

Polymer concentration / wt %	Water content / wt %				
	5.5	6.5	7.5	8.5	9.5
0.5		S	R, S	R, S	
1.0	S	S	LR	LR	B
1.5	S	S, R	LR, XR	XR, B	
2.0	S	R, S			
2.5	S, R	LR	B		
3.0	R, S				
3.5	LR	B, XR	B	B	

[a]Morphologies are indicated as S (spheres), R (rods), LR (long rods), XR (interconnected rods), B (bilayer structures, including vesicles, lamellae, and large compound micelles). The major morphology is first given if there are multiple ones. Reprinted and adapted from ref. 61. Copyright 1999 American Chemical Society.

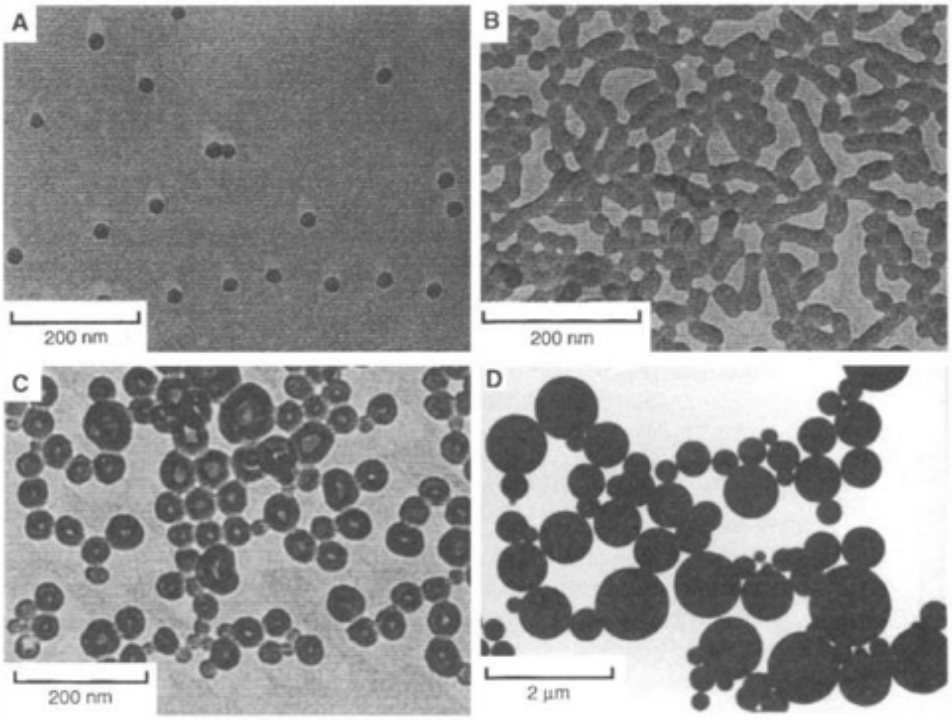

Figure 1-6. Morphologies of micellar aggregates from (A) PS_{200}-*b*-PAA_{21}, (B) PS_{200}-*b*-PAA_{15}, (C) PS_{200}-*b*-PAA_{8}, (D) PS_{200}-*b*-PAA_{4}. Reprinted and adapted from ref. 62. Copyright 1995 American Association of the Advancement of Science.

Polymer composition was also investigated as an influencing factor for PNP formation.[62] As shown in Figure 1-6, with PAA block length decreasing and PS block length constant, the formed PS-*b*-PAA PNPs transform from spheres to rods, vesicles, and eventually large compound micelles (LCMs). Since the decrease in PAA block length would cause the increase of PS chain stretching in the core, the PNPs tend to reduce chain stretching and entropy penalty by transforming morphology to lower-curvature ones. The effect of PAA block length was also investigated and a scaling law was used to show the relationship between core dimension R_{core} and block lengths of the spheres:[63]

$$R_{\text{core}} \propto {N_{\text{PS}}}^{0.4} {N_{\text{PAA}}}^{-0.15}$$

In conclusion, the PNP structure can be tuned by the manipulation of the formulation chemistry (copolymer composition) and intramolecular forces (water content, solvent type, copolymer concentration, etc.), which we call "*bottom-up*" control. Instead of changing the formulation component of both copolymer and solvent environment to modulate PNP structure, an entirely different approach utilizing external forces (including electric/magnetic field, temperature, and shear), which we call "*top-down*" control, gives promising potential of the precise PNP preparation without chemical control. In section 1.4, the "top-down" control *via* a microfluidic device will be discussed in further details.

1.2.3 Block Polymer Nanoparticles for Drug Delivery

As previously mentioned, PNPs self-assembled from amphiphilic block copolymers are of particular interest for drug delivery applications because their size and morphological variability are well suited to passive targeting, and the ease of surface functionalization provides opportunities for active targeting.[11-16] In PNP delivery systems, the hydrophilic corona (usually consisting of polyethylene oxide, or PEO) acts as a shield

against the reticular endothelial system (RES) and renal clearance, improving circulation time and biodistribution.[65] Furthermore, the hydrophilic chains can be functionalized with various ligands (proteins or antibodies) inducing active targeting to specific type of cells.[66] For targeting cancerous tissue, PNPs on the colloidal scale (~10 – 100 nm) are favorably extravasated *via* enhanced permeability and retention (EPR) effect, thus decreasing the side effects of the encapsulated drug to healthy tissues.[20-23]

In the previous section, the composition and relative lengths of both hydrophobic and hydrophilic blocks were shown to be critical factors influencing the size, morphology, and drug delivery properties of the self-assembled PNPs. For example, the composition of hydrophobic chains can be modulated to improve drug encapsulation,[67] while changes in the hydrophilic chain composition can improve PNP pharmacokinetics.[68] Along with the effects of polymer composition on PNP structure and drug delivery properties, manufacturing approaches offer continuous and convenient variability of PNP structure as discussed in the previous section. In general, composition (synthetic chemistry) and manufacturing (engineering and physical chemistry) will jointly affect PNP structure and drug delivery properties.

Our group has extensively studied the effects of both composition and manufacturing variables on PNP drug delivery properties. For example, Xu *et al.* investigated the self-assembly and drug delivery properties of a series of poly(methyl caprolactone-*co*-caprolactone)-*block*-poly(ethylene oxide) [P(MCL-*co*-CL)-*b*-PEO] with variable MCL contents.[69] The resulting PNPs showed nonmonotonic trends in sizes and morphologies with increasing MCL content, while PNPs incorporated with paclitaxel (PAX) showed faster release and increased antiproliferation potency against human breast

adenocarcinoma (MCF-7) cells with increased MCL contents. A selected copolymer with fixed MCL content was also used for PNP manufacturing using the two-phase microfluidic reactor, which further showed release rates and antiproliferation potency that depended on the manufacturing flow rate.

Also in our group, Bains *et al.* investigated the effect of hydrophobic PCL length and manufacturing method on PNP structure and drug delivery characteristics using PEO-*b*-PCL.[44] The resulting PNPs show sizes, morphologies, and loading efficiencies that depend on both the PCL block length and the manufacturing condition. Furthermore, PNPs prepared using microfluidic manufacturing showed slower drug release and higher potency against MCF-7 cells than those formed using conventional bulk nanoprecipitation, demonstrating the utility of using microfluidic manufacturing variables such as flow rate to tune and optimize drug delivery properties of PNP formulations.

1.3 Stimuli-Responsive Polymer Nanoparticles

1.3.1 Basic Concepts of Stimuli-Responsive Degradation (SRD)

By tuning PNP sizes, morphologies, and surface properties, scientists have demonstrated the ability to control the pharmacokinetics and biodistributions of delivery vehicles, providing control over where drugs localize within the body.[11-16] However, more selective delivery strategies are needed at the intracellular level. Specifically, tailored on-demand (switch on/off) drug release is needed to further enhance targeting at the cellular level and thus minimizing side effects. Recently, the concept of stimuli-responsive degradation (SRD) has generated interest as a strategy for polymeric drug delivery vehicles with programmed intracellular drug release.[24-25] Stimuli-responsive polymers refer to a class of polymers that undergo significant physical or chemical changes in response to

external environmental stimuli (temperature, pH, light, ionic strength, electric field, pressure, etc.).[70] In terms of drug delivery applications, PNPs self-assembled from copolymers with SRD characteristics can recognize specific biochemical stimuli within the target cells, hence degrading and releasing their drug *via* bond cleavage and PNP degradation. The design principles of specific stimuli-responsive PNPs are based on the microenvironment of the target cells. Taking cancer cells as an example, lower pH and higher levels of oxidization-reduction agents are found in cancer cells due to their accelerated metabolism cycles.[26] Therefore, it is possible to design pH- or redox-sensitive PNPs that exploit these endogenous stimulus for targeted anti-cancer drug delivery.

1.3.2 Glutathione-Responsive Polymer Nanoparticles for Drug Delivery

Glutathione is a tripeptide-based mixture ubiquitous in the environment of human cells.[27] The existing forms of glutathione in the human body are mainly reduced glutathione (GSH) and oxidized glutathione (GSSG). As shown in Figure 1-7, the molecular structure of GSH is glutamic acid-cysteine-glycine (Glu-Cys-Gly), while two GSH molecules would be covalently bonded by a disulfide (-S-S-) to form GSSG *via* an oxidation reaction.[27]

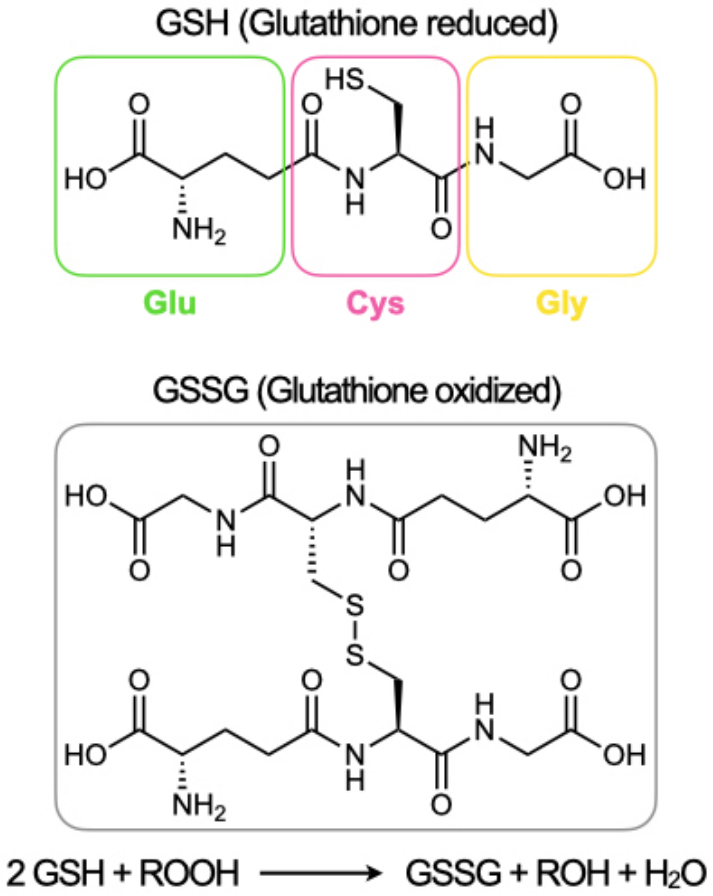

Figure 1-7. Molecular structure of GSH and GSSG.

GSH and GSSG are the most abundant redox pair in human cells. They are present in mitochondria, cytoplasm and nucleic acids in cells and participate in maintaining the dynamic balance of reduction potentials in cell signaling and secretory pathways.[27] GSH accounts for the vast majority of total glutathione under normal physiological conditions.[27] In humans, micromolar concentrations of GSH are found in the extracellular environment. For example, Jones and coworkers measured the glutathione concentration in human plasma, which was found to be 1.53 μM,[71] while Smith and coworkers measured the GSH concentration to be 2.4 μM in arterial plasma of newborn infants.[72] In the intracellular environment, due to the presence of reduced coenzyme II (NADPH) and glutathione reductase, GSH is found in the cytosol of most normal cells to be in the range 1 – 2 mM,[73]

or about three orders of magnitude higher than in the extracellular environment. On the other hand, cancerous cells show much more elevated levels of GSH compared to normal cells. For example, it has been shown that cellular GSH concentrations were 7-fold higher in human lung adenocarcinoma (A549) cells compared to a normal human lung fibroblast (CCL-210) cells, which was attributed to the faster metabolism cycles and lower pH in the cancer cells.[74] Furthermore, a recent study showed GSH concentrations of multiple cancer cell lines to vary from 5 mM to 10 mM.[75]

The different GSH levels of extracellular, healthy intracellular, and cancerous intracellular environments can be exploited for selective drug release in cancerous intracellular environments. Therefore, researchers have designed GSH-responsive polymer materials for producing drug delivery vehicles. The main strategy for GSH-responsive polymer design is disulfide chemistry.[28-29] Disulfide bonds (-S-S-) are formed by covalent attachment of two thiol groups, while the presence of GSH can promote disulfide degradation to thiols.[28-29] Thus, disulfide linkages introduced into the structure of a block copolymer provides a mechanism for GSH-triggered degradation.

Within a block copolymer, disulfide linkages can be located at the junction of the hydrophilic and hydrophobic blocks, providing self-assembled PNPs with GSH-cleavable coronal chains. For example, Tang and coworkers reported a design of biodegradable block copolymer of composition poly(caprolactone)-poly(ethyl ethylene phosphate) with a disulfide at the block junction (PCL-ss-PEEP).[30] The resulting copolymer self-assembled into PNPs with detachable coronal chains under GSH stimulus. The PNPs showed rapid size increase upon GSH incubation, indicating the hydrophilic coronal chains were detached and thus the PNPs formed large aggregates in the aqueous media. Accordingly,

the PNPs also showed faster drug release upon incubation in GSH-containing media than in media without GSH. A549 cell-based assays confirmed enhanced growth inhibition using drug-loaded PNPs with disulfide junctions compared to PNPs without disulfide junctions (PCL-*b*-PEEP), indicating GSH-triggered intracellular drug release.[30]

Alternatively, the disulfide linkages can be introduced within the hydrophobic block, leading to GSH-triggered degradation of the PNP hydrophobic cores and subsequent drug release. Khorsand and coworkers synthesized a block copolymer (PEO-*b*-PHMssEt) consisting of a hydrophilic PEO and a hydrophobic methacrylate block bearing pendant disulfides (PHMssEt).[31] Upon GSH incubation, the cleavage of the pendant disulfides within the hydrophobic core led to fast PNP destabilization (i.e., rapid size increase and drug release from the core). In HeLa cells with GSH pre-treatment, the PNPs showed enhanced antiproliferation potency compared to cells without GSH pre-treatment, confirming GSH-responsive intracellular release.[31]

More recently, a dual-location strategy was introduced in the design of stimuli-responsive block polymers bearing disulfides. Chan and coworkers reported the synthesis and characterization of a block polymer with dual-locations of disulfides.[32] The block copolymer consists of a hydrophilic PEO block and hydrophobic PHMssEt block, similar to the one in ref. 31. However, disulfides are also located at the junction between the hydrophilic and hydrophobic blocks (PEO-ss-PHMssEt). Such a dual-location strategy provides the mechanism for PNP coronal chain detachment (causing PNPs aggregation) and PNP core destabilization (causing drug release) upon GSH stimulus. A similar PEO-ss-PHMssEt polymer is also used in the work described in this thesis as a representative GSH-responsive polymeric system.[32]

Current approaches to controlling the structure and drug delivery properties of GSH-responsive PNPs are mostly chemical in nature,[29] requiring changes in the formulation chemistry (solvent, water content, drug and polymer concentration) or else requiring the design and synthesis of new copolymers with variable composition, number, and locations of disulfide linkages.[30-32] In contrast with such bottom-up methods involving changes in chemical variables, top-down approaches utilize external force fields such as mechanical shear to manipulate PNP structure and function. For example, rapid mixing and tunable shear-field processing in two-phase microfluidics reactors have been shown to provide a simple control handle based on variable flow rate on PNP manufacturing.[33-34] The fundamental concepts of microfluidics and the application of microfluidics to PNP manufacturing will be discussed in the next section.

1.4 Microfluidics

1.4.1 Basic Concepts of Microfluidics

Microfluidics, or lab-on-a-chip, which is defined as controlling fluid flow in the volume range of 10^{-6} – 10^{-8} L with length scales on the range of 10^{-5} – 10^{-4} m, provides advantages of controlled mixing, increased heat and mass transfer, and high throughput compared to fluid flow on the macroscale.[76] Flow at the microscale shows vast different characteristics from macroscale flows (> 10^{-3} m). Generally, the fluid surface-to-volume ratio increases with the length scale shrinking. Surface tension and viscous forces which are inversely proportional to the channel diameter *d* would become dominant over gravity and inertial forces for microchannels.[76] The flow characteristics can be described by a dimensionless Reynolds number *Re*:[77-78]

$$Re = \frac{\rho v d}{\mu}$$

where ρ, v, and μ is the density, velocity and dynamic viscosity of the described fluid, while d is the diameter of the flow channel.[77]

Re is normally less than 1 within microfluidics because of the relatively small channel dimensions. In fact, a $Re < 2\,300$ characterizes *laminar flow*, in which fluid elements move slowly in parallel ordered streamlines.[77] On the contrary, a $Re > 4\,000$ describes *turbulent flow*, in which flow elements move in a chaotic fashion.[77] The laminar microfluidic flow is effectively instantaneous in the absence of inertia. There is no obvious irregular pulsation in the trajectory of the laminae, with only momentum exchange between adjacent fluid layers due to molecular thermal motion, and the layer-to-layer diffusional heat transfers.[77]

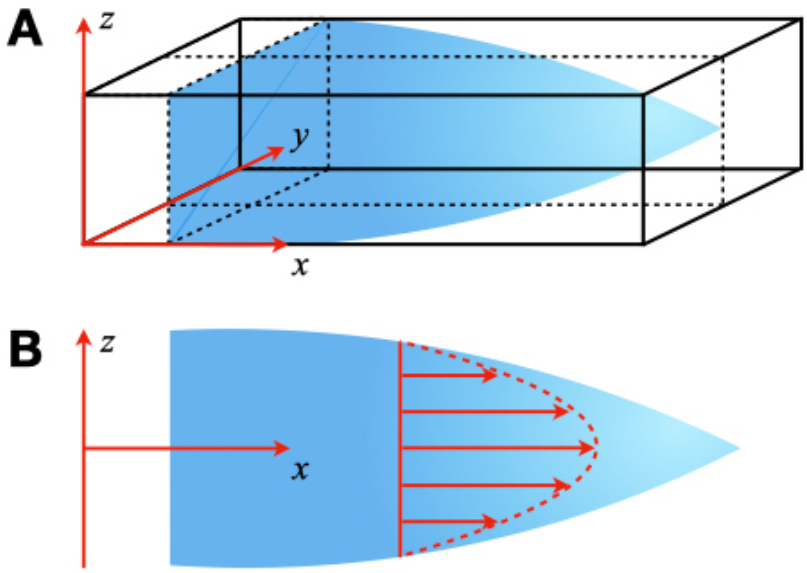

Figure 1-8. Schematics of (A) Poiseuille flow and (B) its *y*-sectional view. Adapted from Ref. 80. Copyright 2001 AIP Publishing LLC.

Microfluidic flow is generally pumped by external mechanical forces (pressure, electro-osmotic forces, etc.). In fact, pressure-driven flow (or *Poiseuille flow*, Figure 1-8) has been extensively studied and well-characterized. Poiseuille flow describes how a

incompressible viscous fluid moves through a long narrow cylindrical channel in a fashion of laminar flow, which is characterized by a parabolic velocity profile over the cross section of the channel (Figure 1-8):[79-80]

$$u_x = \frac{\Delta p}{4\eta L}(R^2 - z^2)$$

where the *x*-axial velocity u_x of a given coordinate (*x*, *y*, *z*) depends on the pressure drop Δp, fluid viscosity coefficient η, length *L* and radius *R* of the channel. According to the above equation, the maximum fluid velocity occurs at the center line ($z = 0$): $u_{x,\max} = \frac{\Delta p R^2}{4\eta L}$, while the minimum fluid velocity $u_{x,\min} = 0$ is at the interface between fluid layer and inner channel wall ($z = R$).[79-80] Since the velocity of fluid layer in direct contact with the channel wall (boundary) is identical to the velocity of the boundary, there is no relative movement between the boundary and fluid layer, therefore there is no slip and such condition is called *no-slip boundary condition*.[79-80]

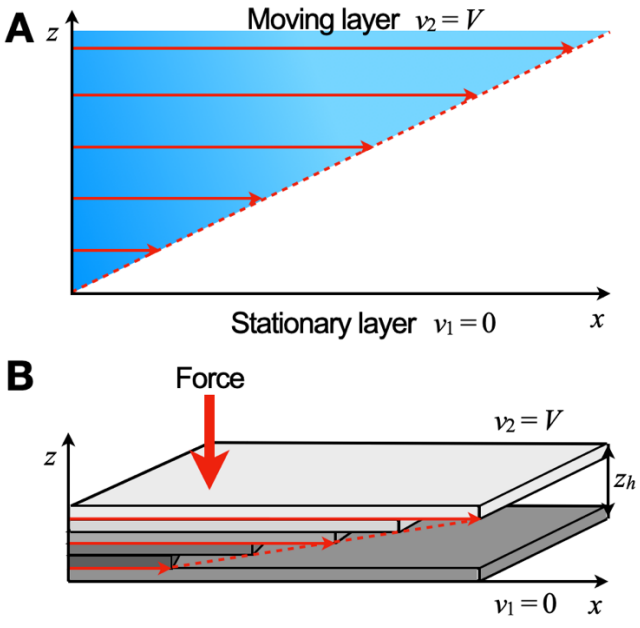

Figure 1-9. Schematic of the layer-to-layer translation of shear rate (A) and shear stress (B) in a simple shear model.

Shear rate can also describe the microfluidic flow characteristics. Shear rate is the rate of change in velocity at which one fluid layer passes over an adjacent layer. Shear rate is determined by both the geometry and velocity of the flow.[76,78] Figure 1-9A shows an example of simple shear, in which one layer of an incompressible viscous fluid moves parallel to another, and the friction is the driving force for motion transfer. If a layer moving with a velocity $v_2 = V$ transfers momentum downward layer-to-layer to a plate with no-slip condition (stationary layer, $v_1 = 0$), and the distance between moving and stationary layer is z_h, the shear rate $\dot{\gamma}$ of the moving layer can be calculated:

$$\dot{\gamma} = \frac{V}{z_h}$$

Incompressible flow will be affected by a reaction force in the cross-sectional direction F from the channel wall, and F can also be translated downward through the layers (Figure 1-9B). The shear stress τ is defined as the force F per area A. Viscosity η of the fluid can be further defined as the relationship between the shear stress τ and the shear rate $\dot{\gamma}$:

$$\tau = \eta\dot{\gamma}$$

For Newtonian fluids that have constant viscosity η, the shear force is proportional to shear rate $\dot{\gamma}$.[78] Generally, both rational design of microchannel geometry and increasing the pressure for pumping fluids would produce high shear force field within the channel, which could act as an external mechanical force for material manufacturing and processing in microfluidics. This will be discussed in further details in a next section.

A microfluidic reactor normally consists of a set of microchannels and incompressible viscous fluids moving through the channels.[78] In single-phase microfluidics, flow consisting of one fluid continuously occupies space within the microfluidic channels. In

two-phase microfluidics, two or more immiscible fluids (either liquid–liquid or liquid–gas) are injected into the microchannels and the *dispersed phase* is formed into segments with controlled volume under shear and compression from the *continuous phase*.[77] The microfluidic flow can be defined as *plug flow* when the dispersed phase is in contact with the channel walls (Figure 1-10A), while *droplet flow* describes the dispersed phase is completely surrounded by the continuous phase without contacting the inner walls (Figure 1-10B). Unless otherwise stated, the flow described in this thesis is plug flow.

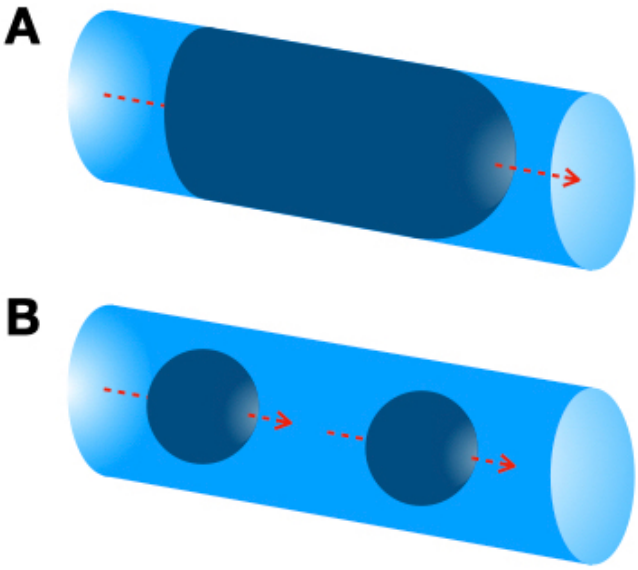

Figure 1-10. Schematics of (A) plug flow and (B) droplet flow in a microfluidic channel.

The manufacturing approach of microfluidic chips originates from the processing of semiconductors and integrated circuits, but the spatial scale of microfluidic chips is much larger than integrated circuits.[76] The size of a microfluidic reactor is usually constrained to several square centimeters, and the width and depth of microchannels are usually within the scale of micrometers. The microfluidic chip generally consists of microchannels molded in a polymer material which is bonded to a flat surface. The most commonly used polymer material and surface is polydimethylsiloxane (PDMS) and glass slide,

respectively.[76] In our group, we have been applying soft-lithography method for microfabrication which consists of several steps as described below:[81]

1. Design of microchannels: the layout of the microchannels is firstly designed with a dedicated software (such as AutoCAD), then it is printed on a photomask with UV opaque ink using specialized equipment.

2. Fabrication of microfluidic male-mold by photolithography (Figure 1-11): negative resin SU-8 is spin-coated and fixed on a silicon wafer with thickness which is equal to the height of microfluidic channels. Then the resin covered by the photomask with the microchannel pattern is exposed to ultraviolet light. Only the area presenting the microchannels are exposed to UV light and cured, while area covered by the opaque ink is protected. The mold is then submerged in a developer with the unexposed area etched. The mold is further washed by isopropanol to remove any etched portion.

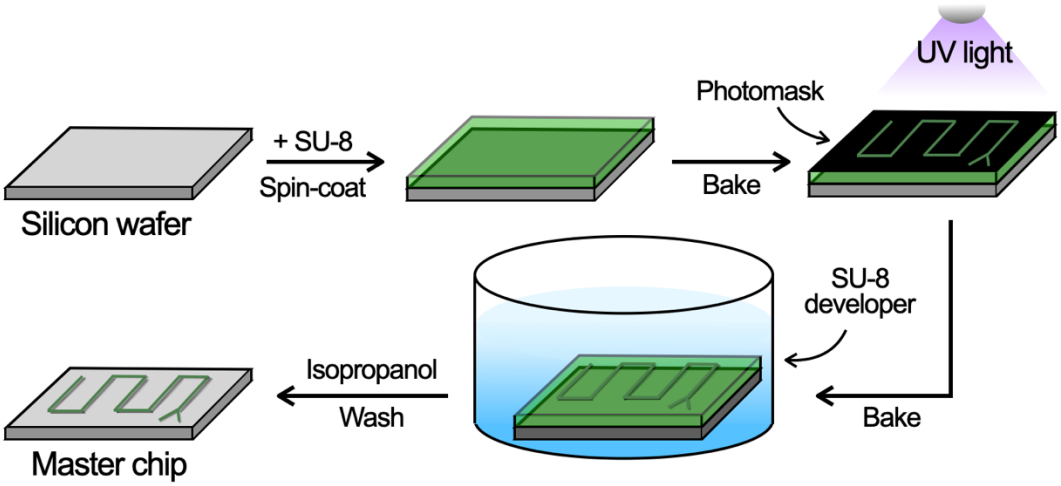

Figure 1-11. Schematic of fabrication of microfluidic male-mold by photolithography.

3. Molding of microfluidic chip (Figure 1-12): a mixture of PDMS and cross-linking (curing) agent is prepared, after degassed it is poured into the mold and heated. Once PDMS is hardened a replica of the microchannels can be taken off the mold. The glass slide is then covered by the PDMS face with microchannels and plasma-treated, during which

the plasma treatment allows PDMS on the mold and glass surface cross-linked to close the microfluidic chip.[82]

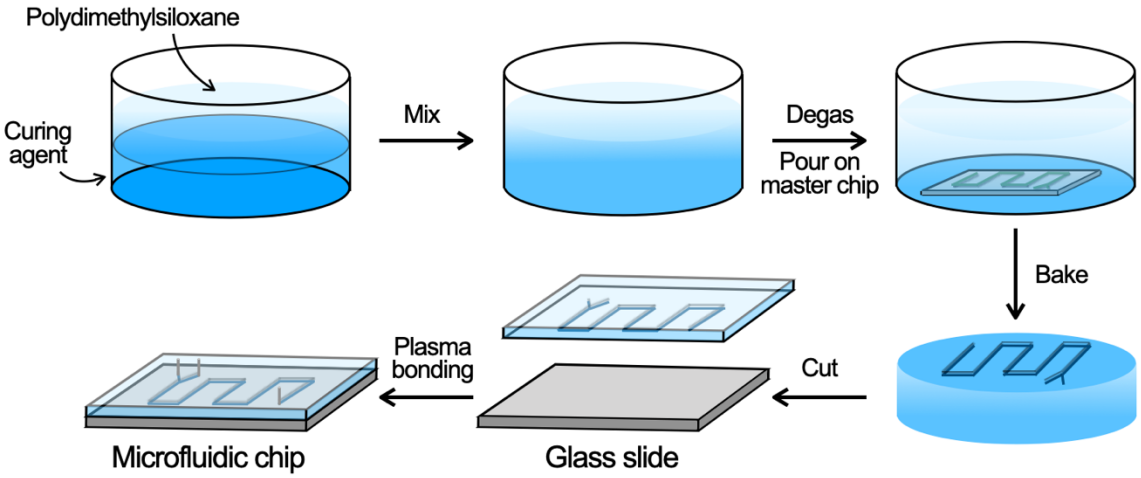

Figure 1-12. Schematic of microfluidic chip molding.

1.4.2 Gas-Segmented Microfluidic Reactor

The core strategy for microfluidic reactor design is fast and homogenous mixing for applications in materials synthesis. In single-phase microfluidic reactors, mixing within the flow is mainly by diffusion and is extremely slow due to the absence of turbulence and generating turbulence would require high velocity and pressure.[76,78] In addition, the variation of flow velocity in Poiseuille flow causes a heterogenetic distribution of mixing time cross the stream.[76,78] Comparing to single-phase microfluidic reactors that could not provide effective control in mixing, two-phase microfluidic reactors involving other streams of immiscible fluids shows enhanced control capability.

There are mainly two types of two-phase microfluidic reactor, liquid–liquid and liquid–gas, as shown in Figure 1-13.[83-85] In liquid–liquid segmented microfluidic reactor, liquid plugs with higher interfacial tension generally form the dispersed phase, while the other liquid acts as the continuous phase driving dispersed phase moving through the

microchannel (Figure 1-13A). While in liquid-gas segmented reactors, the liquid plugs are the continuous phase and are segmented by gas bubbles (Figure 1-13B).[83-85]

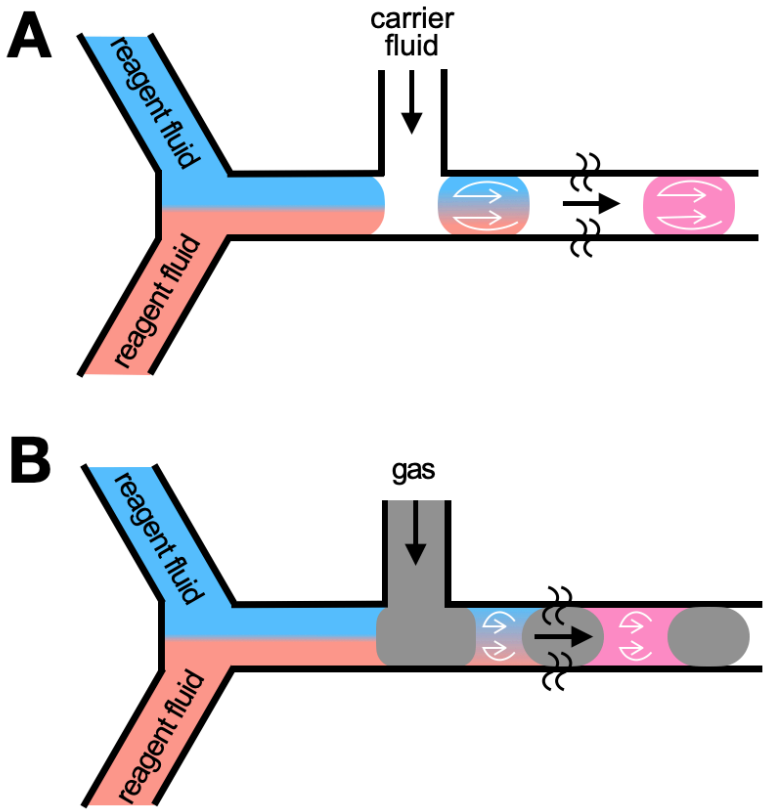

Figure 1-13. Schematics of (A) liquid–liquid and (B) liquid–gas microfluidic reactor, in which red circled arrows indicate the rotating vortices within the dispersed phase. Adapted from ref. 84. Copyright 2006 Wiley-VCH Verlag GmbH & Co. KGaA, Weinheim.

Our group has studied the fluid mechanics within a two-phase liquid–gas microfluidic reactor.[35-39] It has been confirmed that the recirculation of liquid plugs induces the formation of rotating vortices which increases mixing dramatically *via* chaotic advection. Moreover, the recirculating flow produced localized high-shear "hot spots" in the corner regions where the liquid plug and film contacts (Figure 1-14).[35-39] In the "hot spots", the significant velocity changes at the nanoscale (i.e., high shear rate $\dot{\gamma}$) could be a practical driving force field for controlling the nanoparticle synthesis.

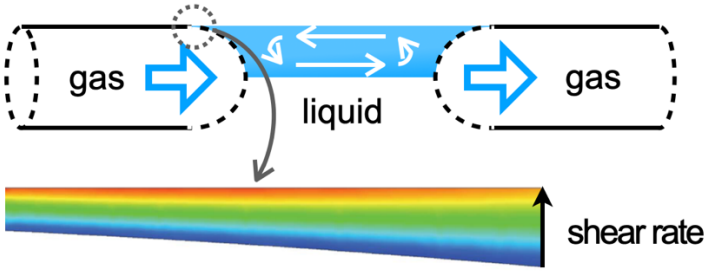

Figure 1-14. Schematic of rotating vortices and resulting localized high-shear "hot spots" within the liquid plugs in the two-phase liquid–gas microfluidic reactor. Adapted from ref. 36. Copyright 2008 American Chemical Society.

1.4.3 Microfluidics in Polymer Nanoparticle Manufacturing

As discussed in the previous section, microfluidics enable improved mixing between various components within the microchannels. In the gas-segmented microfluidic reactors particularly, the localized "hot spots" provide external high-shear fields, which is powerful for manipulation of PNP formation. For example, Chi-Wei Wang in our group has studied the PNP formation mechanism in the shear-environment using PS-*b*-PAA and a two-phase liquid–gas microfluidic reactor.[38] The experiments were carried out by injecting copolymer solution, solvent, and water/solvent mixture into the microchannels at a programmed flow rate. Compared to spherical PNPs self-assembled off-chip with an average size of ~40 nm, the on-chip PNPs show distinct cylindrical morphologies.[38] Such a difference between off-chip thermodynamically equilibrium structures and kinetically stable morphologies that are not globally equilibrated is explained by a mechanism of collision-coalescence enabled by strong and localized on-chip shear fields.[38] In the authors' postulated mechanism, the chaotic advection in the sinusoidal mixing channel firstly gave rise to initial PNPs formed by fast mixing of water with the copolymer solution (~1 s). Then the resulting PNPs within the liquid plugs traveled through the processing channel, undergoing localized shear-

environment at the plug corners and experiencing various shear-induced events, namely shear-induced collision-coalescence.[38]

In general, PNPs would undergo coalescence-collision during Brownian motion. The effect of shear force on PNP coalescence rates can be described by the dimensionless Peclet number:[86]

$$Pe = \frac{\dot{\gamma} a^2}{D_0}$$

where $\dot{\gamma}$ is the shear rate (proportional to shear force), a and D_0 is the PNP size and diffusion coefficient, respectively. It is clear that thermal diffusion dominates the coalescence rate when ($Pe \ll 1$), whereas the increase in Peclet number indicates the shear force has a stronger influence. In Wang's system, the PNPs with sizes of ~40 nm would undergo shear-induced coalescence at $\dot{\gamma}$ = ~10^4 s^{-1}, giving rise to shear-induced PNPs with larger size.[38]

On the other hand, the susceptibility of PNPs to breakup increase as the PNP size increases, generating smaller daughter particles. Capillary number, Ca, describes the effect of PNP size on breakup rate:[36-37]

$$\mathrm{Ca} = \frac{\eta_m \dot{\gamma} a}{2\Gamma}$$

where η_m is the viscosity of the dispersed phase, $\dot{\gamma}$ is the shear rate, a is the PNP size, and Γ is the interfacial tension between the dispersion phase and PNP core.

In summary, on-chip shear-induced coalescence and shear-induced breakup events and following intraparticle rearrangement could give rise to kinetically stable PNPs with size, morphology, and structure-determined characteristics that are distinct from the thermodynamically equilibrium structures. Moreover, both mechanisms are in competition

depending on particle size and shear rate, which opens up a possibility to construct colloids with specific structures and properties for various applications by simply tuning shear rate on the microfluidic devices. In contrast with bottom-up methods in which PNP synthesis and structure design exclusively depends on manipulations of chemical parameters (copolymer composition, solvent type, polymer concentration, pH, ionic strength, etc.), a top-down microfluidic approach that only requires the change in shear rate enables the preparation of PNP with specific structure and functions with high time-efficiency and throughput, which provides fascinating potential in material development.

1.5 Outline of This Thesis

In this thesis, we intend to establish a "nano-toolbox" for producing finely-tuned physicochemical and pharmacological properties in biological stimuli-responsive PNPs, by combining chemical synthetic control of cleavable function group location with microfluidic shear processing control of PNP sizes and morphologies. The remainder of this thesis consists of two experimental chapters, one literature review chapter, and one conclusion and future outlook chapter. Specific content for each chapter is summarized below:

Chapter 2 provides fundamental insights into the formation of biological stimuli-responsive PNPs under high shear in microfluidic channels. Using a two-phase gas-liquid segmented microfluidic reactor, a previously studied "DualM" copolymer that contains disulfides at the junction between hydrophilic poly(ethylene oxide) (PEO) block and hydrophobic methacrylate block and within the pendant chains of the hydrophobic blocks (PHMssEt) were fabricated into PNPs without encapsulation of drugs. We systematically investigated the effect of shear rate on the physicochemical properties of the on-chip PNPs,

including size, polydispersity, and morphology. Also, we illustrated the mechanism of microfluidic PNP formation in the presence of flow-variable high shear. Moreover, we found GSH-triggered changes in PNP size and internal structure were strongly and predictably dependent on both the manufacturing flow rate and the location of the cleavable lineages. The knowledge of such process-structure-responsivity relationship provides template for a *priori* design of specific PNP responsivities, and sheds a light on using microfluidics to control the drug delivery properties of the PNPs. This chapter has been published in *ACS Applied Materials & Interfaces* as an Article.[87]

Chapter 3 expands our mechanistic study on the microfluidic formation and physicochemical properties of the PNPs without encapsulated drug to a new focus on microfluidic control of the pharmacological properties of the PNPs containing either an anticancer drug or a florescent drug surrogate. We systematically investigated the effect of flow rate on various PNP drug delivery functions, including encapsulation efficiency, encapsulation homogeneity, GSH-triggered release rate, cellular uptake rate, cytotoxicity, and cell selectivity. We found that many of these flow-tunable properties scale linearly with PNP sizes, providing remarkably simple structure-property relationships that can be leveraged using the microfluidic control handle. This strategy should open up a microfluidic optimization pathway to design better and smarter nanomedicines. This chapter has been submitted to *ACS Biomaterials Science & Engineering* as an Article.

Chapter 4 summarizes recent advances of the development of biological reduction-responsive PNPs. We showed different design strategies for reduction-responsive block copolymers and the PNPs formed by their self-assembly with a main focus on illustrating the formation and redox-triggered degradation mechanisms. In addition, we carried out

data reanalysis for selected literatures that provided new insight on structure-responsivity relationship for various types of PNPs. Through numerous examples, we showed how established principles from copolymer design to PNP formation would open up vast possibilities for manufacturing smarter nanomedicines with controllable responsivities.

Chapter 5 contains main findings and conclusions from the thesis work, and suggests some directions for future work.

1.6 References

1. Gupta, S. P., Quantitative structure-activity relationship studies on anticancer drugs. *Chem. Rev.* **1994**, *94*, 1507-1551.

2. Perkins, R.; Fang, H.; Tong, W.; Welsh, W. J., Quantitative structure-activity relationship methods: perspectives on drug discovery and toxicology. *Environ. Toxicol. Chem.* **2003**, *22*, 1666-1679.

3. Baghel, S.; Cathcart, H.; O' Reilly, N. J., Polymeric amorphous solid dispersions: a review of amorphization, crystallization, stabilization, solid-state characterization, and aqueous solubilization of biopharmaceutical classification system class II drugs. *J. Pharm. Sci.* **2016**, *105*, 2527-2544.

4. Zhang, Y.; Chan, H. F.; Leong, K. W., Advanced materials and processing for drug delivery: the past and the future. *Adv. Drug Delivery Rev.* **2013**, *65*, 104-120.

5. Björnmalm, M.; Thurecht, K. J.; Michael, M.; Scott, A. M.; Caruso, F., Bridging bio–nano science and cancer nanomedicine. *ACS Nano* **2017**, *11*, 9594-9613.

6. Schreier, H.; Bouwstra, J., Liposomes and niosomes as topical drug carriers: dermal and transdermal drug delivery. *J. Controlled Release* **1994**, *30*, 1-15.

7. Sharma, A.; Sharma, U. S., liposomes in drug delivery: progress and limitations. *Int. J. Pharm.* **1997**, *154*, 123-140.

8. Lian, T.; Ho, R. J. Y., trends and developments in liposome drug delivery systems. *J. Pharm. Sci.* **2001**, *90*, 667-680.

9. Hörmann, K.; Zimmer, A., Drug delivery and drug targeting with parenteral lipid nanoemulsions – a review. *J. Controlled Release* **2016**, *223*, 85-98.

10. Singh, Y.; Meher, J. G.; Raval, K.; Khan, F. A.; Chaurasia, M.; Jain, N. K.; Chourasia, M. K., Nanoemulsion: concepts, development and applications in drug delivery. *J. Controlled Release* **2017**, *252*, 28-49.

11. Allen, C.; Maysinger, D.; Eisenberg, A., Nano-engineering block copolymer aggregates for drug delivery. *Colloids Surf. B* **1999**, *16*, 3-27.

12. Kataoka, K.; Harada, A.; Nagasaki, Y., Block copolymer micelles for drug delivery: design, characterization and biological significance. *Adv. Drug Delivery Rev.* **2001**, *47*, 113-131.

13. Rösler, A.; Vandermeulen, G. W. M.; Klok, H.-A., Advanced drug delivery devices via self-assembly of amphiphilic block copolymers. *Adv. Drug Delivery Rev.* **2001**, *53*, 95-108.

14. Tyrrell, Z. L.; Shen, Y.; Radosz, M., Fabrication of micellar nanoparticles for drug delivery through the self-assembly of block copolymers. *Prog. Polym. Sci.* **2010**, *35*, 1128-1143.

15. Gong, J.; Chen, M.; Zheng, Y.; Wang, S.; Wang, Y., Polymeric micelles drug delivery system in oncology. *J. Controlled Release* **2012**, *159*, 312-323.

16. Sun, T.; Zhang, Y. S.; Pang, B.; Hyun, D. C.; Yang, M.; Xia, Y., Engineered nanoparticles for drug delivery in cancer therapy. *Angew. Chem. Int. Ed.* **2014**, *53*, 12320-12364.

17. Gaumet, M.; Vargas, A.; Gurny, R.; Delie, F., Nanoparticles for drug delivery: the need for precision in reporting particle size parameters. *Eur. J. Pharm. Biopharm.* **2008**, *69*, 1-9.

18. Geng, Y.; Dalhaimer, P.; Cai, S.; Tsai, R.; Tewari, M.; Minko, T.; Discher, D. E., Shape effects of filaments versus spherical particles in flow and drug delivery. *Nat. Nanotechnol.* **2007**, *2*, 249-255.

19. Elsabahy, M.; Wooley, K. L., Design of polymeric nanoparticles for biomedical delivery applications. *Chem. Soc. Rev.* **2012**, *41*, 2545-2561.

20. Alexis, F.; Pridgen, E.; Molnar, L. K.; Farokhzad, O. C., Factors affecting the clearance and biodistribution of polymeric nanoparticles. *Mol. Pharmaceutics* **2008**, *5*, 505-515.

21. Maeda, H.; Wu, J.; Sawa, T.; Matsumura, Y.; Hori, K., Tumor vascular permeability and the EPR effect in macromolecular therapeutics: a review. *J. Controlled Release* **2000**, *65*, 271-284.

22. Maeda, H.; Nakamura, H.; Fang, J., The EPR effect for macromolecular drug delivery to solid tumors: improvement of tumor uptake, lowering of systemic toxicity, and distinct tumor imaging in vivo. *Adv. Drug Delivery Rev.* **2013**, *65*, 71-79.

23. Perry, J. L.; Reuter, K. G.; Luft, J. C.; Pecot, C. V.; Zamboni, W.; DeSimone, J. M., Mediating passive tumor accumulation through particle size, tumor type, and location. *Nano Lett.* **2017**, *17*, 2879-2886.

24. Ganta, S.; Devalapally, H.; Shahiwala, A.; Amiji, M., A review of stimuli-responsive nanocarriers for drug and gene delivery. *J. Controlled Release* **2008**, *126*, 187-204.

25. Mura, S.; Nicolas, J.; Couvreur, P., Stimuli-responsive nanocarriers for drug delivery. *Nat. Mater.* **2013**, *12*, 991-1003.

26. Joyce, J. A., Therapeutic targeting of the tumor microenvironment. *Cancer Cell* **2005**, *7*, 513-520.

27. Saito, G.; Swanson, J. A.; Lee, K.-D., Drug delivery strategy utilizing conjugation via reversible disulfide linkages: role and site of cellular reducing activities. *Adv. Drug Delivery Rev.* **2003**, *55*, 199-215.

28. Cheng, R.; Feng, F.; Meng, F.; Deng, C.; Feijen, J.; Zhong, Z., Glutathione-responsive nano-vehicles as a promising platform for targeted intracellular drug and gene delivery. *J. Controlled Release* **2011**, *152*, 2-12.

29. Oh, J. K., disassembly and tumor-targeting drug delivery of reduction-responsive degradable block copolymer nanoassemblies. *Polym. Chem.* **2019**, *10*, 1554-1568.

30. Tang, L.-Y.; Wang, Y.-C.; Li, Y.; Du, J.-Z.; Wang, J., Shell-detachable micelles based on disulfide-linked block copolymer as potential carrier for intracellular drug delivery. *Bioconjug. Chem.* **2009**, *20*, 1095-1099.

31. Khorsand, B.; Lapointe, G.; Brett, C.; Oh, J. K., Intracellular drug delivery nanocarriers of glutathione-responsive degradable block copolymers having pendant disulfide linkages. *Biomacromolecules* **2013**, *14*, 2103-2111.

32. Chan, N.; Khorsand, B.; Aleksanian, S.; Oh, J. K., A dual location stimuli-responsive degradation strategy of block copolymer nanocarriers for accelerated release. *Chem. Commun.* **2013**, *49*, 7534-7536.

33. Xu, S.; Nie, Z.; Seo, M.; Lewis, P.; Kumacheva, E.; Stone, H. A.; Garstecki, P.; Weibel, D. B.; Gitlin, I.; Whitesides, G. M., Generation of monodisperse particles by using microfluidics: control over size, shape, and composition. *Angew. Chem. Int. Ed.* **2005**, *117*, 734-738.

34. Karnik, R.; Gu, F.; Basto, P.; Cannizzaro, C.; Dean, L.; Kyei-Manu, W.; Langer, R.; Farokhzad, O. C., Microfluidic platform for controlled synthesis of polymeric nanoparticles. *Nano Lett.* **2008**, *8*, 2906-2912.

35. Schabas, G.; Yusuf, H.; Moffitt, M. G.; Sinton, D., controlled self-assembly of quantum dots and block copolymers in a microfluidic device. *Langmuir* **2008**, *24*, 637-643.

36. Schabas, G.; Wang, C.-W.; Oskooei, A.; Yusuf, H.; Moffitt, M. G.; Sinton, D., Formation and shear-induced processing of quantum dot colloidal assemblies in a multiphase microfluidic chip. *Langmuir* **2008**, *24*, 10596-10603.

37. Wang, C.-W.; Oskooei, A.; Sinton, D.; Moffitt, M. G., Controlled self-assembly of quantum dot−block copolymer colloids in multiphase microfluidic reactors. *Langmuir* **2010**, *26*, 716-723.

38. Wang, C.-W.; Sinton, D.; Moffitt, M. G., Flow-directed block copolymer micelle morphologies via microfluidic self-assembly. *J. Am. Chem. Soc.* **2011**, *133*, 18853-18864.

39. Wang, C.-W.; Sinton, D.; Moffitt, M. G., Morphological control via chemical and shear forces in block copolymer self-assembly in the lab-on-chip. *ACS Nano* **2013**, *7*, 1424-1436.

40. Bains, A.; Cao, Y.; Moffitt, M. G., multiscale control of hierarchical structure in crystalline block copolymer nanoparticles using microfluidics. *Macromol. Rapid Commun.* **2015**, *36*, 2000-2005.

41. Xu, Z.; Yan, B.; Riordon, J.; Zhao, Y.; Sinton, D.; Moffitt, M. G., Microfluidic synthesis of photoresponsive spool-like block copolymer nanoparticles: flow-directed formation and light-triggered dissociation. *Chem. Mater.* **2015**, *27*, 8094-8104.

42. Bains, A.; Wulff, J. E.; Moffitt, M. G., Microfluidic synthesis of dye-loaded polycaprolactone-block-poly(ethylene oxide) nanoparticles: insights into flow-directed loading and in vitro release for drug delivery. *J. Colloid Interface Sci.* **2016**, *475*, 136-148.

43. Xu, Z.; Lu, C.; Riordon, J.; Sinton, D.; Moffitt, M. G., Microfluidic manufacturing of polymeric nanoparticles: comparing flow control of multiscale structure in single-phase staggered herringbone and two-phase reactors. *Langmuir* **2016**, *32*, 12781-12789.

44. Bains, A.; Cao, Y.; Kly, S.; Wulff, J. E.; Moffitt, M. G., Controlling structure and function of polymeric drug delivery nanoparticles using microfluidics. *Mol. Pharmaceutics* **2017**, *14*, 2595-2606.

45. Xu, Z.; Lu, C.; Lindenberger, C.; Cao, Y.; Wulff, J. E.; Moffitt, M. G., Synthesis, self-assembly, and drug delivery characteristics of poly(methyl caprolactone-co-caprolactone)-b-poly(ethylene oxide) copolymers with variable compositions of hydrophobic blocks: combining chemistry and microfluidic processing for polymeric nanomedicines. *ACS Omega* **2017**, *2*, 5289-5303.

46. Chen, R.; Wulff, J. E.; Moffitt, M. G., Microfluidic processing approach to controlling drug delivery properties of curcumin-loaded block copolymer nanoparticles. *Mol. Pharmaceutics* **2018**, *15*, 4517-4528.

47. Cao, Y.; Silverman, L.; Lu, C.; Hof, R.; Wulff, J. E.; Moffitt, M. G., Microfluidic manufacturing of SN-38-loaded polymer nanoparticles with shear processing control of drug delivery properties. *Mol. Pharmaceutics* **2019**, *16*, 96-107.

48. Hamley, I. W.; Hamley, I. W., *The Physics of Block Copolymers*; Oxford University Press, 1998.

49. Sperling, L. H., *Introduction to Physical Polymer Science*; John Wiley & Sons, 2005.

50. Cowie, J. M. G.; Arrighi, V., *Polymers: Chemistry and Physics of Modern Materials*; CRC press, 2007.

51. Mai, Y.; Eisenberg, A., Self-assembly of block copolymers. *Chem. Soc. Rev.* **2012**, *41*, 5969-5985.

52. Atkins, P. W.; De Paula, J.; Keeler, J., *Atkins' Physical Chemistry*; Oxford University Press, 2018.

53. Panchal, A.; Fakhrullina, G.; Fakhrullin, R.; Lvov, Y., Self-assembly of clay nanotubes on hair surface for medical and cosmetic formulations. *Nanoscale* **2018**, *10*, 18205-18216.

54. Luk, B. T.; Zhang, L., Current advances in polymer-based nanotheranostics for cancer treatment and diagnosis. *ACS Appl. Mater. Interfaces* **2014**, *6*, 21859-21873.

55. Shen, H.; Zhang, L.; Eisenberg, A., Thermodynamics of crew-cut micelle formation of polystyrene-b-poly(acrylic acid) diblock copolymers in DMF/H_2O mixtures. *J. Phys. Chem. B* **1997**, *101*, 4697-4708.

56. Alexandridis, P.; Holzwarth, J. F.; Hatton, T. A., Micellization of poly (ethylene oxide)-poly(propylene oxide)-poly(ethylene oxide) triblock copolymers in aqueous solutions: thermodynamics of copolymer association. *Macromolecules* **1994**, *27*, 2414-2425.

57. Price, C.; Chan, E.; Mobbs, R.; Stubbersfield, R., A thermodynamic investigation of micelle formation by a polystyrene-b-polyisoprene block copolymer in n-hexadecane. *Eur. Polym. J.* **1985**, *21*, 355-360.

58. Maibaum, L.; Dinner, A. R.; Chandler, D., Micelle formation and the hydrophobic effect. *J. Phy. Chem. B* **2004**, *108*, 6778-6781.

59. Halperin, A.; Tirrell, M.; Lodge, T., Tethered chains in polymer microstructures. *Macromolecules: Synthesis, Order and Advanced Properties*, Springer, 1992. pp 31-71.

60. Zhang, L.; Eisenberg, A., Formation of crew-cut aggregates of various morphologies from amphiphilic block copolymers in solution. *Polym. Adv. Technol.* **1998**, *9*, 677-699.

61. Zhang, L.; Eisenberg, A., Thermodynamic vs kinetic aspects in the formation and morphological transitions of crew-cut aggregates produced by self-assembly of polystyrene-b-poly(acrylic acid) block copolymers in dilute solution. *Macromolecules* **1999**, *32*, 2239-2249.

62. Zhang, L.; Eisenberg, A., Multiple morphologies of "crew-cut" aggregates of polystyrene-b-poly(acrylic acid) block copolymers. *Science* **1995**, *268*, 1728-1731.

63. Zhang, L.; Eisenberg, A., Multiple morphologies and characteristics of "crew-cut" micelle-like aggregates of polystyrene-b-poly(acrylic acid) diblock copolymers in aqueous solutions. *J. Am. Chem. Soc.* **1996**, *118*, 3168-3181.

64. Davis, M. E.; Chen, Z.; Shin, D. M., Nanoparticle therapeutics: an emerging treatment modality for cancer. *Nat. Rev. Drug Discov.* **2008**, *7*, 771-782.

65. Owens III, D. E.; Peppas, N. A., Opsonization, biodistribution, and pharmacokinetics of polymeric nanoparticles. *Int. J. Pharm.* **2006**, *307*, 93-102.

66. Byrne, J. D.; Betancourt, T.; Brannon-Peppas, L., Active targeting schemes for nanoparticle systems in cancer therapeutics. *Adv. Drug Delivery Rev.* **2008**, *60*, 1615-1626.

67. Wan, Y.; Bu, Y.; Liu, J.; Yang, J.; Cai, W.; Yin, Y.; Xu, W.; Xu, P.; Zhang, J.; He, M., pH and reduction-activated polymeric prodrug nanoparticles based on a 6-thioguanine-dialdehyde sodium alginate conjugate for enhanced intracellular drug release in leukemia. *Polym. Chem.* **2018**, *9*, 3415-3424.

68. Hamidi, M.; Azadi, A.; Rafiei, P., Pharmacokinetic consequences of PEGylation. *Drug delivery* **2006**, *13*, 399-409.

69. Xu, Z.; Lu, C.; Lindenberger, C.; Cao, Y.; Wulff, J. E.; Moffitt, M. G., Synthesis, self-assembly, and drug delivery characteristics of poly(methyl caprolactone-co-caprolactone)-b-poly(ethylene oxide) copolymers with variable compositions of hydrophobic blocks: combining chemistry and microfluidic processing for polymeric nanomedicines. *ACS omega* **2017**, *2*, 5289-5303.

70. Stuart, M. A. C.; Huck, W. T.; Genzer, J.; Müller, M.; Ober, C.; Stamm, M.; Sukhorukov, G. B.; Szleifer, I.; Tsukruk, V. V.; Urban, M., Emerging applications of stimuli-responsive polymer materials. *Nat. Mater.* **2010**, *9*, 101-113.

71. Jones, D. P.; Carlson, J. L.; Samiec, P. S.; Sternberg, P.; Lou, A. S. B., Glutathione measurement in human plasma: evaluation of sample collection, storage and derivatization conditions for analysis of dansyl derivatives by HPLC. *Clinica Chimica Acta* **1998**, *275*, 175-184.

72. Smith, C. V.; Jones, D. P.; Guenthner, T. M.; Lash, L. H.; Lauterburg, B. H., Compartmentation of glutathione: implications for the study of toxicity and disease. *Toxicol. Appl. Pharmacol.* **1996**, *140*, 1-12.

73. Forman, H. J.; Zhang, H.; Rinna, A., Glutathione: overview of its protective roles, measurement, and biosynthesis. *Mol. Aspects Med.* **2009**, *30*, 0-12.

74. Russo, A.; DeGraff, W.; Friedman, N.; Mitchell, J. B., Selective modulation of glutathione levels in human normal versus tumor Cells and subsequent differential response to chemotherapy drugs. *Cancer Res.* **1986**, *46*, 2845.

75. Jiang, X. Q.; Yu, Y.; Chen, J. W.; Zhao, M. K.; Chen, H.; Song, X. Z.; Matzuk, A. J.; Carroll, S. L.; Tan, X.; Sizovs, A.; Cheng, N. H.; Wang, M. C.; Wang, J. Quantitative imaging of glutathione in live cells using a reversible reaction-based ratiometric fluorescent probe. *ACS Chem. Biol.* **2015**, *10*, 864-874.

76. Whitesides, G. M., The origins and the future of microfluidics. *Nature* **2006**, *442*, 368-373.

77. Purcell, E. M., Life at low reynolds number. *Am. J. Phys.* **1977**, *45*, 3-11.

78. Stone, H. A.; Stroock, A. D.; Ajdari, A., Engineering flows in small devices: microfluidics towards a lab-on-a-chip. *Annu. Rev. Fluid Mech.* **2004**, *36*, 381-411.

79. Probstein, R. F., *Physicochemical Hydrodynamics: An Introduction*; John Wiley & Sons, 2005.

80. Whitesides, G. M.; Stroock, A. D., Flexible methods for microfluidics. *Phys. Today* **2001**, *54*, 42-48.

81. Xia, Y.; Whitesides, G. M., Soft lithography. *Annu. Rev. Mater. Sci.* **1998**, *28*, 153-184.

82. Owen, M. J.; Smith, P. J., Plasma treatment of polydimethylsiloxane. *J. Adhes. Sci. Technol.* **1994**, *8*, 1063-1075.

83. Günther, A.; Khan, S. A.; Thalmann, M.; Trachsel, F.; Jensen, K. F., Transport and reaction in microscale segmented gas–liquid flow. *Lab on a Chip* **2004**, *4*, 278-286.

84. Song, H.; Chen, D. L.; Ismagilov, R. F., Reactions in droplets in microfluidic channels. *Angew. Chem. Int. Ed.* **2006**, *45*, 7336-7356.

85. Günther, A.2; Jensen, K. F., Multiphase microfluidics: from flow characteristics to chemical and materials Synthesis. *Lab on a Chip* **2006**, *6*, 1487-1503.

86. Melis, S.; Verduyn, M.; Storti, G.; Morbidelli, M.; Bałdyga, J., Effect of fluid motion on the aggregation of small particles subject to interaction forces. *AIChE J.* **1999**, *45*, 1383-1393.

87. Huang, Y. H.; Moini Jazani, A.; Howell, E. P.; Oh, J. K.; Moffitt, M. G. Controlled microfluidic synthesis of biological stimuli-responsive polymer nanoparticles. *ACS Appl. Mater. Interfaces* **2020**, *12*, 177-190.

Chapter 2 Controlled Microfluidic Synthesis of Biological Responsive Polymer Nanoparticles

This chapter is reprinted from ref. 1 with permission. Copyright 2020 American Chemical Society. Arman Moini Jazani, Elliot P. Howell, Dr. Jung Kwon Oh, and Dr. Matthew G. Moffitt are the coauthors of the paper. I performed all experiments and data analyses, and drafted the manuscript. A. M. J. and J. K. O. provided the polymer materials. E. P. H. participated in experiments of nanoparticle preparation and light scattering characterization. M. G. M. edited and approved the manuscript.

2.1 Introduction

Amphiphilic block copolymers self-assemble in aqueous media to form polymer nanoparticles (PNPs) of variable morphologies that are promising nanocarriers for drug delivery.[2-17] Drug delivery PNPs encapsulate hydrophobic drugs within the hydrophobic cores surrounded by hydrophilic coronal chains, increasing bioavailability[7,9] and size selectivity (EPR effect)[3,13,15,16] of the drug. However, a central challenge in the design of PNP-based drug delivery vehicles is presence of uncontrolled drug release outside of the target region.[18-20] For chemotherapeutics in particular, it is important to enhance release in the tumor in order to increase efficacy and minimize side effects within healthy tissue. Block copolymers that dissociate in response to external stimuli, including temperature,[21-23] light,[24-27] and pH,[28-33] provide the potential for "smart" enhanced release in cancerous tumor microenvironments.[34,35]

Overexpressed reduction-oxidation reactions within cancer cells have recently been explored as potential triggers for stimuli-responsive block copolymers.[36-38] For example,

glutathione (GSH) is a tripeptide-containing cysteine with a pendant thiol (-SH) group which acts as a cellular reducing agent. GSH is found at different concentrations in intracellular and extracellular regions of healthy tissue and at highly elevated concentrations (>10 mM) within cancer cells,[39,40] providing a chemical stimulus for specially-designed block copolymers. Specifically, disulfide linkages introduced into the structure of a block copolymer can be cleaved to the corresponding thiols in the presence of GSH or other reducing agents.[41-51] These disulfide linkages can be located at the junction of hydrophilic and hydrophobic blocks (junction linkages), producing PNPs with GSH-cleavable coronal chains. [41-43, 45-48] Alternatively, the disulfide linkages can be introduced at the junction of pendant chains within the hydrophobic block (pendant linkages), leading to GSH-induced destabilization of the PNP hydrophobic cores and a dramatic increase in release rate of the drug.[44,49,50]

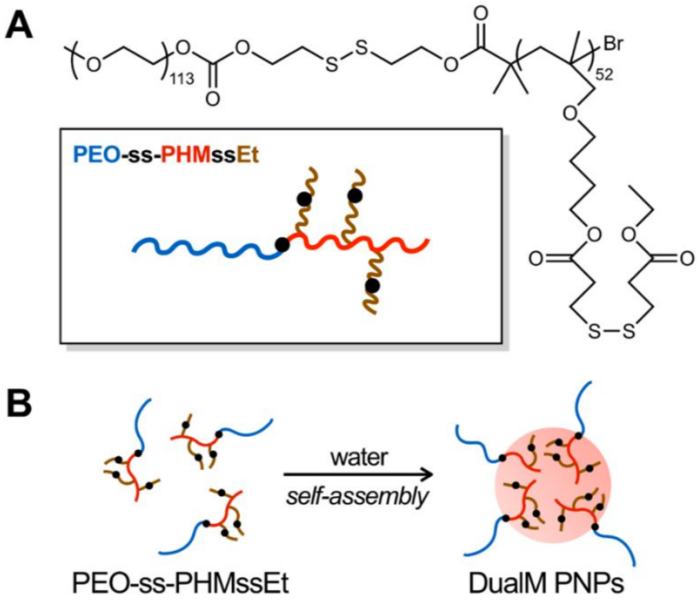

Figure 2-1. (A) Molecular structure of PEO-ss-PHMssEt copolymers. (B) Schematic of DualM PNP formation through self-assembly in aqueous solution.

Recently, dual GSH-responsive block copolymers with disulfide linkages in *both* junction *and* pendant locations were synthesized and used to prepare "DualM" PNPs for drug delivery.[51] The block copolymer consists of a hydrophilic poly(ethylene oxide) (PEO) block and a hydrophobic polymethacrylate block having disulfide pendants (PHMssEt), with a disulfide junction between the hydrophobic and hydrophilic blocks (PEO-ss-PHMssEt). PNPs showed controlled drug release inside Hela cells with 10 mM GSH due to the cleavage of disulfides at both locations within the reductive cellular environment. The results demonstrate the potential for synergistically-enhanced drug release enabled by dual locations of stimuli-responsive cleavable linkages.

Current approaches to controlling the responsivity of stimuli-responsive PNPs are chemical in nature, involving the design and synthesis of new copolymers with cleavable groups of variable composition, number, and location within the copolymer molecule.[43,44,48,52] Microfluidic approaches offer new routes to the synthesis of nanomedicines with high throughput and improved control.[12,53-55] In our group, we have shown that variable flow-directed shear forces within high-shear "hot spots" of two-phase segmented microfluidic reactors provides processing control over self-assembly, leading to PNPs with controllable structure and properties[56-68], including drug encapsulation efficiencies,[58,60,63-68] release rates,[58,60,63-68] and *in vitro* cytotoxicity.[64-68] In addition, we recently showed that microfluidic self-assembly of photoresponsive poly(*o*-nitrobenzyl acrylate)-*block*-polydimethylacrylamide (PNBA-*b*-PDMA) block copolymers provides processing control of photo-triggered dissociation rates of the resulting PNPs.[61]

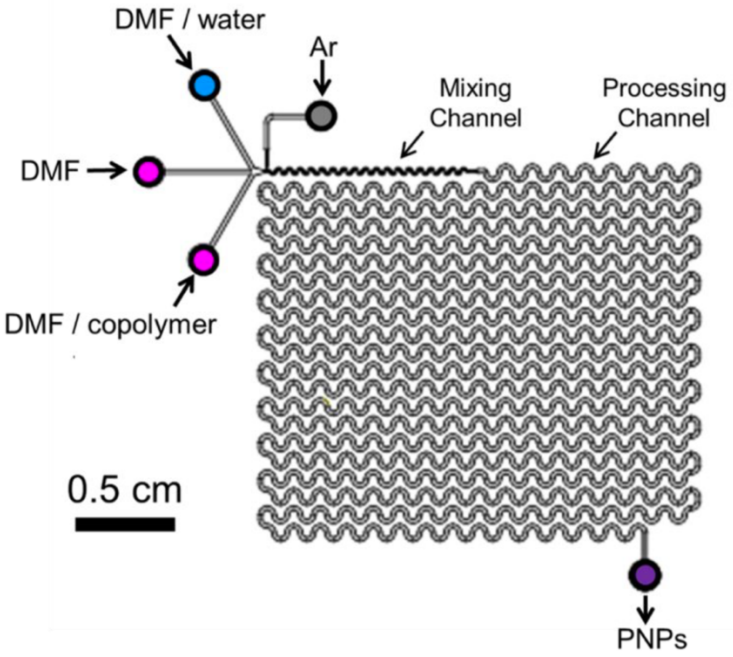

Figure 2-2. Schematic of the two-phase gas-liquid segmented microfluidic reactor.

In this chapter, we demonstrate the preparation and characterization of DualM GSH-responsive PNPs from a PEO-ss-PHMssEt block copolymer (Figure 2-1) in a two-phase microfluidic reactor at various flow rates. We show that tunable shear forces within the microchannels provide control over the size distributions, morphologies, internal structure, and GSH responsivities of the PNPs. Mainly spherical solid PNPs with broad size dispersity are formed by conventional bulk nanoprecipitation, whereas microfluidic PNP formation yields intriguing flow-dependent morphologies, including spheres, cylinders, vesicles, and complex multi-compartment vesicles with internal symmetry. Previous work from our group has demonstrated microfluidic morphological control of block copolymer PNPs, although the detailed mechanisms of on-chip morphology formation were not elucidated in those systems. However, we find that microfluidic assembly of DualM copolymer gives rise to complex and intriguing kinetically-trapped intermediates between shear-dependent states, providing the most detailed mechanism to date of microfluidic PNP

formation in the presence of flow-variable high shear. Moreover, we find distinct differences in GSH-triggered responsivities for PNPs formed under different conditions of microfluidic flow, pointing to combined roles of linkage location and shear processing in controlling the rates of both particle and inner compartment growth upon GSH exposure. These results point to the potential for combining bottom-up chemical design of polymer materials with top-down mechanical processing in microfluidic channels, in order to open up new routes to finely-tuned smart nanomedicines.

2.2 Experimental Section

2.2.1 Materials

Copper(II) bromide ($CuBr_2$, >99.99%), anisole (anhydrous, >99%), tin(II) 2-ethylhexanoate ($Sn(EH)_2$, 95%), and $_L$-glutathione (GSH, >98%) purchased from Sigma-Aldrich, *N*,*N*-dimethylformamide (DMF, >99.9%) from Fisher Scientific was used as received without further purification. Tris(2-pyridylmethyl)amine (TPMA),[69] a poly(ethylene glycol)-based bromine labeled with a disulfide linkage (PEO-ss-Br),[48] and a methacrylate bearing a pendant disulfide linkage (HMssEt)[70] were synthesized according to literature procedures.

2.2.2 Synthesis of GSH-Responsive PEO-ss-PHMssEt Block Copolymer

The synthesis of GSH-responsive PEO-ss-PHMssEt block copolymer is described previously.[51] Briefly, atom transfer radical polymerization was conducted for HMssEt mediated with $CuBr_2$/TPMA complex in the presence of PEO-ss-Br macroinitiator in anisole at 40 °C. $Sn(EH)_2$ was used to reduce Cu(II) species to active Cu(I) species to

initiate the polymerization. The formed copolymer was purified by passing through a basic alumina column to remove residual copper and following precipitation from hexane.

After purification, the resulting block copolymer was characterized by gel permeation chromatography (GPC, Figure A-1) and found to have a number-average molecular weight of M_n = 29 000 g/mol and a dispersity of $Đ$ = 1.12. Proton nuclear magnetic resonance (^{1}H NMR, Figure A-2) was used to determine the degree of polymerization (DP) of the PHMssEt block, which was found to be 52 by comparing proton integrations from the PEO (previously known DP = 113) and PHMssEt blocks, as described previously.[51]

2.2.3 Critical Water Content (cwc) Determination

The cwc is the minimum water content that is required for block copolymer self-assembly into micellar aggregates. Static light scattering (SLS) measurements were carried out to determine the cwc of 0.33 wt % copolymer in DMF solution, which was the initial condition for all self-assembly experiments in this study. SLS experiments were performed on a Brookhaven Instruments photo-correlation spectrometer equipped with a BI-200SM goniometer, a BI-9000AT digital autocorrelator, and a BI-Mini-L30 30 mW red (636 nm) compact diode laser, at a scattering angle of 90° and a temperature of 25 °C.

Briefly, 1 wt % copolymer stock solution in DMF was prepared and stirred overnight. This solution was filtered through 2 × 0.45 μm nominal pore size Teflon syringe filters (VWR) into pre-cleaned scintillation vials, and then was diluted to a final concentration of 0.33 wt % by gravimetric addition of DMF. To the resulting ~5 g of solution, deionized water was added in successive 0.03−0.06 g quantities using a microsyringe equipped with 2 × 0.20 μm nominal pore size nylon syringe filters (National Scientific). After each addition of water the sample was allowed to equilibrate for 15 min before the scattered

light intensity was measured. The resulting scattered light intensity was plotted vs. water concentration. Then the cwc value was determined from the intercept of linear fits to the baseline and the sharply-increasing intensity region. A representative titration plot and cwc determination for the copolymer is shown in Figure A-3. Determinations of cwc were carried out in triplicate from the same stock solution and the mean value and standard error of the three measurements were used to calculate the reported cwc and experimental error of 11.7 ± 0.2 wt %.

2.2.4 Bulk Preparation of DualM PNPs

The DualM PNPs were firstly prepared by the conventional bulk method of nanoprecipitation. Specifically, ~1 g of 0.33 wt % copolymer stock solution in DMF was prepared and stirred overnight to equilibrate. The resulting 1 mL of solution was then added at a constant injection rate of 120 μL/min using a syringe pump into a 10× excess volume of deionized water with vigorous stirring. In order to remove residual DMF, the resulting PNP dispersions were immediately transferred to a 6−8 kDa MWCO dialysis membrane (Spectrum Laboratories) and dialyzed against deionized water for at least 18 h, changing the deionized water every hour for the first 4 h. The extremely small amounts of DMF remaining in different block copolymer PNPs following an identical dialysis process were found not to contribute to in vitro cell toxicity in a drug delivery application.[63] A follow-up study will address the question of residual DMF toxicity following dialysis of the PNP materials described in this chapter. Bulk samples were prepared in triplicate. Unless otherwise stated, bulk samples were analyzed immediately following dialysis.

2.2.5 Microfluidic Reactor Fabrication

The microfabrication steps followed previously described procedures.[56-68] Firstly, negative masters were fabricated on silicon wafers (Silicon Materials) using the negative photoresist SU-8 100 (Microchem). A 150 μm-thick SU-8 film was spin-coated at 2000 rpm onto the silicon wafer and heated at 65 °C for 12 min and then at 95 °C for 50 min. After the wafer was cooled, a photomask was placed directly above, and the wafer was exposed to UV light for 100 s. Then, the UV-treated film was heated at 65 °C for 1 min and then 95 °C for 20 min. Finally, the silicon wafer was submerged in SU-8 developer (Microchem) and rinsed with isopropanol until all unexposed photoresist was removed.

Microfluidic chips were fabricated from polydimethylsiloxane (PDMS) using a SYLGARD 184 silicon elastomer kit (Dow Corning). For fabrication of all PDMS chips, the elastomer and curing agent were mixed at a 7:1 ratio and degassed under vacuum. The resulting mixture was poured over a clean negative master chip in a Petri dish and further degassed until all remaining air bubbles were removed. The PDMS was heated at 85 °C until cured (∼20 min) and then peeled from the negative master; holes were punched through the reservoirs of the resulting PDMS chip to allow for the insertion of tubing. A thin PDMS film (substrate layer) was also made on a glass slide by spin-coating a 20:1 elastomer/curing agent mixture followed by curing. The substrate layer was then permanently bonded to the base of the microfluidic reactor (channel layer) after both components were exposed to oxygen plasma for 45 s. The resulting reactor (Figure 2-2) has a set channel depth of 150 μm and consists of a sinusoidal mixing channel 100 μm wide and a sinusoidal processing channel 200 μm wide, identical to the reactor described in previous publications from our group.[56-68]

2.2.6 Flow Delivery and Control

The steps of flow delivery and control followed previously described procedures.[56-68] Pressure-driven flow of liquids to the reactor inlet was provided using 1 mL gastight syringes (Hamilton) mounted on syringe pumps (Harvard Apparatus). The microfluidic chip was connected to the liquid syringes via 1/16th-inch (OD) Teflon tubing (Mandel Scientific). Argon (Ar) gas flow was introduced to the chip via an Ar tank regulator and a downstream regulator (Johnston Controls) for fine adjustments. The chip was connected to the downstream regulator through a 1/16th-inch (OD)/100-μm (ID) Teflon tube (Mandel Scientific). The liquid flow rate (Q_{liq}) was programmed via the syringe pumps, and the gas flow rate (Q_{gas}) was fine-tuned via the downstream pressure regulator in order to set the nominal total flow rates (Q) of 50, 100, and 200 μL/min described in the main text. Due to the compressible nature of the gas and the high gas/liquid interfacial tension, discrepancies arise between the nominal (programmed) and actual values of Q_{gas}, Q_{gas}/Q_{liq}, and the total flow rate (Q_{total}). Therefore, actual values of Q_{gas}, Q_{gas}/Q_{liq}, and $Q_{total} = Q_{gas} + Q_{liq}$ for each microfluidic experiment were calculated from the average volume of gas bubbles in the microchannels and are reported Table A-1. Specifically, three images of the microchannels were captured using a Genie Nano-C1280 camera (1stVision) equipped with an On-Semi Python1300 sensor and a C-Mount Manual Iris Varifocal lens (1/1.8", 4-13mm, *f*/1.5) (Tamron) at each of three different time periods at the beginning, middle, and end of the sample collection process. A typical image of stable two-phase gas-liquid flow during sample collection is shown in Figure A-4. Analysis of the gas bubbles and liquid plugs within the microfluidic reactor was achieved using image analysis software (ImageJ), which gives the end-to-end distance of individual gas bubbles and liquid plugs, $L_{gas,i}$ and

$L_{\mathrm{liq},i}$, respectively, under a given set of flow conditions. The gas-to-liquid flow ratio, $Q_{\mathrm{gas}}/Q_{\mathrm{liq}}$, was determined from each image as the ratio between measured $\sum_i L_{\mathrm{gas},i}$ and $\sum_i L_{\mathrm{liq},i}$ ($i \geq 150$). Actual gas-to-liquid flow ratios for all experimental runs are reported as average values determined from 9 images (3 images × 3 time points) for each run. All actual Q_{total} values within Table A-1 are within 10 % of nominal Q values.

2.2.7 Microfluidic Preparation of DualM PNPs

For microfluidic preparation of DualM PNPs, the following three fluid streams were combined to give stable gas-segmented liquid plugs within the reactor, (1) 1.0 wt % PEO-ss-PHMssEt solution in DMF; (2) pure DMF; and (3) DMF/water. The flow rates of the three liquid streams were equal for all runs, and the water content of the DMF/water stream was selected to yield steady-state on-chip concentrations of 0.33 wt % copolymer and 21.7 wt % water. The critical water content of 0.33 wt % PEO-ss-PHMssEt in DMF was previously determined to be 11.7 ± 0.2 wt %, so that the water content for microfluidic DualM PNP preparation is designated cwc + 10 wt % for all investigated flow rates.

Unless otherwise stated, the PNPs were collected from the chip into vials containing 10× excess by volume of deionized water. In order to remove residual DMF, the resulting PNP dispersions were then immediately transferred into a 6−8 kDa MWCO dialysis membrane (Spectrum Laboratories) and dialyzed against deionized water for at least 18 h, with changing of deionized water every hour for the first 4 h. Microfluidic samples at each flow rate were prepared in triplicate. With the exception of two-week stability tests, all microfluidic samples were analyzed immediately following dialysis.

2.2.8 Determination of Equilibrium PNP Structures

To determine the equilibrium PNP state, the copolymer was dissolved in DMF at an initial polymer concentration of 0.33 wt % then deionized water was added dropwise at a rate of 1 drop every 10 s under rapid stirring to a water content of cwc + 10 wt % (identical to the on-chip water content for all microfluidic preparations). The resulting dispersion was allowed to anneal for 2 weeks in the dark at 23 ºC. To quench the dispersion, it was poured all at once into a 10× excess volume of deionized water with vigorous stirring then finally dialyzed. A drop of both unquenched and quenched dispersion was deposited on transmission electron microscopy (TEM) grids for imaging.

2.2.9 Determining Effects of GSH Incubation on PNP Sizes and Morphologies

GSH-triggered degradation experiments were carried out by incubating DualM PNPs with 1.0×10^{-2} M GSH, to mimic the cancerous intracellular environment based on a recent study, which showed GSH concentrations in multiple cancer cell lines varied from 5 to 10 mM.[71] Specifically, 2.0 mL of 2.0×10^{-2} M GSH stock solution was added dropwise to 2.0 mL of each PNP dispersion with vigorous stirring. The final concentrations of GSH and PNPs in the mixture were 3.1 mg/mL (1.0×10^{-2} M) and ~0.1 mg/mL, respectively. The resulting dispersion was stirred at 23 °C for 24 h. Changes in hydrodynamic sizes, size distributions, and morphologies during GSH incubation were monitored by dynamic light scattering (DLS) and TEM by taking aliquots of the dispersion for measurement at various incubation times (t = 2 h, 4 h, and 24 h). For DLS measurements, 0.5 mL aliquots were extracted and transferred to a pre-cleaned scintillation vial containing ~5 mL of filtered deionized water (2 × 0.20 μm Nylon syringe filters, National Scientific) to give a final PNP concentration of ~0.01 mg/mL, followed by an immediate DLS measurement. Triplicate

DLS measurements were completed within 20 minutes of extracting the aliquot. For TEM measurements, a single drop of dispersion was extracted and deposited onto a TEM grid, followed by uranyl acetate staining, as described in the subsequent section. All GSH incubation experiments were performed within 24 h of sample preparation. PNP samples were stored in the dark in sealed vials before mixing with GSH. To elucidate the effects of other experimental conditions (besides GSH) on PNP size and morphology, control experiments were also carried out for each PNP sample. In each control experiment, 2.0 mL of deionized water was added dropwise to 2.0 mL of each PNP dispersion with vigorous stirring and the final dispersions (~0.1 mg/mL) were stirred at 23 °C for 24 h, identical to the GSH incubation experiments. DLS and TEM measurements taken immediately after water addition were used to represent the initial time point (t = 0 h) for both control and incubation experiments. Subsequent DLS measurements of the control sample (no GSH) were also taken at t = 2 h, 4 h, and 24 h time points.

2.2.10 Dynamic Light Scattering

DLS measurements were carried out for determination of hydrodynamic sizes, polydispersities, and size distributions of DualM PNPs. DLS experiments were performed on a Brookhaven Instruments photo-correlation spectrometer equipped with a BI-200SM goniometer, a BI-9000AT digital autocorrelator, and a BI-Mini-L30 30 mW red (636 nm) compact diode laser, at a scattering angle of 90° and a temperature of 25 °C. PNP concentrations for all DLS measurements were ~0.01 mg/mL. For each PNP dispersion, mean effective hydrodynamic sizes and polydispersities were determined from three measurements of the autocorrelation function using cumulant analysis. Representative intensity-weighted size distributions were determined from CONTIN analysis. Reported

mean effective hydrodynamic sizes and polydispersities for each condition were determined by averaging values from triplicate preparations. Standard errors (σ) on hydrodynamic sizes and polydispersities were calculated from the standard deviation (s) of triplicate values: $\sigma = \frac{s}{\sqrt{3}}$.

2.2.11 Transmission Electron Microscopy

Negatively stained samples for TEM imaging were prepared by depositing a drop of ~0.1 mg/mL DualM PNP dispersion on a Formvar/carbon-coated 200-mesh copper TEM grid (Ted Pella Inc.) followed by a drop of 1 wt % uranyl acetate aqueous solution as a negative staining agent. Excess liquid was immediately removed using lens paper, followed by drying of the remaining liquid under ambient conditions. For unquenched PNP samples either collected from the chip or prepared in the section on the Relaxation of PNPs to Equilibrium Structures, the remaining DMF in the final solutions was found to dissolve the Formvar film, and so the carbon-coated 200-mesh copper TEM grids (Ted Pella Inc.) were used. Imaging was performed on a JEOL JEM-1400 transmission electron microscope, operating at an accelerating voltage of 80 kV and equipped with a Gatan Orius SC1000 CCD camera. Size determinations were carried out using ImageJ from three separate images of different regions of the TEM grid. As morphologies other than spheres (vesicles and cylinders) were less numerous than spheres, non-spherical morphology dimensions were determined from a total of at least 50 PNPs whereas sphere dimensions were determined from a total of $N > 300$. The number percentage of reported morphologies was also measured from three separate images of different regions of the TEM grid using the

particle analysis function in ImageJ. Reported uncertainties σ were calculated from the standard deviation *s* of average dimensions taken from the three images: $\sigma = \frac{s}{\sqrt{3}}$.

The inner hydrophilic compartments of small vesicles (SVs) and large vesicles (LVs) appeared dark in TEM images due to reverse staining. This allowed spheres to be distinguished from vesicles, since the hydrophobic cores of spheres appeared uniformly bright, while SVs and LVs contained one or more dark compartments. For SVs and LVs, the areal percentage of the dark inner compartments relative to the entire particle area was analyzed using ImageJ. Briefly, a cropped image of each selected PNP was adjusted by selecting appropriate contrast, sharpness, and brightness levels. Then boundaries of the PNP and its internal compartments were defined using the binarization function of the software. Finally the total inner compartment area, A_{compart}, and the total PNP area, A_{PNP} were calculated by the software. The relative area of the inner compartments was then calculated for each PNP:

$$RA_{\text{compart}}\ (\%) = \frac{A_{\text{compart}}}{A_{\text{PNP}}} \times 100$$

Reported RA_{compart} values represent averages calculated from $N \geq 50$ PNPs containing compartments selected from at least 3 images taken in different regions of the TEM grid. Reported uncertainties σ were determined by the standard deviation of relative areas for *N* measured PNPs: $\sigma = \frac{s}{\sqrt{N}}$.

2.3 Results and Discussion

2.3.1 Effect of Flow Rate on Mean Hydrodynamic Sizes and Size Distributions of DualM PNPs

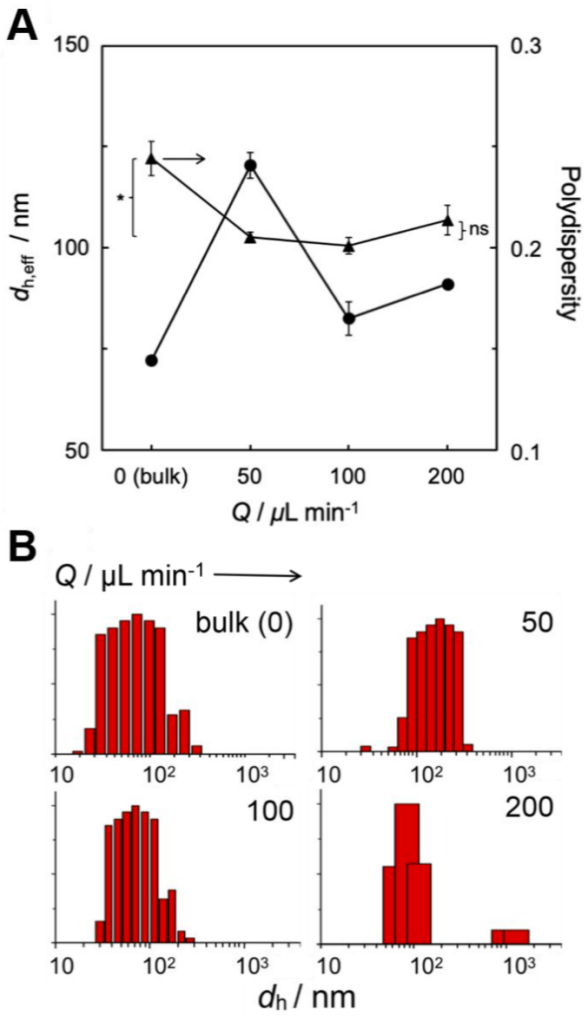

Figure 2-3. (A) Effect of microfluidic flow rate Q on DualM PNP hydrodynamic diameter and polydispersity. (B) CONTIN intensity-weighted size distributions. Q = 0 μL/min designates the bulk method of nanoprecipitation. Brackets in (A) indicate statistical comparisons between polydispersities of PNPs generated under different conditions: * indicates $p < 0.05$ and ns indicates $p > 0.05$.

We first investigated the effect of microfluidic flow rate on the PNP hydrodynamic sizes and size distributions determined from DLS. Figure 2-3A shows effective

hydrodynamic diameters ($d_{h,eff}$) and polydispersities of DualM PNPs prepared using the microfluidic reactor at various flow rates (Q = 50, 100, and 200 μL/min) and using bulk nanoprecipitation (Q = 0 μL/min). All data in Figure 2-3A were obtained from cumulant analyses of DLS autocorrelation functions. The polydispersity value is a measure of the broadness of the PNP size distribution and is calculated based on the following equation:

$$\text{Polydispersity} = \frac{\mu_2}{\bar{\Gamma}^2}$$

where $\bar{\Gamma}$ and μ_2 describe the first and second moments in the cumulant expansion of the decay rate with respect to delay time, τ.

In Figure 2-3A, we see that all $d_{h,eff}$ values for microfluidic-prepared samples are larger than the bulk value of 72 nm. Within the set of flow-variable microfluidic samples, $d_{h,eff}$ first decreases (from 120 nm to 82 nm) and then increases (from 82 nm to 91 nm) as the manufacturing flow rate increases from Q = 50 to Q = 200 μL/min. We attribute this nonmonotonic trend to the competing roles of shear-induced particle coalescence and shear-induced particle breakup as PNPs above the cwc circulate through high-shear "hot spots" within the microchannels. Specifically, compared to bulk nanoprecipitation (Q = 0 μL/min), the increased shear environment in the microfluidic channels at Q = 50 μL/min results in an increase in particle size due to shear-induced coalescence of small PNPs. However, as PNP size increases, the critical capillary number also increases, leading to a dominant contribution from shear-induced breakup. This explains the observed drop in hydrodynamic size between Q = 50 μL/min and Q = 100 μL/min. Finally, with a further increase in flow rate, the competition between coalescence and breakup leads to a slight increase in $d_{h,eff}$ between Q = 100 μL/min and Q = 200 μL/min. Intensity-weighted size

distributions for PNPs prepared at different flow rates were obtained from CONTIN analysis of DLS data as shown in Figure 2-3B.

Along with hydrodynamic sizes, PNP polydispersities are also affected by flow rate as shown in Figure 2-3A. Specifically, PNP polydispersity decreases significantly between the bulk (Q = 0 μL/min) and Q = 50 μL/min microfluidic preparations, while further increases in flow rate are not found to change polydispersities significantly. Further insights into the effect of flow rate on polydispersities are provided by considering CONTIN distributions (Figure 2-3B). Comparison of CONTIN distributions show that the broad spread of small PNPs (d_h < 100 nm) that are present in the bulk case is reduced significantly in the microfluidic Q = 50 μL/min case. This is explained by exposure of PNPs to the high-shear "hot spots" in the microchannels leading to shear-induced coalescence of smaller particles in the distribution. Similar CONTIN distribution widths are found for Q = 50 μL/min and Q = 100 μL/min PNPs, consistent with the trend in Figure 2-3A. Finally, in the CONTIN distribution at Q = 200 μL/min, we note the first appearance of a large PNP population (d_h > 1000 nm). Similar polydispersity values at different microfluidic flow rates (Figure 2-3A) is attributed to the competition between shear-induced coalescence and shear-induced breakup discussed previously.

2.3.2 Effect of Flow Rate on DualM PNP Morphology

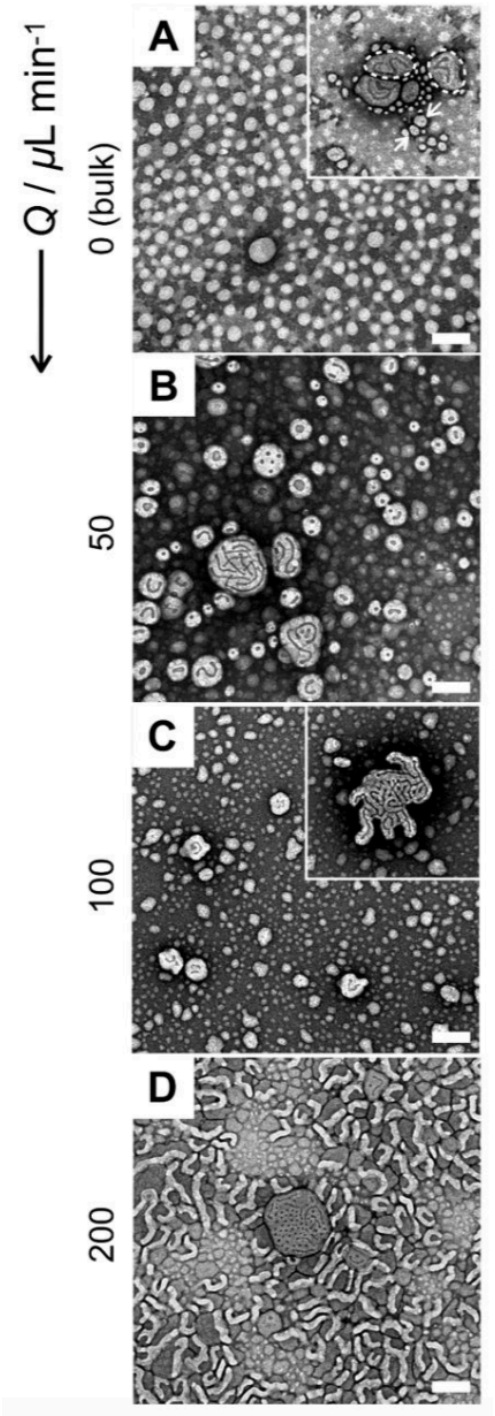

Figure 2-4. Effect of microfluidic flow rate Q on the morphologies of DualM PNPs. Representative TEM images for PNPs formed at (A) $Q = 0$ μL/min (bulk); (B) $Q = 50$ μL/min; (C) $Q = 100$ μL/min; and (D) $Q = 200$ μL/min. White arrows and white dashed circles in (A) indicate examples of SVs and LVs, respectively. All scale bars are 200 nm; main images and insets share the same scale bar.

Along with hydrodynamic sizes and polydispersities, we find that flow-tunable microfluidic shear forces have a strong effect on the morphologies of DualM PNPs. Figure 2-4 shows representative TEM images of PNPs prepared in the bulk ("zero flow" condition) and in the microfluidic reactor at different flow rates. Within these images, the uranyl acetate staining agent is selectively bonded to the PEO coronal chains, providing reverse contrast for the bright hydrophobic PHMssEt cores. Table 2-1 lists the observed morphologies, mean core dimensions, and number percentages of reported morphologies, determined from statistical analysis of multiple TEM images for each sample.

Table 2-1. Morphologies,[a] Mean Dimensions,[b] and Number Percentages for DualM PNPs Manufactured Using Bulk and Microfluidics at Variable Flow Rate

Q / μL min^{-1}	Morphology	Dimension / nm	Number Percentage / %
0 (bulk)	S	68 ± 5	98.5 ± 0.4
	SV	60 ± 4	1.1 ± 0.2
	LV	233 ± 12	1.4 ± 0.1
50	S	69 ± 9	79 ± 3
	SV	69 ± 5	18.1 ± 0.2
	LV	185 ± 15	3 ± 1
100	S	38 ± 4	99.5 ± 0.3
	SV	65 ± 7	0.5 ± 0.1
	LV	159 ± 15	0.5 ± 0.2
200	S	47 ± 4	55 ± 2
	SV	52 ± 10	1.5 ± 0.1
	LV	291 ± 81	2.3 ± 0.4
	C	31 ± 2	42 ± 3

[a]Morphologies are indicated as S (spheres), SV (small vesicles), LV (large vesicles), or C (cylinders). [b]Dimensions refer to sphere and small vesicle diameters and cylinder widths determined from TEM images. For non-spherical large vesicles, dimensions refer to the longest measurable internal distance. Standard errors are reported to represent the uncertainty of mean dimensions and number percentages determined from triplicate images in different regions of the TEM grid.

As shown in Figure 2-4A and Table 2-1, the bulk nanoprecipitation method of PNP manufacturing gives rise to a large majority (98%) of spheres with mean core diameter of 68 nm. Also present in the bulk sample are a small number of two types of vesicles (Figure 2-4A, inset): 1. small vesicles (d < 100 nm), which unlike spheres contain a distinct small spherical compartment (SVs, white arrow) and 2. large vesicles (d > 100 nm) containing either large spherical compartments or one or more cylindrical compartments (LVs, dashed white circles). These two vesicles types each constitute ~1% of the total number of PNPs formed in the bulk (Table 2-1).

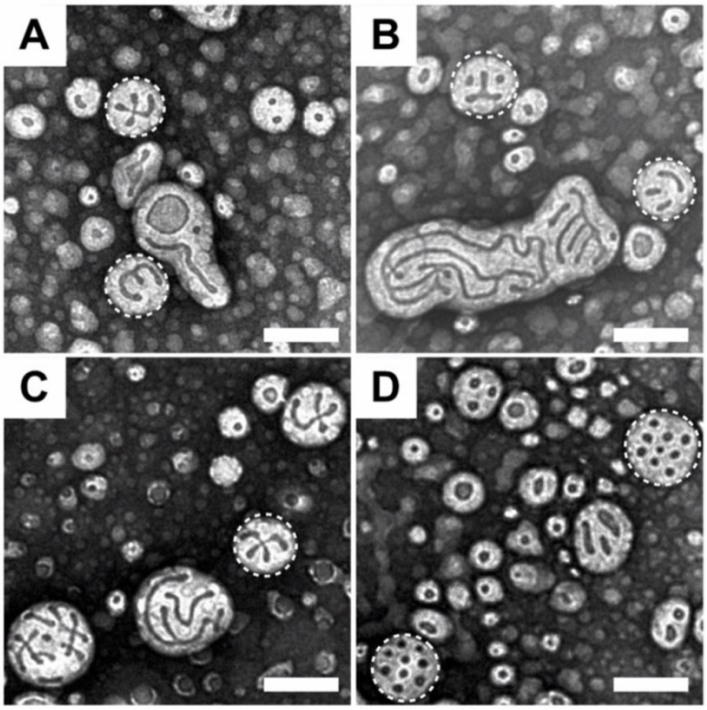

Figure 2-5. Examples of various LV internal compartment structures formed at Q = 50 μL/min. White dashed circles highlight LVs with one or more planes of mirror symmetry (A−D). All scale bars are 200 nm.

Compared to the bulk-prepared PNPs, we find a number of interesting differences in the observed morphologies when PNPs are manufactured in the microfluidic reactor at the lowest on-chip flow rate (Q = 50 μL/min, Figure 2-4B). First, the percentage of SVs

increases dramatically from 1% to 18% (Table 2-1). Second, the percentage of LVs increases from 1% to 3%; considering the much larger dimensions of LVs compared to SVs and spheres, this small percentage increase explains the corresponding sharp increase in intensity-averaged hydrodynamic diameter observed by DLS between Q = 0 μL/min (bulk) and Q = 50 μL/min (Figure 2-3A). Third, mean relative internal compartment areas of SVs and LVs were determined out by TEM image analysis (*Appendix A*, Figure A-5), revealing an expansion of inner compartments between the bulk and the Q = 50 μL/min case (*Appendix A*, Figure A-6). Finally, there is a marked increase in the complexity of the inner compartments at Q = 50 μL/min (Figure 2-5), both in terms of the mixture of highly interconnected cylindrical compartments and discrete spherical compartments, and in the appearance of numerous LVs with one or more planes of mirror symmetry (examples highlighted with dashed white circles, Figure 2-5). The presence of mirror symmetry in polymer nanoparticles has been previously attributed to nonergodicity and local free energy minimization via chain rearrangements within individual PNPs.[72]

Increasing the microfluidic flow rate to Q = 100 μL/min (Figure 2-4C) induces further changes in the observed PNP morphologies compared to the Q = 50 μL/min case. When the flow rate is increased, the percentage of SVs (18%) drops dramatically to <1% (Table 2-1). The percentage of LVs also decreases from 3% to <1%, which likely explains to the corresponding drop in the intensity-averaged hydrodynamic diameter (Figure 2-3A). At the same time, the percentage of spheres, which are smaller than those formed in the bulk and at Q = 50 μL/min (38 nm, Table 2-1), increases to 99%. In addition, TEM images reveal that the SVs and LVs become irregularly shaped (Figure 2-4C), while quantitative image

analysis shows that the relative area of their inner compartments contract compared to vesicles observed at the lower flow rate (*Appendix A*, Figure A-6).

Finally, the increase in the flow rate from Q = 100 μL/min to Q = 200 μL/min gives rise to the first appearance of cylinders (Figure 2-4D), which represent a significant percentage (42%, Table 2-1) of the morphology mixture. At the same time, the percentage of spheres drops sharply (from 99% to 55%) while the percentage of LVs increases from <1% to 2% and their mean size increases by a factor of 2 (from 159 to 291 nm). We also note that the hydrophilic compartments of LVs formed at Q = 200 μL/min are much less interconnected than at any of the previous flow conditions, including the bulk preparation. This is evidenced by the number of discrete compartments per LV at the various flow rates (*Appendix A*, Figure A-6, inset), which jumps sharply from <2 to ~10 at Q = 200 μL/min. A typical "raspberry-like" LV formed at Q = 200 μL/min with a large number of discrete cylindrical and spherical compartments is shown at the center of the image in Figure 2-4D. This can be contrasted to "sponge-like" LVs with interconnected compartments formed at Q = 50 μL/min (Figure 2-4B).

2.3.3 Kinetic Stability and Thermodynamic Equilibration of Shear-Induced DualM PNPs

As demonstrated previously for microfluidic formation of shear-induced morphologies, we find that the off-chip stability of DualM PNPs depends strongly on removal of organic solvent following collection from the microfluidic reactor.[56,61] All PNPs described in the previous sections were collected into an excess of pure water followed by removal of the organic solvent by dialysis (quenched condition). We tested the long-term stability of quenched PNPs by comparing TEM and DLS data of Q = 50 μL/min and Q = 200 μL/min samples immediately after dialysis (t = 0 days) and two weeks

after dialysis (t = 14 days). PNPs prepared under both flow conditions showed qualitatively similar morphologies after two weeks (*Appendix A*, Figure A-7, A−D). The DLS mean hydrodynamic diameter decreased slightly (by ~13%) for the Q = 50 μL/min sample but remained constant for the Q = 200 μL/min sample over the two week period. Quantitative analysis of TEM images from Q = 50 μL/min and Q = 200 μL/min samples showed that the dimensions of the various morphologies were consistent after two weeks, although we found small but significant changes in the percentages of the various morphologies over that time period (Table A-2).

Next, we investigated the off-chip stability of shear-induced PNPs without quenching into an excess of water. For these experiments, a representative PNP sample prepared at the Q = 200 μL/min flow rate was collected into an empty vial so that the water content after collection was the same as the on-chip water content (unquenched condition). We then monitored changes by TEM at different times after collection from the chip (t = 0, 1, 7, and 14 days; Figure 2-6, A−D). Statistical analysis of the dimensions and number percentages of various morphologies at the various time points are presented in Table 2, along with values for the quenched Q = 200 μL/min PNPs for comparison. We note that the quenched sample represents the PNP state immediately upon collection, whereas the unquenched sample at t = 0 days represents an off-chip relaxation time of ~20 minutes, which was the required preparation time between collection and sample deposition on the TEM grid. We find that the t = 0 sample (Figure 2-6A) qualitatively resembles the corresponding quenched Q = 200 μL/min sample (Figure 2-4D) with mixtures of spheres, cylinders, SVs and LVs of comparable dimensions. However, quantitative analysis of TEM images (Table 2-2) reveals important differences between these samples, including an

increase in the percentage of SVs from 1.5% (quenched) to 6% (t = 0 days, unquenched). We also note that whereas many of the larger LVs in the quenched sample contain multiple, mostly spherical, compartments (Figure 2-4D), these have elongated to short cylindrical compartments in the unquenched t = 0 days sample (Figure 2-6A).

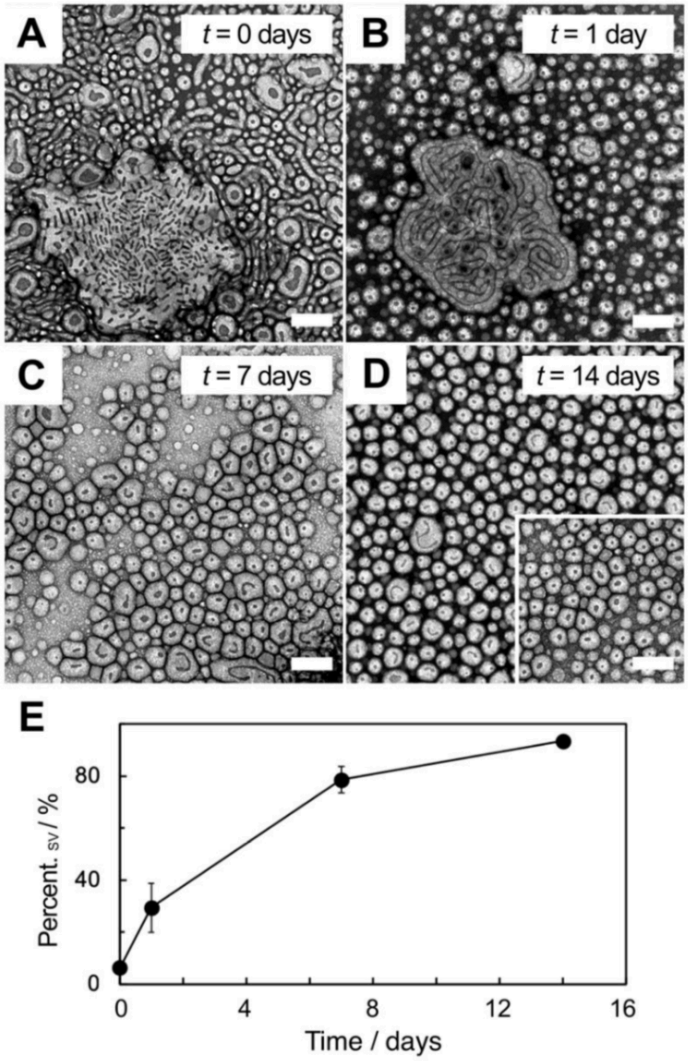

Figure 2-6. Off-chip relaxation of DualM PNPs formed at Q = 200 μL/min without quenching into excess water. TEM images (A–D) were taken at various times after collection showing increasing predominance of SVs. For comparison, a TEM image of mainly SVs formed under equilibrium PNP formation (drop-wise water addition followed by 14-day annealing) is shown in inset of (D). The number percentage of SVs plotted vs. off-chip relaxation time is shown in (E). All scale bars are 200 nm.

Table 2-2. Time-Dependent Morphologies,[a] Mean Dimensions,[b] and Number Percentages for Unquenched DualM PNPs Manufactured On-Chip at Q = 200 μL/min

t / day	Morphology	Dimension / nm	Number Percentage / %
quenched	S	47 ± 4	55 ± 2
	SV	52 ± 10	1.5 ± 0.1
	LV	291 ± 81	2.3 ± 0.4
	C	31 ± 2	42 ± 3
0	S	60 ± 4	59 ± 6
	SV	68 ± 2	6 ± 1
	LV	282 ± 38	4 ± 1
	C	36 ± 3	31 ± 8
1	S	47 ± 2	70 ± 10
	SV	73 ± 1	30 ± 10
	LV	234 ± 18	1.7 ± 0.3
7	S	56 ± 5	15 ± 5
	SV	74 ± 4	79 ± 5
	LV	201 ± 7	6 ± 9
14	S	46 ± 9	1.5 ± 0.3
	SV	64 ± 1	94 ± 2
	LV	130 ± 2	4 ± 2

[a]Morphologies are indicated as S (spheres), SV (small vesicles), LV (large vesicles), or C (cylinders). [b]Dimensions refer to sphere and small vesicle diameters and cylinder widths determined from TEM images. For non-spherical large vesicles, dimensions refer to the longest measurable internal distance. Standard errors are reported to represent the uncertainty of mean dimensions and number percentages determined from triplicate images in different regions of the TEM grid.

Figure 2-6 and Table 2-2 also show marked changes in the unquenched PNPs over time on the time scale of days. After one day (t = 1 day, Figure 2-6B) the sample no longer contains cylinders and the percentage of SVs has increased sharply from 6% to 30% (Figure 2-6E). In addition, the short cylindrical compartments of LVs have further elongated to become highly interconnected. Figure A-8 (*Appendix A*) shows multiple TEM images of LVs from the quenched, t = 0 days (unquenched) and t = 1 day (unquenched)

samples, highlighting the transition of LVs from discrete spherical to discrete cylindrical to interconnected cylindrical compartments. After one week (t = 7 days, Figure 2-6C) the PNP morphologies further develop such that there are no longer LVs with interconnected cylindrical compartments and the percentage of SVs has increased to 79% (Figure 2-6E). Finally, after two weeks (t = 14 days, Figure 2-6D), almost all of the PNPs are ~60 nm SVs (94%) with only a few residual LVs and spheres observed in the TEM images.

The observed relaxation of unquenched PNPs to mostly SVs over two weeks indicates that the shear-induced morphologies formed at variable flow rate in the microfluidic channels are thermodynamically unstable under off-chip quiescent conditions. Furthermore, the predominance of SVs after two weeks equilibration (Figure 2-6D) suggests that SVs represent the Gibbs free energy minimum at the on-chip water content of cwc + 10 wt %. To confirm this, we also prepared PNPs by slow drop-wise water addition to a 0.33 wt % copolymer solution in DMF up to cwc + 10 wt %, followed by equilibration for two weeks. This experiment allowed us to reach the equilibrium state by slowly increasing the water content from the dynamic initial state of copolymer single chains. TEM of the resulting PNPs (Figure 2-6D, inset) revealed a vast majority of SVs (96 ± 3%) with mean diameter 62 ± 2 nm, confirming SVs to be the equilibrium morphology. Despite the thermodynamic instability of the shear-induced morphologies, our stability test of quenched PNPs reveals that the observed off-chip relaxation is slowed significantly by a sudden increase in water content followed by overnight dialysis. The relative kinetic stability of the quenched morphologies over two weeks points the feasibility of testing flow-dependent GSH responsivity in these samples. Finally, we note that the observed evolution of LV inner compartments from discrete spherical to discrete

cylindrical to interconnected cylindrical (Figure A-8) suggests a possible relaxation mechanism from LVs to equilibrium SVs. In the next section, we propose that a similar rearrangement pathway is also part of the complex interplay of thermodynamics and kinetics in shear-directed DualM PNP formation.

2.3.4 Discussion of Shear-Directed Microfluidic PNP Formation from DualM Copolymer

The effects of flow rate on the sizes and morphologies of DualM PNPs reported in the previous sections point to the important role of high shear on PNP formation within the microfluidic channels. Previous work from our group on block copolymer self-assembly in two-phase gas-liquid microfluidic reactors has demonstrated that PNP circulation through high-shear hot-spots within the microchannels strongly influences the final morphologies through an interplay of shear-induced coalescence, shear-induced break-up, and intraparticle chain rearrangements.[56,59] However, the detailed mechanism of on-chip morphology formation could not be elucidated in those previous studies, due to an absence of recognizable intermediate structures within the final PNP samples. In contrast, we find that the DualM copolymer investigated in this work gives rise to unique flow-dependent PNP mixtures that include complex morphologies identifiable as kinetically trapped intermediates between shear-dependent states. Careful qualitative and quantitative analysis of the resulting morphologies allows us to propose the most detailed mechanism to date of microfluidic PNP formation in the presence of flow-variable high shear.

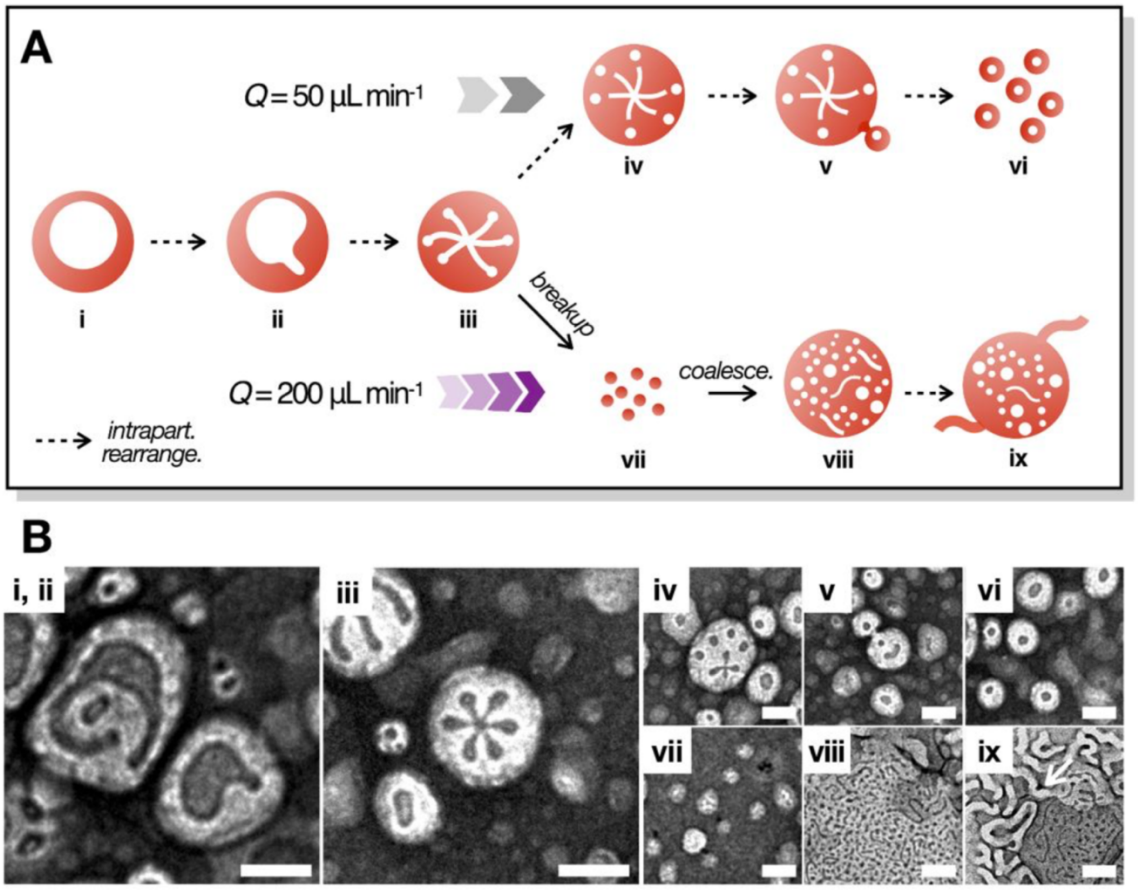

Figure 2-7. (A) Schematic of proposed mechanisms of flow-directed morphological transitions and (B) TEM images of the intermediate PNPs represented in (A). In (B), TEM images of structures (i) - (vi) are from Q = 50 μL/min sample, while images of structures (vii) - (ix) are from Q = 200 μL/min sample. All scale bars are 100 nm.

Figure 2-7 outlines the proposed mechanisms of flow-dependent morphological transitions (Figure 2-7A). The accompanying TEM images in Figure 2-7B show specific PNPs collected at the indicated flow rates which are kinetically trapped intermediate structures evincing various stages of the mechanisms in Figure 2-7A. Of the four PNP preparation conditions, the microfluidic low-flow rate case (Q = 50 μL/min) shows the highest percentage of the equilibrium morphology of SVs. The source of these SVs appears to be the numerous LVs with complex internal structure found at this flow rate. In the

proposed mechanism, LVs start with a single large spherical compartment (i), then undergo a series of spontaneous intraparticle rearrangements in order to generate low-free energy SVs. First, the large spherical compartments distort and pinch off cylindrical-shaped appendages (ii). These appendages evolve into an interconnected network of cylindrical compartments, often with mirror symmetry, with cylindrical arms extending outwards, towards the interface of the PNP core (iii). The internal curvature of cylindrical arm caps increases until a small spherical compartment breaks off from the end of each arm, leading to multiple discrete compartments situated near the LV core interface (iv). Finally, these small compartments bud off from the LV core (v) to form multiple SVs (vi).

At higher flow rates, the intraparticle rearrangement pathway from LVs to SVs described above is interrupted by the interplay of shear-induced breakup (Q = 100 μL/min and Q = 200 μL/min) and shear-induced coalescence (Q = 200 μL/min) events, activating an alternate rearrangement pathway to form cylinders. Starting at Q = 100 μL/min, the maximum shear rate increases such that PNPs above a critical size, including LV-to-SV intermediates, exceed their critical capillary number and undergo shear-induced breakup to form mainly small spheres (vii). Finally, at the highest flow rate (Q = 200 μL/min), the maximum shear rate is sufficiently high to induce shear-induced coalescence of small spheres to form a new population of LVs (viii), despite continued competition with shear-induced breakup.

In contrast to sponge-like LVs found at Q = 50 μL/min (iii), which develop highly interconnected internal compartments, raspberry-like LVs at Q = 200 μL/min (viii) contain a large number of small discrete compartments. We believe that this raspberry-like internal structure arises from the random collision and coalescence of small spheres, resulting in

hydrophilic coronal chains being internalized and forming discrete domains dispersed throughout the LV core. Unlike the slow evolution of LVs found at Q = 50 μL/min (i – v), competition with shear-induced breakup prevents raspberry-like LVs (viii) from following the relaxation pathway to equilibrium SVs. Instead, these LVs appear to lower their free energy *via* an alternate pathway, spinning cylindrical PNPs from their surfaces (ix). An example of a cylinder evolving from a raspberry-like LV is indicated by a white arrow in Figure 2-7B(ix).

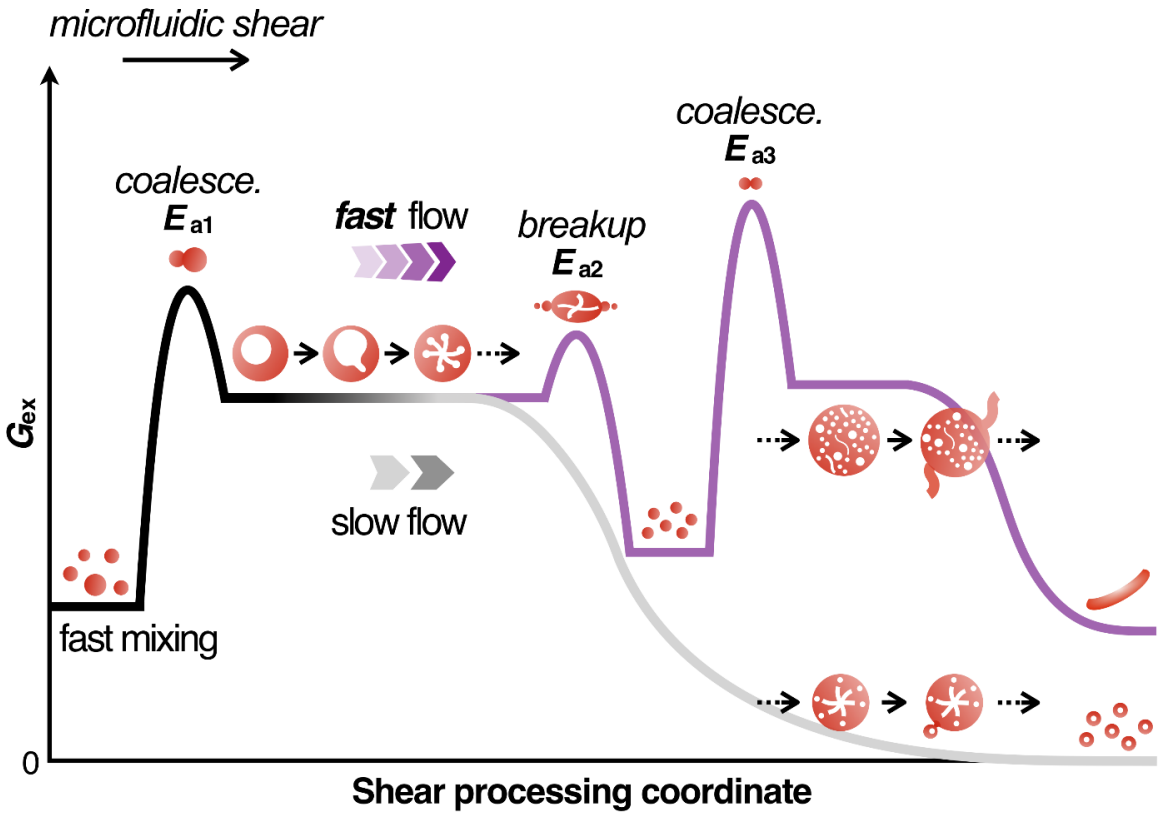

Figure 2-8. Energy diagram depicting formation and shear processing of DualM PNPs in the microfluidic reactor under different flow conditions.

Figure 2-8 presents a qualitative free energy diagram summarizing the interplay of shear-induced coalescence, shear-induced breakup, and intraparticle chain rearrangements, in the generation of flow-dependent PNP morphologies from the DualM copolymer. We

note that the proposed shear-induced formation pathways described in Figures 2-7 and 2-8 were not observed directly in real time, but rather were deduced from the various mixtures of kinetically-trapped transition morphologies at different flow rates. Such deductions of time-dependent processes from static TEM images require the assumption that PNPs observed off-chip correspond to snapshots of dynamic on-chip structures, from which a time sequence can be postulated. More direct time-dependent mechanistic evidence could possibly be obtained using redesigned chips allowing samples to be collected at different distances along the processing channel (Figure 2-2), where distance would be correlated to shear exposure time, although such experiments were beyond the scope of the present study. For all microfluidic preparations, we assume that fast mixing with water early in the microchannel gives rise to non-equilibrium spheres (~70 nm), similar to those formed by bulk nanoprecipitation (Table 2-1). In the slow flow case (Q = 50 μL/min), shear-induced coalescence of spheres generates intermediate LVs within the hot spots, as shear forces overcome the activation barrier E_{a1}. These LVs then undergo intraparticle rearrangements as they relax to equilibrium SVs. As a result, PNPs formed at Q = 50 μL/min contain a significant percentage of SVs (18%), along with intermediate LVs (3%), and the original spheres (79%).

In the fast flow cases (Q = 100 μL/min and Q = 200 μL/min), the increased shear rate activates shear-induced breakup of LVs and other particles exceeding the critical capillary number, interrupting the relaxation pathway to equilibrium SVs. At Q = 100 μL/min, the system is kinetically trapped in a high-excess free energy state in between the activation barriers E_{a2} and E_{a3}, where the vast majority of PNPs are small spheres (99%). Due to shear-induced particle breakup to the right of E_{a2}, spheres formed in fast flow rate cases

are smaller (~40 nm) than spheres formed under slow flow conditions (~70 nm). Finally, at the highest investigated flow rate, Q = 200 μL/min, the maximum shear rate increases again such that the activation barrier E_{a3} can be overcome, allowing some small spheres to coalescence to form raspberry-like LVs with multiple discrete compartments. Competition with shear-induced breakup prevents these LVs from following the same relaxation pathway to SVs that predominates under slow flow conditions. Instead, these LVs follow an alternate relaxation pathway to form cylinders (42%), which coexist with the intermediate LVs (3%) and small spheres (55%) at Q = 200 μL/min.

2.3.5 Microfluidic Flow Dependence of GSH-Triggered PNP Degradation

Next, the four PNP samples prepared in the bulk and at three microfluidic flow rates (Q = 50, 100, and 200 μL/min) were incubated in 1.0×10^{-2} M GSH and monitored over 24 h by conducting DLS and TEM measurements at the following time points: t = 0, 2, 4, and 24 h (Figure 2-9). Accompanying controls involved DLS measurements at the same time points for each PNP sample incubated under the same conditions but without GSH.

Figure 2-9A shows DLS effective hydrodynamic diameters at the various time points. All samples in GSH show increases in hydrodynamic size over time, while the control samples (without GSH) show consistent sizes over the 24 h period, confirming the GSH-triggered response. The rate of size increase was found to change over the 24 h incubation period for all four samples, with faster increase in the first 4 hours and slower increase in the subsequent 20 h. However, the total GSH-triggered PNP growth appears to depend strongly on the microfluidic flow conditions of sample preparation. Specifically, PNP samples with smaller initial hydrodynamic sizes (before GSH exposure, $d_{h,eff,i}$; t = 0 h)

show more extensive growth over 24 h of GSH exposure. To quantify this, we determined the average rate of growth in $d_{\mathrm{h,eff}}$, R_{dh} for each sample:

$$R_{dh} = \frac{d_{\mathrm{h,eff,f}} - d_{\mathrm{h,eff,i}}}{24\ \mathrm{h}}$$

and then plotted R_{dh} versus $d_{\mathrm{h,eff,i}}$. The resulting plot (Figure 2-9B) fits a linear trend line reasonably well with a negative slope of –0.32 ± 0.08 h^{-1}.

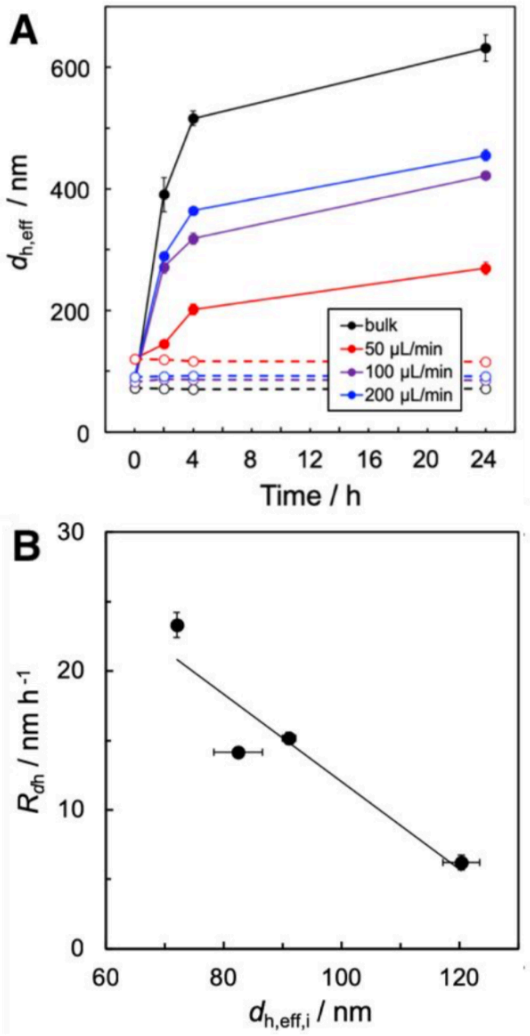

Figure 2-9. GSH-triggered size increase for bulk and microfluidic DualM PNPs formed at different flow rates, Q. (A) DLS hydrodynamic diameter ($d_{\mathrm{h,eff}}$) vs. GSH incubation time. Corresponding open symbols indicate control experiments without added GSH. (B) Average growth rate R_{dh} vs. initial $d_{\mathrm{h,eff}}$; the linear regression trend line is shown as black line.

Next, we determined the time-dependent effects of GSH exposure on PNP morphologies from TEM images. Figure 2-10 shows representative TEM images of the four investigated samples at each of the four incubation times. For each sample, the TEM images support the increases in size over 24 h observed by DLS. In addition to an overall increase in PNP size, the images reveal that the internal structure of the PNPs is strongly affected by GSH exposure. Specifically, we observe a general increase in the relative area of the dark inner regions in the TEM images with GSH exposure time, corresponding to an increase in the relative volume of the hydrophilic inner PNP compartments.

To quantify the increase in the inner compartment volume upon GSH exposure, we calculated mean relative compartment areas RA_{compart} from multiple TEM images for each time point, then plotted RA_{compart} versus GSH exposure time (Figure 2-11A). Similar to d_{h} values, we find that RA_{compart} growth with GSH exposure time depends strongly on the PNP preparation conditions, including microfluidic flow rate. In this case, the Q = 50 μL/min sample shows the smallest growth and the Q = 100 μL/min sample shows the greatest growth in RA_{compart} over the 24 h incubation time. Both the bulk and Q = 200 μL/min samples show intermediate overall changes in RA_{compart}, with both of these samples showing an initial increase in the first 4 h followed by a decrease in the subsequent 20 h. To obtain further insight into the dependence of GSH-triggered RA_{compart} growth on the initial PNP structure, we determined the average rate of growth in RA_{compart}, R_{RA} for each sample:

$$R_{RA} = \frac{RA_{\text{compart,f}} - RA_{\text{compart,i}}}{24\ \text{h}}$$

and then plotted R_{RA} versus $RA_{\text{compart,i}}$. We again obtain a straight line plot (Figure 2-11B), from which the linear trend line yields a negative slope of –0.08 ± 0.02 h^{-1}.

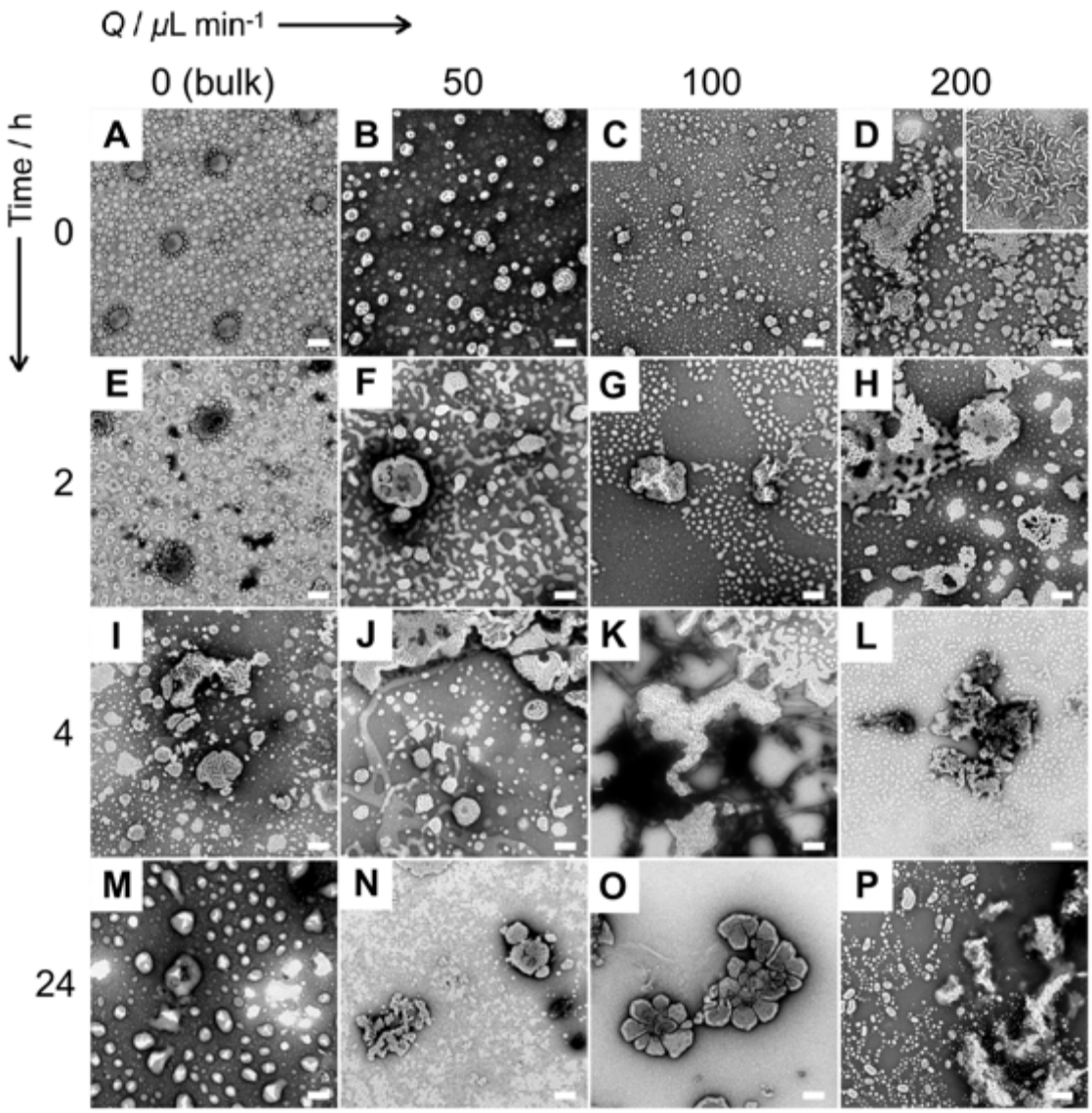

Figure 2-10. Time-dependent effects of GSH exposure on flow-directed DualM PNP morphologies. Representative TEM images of DualM PNPs formed at (A) Q = 0 μL/min (bulk); (B) Q = 50 μL/min; (C) Q = 100 μL/min; and (D) Q = 200 μL/min, at four different time points of GSH exposure at (A−D) 0 h; (B−H) 2h; (I−L) 4 h; and (M−P) 24 h. All scale bars are 200 nm; main images and insets share the same scale bar.

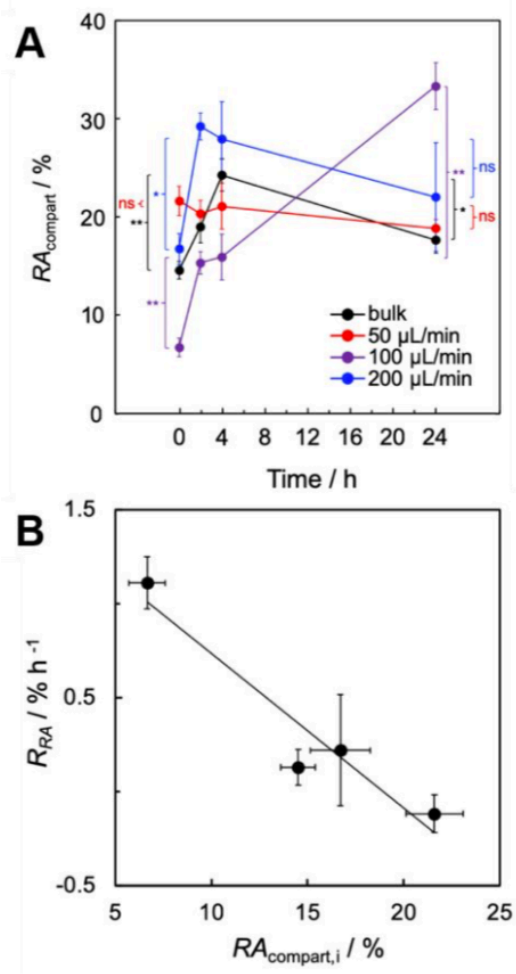

Figure 2-11. GSH-triggered $RA_{compart}$ increase for bulk and microfluidic DualM PNPs formed at different flow rates, Q. (A) $RA_{compart}$ from TEM images vs. GSH incubation time. (B) Average growth rate R_{RA} vs. initial $RA_{compart}$; the linear regression trend line is shown as black line. Brackets in (A) indicate statistical comparisons between $RA_{compart}$ values at different time points of GSH exposure: ** indicates $p < 0.005$, * indicates $p < 0.05$ and ns indicates $p > 0.05$.

By tracking time-dependent changes in both $d_{h,eff}$ (Figure 2-9) and $RA_{compart}$ (Figure 2-11) upon GSH exposure, it is possible to at least partly separate disulfide cleavage kinetics at the junction (Figure 2-12A) and pendant (Figure 2-12B) linkages, respectively. For example, the majority of junction linkages are on the outer surfaces of the PNP cores attached to stabilizing hydrophilic blocks. When these linkages cleave in the presence of GSH, hydrophilic blocks will detach from the cores, leading to surface instability and PNP

coalescence, increasing $d_{h,eff}$ over time (Figure 2-12A). In contrast, the majority of pendant linkages are embedded in the hydrophobic regions of the PNP cores. When these linkages cleave in the presence of GSH, the hydrophobic blocks become more hydrophilic and phase separate from the uncleaved regions of the core, leading to growing hydrophilic compartments, increasing $RA_{compart}$ over time (Figure 2-12B). Of course, plots of $d_{h,eff}$ (Figure 2-9A) and $RA_{compart}$ (Figure 2-11A) versus time also include other kinetic contributions from numerous processes on different time scales, including polymer and particle diffusion, phase separation, and particle coalescence, and therefore do not directly provide reaction kinetics for the junction and pendant cleavage reactions, respectively. However, due to the primary roles of the GSH-triggered junction and pendant cleavage reactions in driving the time-dependent processes in Figures 2-9A and 2-11A, respectively, it is possible to obtain some important insights into the specific roles of microfluidic shear on the GSH-triggered response at both cleavable linkage locations. Analytical techniques such as GPC and NMR that allow for the characterization of degraded products can be used to monitor quantitatively the cleavage of junction and pendant disulfide linkages as a function of incubation time with the reducing agent, although purification and chemical analysis by these methods is not straightforward.[51] However, due to the primary roles of the GSH-triggered junction and pendant cleavage reactions in driving the nanoscale time-dependent processes in Figures 2-9A and 2-11A, respectively, the current TEM and DLS analyses provide important insights into the specific roles of microfluidic shear on the GSH-triggered response at both cleavable linkage locations. Additionally, unlike the analytical techniques described in ref. 51, the current analysis directly correlates the chemical response of disulfide linkages to time-dependent changes in PNP sizes and

morphologies, which is essential information for the future understanding the transport and function of DualM PNPs in living systems.

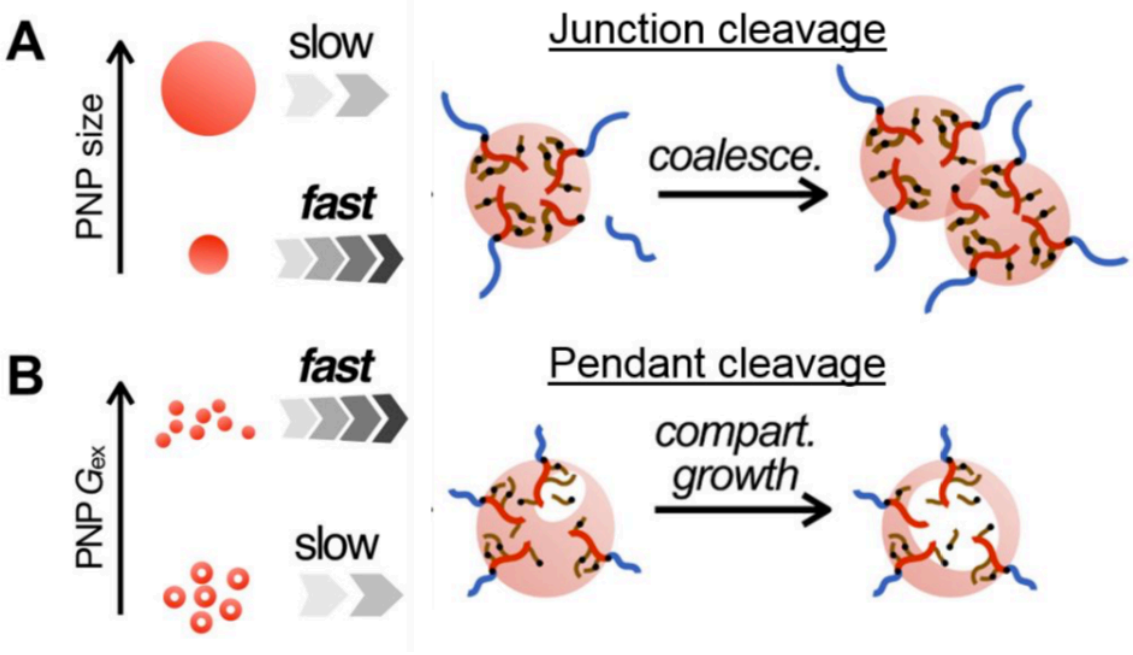

Figure 2-12. Schematic depicting (A) PNP size dependence of junction disulfide cleavage and (B) PNP excess Gibbs free energy (G_{ex}) dependence of pendant disulfide cleavage.

Figure 2-9B shows that the rate of GSH-triggered $d_{h,eff}$ growth, R_{dh}, decreases as the initial hydrodynamic size of PNPs increases. This is explained by a decrease in the surface area of the core-corona interface of PNPs leading to a decrease in the exposure of cleavable junction linkages to GSH in the surrounding medium. This suggests that mean PNP size is the primary figure of merit governing the rate junction cleavage in DualM PNPs. Therefore, flow rates giving smaller PNP sizes lead to faster junction cleavage (Figure 2-12A). In contrast, no comparative trend was found when the average rate of GSH-triggered compartment growth, R_{RA}, was plotted against initial hydrodynamic size (*Appendix A*, Figure A-9). However, as shown in Figure 2-11B, R_{RA} was found to decrease in an approximately linear manner as the initial relative compartment area from TEM images,

$RA_{compart,i}$ (proportional to the relative compartment volume) increased. Unlike the relationship between R_{dh} and $d_{h,eff,i}$, (Figure 2-9B), this cannot be a simple surface area effect, since the exposure of pendant linkages in the hydrophobic regions to GSH would increase, not decrease, as the compartment volume increases. Rather, we attribute this trend to the correlation between $RA_{compart}$ and the excess Gibbs free energy of shear-directed PNPs. As represented in the energy diagram in Figure 2-8, the lowest-G_{ex} PNPs are SVs, which form predominantly at the flow rate Q = 50 μL/min, also corresponding to the highest value of $RA_{compart}$ (*Appendix A*, Figure A-6). Conversely, the highest-G_{ex} PNPs are mainly small spheres formed *via* shear-induced breakup (Figure 2-8); these are formed at Q = 100 μL/min, which also gives the lowest value of $RA_{compart}$ (Figure A-6). Bulk and Q = 200 μL/min samples are associated with intermediate G_{ex} values (Figure 2-8) and result in similar, intermediate values of $RA_{compart}$ (Figure A-6). We tentatively ascribe the observed inverse relationship between $RA_{compart}$ and G_{ex} to the role of multi-compartment LVs in the relaxation mechanism to low-energy SVs (Figure 2-7). As exemplified by the Q = 50 μL/min case, an increase in the prominence of multi-compartment LVs tends to increase $RA_{compart}$ while also providing a pathway to low-energy SVs, thus decreasing G_{ex}. We conclude that G_{ex}, describing both the PNP size and internal molecular configuration, is the primary figure of merit governing the rate of pendant cleavage in DualM PNPs. Therefore microfluidic flow rates giving PNPs of higher G_{ex} (or lower $RA_{compart}$) lead to faster pendant cleavage (Figure 2-12B).

Our studies of various PNP systems in segmented microfluidic reactors have shown that on-chip shear processing can direct both the mean size and internal structure (including morphologies and core crystallinities) of PNPs formed in the microchannels.[56-68] Here, we

show for the first time that the *location of chemically responsive groups* within flow-directed PNPs can determine the relative roles of size and internal structure in the resulting reaction kinetics. For junction linkages localized on PNP surfaces, the mean size is primarily important since the accessibility of linkages mean that reaction kinetics will depend on surface area alone and not on the internal PNP microstructure. On the other hand, for pendant linkages embedded within the PNP cores, the local environment and thus reactivity of linkages will depend on the specific molecular configuration of chains within the PNPs (described by G_{ex}). Similarly, our previous study of shear-directed photoresponsive PNPs, in which light-triggered reactive groups were embedded within the PNP core, also showed a strong correlation between reaction kinetics and PNP G_{ex},[61] supporting the current analysis.

2.4 Conclusions

In this work, we demonstrate microfluidic flow-directed self-assembly of biological stimuli-responsive block copolymers with cleavable linkages at dual-locations, namely the junction between hydrophilic and hydrophobic blocks and on pendant groups within the hydrophobic blocks. We show that self-assembly within a two-phase microfluidic reactor forms various "DualM" polymer nanoparticles (PNPs), including cylinders and multi-compartment vesicles, with sizes, morphologies, and complex inner compartment structures that are tunable with manufacturing flow rate. Microfluidic manufacturing leads to numerous kinetically-trapped intermediates between shear-dependent states, providing the most detailed mechanism to date of microfluidic PNP formation in the presence of flow-variable high shear. Moreover, glutathione (GSH)-triggered changes in PNP size and internal structure are found to depend strongly on the manufacturing method and flow rate

as well as the location of linkages within the PNPs. Upon incubation in GSH, flow-directed PNPs with smaller mean sizes showed faster size increase, attributed to junction cleavage, and those with higher excess Gibbs free energy (lower thermodynamic stability) showed faster inner compartment growth, attributed to pendant cleavage. These results suggest that by combining chemical synthetic control of functional group location and microfluidic shear control of PNP size and microstructure, finely-tuned biological responsivities can be achieved for specific nanomedicine applications.

2.5 Supporting Information

GPC and ^{1}H NMR characterization of the copolymer; plot of cwc determination; sample image for microfluidic two-phase gas-liquid flow; table of actual flow conditions; work flow of PNP RA_{compart} determination; RA_{compart} and N_{compart} plotted vs. microfluidic flow rate; stability test of quenched DualM PNPs by TEM and DLS and resulting tabulated data; additional TEM images showing evolution of LVs from discrete spherical to discrete cylindrical to highly interconnected cylindrical compartments; plot of R_{RA} vs. $d_{\text{h,eff,i}}$; and tables of statistical comparisons are included in *Appendix A*.

2.6 References

1. Huang, Y. H.; Moini Jazani, A.; Howell, E. P.; Oh, J. K.; Moffitt, M. G. Controlled microfluidic synthesis of biological stimuli-responsive polymer nanoparticles. *ACS Appl. Mater. Interfaces* **2020**, *12*, 177-190.

2. Allen, C.; Maysinger, D.; Eisenberg, A. Nano-engineering block copolymer aggregates for drug delivery. *Colloids Surf. B* **1999**, *16*, 3-27.

3. Maeda, H.; Wu, J.; Sawa, T.; Matsumura, Y.; Hori, K. Tumor vascular permeability and the EPR effect in macromolecular therapeutics: a review. *J. Controlled Release* **2000,** *65*, 271-284.

4. Kataoka, K.; Harada, A.; Nagasaki, Y. Block copolymer micelles for drug delivery: design, characterization and biological significance. *Adv. Drug Delivery Rev.* **2001,** *47*, 113-131.

5. Duncan, R. The dawning era of polymer therapeutics. *Nat. Rev. Drug Discov.* **2003,** *2,* 347-360.

6. Moghimi, S. M.; Hunter, A. C.; Murray, J. C. Nanomedicine: current status and future prospects. *Faseb J.* **2005,** *19*, 311-330.

7. Owens, D. E.; Peppas, N. A. Opsonization, biodistribution, and pharmacokinetics of polymeric nanoparticles. *Int. J. Pharm.* **2006,** *307*, 93-102.

8. Davis, M. E.; Chen, Z.; Shin, D. M. Nanoparticle therapeutics: an emerging treatment modality for cancer. *Nat. Rev. Drug Discov.* **2008,** *7*, 771-782.

9. Alexis, F.; Pridgen, E.; Molnar, L. K.; Farokhzad, O. C. Factors affecting the clearance and biodistribution of polymeric nanoparticles. *Mol. Pharmaceutics* **2008,** *5*, 505-515.

10. Kamaly, N.; Xiao, Z. Y.; Valencia, P. M.; Radovic-Moreno, A. F.; Farokhzad, O. C. Targeted polymeric therapeutic nanoparticles: design, development and clinical translation. *Chem. Soc. Rev.* **2012,** *41*, 2971-3010.

11. Parveen, S.; Misra, R.; Sahoo, S. K. Nanoparticles: a boon to drug delivery, therapeutics, diagnostics and imaging. *Nanomed.: Nanotechnol. Biol. Med.* **2012,** *8*, 147-166.

12. Zhang, Y.; Chan, H. F.; Leong, K. W. Advanced materials and processing for drug delivery: the past and the future. *Adv. Drug Delivery Rev.* **2013,** *65*, 104-120.

13. Maeda, H.; Nakamura, H.; Fang, J. The EPR effect for macromolecular drug delivery to solid tumors: improvement of tumor uptake, lowering of systemic toxicity, and distinct tumor imaging in vivo. *Adv. Drug Delivery Rev.* **2013,** *65*, 71-79.

14. Bjornmalm, M.; Thurecht, K. J.; Michael, M.; Scott, A. M.; Caruso, F. Bridging bio-nano science and cancer nanomedicine. *ACS Nano* **2017,** *11*, 9594-9613.

15. Chen, B. L.; Dai, W. B.; He, B.; Zhang, H.; Wang, X. Q.; Wang, Y. G.; Zhang, Q. Current multistage drug delivery systems based on the tumor microenvironment. *Theranostics* **2017,** *7*, 538-558.

16. Perry, J. L.; Reuter, K. G.; Luft, J. C.; Pecot, C. V.; Zamboni, W.; DeSimone, J. M. Mediating passive tumor accumulation through particle size, tumor type, and location. *Nano Lett.* **2017,** *17*, 2879-2886.

17. Aftab, S.; Shah, A.; Nadhman, A.; Kurbanoglu, S.; Ozkan, S. A.; Dionysiou, D. D.; Shukla, S. S.; Aminabhavi, T. M. Nanomedicine: an effective tool in cancer therapy. *Int. J. Pharm.* **2018,** *540*, 132-149.

18. Brigger, I.; Dubernet, C.; Couvreur, P. Nanoparticles in cancer therapy and diagnosis. *Adv. Drug Delivery Rev.* **2002,** *54*, 631-651.

19. Ferrari, M. Cancer nanotechnology: opportunities and challenges. *Nat. Rev. Cancer* **2005,** *5*, 161-171.

20. Peer, D.; Karp, J. M.; Hong, S.; FaroKhzad, O. C.; Margalit, R.; Langer, R. Nanocarriers as an emerging platform for cancer therapy. *Nat. Nanotechnol.* **2007,** *2*, 751-760.

21. Liu, F.; Kozlovskaya, V.; Medipelli, S.; Xue, B.; Ahmad, F.; Saeed, M.; Cropek, D.; Kharlampieva, E. Temperature-sensitive polymersomes for controlled delivery of anticancer drugs. *Chem. Mater.* **2015,** *27*, 7945-7956.

22. Xiao, C. S.; Ding, J. X.; Ma, L. L.; Yang, C. G.; Zhuang, X. L.; Chen, X. S. Synthesis of thermal and oxidation dual responsive polymers for reactive oxygen species (ROS)-triggered drug release. *Polym. Chem.* **2015,** *6*, 738-747.

23. Zou, H.; Yuan, W. Z. Temperature- and redox-responsive magnetic complex micelles for controlled drug release. *J. Mater. Chem. B* **2015,** *3*, 260-269.

24. Sharker, S. M.; Lee, J. E.; Kim, S. H.; Jeong, J. H.; In, I.; Lee, H.; Park, S. Y. pH triggered in vivo photothermal therapy and fluorescence nanoplatform of cancer based on responsive polymer-indocyanine green integrated reduced graphene oxide. *Biomaterials* **2015,** *61*, 229-238.

25. Gai, S. L.; Yang, G. X.; Yang, P. P.; He, F.; Lin, J.; Jin, D. Y.; Xing, B. G. Recent advances in functional nanomaterials for light-triggered cancer therapy. *Nano Today* **2018,** *19*, 146-187.

26. Vankayala, R.; Hwang, K. C. Near-infrared-light-activatable nanomaterial-mediated phototheranostic nanomedicines: an emerging paradigm for cancer treatment. *Adv. Mater.* **2018,** *30*, No. 1706320.

27. Zhang, L. L.; Wang, Y. Q.; Wang, J.; Wang, Y. L.; Chen, A. Y.; Wang, C.; Mo, W. T.; Li, Y. X.; Yuan, Q.; Zhang, Y. F. Photon-responsive antibacterial nanoplatform for synergistic photothermal-/pharmaco-therapy of skin infection. *ACS Appl. Mater. Interfaces* **2019,** *11*, 300-310.

28. Chen, W.; Zhong, P.; Meng, F. H.; Cheng, R.; Deng, C.; Feijen, J.; Zhong, Z. Y. Redox and pH-responsive degradable micelles for dually activated intracellular anticancer drug release. *J. Controlled Release* **2013,** *169*, 171-179.

29. Wen, Y. F.; Oh, J. K. Dual-stimuli reduction and acidic pH-responsive bionanogels: intracellular delivery nanocarriers with enhanced release. *RSC Adv.* **2014,** *4*, 229-237.

30. Hu, X. Y.; Wei, W.; Qi, X. L.; Yu, H.; Feng, L. D.; Li, J. J.; Wang, S. M.; Zhang, J. F.; Dong, W. Preparation and characterization of a novel pH-sensitive Salecan-g-

poly(acrylic acid) hydrogel for controlled release of doxorubicin. *J. Mater. Chem. B* **2015,** *3*, 2685-2697.

31. Ellis, E.; Zhang, K. Y.; Lin, Q. Y.; Ye, E. Y.; Poma, A.; Battaglia, G.; Loh, X. J.; Lee, T. C. Biocompatible pH-responsive nanoparticles with a core-anchored multilayer shell of triblock copolymers for enhanced cancer therapy. *J. Mater. Chem. B* **2017,** *5*, 4421-4425.

32. Guan, X. W.; Guo, Z. P.; Wang, T. H.; Lin, L.; Chen, J.; Tian, H. Y.; Chen, X. S. A pH-responsive detachable PEG shielding strategy for gene delivery system in cancer therapy. *Biomacromolecules* **2017,** *18*, 1342-1349.

33. Xu, X. F.; Pan, C. Y.; Zhang, W. J.; Hong, C. Y. Polymerization-induced self-assembly generating vesicles with adjustable pH-responsive release performance. *Macromolecules* **2019,** *52*, 1965-1975.

34. Bajpai, A. K.; Shukla, S. K.; Bhanu, S.; Kankane, S. Responsive polymers in controlled drug delivery. *Prog. Polym. Sci.* **2008,** *33*, 1088-1118.

35. Mura, S.; Nicolas, J.; Couvreur, P. Stimuli-responsive nanocarriers for drug delivery. *Nat. Mater.* **2013,** *12*, 991-1003.

36. Ganta, S.; Devalapally, H.; Shahiwala, A.; Amiji, M. A review of stimuli-responsive nanocarriers for drug and gene delivery. *J. Controlled Release* **2008,** *126*, 187-204.

37. Cheng, R.; Feng, F.; Meng, F. H.; Deng, C.; Feijen, J.; Zhong, Z. Y. Glutathione-responsive nano-vehicles as a promising platform for targeted intracellular drug and gene delivery. *J. Controlled Release* **2011,** *152*, 2-12.

38. Oh, J. K. Disassembly and tumor-targeting drug delivery of reduction-responsive degradable block copolymer nanoassemblies. *Polym. Chem.* **2019,** *10*, 1554-1568.

39. Saito, G.; Swanson, J. A.; Lee, K. D. Drug delivery strategy utilizing conjugation via reversible disulfide linkages: role and site of cellular reducing activities. *Adv. Drug Delivery Rev.* **2003,** *55*, 199-215.

40. Russo, A.; Degraff, W.; Friedman, N.; Mitchell, J. B. Selective modulation of glutathione levels in human normal versus tumor cells and subsequent differential response to chemotherapy drugs. *Cancer Res.* 1986, *46*, 2845-2848.

41. Klaikherd, A.; Nagamani, C.; Thayumanavan, S. Multi-stimuli sensitive amphiphilic block copolymer assemblies. *J. Am. Chem. Soc.* **2009,** *131*, 4830-4838.

42. Tang, L. Y.; Wang, Y. C.; Li, Y.; Du, J. Z.; Wang, J. Shell-detachable micelles based on disulfide-linked block copolymer as potential carrier for intracellular drug delivery. *Bioconjug. Chem.* **2009,** *20*, 1095-1099.

43. Liu, J. Y.; Huang, W.; Pang, Y.; Zhu, X. Y.; Zhou, Y. F.; Yan, D. Y. Hyperbranched polyphosphates for drug delivery application: design, synthesis, and in vitro evaluation. *Biomacromolecules* **2010,** *11*, 1564-1570.

44. Chen, W.; Yang, H. C.; Wang, R.; Cheng, R.; Meng, F. H.; Wei, W. X.; Zhong, Z. Y. Versatile synthesis of functional biodegradable polymers by combining ring-opening polymerization and postpolymerization modification via michael-type addition reaction. *Macromolecules* **2010,** *43*, 201-207.

45. Cai, X. J.; Dong, H. Q.; Xia, W. J.; Wen, H. Y.; Li, X. Q.; Yu, J. H.; Li, Y. Y.; Shi, D. L. Glutathione-mediated shedding of PEG layers based on disulfide-linked catiomers for DNA delivery. *J. Mater. Chem.* **2011,** *21*, 14639-14645.

46. Sourkohi, B. K.; Cunningham, A.; Zhang, Q.; Oh, J. K. Biodegradable block copolymer micelles with thiol-responsive sheddable coronas. *Biomacromolecules* **2011,** *12*, 3819-3825.

47. Zhang, Q.; Ko, N. R.; Oh, J. K. Recent advances in stimuli-responsive degradable block copolymer micelles: synthesis and controlled drug delivery applications. *Chem. Commun.* **2012,** *48*, 7542-7552.

48. Zhang, Q.; Ko, N. R.; Oh, J. K. Modulated morphologies and tunable thiol-responsive shedding of aqueous block copolymer aggregates. *RSC Adv.* **2012,** *2*, 8079-8086.

49. Khorsand, B.; Lapointe, G.; Brett, C.; Oh, J. K. Intracellular drug delivery nanocarriers of glutathione-responsive degradable block copolymers having pendant disulfide linkages. *Biomacromolecules* **2013,** *14*, 2103-2111.

50. Cunningham, A.; Oh, J. K. New design of thiol-responsive degradable polylactide-based block copolymer micelles. *Macromol. Rapid Commun.* **2013,** *34*, 163-168.

51. Chan, N.; Khorsand, B.; Aleksanian, S.; Oh, J. K. A dual location stimuli-responsive degradation strategy of block copolymer nanocarriers for accelerated release. *Chem. Commun.* **2013,** *49*, 7534-7536.

52. Wan, Y. M.; Bu, Y.; Liu, J. M.; Yang, J.; Cai, W. Q.; Yin, Y. H.; Xu, W. J.; Xu, P. H.; Zhang, J. L.; He, M. pH and reduction-activated polymeric prodrug nanoparticles based on a 6-thioguanine-dialdehyde sodium alginate conjugate for enhanced intracellular drug release in leukemia. *Polym. Chem.* **2018,** *9*, 3415-3424.

53. Karnik, R.; Gu, F.; Basto, P.; Cannizzaro, C.; Dean, L.; Kyei-Manu, W.; Langer, R.; Farokhzad, O. C. Microfluidic platform for controlled synthesis of polymeric nanoparticles. *Nano Lett.* **2008,** *8*, 2906-2912.

54. Xu, Q. B.; Hashimoto, M.; Dang, T. T.; Hoare, T.; Kohane, D. S.; Whitesides, G. M.; Langer, R.; Anderson, D. G. Preparation of monodisperse biodegradable polymer

microparticles using a microfluidic flow-focusing device for controlled drug delivery. *Small* **2009,** *5*, 1575-1581.

55. Capretto, L.; Carugo, D.; Mazzitelli, S.; Nastruzzi, C.; Zhang, X. L. Microfluidic and lab-on-a-chip preparation routes for organic nanoparticles and vesicular systems for nanomedicine applications. *Adv. Drug Delivery Rev.* **2013,** *65*, 1496-1532.

56. Wang, C. W.; Sinton, D.; Moffitt, M. G. Flow-directed block copolymer micelle morphologies via microfluidic self-assembly. *J. Am. Chem. Soc.* **2011,** *133*, 18853-18864.

57. Wang, C. W.; Bains, A.; Sinton, D.; Moffitt, M. G. Flow-directed assembly of block copolymer vesicles in the lab-on-a-chip. *Langmuir* **2012,** *28*, 15756-15761.

58. Wang, C. W.; Bains, A.; Sinton, D.; Moffitt, M. G. Flow-directed loading of block copolymer micelles with hydrophobic probes in a gas-liquid microreactor. *Langmuir* **2013,** *29*, 8385-8394.

59. Wang, C. W.; Sinton, D.; Moffitt, M. G. Morphological control via chemical and shear forces in block copolymer self-assembly in the lab-on-chip. *ACS Nano* **2013,** *7*, 1424-1436.

60. Bains, A.; Cao, Y. M.; Moffitt, M. G. Multiscale control of hierarchical structure in crystalline block copolymer nanoparticles using microfluidics. *Macromol. Rapid. Commun.* **2015,** *36*, 2000-2005.

61. Xu, Z. Q.; Yan, B.; Riordon, J.; Zhao, Y.; Sinton, D.; Moffitt, M. G. Microfluidic synthesis of photoresponsive spool-like block copolymer nanoparticles: flow-directed formation and light-triggered dissociation. *Chem. Mater.* **2015,** *27*, 8094-8104.

62. Xu, Z. Q.; Lu, C. H.; Riordon, J.; Sinton, D.; Moffitt, M. G. Microfluidic manufacturing of polymeric nanoparticles: comparing flow control of multiscale structure in single-phase staggered herringbone and two-phase reactors. *Langmuir* **2016,** *32*, 12781-12789.

63. Bains, A.; Wulff, J. E.; Moffitt, M. G. Microfluidic synthesis of dye-loaded polycaprolactone-block-poly(ethylene oxide) nanoparticles: insights into flow-directed loading and in vitro release for drug delivery. *J. Colloid Interface Sci.* **2016,** *475*, 136-148.

64. Bains, A.; Cao, Y. M.; Kly, S.; Wulff, J. E.; Moffitt, M. G., Controlling structure and function of polymeric drug delivery nanoparticles using microfluidics. *Mol. Pharmaceutics* **2017,** *14*, 2595-2606.

65. Bains, A.; Moffitt, M. G. Effects of chemical and processing variables on paclitaxel-loaded polymer nanoparticles prepared using microfluidics. *J. Colloid Interface Sci.* **2017,** *508*, 203-213.

66. Xu, Z. Q.; Lu, C. H.; Lindenberger, C.; Cao, Y. M.; Wulff, J. E.; Moffitt, M. G. Synthesis, self-assembly, and drug delivery characteristics of poly(methyl caprolactone-

co-caprolactone)-b-poly(ethylene oxide) copolymers with variable compositions of hydrophobic blocks: combining chemistry and microfluidic processing for polymeric nanomedicines. *ACS Omega* **2017,** *2*, 5289-5303.

67. Chen, R. Y.; Wulff, J. E.; Moffitt, M. G. Microfluidic processing approach to controlling drug delivery properties of curcumin-loaded block copolymer nanoparticles. *Mol. Pharmaceutics* **2018,** *15*, 4517-4528.

68. Cao, Y. M.; Silverman, L.; Lu, C. H.; Hof, R.; Wulff, J. E.; Moffitt, M. G. Microfluidic manufacturing of SN-38-loaded polymer nanoparticles with shear processing control of drug delivery properties. *Mol. Pharmaceutics* **2019,** *16*, 96-107.

69. Britovsek, G. J. P.; England, J.; White, A. J. P. Non-heme lron(II) complexes containing tripodal tetradentate nitrogen ligands and their application in alkane oxidation catalysis. *Inorg. Chem.* **2005,** *44*, 8125-8134.

70. Zhang, Q.; Aleksanian, S.; Nohbc, S. M.; Oh, J. K. Thiol-responsive block copolymer nanocarriers exhibiting tunable release with morphology changes. *Polym. Chem.* **2013,** *4*, 351-359.

71. Jiang, X. Q.; Yu, Y.; Chen, J. W.; Zhao, M. K.; Chen, H.; Song, X. Z.; Matzuk, A. J.; Carroll, S. L.; Tan, X.; Sizovs, A.; Cheng, N. H.; Wang, M. C.; Wang, J. Quantitative imaging of glutathione in live cells using a reversible reaction-based ratiometric fluorescent probe. *ACS Chem. Biol.* **2015**, *10*, 864-874.

72. Jain, S.; Bates, F. S. On the origins of morphological complexity in block copolymer surfactants. *Science* **2003,** *300*, 460-464.

Chapter 3 Microfluidic Shear Processing Control of Biological Stimuli-Responsive Polymer Nanoparticles for Drug Delivery

This chapter is reprinted from ref. 1 with permission. Copyright 2020 American Chemical Society. Arman Moini Jazani, Elliot P. Howell, Dr. Lisa A. Reynolds, Dr. Jung Kwon Oh, and Dr. Matthew G. Moffitt are the coauthors of the paper. I performed all experiments and data analyses, and drafted the manuscript. A. M. J. and J. K. O. provided the polymer materials. E. P. H. participated in experiments of nanoparticle preparation, light scattering characterization, and long-term stability test. L. A. R. helped perform experiments of flow cytometry. M. G. M. edited and approved the manuscript.

3.1 Introduction

Polymer nanoparticles (PNPs) formed from self-assembly of amphiphilic block copolymers in aqueous media are promising candidates for drug delivery.[2-10] The hydrophobic cores of PNPs encapsulate hydrophobic drugs while the surrounding hydrophilic coronae enable dispersion in the blood, increasing drug bioavailability.[3, 7, 11-12] Encapsulation in PNPs has also been shown to decrease the side effects of relatively indiscriminate anticancer agents by increasing tumor localization.[11, 13-15] Furthermore, the sizes and morphologies of PNPs, which are critical factors influencing nanoparticle transport and cell uptake, can be controlled *via* the self-assembly conditions.[16-19]

The cellular reducing agent glutathione (GSH) is overexpressed in cancer cells,[20-21] providing a strategy for increased selectivity *via* GSH-triggered degradation of stimuli-responsive block copolymers and concomitant drug release from the PNPs at the tumor site (Figure 3-1A). For example, in the presence of GSH, disulfide linkages introduced into block copolymers will be cleaved to the corresponding thiols.[22-28] We have previously

demonstrated the synthesis of GSH-responsive block copolymers with disulfide linkages in both junction and pendant locations.[29] Self-assembly of the resulting block copolymers in aqueous media form "DualM" PNPs consisting of hydrophilic poly(ethylene oxide) (PEO) coronal chains and hydrophobic polymethacrylate cores (Figure 3-1B). The core-forming blocks possess disulfide pendants (PHMssEt) with disulfide junctions between the hydrophobic and hydrophilic blocks (PEO-ss-PHMssEt). The DualM PNPs showed evidence of synergistically-enhanced drug release inside HeLa cells supplemented with 10 mM GSH enabled by the dual locations of cleavable disulfide linkages.[29]

Conventional bottom-up manufacturing of PNPs relies on changes in the chemistry of the formulation, including the block copolymer composition, initial solvent, and drug-to-polymer ratio, for tuning the structure and drug delivery properties of the resulting PNPs.[30-33] Microfluidic approaches to PNP manufacturing provide opportunities for increased control over the drug delivery functionality of nanomedicines.[34-37] Further, microfluidics shows promising potential for scaling-up PNP manufacturing since parallel production and fast screening of formulation conditions can be achieved.[35] Our group has employed a two-phase gas-liquid segmented microfluidic reactor (Figure 3-2) for PNP manufacturing from various block copolymer materials, demonstrating that variable flow rate provides a convenient experimental handle on top-down processing control over PNP structure and properties.[38-53] Microfluidic PNP control in these reactors is attributed to a combination of particle coalescence, particle break-up, and intraparticle chain rearrangements enabled by flow-variable processing in high-shear "hot spots" within the microchannels.[38-41, 44] This is in contrast to more common single-phase microfluidic reactors for PNP manufacturing,

including a commercial staggered herringbone microfluidic mixer, which provide fast mixing but without the structural control enabled by high-shear processing.[48]

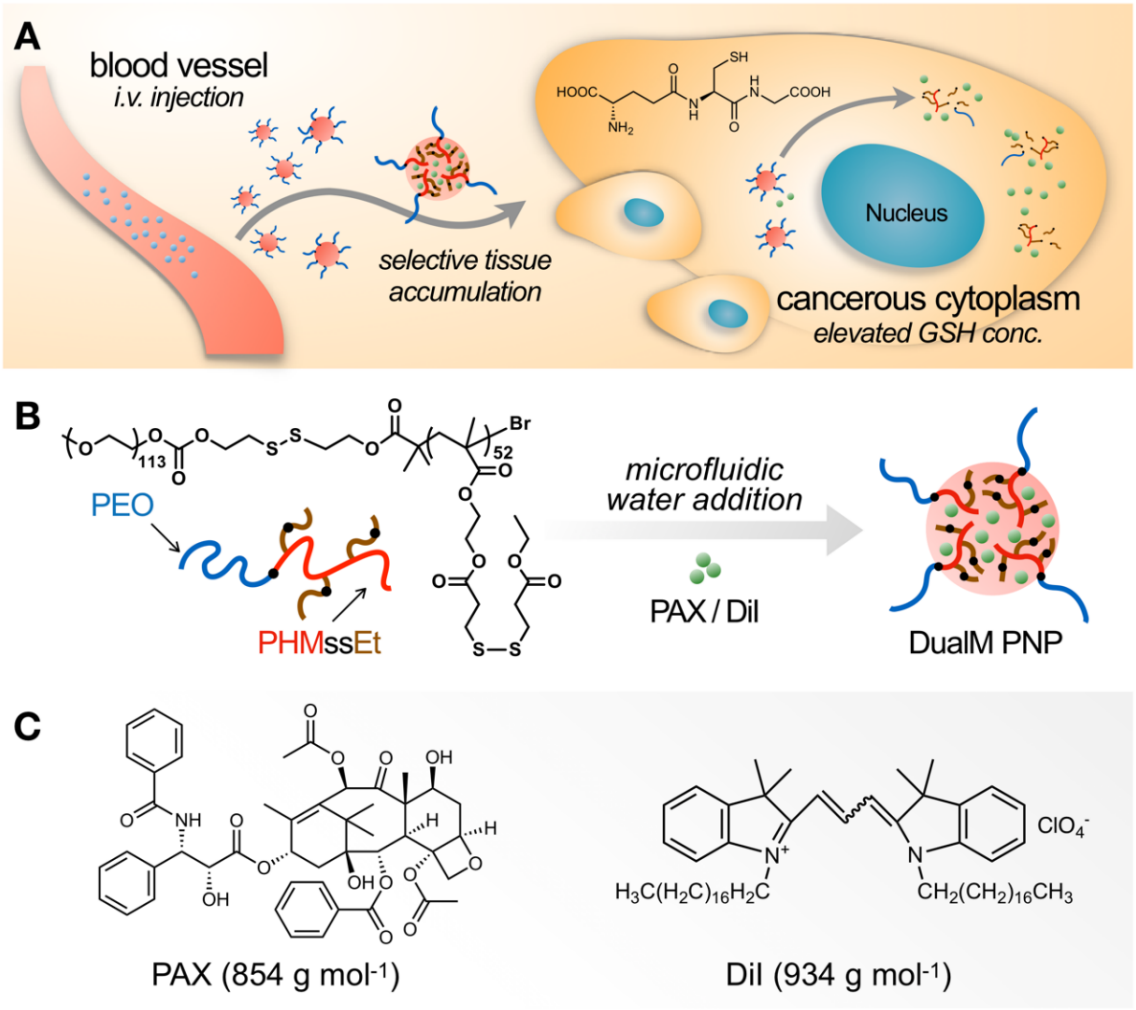

Figure 3-1. Schematics of (A) the hypothesized targeting and controlled release of drug encapsulated in DualM PNPs; (B) the molecular structure and aqueous self-assembly of PEO-ss-PHMssEt block copolymers and the general structure of the resulting DualM PNPs; and (C) the molecular structures of PAX and DiI.

In chapter 2, we used a two-phase microfluidic reactor to produce DualM PNPs (Figure 3-1B) with sizes, morphologies, and internal structures that were tunable with manufacturing flow rate.[53] This initial study focused on a fundamental understanding of on-chip DualM PNP manufacturing, including a self-assembly mechanism based on the

interplay of PNP thermodynamics and shear-activated formation pathways. We also showed that GSH responsivities of the PNPs depended strongly on their flow-controlled size and structure. Specifically, PNPs with smaller mean sizes showed faster GSH-triggered size increase, attributed to junction cleavage, and PNPs with higher excess Gibbs free energy showed faster inner compartment growth, attributed to pendant cleavage. We concluded that the combination of chemical control of functional group location and microfluidic processing control of PNP size and structure enables increased tunability of biological responsivities, with promising implications for drug delivery applications. However, no hydrophobic drugs or drug surrogates were encapsulated within the DualM PNPs in that initial study, so that microfluidic control of drug delivery properties could not be determined.

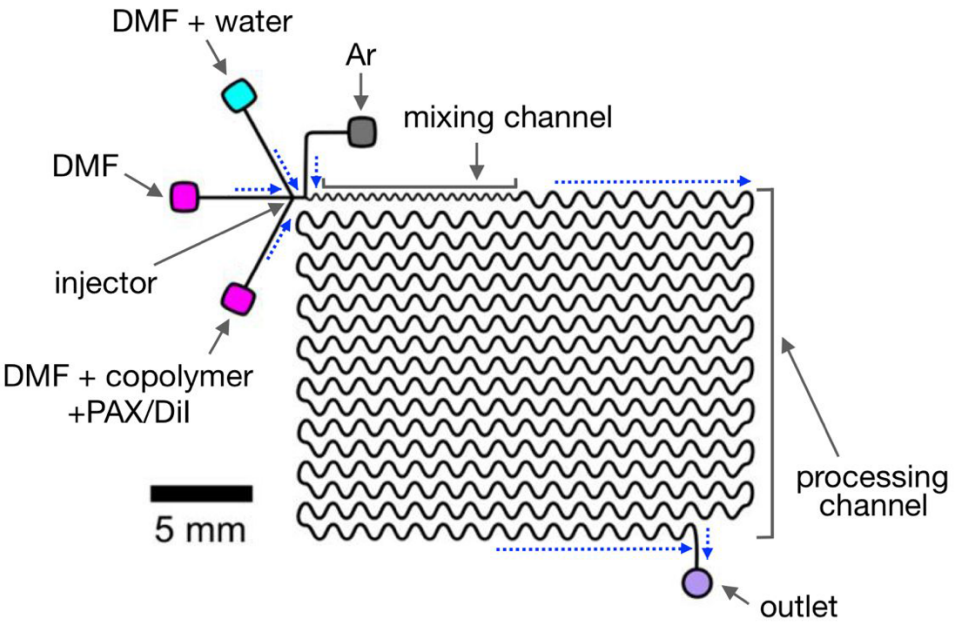

Figure 3-2. Schematic of two-phase gas-liquid microfluidic reactor.

In this chapter, we extend the fundamental insights into microfluidic control of nanoparticle structure provided in chapter 1, in order to establish manufacturing flow

tunability of the pharmacological properties of biologically responsive PNPs. Through a process chain of microfluidic formulation, physical characterization, and biological assessment, we develop powerful manufacturing-structure-property relationships that provide a pathway to optimization of selective nanomedicines through engineering. Specifically, we apply flow-controlled microfluidic manufacturing to produce DualM GSH-responsive PNPs (Figure 3-1B) containing either the anticancer drug paclitaxel (PAX) or the fluorescent drug surrogate dye 1,1′-dioctadecyl-3,3,3′,3′-tetramethylindocarbocyanine perchlorate (DiI). By encapsulating two hydrophobic molecules with similar molecular weights but different molecular structures (Figure 3-1C) and miscibilities with PHMssEt cores, we obtain important insights into the effect of the drug molecules on the sizes and morphologies of different nanomedicines prepared under the same microfluidic conditions. In addition, the anticancer properties of PAX-PNPs and the fluorescent properties of DiI-PNPs provide opportunities for probing different drug delivery properties of flow-directed DualM PNPs. Similar to DualM PNPs without PAX, we demonstrate microfluidic flow control over initial sizes, morphologies, internal structures, and GSH responsivities. More importantly, we show that microfluidic flow rate provides a unique control handle over various DualM PNP drug delivery characteristics, including encapsulation efficiencies and homogeneities, GSH-triggered release kinetics, cell uptake, and GSH-dependent *in vitro* cytotoxicities.

3.2 Experimental Section

3.2.1 Materials

The PEO-ss-PHMssEt block copolymer with a number-average molecular weight of M_n = 29 000 g/mol and a dispersity of $Đ$ = 1.12 was synthesized and characterized as

described in detail in a recent publication.[29] Paclitaxel (PAX, >99.9%) was purchased from PolyMed Therapeutics. L-Glutathione (GSH, >98%), glutathione reduced ethyl ester (GSH-OEt, ≥90%), and 1,1′-dioctadecyl-3,3,3′,3′-tetramethylindocarbocyanine perchlorate (DiI) purchased from Sigma-Aldrich, *N*,*N*-dimethylformamide (DMF, >99.9%), acetonitrile (HPLC grade), and dimethyl sulfoxide (DMSO, ≥99.9 %) from Fisher Scientific was used as received without further purification. NaCl (BioBasic Canada, 99.9%), KCl (Caledon, 99.0%), Na_2HPO_4 (BioBasic Canada, 98.0%), and KH_2PO_4 (Caledon, 99.0%) were used to prepare phosphate-buffered saline (PBS, pH=7.4).

3.2.2 Bulk Preparation of Drug-Loaded DualM PNPs

The DualM PNPs containing drug (PAX) or dye (DiI) were first prepared by the conventional bulk method of nanoprecipitation. Specifically, ~1 g of 0.33 wt % copolymer in DMF stock solution containing a drug (or dye)-to-polymer ratio (w/w) of $r = 0.25$ was prepared and stirred overnight to equilibrate. The resulting 1 mL of solution was then added at a constant injection rate of 120 μL/min using a syringe pump into a 10× excess volume of deionized water with vigorous stirring. In order to remove residual DMF, the resulting PNP dispersions were immediately transferred to a 6−8 kDa MWCO dialysis membrane (Spectrum Laboratories) and dialyzed against deionized water for 18 h, changing the deionized water every hour for the first 4 h. To remove precipitated drug, the aqueous PNP dispersion was centrifuged at 16,000×g for 10 min; the resulting supernatant containing PAX-PNPs or DiI-PNPs was then decanted into a pre-weighted vial. Bulk samples were prepared in triplicate and were analyzed immediately following dialysis.

3.2.3 Microfluidic Reactor Fabrication

The microfabrication steps followed previously described procedures.[41-53] Firstly, negative masters were fabricated on silicon wafers (Silicon Materials) using the negative photoresist SU-8 100 (Microchem). A 150 μm-thick SU-8 film was spin-coated at 2,000 rpm onto the silicon wafer and heated at 65 °C for 12 min and then at 95 °C for 50 min. After the wafer was cooled, a photomask was placed directly above, and the wafer was exposed to UV light for 100 s. Then, the UV-treated film was heated at 65 °C for 1 min and then 95 °C for 20 min. Finally, the silicon wafer was submerged in SU-8 developer (Microchem) and rinsed with isopropanol until all unexposed photoresist was removed.

Microfluidic chips were fabricated from polydimethylsiloxane (PDMS) using a SYLGARD 184 silicon elastomer kit (Dow Corning). For fabrication of all PDMS chips, the elastomer and curing agent were mixed at a 7:1 ratio and degassed under vacuum. The resulting mixture was poured over a clean negative master chip in a Petri dish and further degassed until all remaining air bubbles were removed. The PDMS was heated at 85 °C until cured (~20 min) and then peeled from the negative master; holes were punched through the reservoirs of the resulting PDMS chip to allow for the insertion of tubing. A thin PDMS film (substrate layer) was also made on a glass slide by spin-coating a 20:1 elastomer/curing agent mixture followed by curing. The substrate layer was then permanently bonded to the base of the microfluidic reactor (channel layer) after both components were exposed to oxygen plasma for 45 s. The resulting reactor (Figure 3-2) has a set channel depth of 150 μm and consists of a sinusoidal mixing channel 100 μm wide and a sinusoidal processing channel 200 μm wide, identical to the reactor described in previous publications from our group.[41-53]

3.2.4 Flow Delivery and Control

The steps of flow delivery and control followed previously described procedures.[53] Pressure-driven flow of liquids to the reactor inlet was provided using 1 mL gastight syringes (Hamilton) mounted on syringe pumps (Harvard Apparatus). The microfluidic chip was connected to the liquid syringes via 1/16th-inch (OD) Teflon tubing (Mandel Scientific). Argon (Ar) gas flow was introduced to the chip via an Ar tank regulator and a downstream regulator (Johnston Controls) for fine adjustments. The chip was connected to the downstream regulator through a 1/16th-inch (OD)/100-μm (ID) Teflon tube (Mandel Scientific). The liquid flow rate (Q_{liq}) was programmed via the syringe pumps, and the gas flow rate (Q_{gas}) was fine-tuned via the downstream pressure regulator in order to set the nominal total flow rates (Q) of 50, 100, and 200 μL/min described in the main text. Due to the compressible nature of the gas and the high gas/liquid interfacial tension, discrepancies arise between the nominal (programmed) and actual values of Q_{gas}, Q_{gas}/Q_{liq}, and the total flow rate (Q_{total}). Therefore, actual values of Q_{gas}, Q_{gas}/Q_{liq}, and $Q_{total} = Q_{gas} + Q_{liq}$ for each microfluidic experiment were calculated from the average volume of gas bubbles in the microchannels and are reported in *Appendix B* (Tables B-1 and B-2). Specifically, three images of the microchannels were captured using a Genie Nano-C1280 camera (1stVision) equipped with an On-Semi Python1300 sensor and a C-Mount Manual Iris Varifocal lens (1/1.8", 4-13mm, *f*/1.5) (Tamron) at each of three different time periods at the beginning, middle, and end of the sample collection process. Analysis of the gas bubbles and liquid plugs within the microfluidic reactor was achieved using image analysis software (ImageJ), which gives the end-to-end distance of individual gas bubbles and liquid plugs, $L_{gas,i}$ and $L_{liq,i}$, respectively, under a given set of flow conditions. The gas-to-liquid flow ratio,

Q_{gas}/Q_{liq}, was determined from each image as the ratio between measured $\sum_i L_{gas,i}$ and $\sum_i L_{liq,i}$ ($i \geq 150$). Actual gas-to-liquid flow ratios for all experimental runs are reported as average values determined from 9 images (3 images × 3 time points) for each run. All actual Q_{total} values within Tables B-1 and B-2 are within 10 % of nominal Q values.

3.2.5 Microfluidic Preparation of Drug-Loaded DualM PNPs

For microfluidic preparation of drug-loaded DualM PNPs, the following three fluid streams were combined to give stable gas-segmented liquid plugs within the reactor, (1) 1.0 wt % copolymer in DMF solution with a drug (or dye)-to-polymer ratio (w/w) of r = 0.25 (PAX or DiI); (2) pure DMF; and (3) DMF/water. The flow rates of the three liquid streams were equal for all runs, and the water content of the DMF/water stream was selected to yield steady-state on-chip concentrations of 0.33 wt % copolymer and 21.7 wt % water. The critical water content of 0.33 wt % copolymer in DMF was previously determined to be 11.7 ± 0.2 wt %,[53] so that the water content for microfluidic DualM PNP preparation is designated cwc + 10 wt % for all investigated flow rates. After microfluidic mixing, the PNPs were collected from the chip into vials containing 10× excess by volume of deionized water. In order to remove residual DMF, the resulting PNP dispersions were then immediately transferred into a 6−8 kDa MWCO dialysis membrane (Spectrum Laboratories) and dialyzed against deionized water for 18 h, with changing of deionized water every hour for the first 4 h. To remove precipitated drug, the aqueous PNP dispersion was centrifuged at 16,000×g for 10 min; the resulting supernatant containing PAX-PNPs or DiI-PNPs was then decanted into a pre-weighted vial. Microfluidic samples at each flow rate were prepared in triplicate and were analyzed immediately following dialysis.

3.2.6 Determination of DualM PNP Encapsulation Efficiencies

For each PAX-loaded PNP sample, ~1 g of a gravimetrically determined quantity of dispersion was used for encapsulation efficiency (*EE*) and drug loading (*DL*) determination. Water was first removed by rotary evaporation for 15 min at 25 °C; then a known gravimetrically determined quantity of acetonitrile (~0.5 g) was added to dissolve the resulting solid film. The mixture was vortexed for 5 min first and stirred overnight at room temperature (22 °C) to ensure complete breakup of the PNPs and dissolution of the drug. High performance liquid chromatography (HPLC) (Agilent 1100) equipped with a Luna 5u C18 column (Phenomenex) and a diode array detector (DAD) set at 227 nm was used to quantify the drug concentration. 50 μL of the drug/acetonitrile solution was injected into the HPLC by an auto-sampler. The eluent consisting of acetonitrile and water (65:35, v/v) with 0.1 v% formic acid was run at 1 mL/min. The column temperature was kept at 25 °C during all measurements. A calibration curve for the DAD was generated by analyses of 5 standards containing known PAX concentrations in acetonitrile. Quantities of PAX in the various dissolved PNP solutions were determined using the calibration curve.

For the *EE* and *DL* determination of DiI-loaded PNPs, 1 drop (~0.02 g of a gravimetrically determined quantity) of each sample was dissolved in a gravimetrically determined quantity of DMF (~5 g) then stirred overnight at room temperature (22 °C) in the dark. 200 μL of the resulting DiI/DMF solution was transferred into a 96-well chemically resistant microplate (Whatman Multi-Chem), and the fluorescence intensities of the samples were determined by a SpectraMax M5 microplate reader (Molecular Devices) at the emission maximum (λ_{ex} = 549 nm; λ_{em} = 565 nm). A linear fluorescence intensity-concentration calibration curve for DiI at the same excitation and emission

wavelengths was also generated using 5 standards containing known DiI concentrations in DMF. The fluorescence readings for both standards and samples were obtained within 2 min and at 25 °C. The solvent background was subtracted for each sample and standard measurement. Quantities of DiI in the various dissolved PNP solutions were determined using the calibration curve.

EE and *DL* were calculated for each PAX- or DiI-loaded PNP sample using the following equations:

$$EE\ (\%) = \frac{\text{mass encapsulated drug}}{\text{total mass drug}} \times 100$$

$$r = \frac{\text{total mass drug}}{\text{total mass copolymer}} \times 100$$

$$DL\ (\%) = \frac{\text{mass encapsulated drug}}{\text{mass encapsulated drug} + \text{total mass copolymer}} \times 100$$

$$DL\ (\%) = \frac{r\ \times\ EE}{(r\ \times\ EE) + 1} \times 100$$

Reported *EE* and *DL* values for each condition of *Q* was determined by averaging the values from triplicated preparations. Standard errors (σ) on *EE* and *DL* values were calculated from the standard deviation (*s*) of triplicate values: $\sigma = \frac{s}{\sqrt{3}}$.

3.2.7 Determination of Microfluidic Encapsulation Homogeneity

Fluorescence images of DiI-loaded PNPs were taken for encapsulation homogeneity (*EH*) analysis. 100 μL of each investigated aqueous dispersion of DiI-PNPs was transferred into a 96-well chemically resistant microplate (Whatman Multi-Chem), and the fluorescence images were captured using a Cytation5 microplate reader equipped with fluorescent microscope (BioTek), with fluorescent filter cubes of emission (nm)/excitation

(nm) = 586/647. Images were taken using a 4× objective. Bright field/fluorescence merged images excluding any non-encapsulated DiI were processed by the imaging software. The red areal percentage relative to PNP areal percentage was analyzed using ImageJ. Briefly, the black areal percentage ($\%A_{\mathrm{PNP}}$) and red areal percentage ($\%A_{\mathrm{DiI}}$) of the merged image were measured using color threshold and measurement functions. The encapsulation homogeneity of DiI was then calculated:

$$EH(\%) = \frac{\%A_{\mathrm{DiI}}}{\%A_{\mathrm{PNP}}} \times 100$$

Reported *EH* values represent averages calculated from 9 images (3 images × triplicate preparations). Reported uncertainties σ were calculated from the standard deviation *s* of average values of triplicate preparations: $\sigma = \frac{s}{\sqrt{3}}$.

3.2.8 Dynamic Light Scattering

DLS measurements were carried out for determination of hydrodynamic sizes, polydispersities, and size distributions of DualM PNPs. DLS experiments were performed on a Brookhaven Instruments ZataPALS Analyzer equipped with a solid state Laser (660 nm) with a maximum power output of 35 mW. All DLS measurements of the PNPs were performed in pure water, with an experimental temperature of 25 °C and at a scattering angle of 90°. PNP concentrations for all DLS measurements were ~0.01 mg/mL. For each PNP dispersion, mean effective hydrodynamic sizes and polydispersities were determined from three measurements of the autocorrelation function using cumulant analysis. Reported mean effective hydrodynamic sizes and polydispersities for each condition were determined by averaging values from triplicate preparations. Standard errors (σ) on

hydrodynamic sizes and polydispersities were calculated from the standard deviation (*s*) of triplicate values: $\sigma = \frac{s}{\sqrt{3}}$.

3.2.9 Transmission Electron Microscopy

Negatively stained samples for TEM imaging were prepared by depositing a drop of ~0.1 mg/mL DualM PNP dispersion on a Formvar/carbon-coated 200-mesh copper TEM grid (Ted Pella Inc.) followed by a drop of 1 wt % uranyl acetate aqueous solution as a negative staining agent. Excess liquid was immediately removed using lens paper, followed by drying of the remaining liquid under ambient conditions. Imaging was performed on a JEOL JEM-1400 transmission electron microscope, operating at an accelerating voltage of 80 kV and equipped with a Gatan Orius SC1000 CCD camera. Size determinations were carried out using ImageJ from three separate images of different regions of the TEM grid. As non-spherical morphologies (vesicles and cylinders) were less numerous than spheres, non-spherical morphology dimensions were determined from a total of at least 50 PNPs whereas sphere dimensions were determined from a total of $N > 300$. The number percentage of reported morphologies was also measured from three separate images of different regions of the TEM grid using the particle analysis function in ImageJ. Reported uncertainties σ were calculated from the standard deviation *s* of average dimensions taken from the three images: $\sigma = \frac{s}{\sqrt{3}}$.

The inner hydrophilic compartments of SVs and LVs appeared dark in TEM images due to reverse staining. This allowed spheres to be distinguished from vesicles, since the hydrophobic cores of spheres appeared uniformly bright while SVs and LVs contained one or more dark compartments. For SVs and LVs, the areal percentage of dark inner

compartments relative to the entire particle area was analyzed using ImageJ. Briefly, a cropped image of each selected PNP was adjusted by selecting appropriate contrast, sharpness, and brightness levels. Then boundaries of the PNP and its internal compartments were defined using the binarization function of the software. Finally the total inner compartment area, A_{compart}, and the total PNP area, A_{PNP} were calculated by the software. The relative area of the inner compartments was then calculated for each PNP:

$$RA_{\text{compart}}\,(\%) = \frac{A_{\text{compart}}}{A_{\text{PNP}}} \times 100$$

Reported RA_{compart} values represent averages calculated from $N \geq 50$ PNPs containing compartments selected from at least 3 images taken in different regions of the TEM grid. Reported uncertainties σ were determined by the standard deviation of relative areas for N measured PNPs: $\sigma = \frac{s}{\sqrt{N}}$.

3.2.10 *In Vitro* Release Kinetics of PAX-Loaded PNPs

Near perfect sink conditions were established for *in vitro* release experiments, and HPLC was used to monitor the PAX release kinetics of PAX-loaded PNPs. In a typical experiment, a gravimetrically determined quantity (~10 g) of PAX-loaded PNPs was transferred into a pre-conditioned Float-A-Lyzer dialysis tube (10 mL, MWCO 100 kDa, SpectrumLabs). The tube was then placed in a 2L-baker of the release medium. Two different release media were prepared: 1. ~2 L PBS with ~6.14 g GSH dissolved to reach 10 mM GSH concentration (GSH condition); 2. ~2L PBS only (no GSH condition). Throughout the release experiments, the release medium was constantly stirred at 100 rpm, and maintained at physiological temperature (37 ± 0.2 °C). For each of the first seven pre-determined time points (t = 0, 1, 2, 4, 8, 12, and 24 h), 1 mL of the sample was transferred

into a vial and weighed, while for each of the t = 48 and 72 h time points, 1.5 mL of the sample was transferred into a vial and weighed. At four time points (t = 0, 2, 4, and 24 h), 2 drops of the samples were also taken out for immediate DLS and TEM analyses. For samples used for PAX concentration determination, water was removed by rotary evaporation for 15 min at 25 °C. A known gravimetrically determined quantity of acetonitrile (~0.5 g) was added to dissolve the resulting solid film. The mixture was vortexed for 5 min first and stirred overnight at room temperature (22 °C) to ensure complete breakup of the PNPs and dissolution of the drug. Before injection into the HPLC, the samples were filtered through a Teflon syringe filter with 0.2 μm nominal pore size (Phenomenex). The PAX concentration was measured by HPLC as described in a previous section. Percentages of PAX released were calculated relative to the determined mass of PAX in PAX-PNPs at the t = 0 release time. Reported percentages of PAX released for each condition was determined by averaging the values from triplicate preparations. Standard errors (σ) are reported to represent the precision of the mean release percentages, which were calculated from the standard deviation (s) of triplicate values: $\sigma = \frac{s}{\sqrt{3}}$.

The release profiles for PNPs incubated under GSH conditions were plotted and fit using the following 2-parameter hyperbola model:

$$y = \left(\frac{1}{2B}\right)\left[(x + A) + B - \left((x + A) + B\right)^2 - (4xB)^{0.5}\right]$$

Release profiles for PNPs incubated in pure PBS (no GSH) were plotted and fit using the 5-parameter hyperbola model:

$$y = \frac{Ax}{B + x} + \frac{Cx}{D + x} + E$$

The fits were processed using the Levenberg−Marquardt algorithm within OriginLab (Version 2019b, OriginLab). Release half times, $t_{1/2}$, of the various PAX-PNP formulations under GSH conditions were then extracted by calculating the time required to achieve 50% PAX release based on the fitted curves. Experimental errors of $t_{1/2}$ were represented by standard errors (σ) derived from the goodness of fit.

3.2.11 Cell Culture

MCF-7 (human breast adenocarcinoma) cells were purchased from ATCC, and HaCaT (human healthy keratinocyte) cells were obtained as a generous gift from Dr. Mohsen Akbari (Department of Mechanical Engineering, University of Victoria). MCF-7 and HaCaT cell lines were cultured to represent the environment of cancerous and healthy tissue, respectively. Both cell lines were cultured in Dulbecco's Modified Eagle's Medium (DMEM, Gibco) supplemented with 10% fetal bovine serum (FBS, YWR) and 1% antibiotics (penicillin and streptomycin) in 75 cm^2 tissue culture flasks and maintained at 37 °C with 5% CO_2 in a tissue culture incubator. The HaCaT and MCF-7 cells were sub-cultured periodically using 0.5% trypsin/EDTA (Gibco).

3.2.12 *In Vitro* Cytotoxicity of PAX-Loaded PNPs.

MCF-7 and HaCaT cells were grown to ~80% confluence in 75 cm^2 tissue culture flasks, then trypsinized, collected, and pelleted by centrifugation (5 min at 1,400 rpm). The cell pellet was then suspended in DMEM, and the cell concentration was determined using a hemocytometer. After the initial cell concentration was determined, the suspension was diluted to 1.0×10^5 cells/mL. Next, a mulitichannel pipette was used to fill a 96-well plate (Corning) with 100 μL/well of the diluted cell suspension. The plates were then incubated for 24 h at 37 °C with 5% CO_2 in a tissue culture incubator for cell adhesion.

According to measured drug loading levels, aqueous stock dispersions of each investigated sample of PAX-PNPs were mixed with DMEM, resulting in a 650 μL PNP/DMEM mixture with a working PAX concentration of 2 μg/mL. To prepare the free PAX solution, 6.5 μL of PAX dissolved in dimethyl sulfoxide (DMSO) were diluted in the 643.5 μL of DMEM media to obtain a working PAX concentration at 2 μg/mL. Serial dilutions were carried out, and then 100 μL of each diluted stock was added to the appropriate well of the 96-well plate (containing ~1.0×10^4 cells in 100 μL of DMEM, as described above), to generate a range of different concentrations for analysis (1, 0.308, 0.095, 0.029, 0.0090, 0.0028, and 8.5×10^{-4} μg/mL PAX). The treated cells were incubated for 48 h at 37 °C with 5% CO_2 in a tissue culture incubator. To determine cell viability, 40 μL of CellTiter-Blue (Promega) was added to each well after the predetermined incubation time, according to the manufacturer's instructions. After the addition of CellTiter-Blue, the 96-well plates were incubated for 4 h (37 °C with 5% CO_2), and then fluorescence (λ_{ex} = 560 nm; λ_{em} = 590 nm) readings were recorded on a Cytation5 microplate reader (BioTek). Cell death was calculated for each well based upon the following formula:

$$\%\text{Death} = \left[1 - \frac{(S - B_0)}{(B_t - B_0)}\right] \times 100$$

where S is the sample reading (cells + drug + media), B_t is the average reading for the untreated population of cells (cells + media), and B_0 is the average reading of wells containing media only (media). %Death vs. PAX concentration data sets were fit using the following dose-response model:

$$y = A_1 + \frac{A_2 - A_1}{1 + 10^{p\log(x_0 - x)}}$$

The data sets were processed by the Levenberg−Marquardt algorithm within OriginLab (Version 2019b, OriginLab), and by forcing fits through 0% death at low PAX concentrations. Reported EC_{50} values were determined from three separate PAX- PNP preparations, with each concentration of each preparation being tested 6 times. Standard errors (σ) were obtained from the goodness of fit for each EC_{50} plot and used to report error bars. These same σ were then used to calculate the *p*-values for determination of statistical significance in comparisons between measured EC_{50} results.

For visual representation of the cytotoxicity of PAX- PNPs against MCF-7 cells, the cells were seeded at a density of 2.0×10^5 cells per well in a 6-well plate (Costar) and allowed to incubate in 1 mL of DMEM (containing 10% FBS and 1% antibiotics, as described in the previous section) for 24 h at 37 °C with 5% CO_2 in a tissue culture incubator for cell adhesion. According to measured drug loading levels, aqueous stock dispersions of each investigated sample of PAX-PNPs were mixed with DMEM, resulting in a PNP/DMEM mixture with a working PAX concentration at 0.1 μg/mL. After overnight incubation, cells were washed once with PBS and the media was replaced with 1 mL of the PNP/DMEM mixture. Cells were incubated for 48 h and then were washed twice with cold PBS. Fluorescein diacetate (F-7838F7378, Sigma-Aldrich) was dissolved at a concentration of 0.1 mg/mL in DMSO and further diluted 100-fold in PBS to afford a final concentration of 1 μg/mL. Then 1 mL was added to each well, and the cells were incubated on the benchtop for 5 min, then washed twice with cold PBS, and immediately imaged. Fluorescence images were captured using a Cytation5 microplate reader equipped with fluorescent microscope (BioTek), with fluorescent filter cubes of emission (nm)/excitation (nm) = 469/525. Images were taken using a 4× objective.

3.2.13 Fluorescence Imaging of Cell uptake of DiI-Loaded PNPs

MCF-7 cells were seeded at a density of 1.0×10^5 cells per well in a 6-well plate (Costar) and allowed to adhere, as described in the previous section. Aqueous DiI-PNP formulations were mixed 1:5 with the cell media for a finial PNP concentration of 0.05 mg/mL. After overnight incubation, cells were washed once with PBS, and the media was replaced with 1 mL of the media/PNP mixture. Cells were incubated for 2 h and then were washed twice with cold PBS. 4′,6-diamidino-2-phenylindole (DAPI, Life Technologies) was dissolved at a concentration of 1 μg/mL in DMSO and further diluted 10-fold in PBS to afford a final concentration of 0.1 μg/mL. Then 1 mL was added to each well, and the cells were incubated on the benchtop for 5 min, then washed twice with cold PBS, and immediately imaged. Fluorescence images were captured using a Cytation5 microplate reader equipped with fluorescent microscope (BioTek), with fluorescent filter cubes of emission (nm)/excitation (nm) = 377/447 and 586/647. Images were taken using a 20× objective.

3.2.14 Flow Cytometry

Flow cytometry measurements were performed to quantify the cell uptake of the DiI-PNPs by MCF-7 cells. MCF-7 cells were seeded at a density of 5×10^5 cells per well in a 6-well plate (Costar) and allowed to adhere, as described in previous sections. Aqueous DiI-PNP formulations were mixed 1:5 with the cell media for a finial PNP concentration of 0.05 mg/mL. After overnight incubation, cells were washed once with PBS, and the media was replaced with 2 mL of the media/PNP mixture. Cells were incubated for 2 h, then washed twice with cold PBS, trypsinized, collected, and pelleted by centrifugation (5 min at 1,400 rpm). The cell pellet was then suspended in 200 μL PBS with 10% FBS. Cellular

fluorescence was measured using a Beckman Coulter CytoFLEX and data was analyzed using CytExpert (Beckman Coulter). Mean fluorescence intensities of gated MCF-7 cells was recorded in the PE detection channel (585/42 filter). Reported values were determined from triplicate preparations of each DiI-PNP formulation, with each preparation being tested 3 times. Standard errors (σ) were calculated from the standard deviation (s) of triplicate values: $\sigma = \frac{s}{\sqrt{3}}$.

3.2.15 Statistics and Data Handling

For comparison of any two results in a data set, Excel built-in functions were used. The combined standard error SE_c was calculated from the square of the sum if the squares of the SEs from the individual data points:

$$\mathrm{SE_c} = \sqrt{\mathrm{SE_1^2} + \mathrm{SE_2^2}}$$

Next, the combined degrees of freedom (DOF) were calculated on the basis of the number of values (N) in each data set:

$$\mathrm{DOF} = [(N_1 - 1) + (N_2 - 1)]$$

The difference between measured results (t) was expressed in terms of the difference between mean values, $\bar{x}$, over the combined standard error, SE_c:

$$t = \frac{|\overline{x_1} - \overline{x_2}|}{\mathrm{SE_c}}$$

Finally, a p-value was calculated for pairwise comparisons using the TDIST function:

$$p = \mathrm{TDIST}(t, \mathrm{DOF}, 2)$$

where differences were assumed to be statistically significant when $p < 0.05$.

3.3 Results and Discussion

3.3.1 Effect of Flow Rate on Mean Hydrodynamic Sizes and Polydispersities of PAX-Loaded and DiI-Loaded DualM PNPs

Dynamic light scattering experiments were carried out for all PNP formulations, with cumulant analysis yielding hydrodynamic size and polydispersity information (Figure 3-3). Figure 3-3A shows mean hydrodynamic effective diameters ($d_{h,eff}$) of DualM PNPs at various manufacturing flow rates (Q = 0, 50, 100, and 200 μL/min), where Q = 0 μL/min indicates PNPs prepared by the bulk nanoprecipitation method. For each manufacturing condition, data is shown for three cases of hydrophobic molecule encapsulation: 1. PNPs with no encapsulated molecules ("empty" PNPs, white bars); 2. PNPs with encapsulated PAX (PAX-PNPs, blue bars); and 3. PNPs with encapsulated DiI (DiI-PNPs, red bars). The indicated sizes for empty PNPs were previously reported in chapter 2 and are shown here for comparison purposes.

Although PAX and DiI molecules have similar molecular weights (854 and 934 g mol^{-1}, respectively), the two long alkyl hydrocarbon tails impart DiI with greater free volume than PAX (Figure 3-1C), such that encapsulated DiI would be expected to swell the hydrophobic domains more extensively than PAX. However, for each flow condition we find that the three encapsulation cases (empty, PAX and DiI) show statistically identical $d_{h,eff}$ values (Figure 3-3A), suggesting that the overall PNP sizes are not affected by the addition of either hydrophobic molecule to the PNPs. This interesting result suggests either that the hydrophobic domains are not significantly swollen by either PAX or DiI, or that changes in the internal PNP structure compensate for swelling differences to maintain

consistent PNP sizes. This question will be addressed in the next section with TEM data showing the internal structure of DualM PNPs containing different encapsulated molecules.

Due to the size similarities of empty PNPs, PAX-PNPs and DiI-PNPs for each flow condition, all three cases show the same trend with respect to manufacturing flow rate (Figure 3-3A), This trend was previously explained by the competition between shear-induced particle coalescence and shear-induced particle breakup as the maximum shear rate in the hot spots increased with increasing flow rate.[53] Briefly, shear-induced coalescence events in the microchannels effect increases in mean hydrodynamic sizes between Q = 0 μL/min and Q = 50 μL/min. Next, particle growth in the microchannels increases particle capillary numbers, increasing the role of shear-induce particle breakup such that mean hydrodynamic sizes drop between Q = 50 μL/min and Q = 100 μL/min. Finally, as the maximum shear rate is further increased, the competition between coalescence and breakup events leads to small increases in mean hydrodynamic sizes between Q = 100 μL/min and Q = 200 μL/min.

Similar to mean hydrodynamic sizes, the polydispersities of PAX-PNPs and DiI-PNPs show a similar trend with increasing flow rate to that of empty DualM PNPs (Figure 3-3B). Polydispersity values for the empty DualM PNPs reported in our previous study are shown for comparison.[53] Specifically, polydispersities for all three encapsulation cases are found to drop significantly between Q = 0 μL/min and Q = 50 μL/min, with no significant changes in polydispersities found at higher microfluidic flow rates. In chapter 2, this trend was explained by shear-induced coalescence of small particles in the microchannels decreasing the distribution width compared to bulk-formed PNPs, while the competition between

shear-induced coalescence and shear-induced breakup leads to similar polydispersities as the flow rate is further increased.[53]

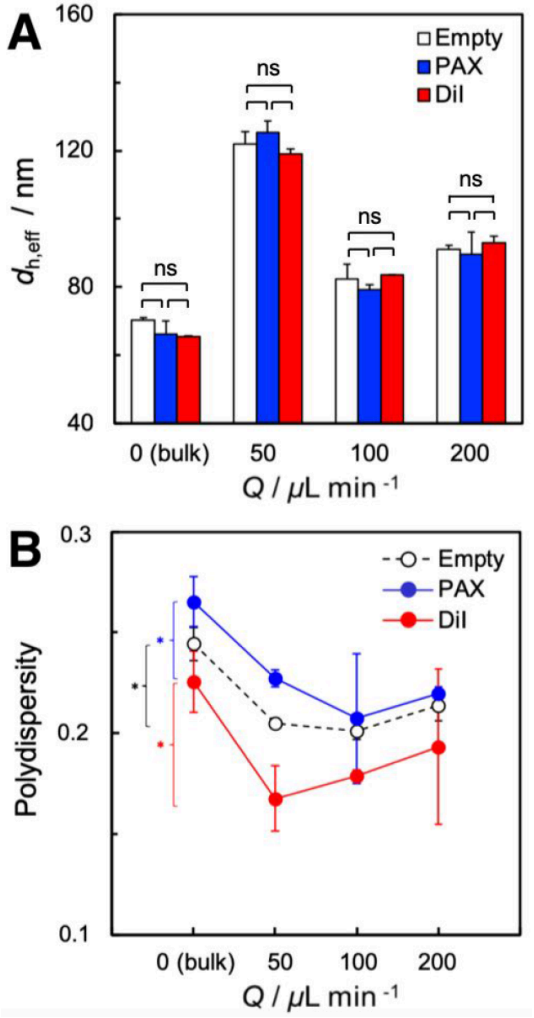

Figure 3-3. Hydrodynamic effective diameters ($d_{h,eff}$, A) and polydispersities (B) of empty PNPs (white), PAX-PNPs (blue), and DiI-PNPs (red) manufactured at various flow rates (Q = 50, 100, and 200 μL/min) using the microfluidic reactor or bulk nanoprecipitation (Q = 0 μL/min). Brackets indicate statistical comparisons between $d_{h,eff}$ and polydispersities of PNPs manufactured under different conditions: * indicates $p < 0.05$ and ns indicates $p > 0.05$.

3.3.2 Effect of Flow Rate on Morphologies of PAX-Loaded and DiI-Loaded DualM PNPs

Flow-tunable shear forces were previously shown to have a strong effect on the morphologies and internal structures of DualM PNPs prepared in the two-phase microfluidic reactor, due to the shear rate-dependent interplay of particle coalescence, particle breakup, and intraparticle chain rearrangements.[53] Remarkably, we find that encapsulating either PAX or DiI using the same DualM copolymer results in nearly identical mixtures of morphologies as the empty PNPs at the same investigated flow condition (Figure 3-4 and Table 3-1). The representative TEM images in Figure 3-4 were obtained following uranyl acetate staining, such that the hydrophilic PEO regions appear dark while the hydrophobic PHMssEt regions appear bright. Table 3-1 lists mean core dimensions and number percentages of each identified morphology in empty PNP, PAX-PNP and DiI-PNP samples under the various flow conditions including bulk preparation. As shown in Figure 3-4, the different preparation conditions result in different mixtures of spheres, cylinders, and vesicles. As in chapter 2, we define two types of vesicles: (1) small vesicles (d < 100 nm) containing a distinct small spherical compartments (SVs) and (2) large vesicles (d > 100 nm) containing either large spherical compartments or mixtures of smaller spherical and cylindrical compartments (LVs). For all three cases of hydrophobic molecule encapsulation (empty, PAX and DiI) and as described in chapter 2 for the empty case, we found that the highest percentage of SVs occurred at Q = 50 μL/min, while cylinders only appeared at Q = 200 μL/min (Figure 3-4 and Table 3-1). At each of the four flow conditions, the observed morphologies, their dimensions, and their percentages, are similar for the empty, PAX, and DiI cases (Table 3-1). We expect that the wide variation of size and shape observed in many of the nanoparticle samples will lead to heterogeneous

interactions and a complex range of nanoparticle behaviors in cell cultures. However, despite the observed sample polydispersity, we will show that average quantities describing PNP-cellular interactions, including EC50 values and rates of cell uptake, can be well correlated to simple average structural parameters such as mean hydrodynamic diameter.

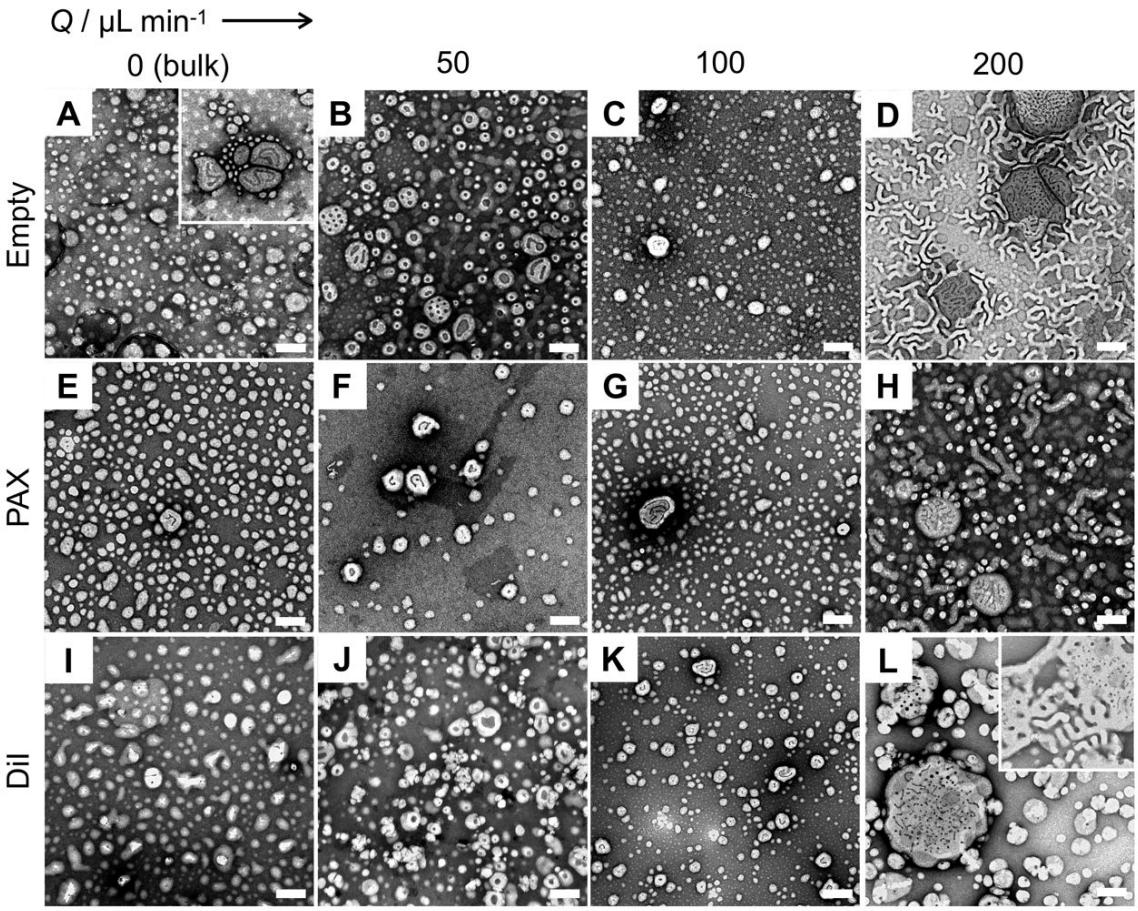

Figure 3-4. Representative TEM images of empty PNPs (A-D), PAX-PNPs (E-H), and DiI-PNPs (I-L) manufactured at various flow rates (Q = 50, 100, and 200 μL/min) using the microfluidic reactor or bulk nanoprecipitation (Q = 0 μL/min). Scale bars are 200 nm.

Table 3-1. Characteristics of PAX-PNPs and DiI-PNPs Manufactured at Variable Flow Rates

Q / μL min^{-1}	Morphology[a]	Empty PNPs[c]		PAX-PNPs		DiI-PNPs	
		Dimension[b] / nm	Number Percentage / %	Dimension / nm	Number Percentage / %	Dimension / nm	Number Percentage / %
0 (bulk)	S	68 ± 5	98.5 ± 0.4	62 ± 1	97.5 ± 0.1	53 ± 3	91.2 ± 0.1
	SV	60 ± 4	1.1 ± 0.2	63 ± 4	0.2 ± 0.1	70 ± 3	4.3 ± 0.7
	LV	233 ± 12	1.4 ± 0.1	118 ± 5	0.6 ± 0.2	133 ± 2	4.5 ± 0.9
50	S	69 ± 9	79 ± 3	59 ± 3	75 ± 6	62 ± 1	76 ± 4
	SV	69 ± 5	18.1 ± 0.2	73 ± 4	13 ± 5	74 ± 1	14 ± 4
	LV	185 ± 15	3 ± 1	160 ± 5	13 ± 2	160 ± 20	11 ± 1
100	S	38 ± 4	99.5 ± 0.3	45 ± 3	98 ± 1	52 ± 1	96 ± 1
	SV	65 ± 7	0.5 ± 0.1	78 ± 3	1.1 ± 0.6	69.8 ± 0.1	0.96 ± 0.6
	LV	159 ± 15	0.5 ± 0.2	260 ± 20	0.6 ± 0.3	190 ± 40	2.6 ± 0.7
200	S	47 ± 4	55 ± 2	43 ± 2	58 ± 7	45 ± 9	62 ± 1
	SV	52 ± 10	1.5 ± 0.1	64 ± 5	6 ± 2	70 ± 7	8.3 ± 0.3
	LV	291 ± 81	2.3 ± 0.4	200 ± 40	7 ± 1	390 ± 80	7 ± 1
	C	31 ± 2	42 ± 3	37 ± 3	29 ± 5	38 ± 9	22 ± 1

[a]Morphologies are indicated as S (spheres), SV (small vesicles), LV (large vesicles), or C (cylinders). [b]Dimensions refer to sphere and small vesicle diameters and cylinder widths determined from TEM images. For non-spherical large vesicles, dimensions refer to the longest measurable internal distance. Standard errors are reported to represent the uncertainty of mean dimensions and number percentages determined from triplicate images in different regions of the TEM grid. [c]empty PNP data are previously reported in chapter 2 and included here for comparison.

Microfluidic morphologies of DualM PNPs arise from a combination of kinetic and thermodynamic factors under variable shear conditions in the microfluidic channel.[53] The observed insensitivity of the morphologies to encapsulation of either PAX or DiI in the hydrophobic PNP regions (Table 3-1) suggests that neither molecule has a large effect on either chain mobility or local free energy within the PNPs at the investigated drug loadings. This may be partly attributed to a relatively large free volume within the hydrophobic regions due to the long cleavable side chains of the PHMssEt block, providing space for hydrophobic molecules to intercalate without significant perturbations to chain mobility or dimensions. Another contributing factor may be the compressibility of the hydrophilic PEO

compartments within vesicle morphologies. For example, as PAX or DiI is solubilized within the hydrophobic cores of SVs and LVs, expansion of the hydrophobic regions can be offset by compression of the hydrophilic compartments, preventing an increase in the chain packing stress that would trigger a morphological transition. Along with the consistent morphologies, this mechanism may also explains the consistent mean hydrodynamic sizes for the three different encapsulation cases described in the previous section.

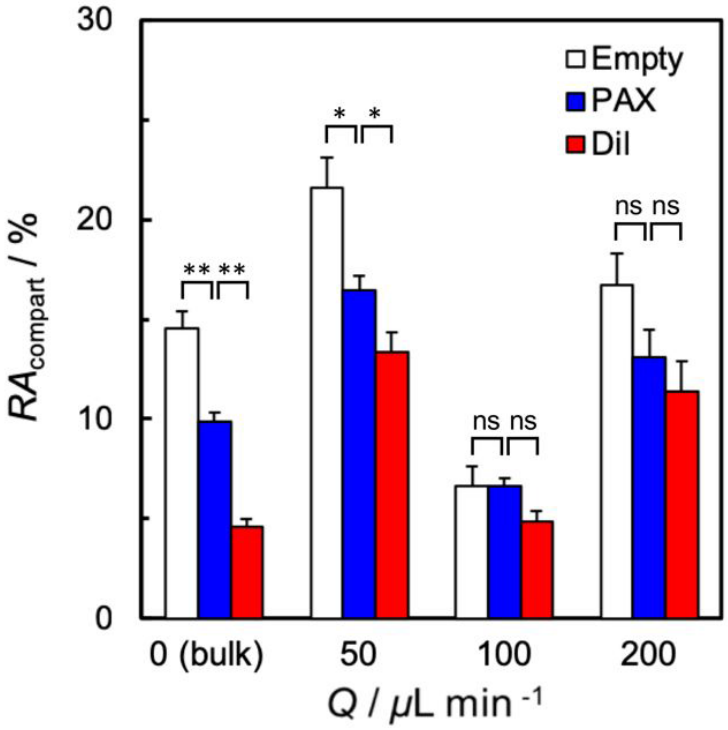

Figure 3-5. Relative areas of inner compartments, $RA_{compart}$, of empty PNPs (white), PAX-PNPs (blue), and DiI-PNPs (red) manufactured at various flow rates (Q = 50, 100, and 200 μL/min) using the microfluidic reactor or bulk nanoprecipitation (Q = 0 μL/min). Brackets indicate statistical comparisons between $RA_{compart}$ values: ** indicates $p < 0.005$, * indicates $p < 0.05$, and ns indicates $p > 0.05$.

We find evidence for compression of the hydrophilic compartments upon encapsulation of hydrophobic molecules by determining mean relative compartment areas RA_{compart} from TEM image analysis of SVs and LVs. RA_{compart} is a measure of the areal percentage of the internal dark area relative to the overall bright vesicle core area in the reverse-stained TEM images, which reflects the relative hydrophilic compartment volume of the cores. An example of the RA_{compart} calculation is provided in *Appendix B* (Figure B-1). Figure 3-5 shows RA_{compart} values determined for the three encapsulation cases (empty, PAX and DiI) under various flow conditions. RA_{compart} values are generally lower in the PAX and DiI cases compared to the corresponding empty PNP case, providing evidence for compression of the hydrophilic compartments as SVs and LVs encapsulate hydrophobic molecules. Moreover, for each flow condition Figure 3-5 shows lower RA_{compart} values in DiI-PNPs than in PAX-PNPs. This may be partly due to the more expanded molecular structure of DiI compared to PAX (Figure 3-1C), leading to greater swelling of hydrophobic domains and concomitantly greater compression of hydrophilic compartments. In addition, another contribution to lower RA_{compart} values in DiI-PNPs may be the slightly higher loading of DiI compared to PAX as discussed in the next section.

3.3.3 Effect of Flow Rate on PAX and DiI Encapsulation Efficiencies in DualM PNPs

Figure 3-6 shows encapsulation efficiency (*EE*) and drug (or dye) loading (*DL*) data for both PAX (blue data points) and DiI (red data points) encapsulation in DualM PNPs plotted as functions of flow rate (where $Q = 0$ μL/min indicates PNPs bulk preparation). For both encapsulated hydrophobic molecules, we find that *EE* (Figure 3-6A) values follow non-monotonic trends which approximately track with the flow rate dependencies of hydrodynamic PNP size (Figure 3-3A); for example, encapsulation of both PAX and DiI

show maxima at Q = 50 μL/min (Figure 3-6A) where the hydrodynamic size also shows a maximum (Figure 3-3A). Plots of *EE* values for both hydrophobic molecules vs. the corresponding PAX-PNP or DiI-PNP $d_{h,eff}$ values from Figure 3-3A are shown in the inset to Figure 3-6A, along with best fit linear trend lines. The general increase in *EE* with increasing $d_{h,eff}$ values can be understood in terms of larger PNPs possessing hydrophobic domains of greater volume, allowing for encapsulation of larger numbers of hydrophobic molecules.[43]

DL values (Figure 3-6B) follow similar trends to the corresponding *EE* values (Figure 3-6A), although differences in *EE* with changes in *Q* are found to be statistically significant, whereas differences in *DL* with changes in *Q* are not found to be statistically significant. Under all flow conditions, DiI shows greater encapsulation than PAX (maximum *DL* = 7% and 4 %, respectively), suggesting generally higher solubility of DiI in the hydrophobic cores of DualM PNPs. We note that despite the solubility differences between the two drugs, the statistically significant differences in both DiI and PAX EE values at different flow rates (Figure 3-6A) indicate the pivotal role of microfluidic flow rate in encapsulation of both species.

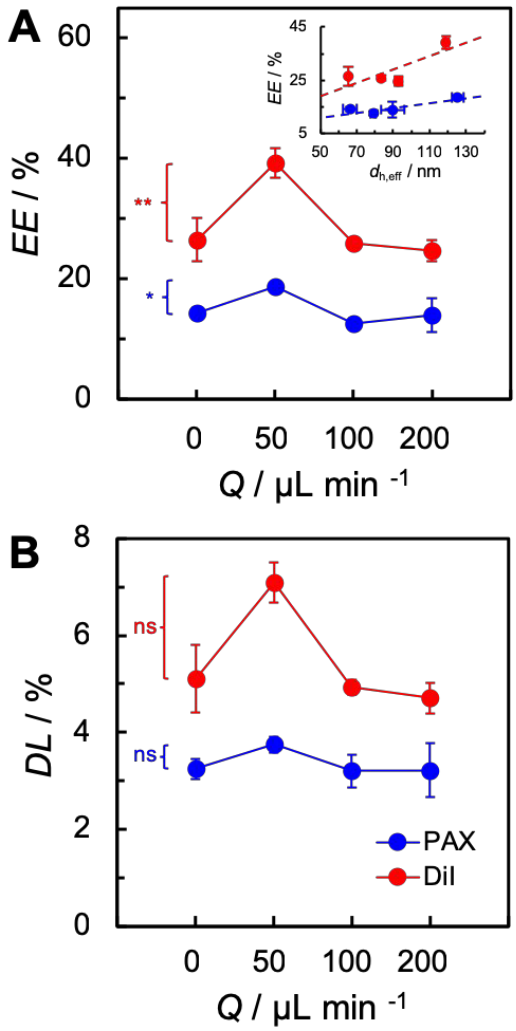

Figure 3-6. Encapsulation efficiency (*EE*, A) and drug loading (*DL*, B) of PNPs containing PAX (blue points) and DiI (red points) manufactured at various flow rates (Q = 50, 100, and 200 μL/min) using the microfluidic reactor or bulk nanoprecipitation (Q = 0 μL/min). Inset to (A) shows *EE* values vs. corresponding $d_{h,eff}$ values with best fit linear trend lines. Brackets indicate statistical comparisons between *EE* and *DL* values: ** indicates $p < 0.005$, * indicates $p < 0.05$, and ns indicates $p > 0.05$.

Taking advantage of the fluorescent properties of DiI, we were able to visualize and compare the homogeneity of dye molecule dispersion within the various PNP formulations. To do this, we merged fluorescence and optical microscopy images of deposited films of DiI-PNPs prepared at the different flow conditions (Figure 3-7, A-D). Although the

diffraction limit of optical microscopy does not allow individual PNPs to be resolved in these images, aggregates of PNPs are clearly visible as dark regions in the regular optical micrographs. Moreover, the overlap between red regions of DiI emission and dark regions of PNPs allows determination of the percentage of PNPs containing the fluorescent drug surrogate. Therefore, we propose defining encapsulation homogeneity (*EH*) as the mean area of overlapping red DiI regions divided by the mean area of dark PNP regions multiplied by 100%. The corresponding overlapping process from the merged images and a sample *EH* calculation is provided in *Appendix B* (Figures B-2 and B-3, respectively).

From the series of image overlays, it is clear that a significant percentage of bulk-prepared PNPs do not contain DiI (Figure 3-7A) and that this percentage decreases considerably on the microfluidic chip (Figure 3-7B) and further still as the microfluidic flow rate is increased (Figure 3-7, C and D). This trend is represented by the increase in *EH* with increasing *Q* shown in Figure 3-7E. To our knowledge, this is the first example of microfluidic flow increasing the homogeneity of hydrophobic molecule encapsulation within PNPs. We tentatively attribute this effect to an increase in shear-induced particle coalescence and breakup events facilitating exchange and dispersion of DiI throughout the PNP population. The observed increase in *EH* associated with microfluidic manufacturing offers a significant advantage for nanomedicine applications, since it decreases the number of therapeutically inactive PNPs, thus increasing the rate of targeted delivery to the tumor site.

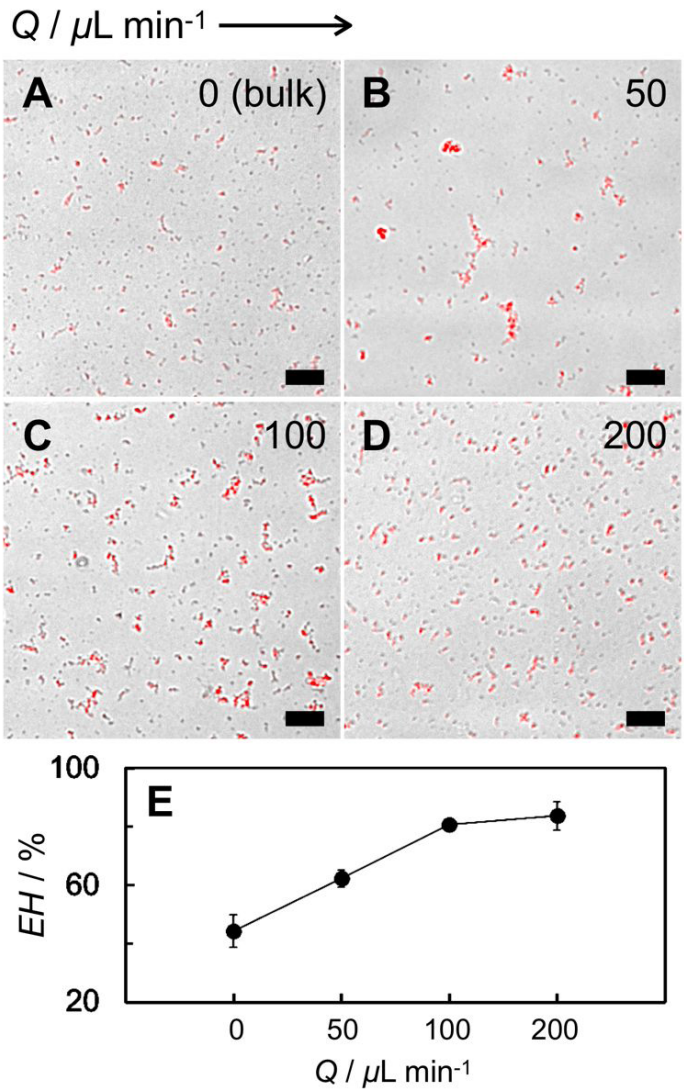

Figure 3-7. (A-D) Merged fluorescence and optical microscopy images of DiI-loaded PNPs manufactured at various flow rates (Q = 50, 100, and 200 μL/min) using the microfluidic reactor or bulk nanoprecipitation (Q = 0 μL/min). Scale bars are 20 μm. (E) Encapsulation homogeneity (*EH*) of the DiI-loaded PNPs.

3.3.4 Effect of Flow Rate on GSH-Triggered Release of PAX-Loaded DualM PNPs

The *in vitro* PAX release kinetics were investigated for PAX-PNPs manufactured under the various flow conditions. Release experiments were conducted at 37 ºC under perfect sink conditions using release media consisting of either PBS + 10 mM GSH or PBS with no GSH (control). Figure 3-8A shows the resulting PAX release profiles and

associated fits of various PAX-PNPs. The first observation from these profiles is clear evidence of GSH-triggered release for all investigated PAX-PNP formulations, with PNPs in GSH medium releasing ~100% of their encapsulated PAX after 48h (solid circles), compared to PNPs in PBS which released only 40-50% of their PAX over the same time period (open circles).

Second, the GSH-triggered release kinetics in Figure 3-8A (solid fit lines) are clearly tunable with different flow conditions, with the bulk sample (black line) showing the fastest PAX release and the Q = 50 μL/min microfluidic sample (red line) showing the slowest release. Release half times ($t_{1/2}$) determined from the fits are plotted vs. flow rate in Figure 8B, showing a similar non-monotonic trend (i.e. an increase followed by a decrease) to hydrodynamic diameters (Figure 3-3A); the associated plot of $t_{1/2}$ vs. $d_{h,eff}$ is found to yield an approximately linear trend (Figure 3-8B, inset). The positive correlation between release half times and PNP size is explained by a combination of longer PAX and GSH diffusion distances within the cores of larger PNPs.

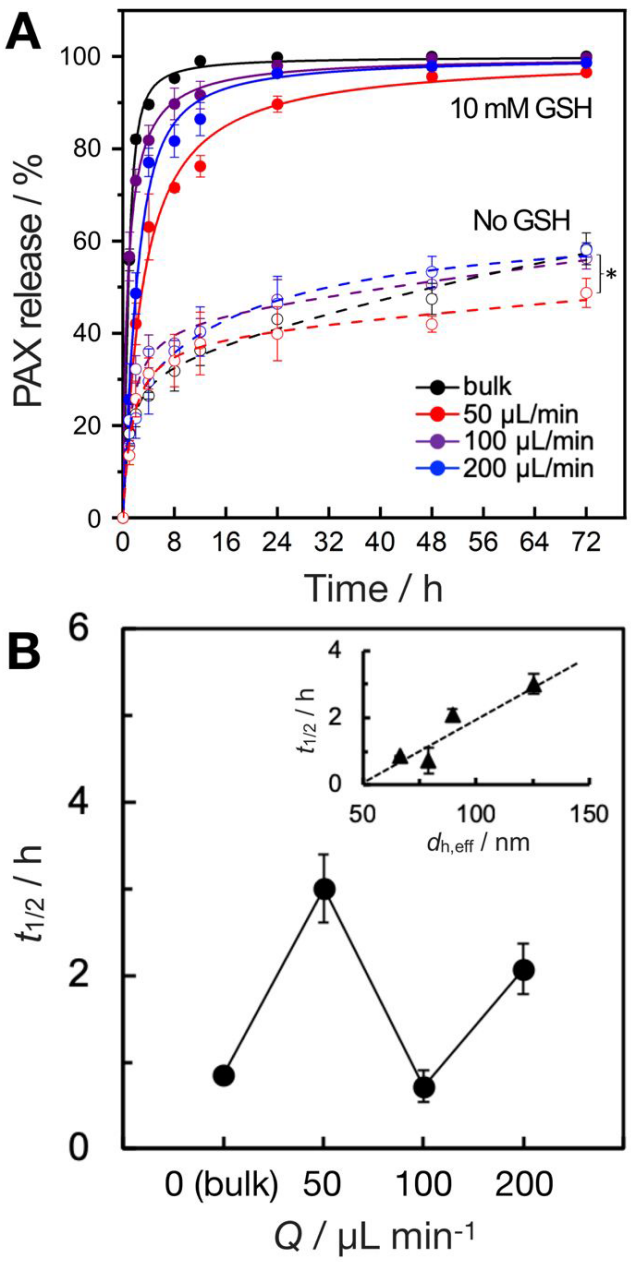

Figure 3-8. (A) PAX release profiles of PAX-PNPs manufactured at various flow rates (Q = 50, 100, and 200 μL/min) using the microfluidic reactor or bulk nanoprecipitation (Q = 0 μL/min). Solid circles represent PAX-PNPs incubated with GSH with solid lines showing associated fits; open circles represent PAX-PNPs incubated without GSH with dashed lines showing associated fits. The bracket indicates statistical comparisons between PAX release percentage values (without GSH) of the Q = 50 μL/min formulation and each of the other three formulations: * indicates p < 0.05. (B) Release half times ($t_{1/2}$) of PAX-PNP formulations (with GSH) vs. the manufacturing flow rate, Q. The inset shows a plot of $t_{1/2}$ vs. $d_{h,eff}$ with linear regression trend line.

Finally, Figure 3-8A demonstrates that along with controlling GSH-triggered release profiles, microfluidic flow rate also provides some control for lowering the extent of diffusional release in the absence of GSH. Non-triggered diffusional release of drugs from PNPs in the body or under in vitro perfect sink conditions is driven by differential chemical potential for drug inside and outside the PNP. For example, all PNP formulations in the absence of GSH release ~55% of their PAX after 72 h, with the notable exception of the Q = 50 μL/min formulation, which releases only ~45% of its PAX over the same time period. This relative attenuation of non-triggered diffusional release for the Q = 50 μL/min sample results in a greater *difference* between GSH and non-GSH release at the 72 h time point (~55%) compared to the other formulations (~45%). Diffusional release of drug in the absence of GSH should be attenuated as much as possible in clinical applications to decrease side effects caused toxic exposure of healthy tissue and to increase drug delivery to the cancerous tumor. Therefore, the current results suggests that appropriate selection of flow conditions in future studies could be used to produce stimuli-responsive nanocarriers that maximize the percentage of injected drug delivered selectively to the tumor site.

We were interested in determining the relationships between GSH-triggered PAX release and associated GSH-triggered structural changes in PAX-PNPs due to cleavage of disulfide linkages. We therefore monitored both structural parameters $d_{\mathrm{h,eff}}$ and RA_{compart} over the first 24 h of the release experiments under release conditions with and without GSH (*Appendix B*, Figures B-4 and B-5, respectively). Also shown in *Appendix B* are TEM images of PAX-PNPs at different time points during the first 24 hours of PAX release under GSH (Figure B-6) and non-GSH (Figure B-7) conditions. We find measurable increases in both $d_{\mathrm{h,eff}}$ and RA_{compart} during the first 24 h of PAX release under both sets of

conditions, although for most formulations these changes are significantly greater in the presence of GSH, confirming the important role of GSH-triggered cleavage of disulfide linkages. Since the most rapid concurrent changes in PAX release, $d_{\mathrm{h,eff}}$ and RA_{compart} in the presence of GSH occur in the first four hours, we plot the changes in these three parameters over this time period in Figure 3-9A, 3-9B, and 3-9C, respectively. From these three plots, we calculated the following average rates for the first four hours of GSH-triggered PAX release:

$$R_{\mathrm{rel}} = \frac{\mathrm{PAX\ released_{4h}} - \mathrm{PAX\ released_{0h}}}{4\ \mathrm{h}}$$

$$R_{d\mathrm{h}} = \frac{d_{\mathrm{h,eff,4h}} - d_{\mathrm{h,eff,0h}}}{4\ \mathrm{h}}$$

$$R_{RA} = \frac{RA_{\mathrm{compart,4h}} - RA_{\mathrm{compart,0h}}}{4\ \mathrm{h}}$$

The insets to Figure 3-9B and 3-9C show plots of R_{rel} vs. $R_{d\mathrm{h}}$ and R_{rel} vs. R_{RA}, respectively, showing approximately linear correlations in both cases. These relationships indicate that GSH-triggered drug release tracks with GSH-triggered structural changes ($d_{\mathrm{h,eff}}$ and RA_{compart}) previously ascribed to cleavage of junction and pendant linkages, respectively,[53] suggesting contributions of both reactions to triggered drug release.[29]

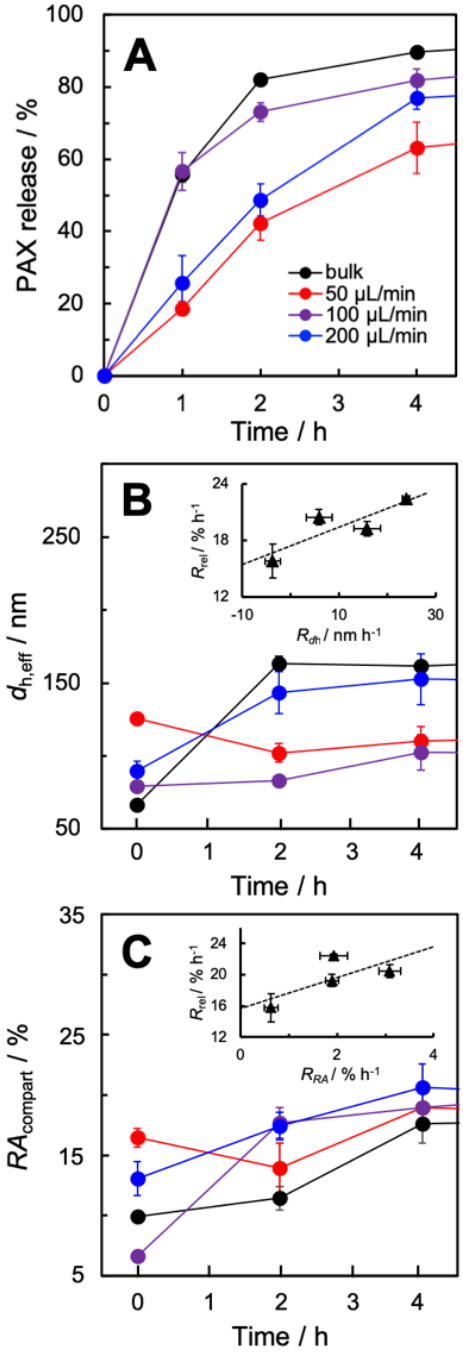

Figure 3-9. (A) PAX release percentage, (B) $d_{h,eff}$, and (C) $RA_{compart}$ values over the first four hours of release experiments in GSH. All plots show data for PAX-PNPs manufactured at various flow rates (Q = 50, 100, and 200 μL/min) using the microfluidic reactor or bulk nanoprecipitation (Q = 0 μL/min). Average rates of change of PAX release, $d_{h,eff}$, and $RA_{compart}$ (R_{rel}, R_{dh}, R_{RA}, respectively) over the four hours were calculated from plots in (A), (B), and (C), respectively. Insets to (B) and (C) show plots of R_{rel} vs. R_{dh} and R_{rel} vs. R_{RA}, respectively, with linear fits.

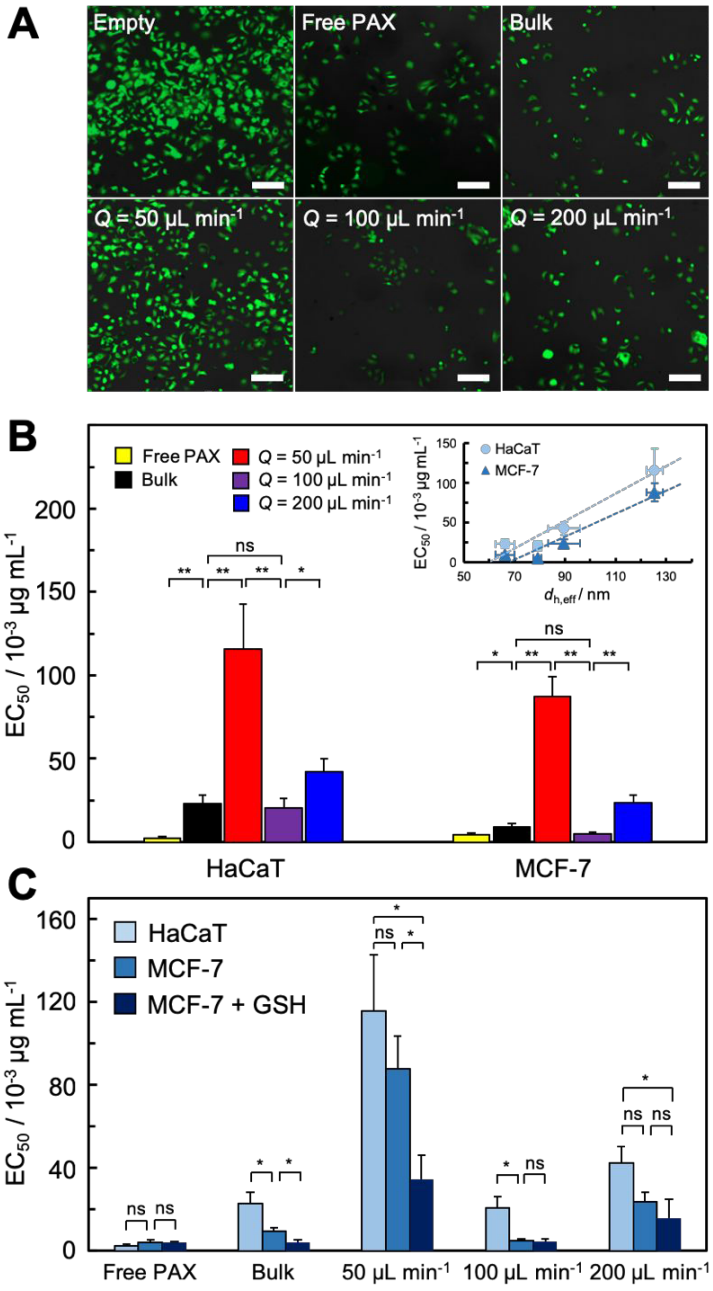

Figure 3-10. (A) Fluorescence images of MCF-7 cells treated with empty DualM PNPs, free PAX, and PAX-PNPs manufactured at various flow rates (Q = 50, 100, and 200 μL/min) using the microfluidic reactor or bulk nanoprecipitation (Q = 0 μL/min). Equivalent PAX concentrations are 0.1 μg/mL. Scale bars are 20 μm. (B) EC_{50} values of free PAX and PAX-PNP formulations for HaCaT (healthy) and MCF-7 (cancerous) cells. Inset shows linear relationships between both sets of EC_{50} values and PAX-PNP $d_{h,eff}$ values. (C) Comparison of EC_{50} values for HaCaT, MCF-7, and MCF-7 + GSH. Incubation times were 48 h. Brackets indicate statistical comparisons between EC_{50} values: ** indicates $p < 0.005$, * indicates $p < 0.05$, and ns indicates $p > 0.05$.

3.3.5 Effect of Flow Rate on Cytotoxicity of PAX-Loaded DualM PNPs

We next investigated the cytotoxicity of DualM PAX-PNP formulations by comparing the responses of HaCaT (healthy) and MCF-7 (cancerous) cells to PAX-loaded PNPs manufactured using the microfluidic reactor at various flow rate (Q = 50, 100, and 200 μL/min) or using bulk nanoprecipitation (Q = 0 μL/min). MCF-7 is a well-studied breast cancer cell line that responds to many different anticancer agents including PAX; HaCaT cells are spontaneously transformed keratinocytes that are easily cultured non-cancerous control cells. We find that the empty DualM PNPs (including any remaining DMF in the dispersion following dialysis) do not show significant cytotoxicity to either HaCaT or MCF-7 cells within the investigated range of copolymer excipient concentrations (*Appendix B*, Figures B-8 and B-9, respectively). Figure 3-10A qualitatively shows the cytotoxicity of free PAX and various PAX-PNPs to MCF-7 cells. Fluorescein diacetate selectively stains living cells which emit fluorescence in the green channel of the microscope. Therefore, by comparing the living cell densities in the images at equivalent PAX dosing levels, we find that microfluidic PAX-PNPs manufactured at Q = 50 μL/min show the lowest cytotoxicity (with the exception of the empty PNP control) whereas microfluidic PAX-PNPs manufactured at Q = 100 μL/min and bulk PAX-PNPs show the highest cytotoxicities (with the exception of free PAX).

More quantitative insights are obtained by analyses and comparison of cell viability data for free PAX and various PAX-PNP formulations over a range of PAX dosing amounts (*Appendix B*, Figures B-10 to B-13). Half maximal effective concentration (EC_{50}) values were determined from fits of 48 h cell viability plots for both HaCaT and MCF-7 cell lines, as shown in *Appendix B* (Figures B-10 to B-13); the resulting EC_{50} values are

shown in Figure 3-10B. In general, encapsulation in PNPs decreases cytotoxicity (increase EC_{50} values) in cell cultures as drug arability is attenuated by encapsulation in the hydrophobic cores.[49.50] Moreover, variation in EC_{50} values between different PNP formulations demonstrates tunability of PNP-cell interactions via processing control of PNP size and shape. Both cell lines afford EC_{50} values with strong dependencies on the preparation method (bulk vs. microfluidic) and on the microfluidic flow rate. In fact, the following similar trend in EC_{50} values is found for both cell lines: Q = 50 μL/min > Q = 200 μL/min > Q = 100 μL/min ≈ bulk > free PAX. We note that this trend tracks well with the trend in PAX-PNP hydrodynamic sizes, as shown by the linear relationships between HaCaT and MCF-7 EC_{50} values and PAX-PNP $d_{h,eff}$ values (Figure 3-10B, inset). This suggests that microfluidic shear control leading to smaller PAX-PNP sizes results in formulations that are more cytotoxic to both healthy and cancerous cells.

Figure 3-10C compares EC_{50} values at each flow rate for three different cell environments: 1. HaCaT cells, 2. MCF-7 cells, and 3. MCF-7 cells pre-treated with 10 mM GSH-OEt, which can induce an increase of cellular GSH concentration (MCF-7 + GSH).[53] Importantly, we find differential cytotoxicity between the two different cell lines, with higher EC_{50} values for HaCaT cells (lower cytotoxicity) than for MCF-7 cells (higher cytotoxicity) in each case of PAX-loaded DualM PNPs. For PNP formulations with the two highest EC_{50} values (Q = 50 and 200 μL/min), the measured differences between the HaCaT and MCF-7 cells are not significant due to statistical errors. However, the PNP formulations with the two lowest EC_{50} values (bulk and Q = 100 μL/min) are found to be significantly more cytotoxic to cancerous MCF-7 than to healthy HaCaT cells. This is in contrast to the free, unencapsulated PAX, which showed no significant difference between

EC_{50} values for cancerous and healthy cells. These results indicate that encapsulation of PAX in DualM PNPs increases selectively between healthy (HaCaT) and cancerous (MCF-7) cells. Moreover, we find that this selectivity is also tunable *via* microfluidic flow. Defining selectivity as:

$$\text{Cytotoxic Selectivity} = \frac{\text{EC}_{50}(\text{HaCaT}) - \text{EC}_{50}(\text{MCF-7})}{\text{EC}_{50}(\text{HaCaT})} \times 100\%$$

we find the greatest cytotoxic selectivity for the Q = 100 μL/min formulation (~76%), which has the smallest PNP size of the microfluidic formulations ($d_{h,eff}$ = 79 nm) and the lowest cytotoxic selectivity for the Q = 50 μL/min formulation (~24%), which has the largest size ($d_{h,eff}$ = 125 nm). This suggests that the current microfluidic approach provides a convenient manufacturing handle on optimizing DualM PNP selectivity for cancer cells *via* the flow tunability of $d_{h,eff}$ described in Figure 3-3A.

To further support the hypothesis that the selectivity of DualM PNP formulations is due to elevated GSH concentrations found in cancerous cells, we also tested free PAX and PAX-PNP formulations against MCF-7 cells that had been pre-treated with GSH-OEt to further increase GSH concentrations relative to intrinsic levels (MCF-7 + GSH) Cell viability data for empty PNPs, free PAX and PAX-PNPs in the MCF-7 + GSH environment are shown in *Appendix B* (Figures B-14 to B-16) and the resulting EC_{50} values are presented in Figure 3-10C. Importantly, GSH-OEt pre-treatments did not show significant toxicity to MCF-7 cells (*Appendix B*, Figure B-17), nor did the increase in GSH concentration show any difference in the cytotoxicity of free PAX (Figure 3-10C). However, each of the DualM PNP formulations showed a noticeable decrease in EC_{50} values against the MCF-7 + GSH cells compared to native MCF-7 cells, with these decreases being statistically significant in two of the four formulations. This provides good evidence that DualM PNP formulations

show enhanced cytotoxicities in cellular environments with elevated GSH concentrations. In fact, the combined effects of GSH concentration and flow rate shown in Figure 3-10C suggest that different manufacturing conditions leads to variable thresholds for GSH responsivity. Specifically, both bulk and Q = 100 μL/min PAX-PNP formulations showed GSH thresholds for increased cytotoxicity relative to HaCaT cells that were at or below the intrinsic GSH levels in MCF-7. On the other hand, the Q = 50 μL/min and Q = 200 μL/min PAX-PNP formulations showed higher GSH thresholds for increased cytotoxicity relative to HaCaT cells, with these thresholds being between the intrinsic MCF-7 GSH levels and the elevated GSH levels in pre-treated MCF-7.

3.3.6 Effect of Flow Rate on MCF-7 Cell Uptake Rates of DualM PNPs

In Figure 3-8B, we showed a linear correlation between GSH-triggered PAX release half times and particle size (Figure 3-8B), with smaller PNP sizes leading to faster PAX release. This relationship may partly explain the linear increases in EC_{50} values with increasing particle size (Figure 3-10B), since slower PAX release in the cell medium would cause lower cytotoxicity (higher EC_{50} values). However, another possible contribution of particle size to cytotoxicity is the rate of cell uptake of PNPs, since release of PAX within the cell would have a greater cytotoxic effect than release of PAX in the extracellular matrix of the tumor. To investigate cell uptake qualitatively, we used fluorescence microscopy to visualize DAPI-stained MCF-7 cells that had been incubated with various DiI-PNP formulations for 2h. In these experiments, the DiI dye served as a fluorescent surrogate for non-fluorescent PAX, based on the result that sizes and morphologies of PAX-PNP and DiI-PNP are similar for all manufacturing conditions (Figures 3-3 and 3-4). Figure 3-11 shows the resulting fluorescence images of MCF-7 uptake of DiI-PNPs. In

each image, the DAPI (blue regions) indicate the cellular nuclei while the DiI (red regions) indicate the PNPs. From the images of merged DAPI and DiI channels, the $Q = 100\ \mu$L/min formulation appears to show the highest extra-nuclear compartmentalization of DiI (Figure 3-11K), while the $Q = 50\ \mu$L/min and 200 μL/min formulations show the lowest extra-nuclear compartmentalization of DiI (Figure 3-11, J and L, respectively).

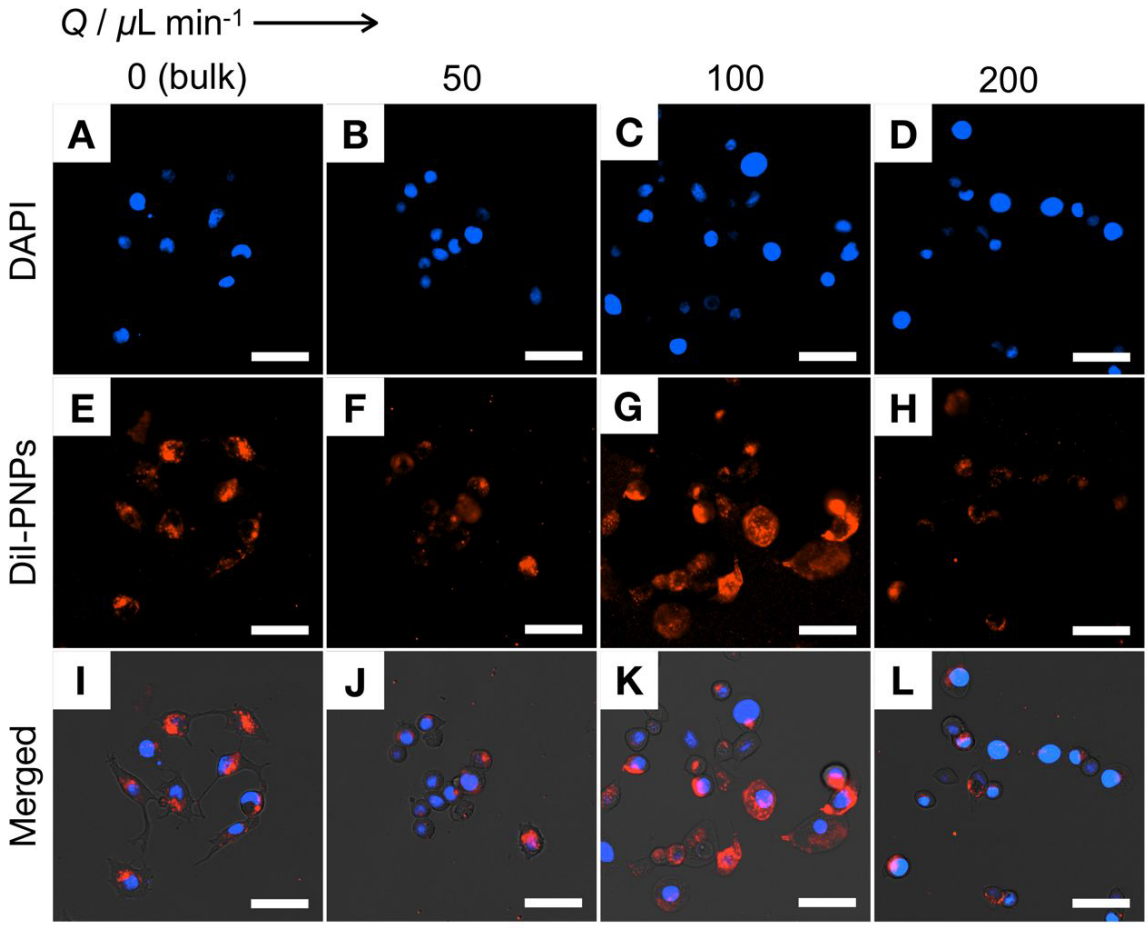

Figure 3-11. Fluorescence images of DAPI-stained MCF-7 cells treated with DiI-PNPs manufactured at various flow rates ($Q = 50$, 100, and 200 μL/min) using the microfluidic reactor or bulk nanoprecipitation ($Q = 0\ \mu$L/min). (A−D) DAPI channel (blue) indicating locus of nuclei; (E−H) DiI channel (red) indicating locus of Di-PNPs; (I−L) merged images combining DAPI (blue) and DiI (red) channels. Scale bars are 20 μm.

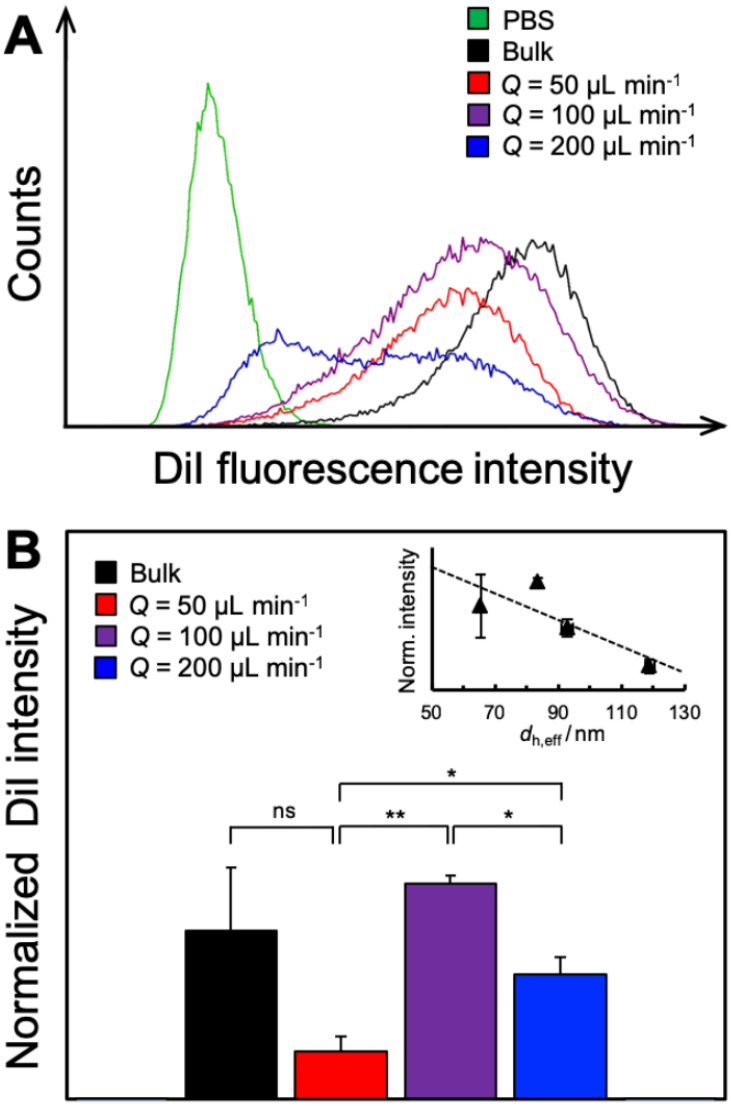

Figure 3-12. (A) Histograms of DiI fluorescence intensity from MCF-7 cells treated with DiI-loaded PNPs manufactured at various flow rates (Q = 50, 100, and 200 µL/min) using the microfluidic reactor or bulk nanoprecipitation (Q = 0 µL/min). (B) Normalized fluorescence intensities of MCF-7 cells treated with various DiI-loaded PNP formulations. The inset plots normalized fluorescence intensities of MCF-7 cells vs. mean effective hydrodynamic diameters of the PNPs showing a negative linear correlation. Brackets indicate statistical comparisons between normalized fluorescence intensities: ** indicates $p < 0.005$, * indicates $p < 0.05$ and ns indicates $p > 0.05$.

Based on fluorescence images such as those in Figure 3-11, it is difficult to quantify differences in cell uptake related to flow rate. Therefore, to quantify cell uptake, we carried

out flow cytometric measurements of the MCF-7 cells following incubation with the various formulations. Figure 3-12A shows the resulting DiI fluorescence intensity histograms of MCF-7 cells treated with different DiI-PNPs (gating strategy is shown in *Appendix B,* Figure B-18). As a negative control, cells treated with same volume of PBS but no DiI-PNPs were also measured (PBS, green histogram). For all cell populations treated with DiI-PNPs, we observe clear shifts to higher DiI intensities relative to the control group, confirming association of DiI-PNPs within MCF-7 cells for all nanoparticle formulations. Based on the fluorescence microscopy data in Figure 3-11, and also on the likelihood of any surface-bound DiI-PNPs being removed during cell washing, we attribute cellular association of DiI-PNPs to their extra-nuclear compartmentalization. Therefore, to elucidate the relative cell uptake of the various DiI-PNP formulations, normalized DiI intensity values for each formulation were obtained by integrating mean fluorescence intensity values (*Appendix B*, Figure B-19) and dividing by the dye loading (*DL*) of the corresponding DiI-PNP sample (Figure 3-6B). The resulting normalized values (Figure 3-12B) provide a relative measure of the rate of PNP uptake into MCF-7 cells, showing the greatest uptake by the Q = 100 μL/min formulation (purple bar) and the lowest uptake by the Q = 50 μL/min formulation (red bar). Plotting normalized DiI intensity vs. the $d_{h,eff}$ values of the corresponding DiI-PNPs (Figure 3-3A) yields a negative linear relation (Figure 3-12B, inset), indicating greater uptake rates for PNPs of smaller size. We conclude that as PNP sizes decrease *via* microfluidic shear processing, *both* increased drug release rates (Figure 3-8B) *and* increased cell uptake (Figure 3-12B) will contribute to the observed increases in cytotoxicities against MCF-7 cells (Figure 3-10B, inset).

3.4 Conclusions

Polymer nanoparticles (PNPs) providing encapsulation of anticancer drugs with selective stimuli-responsive release at tumor sites are promising candidates in the development of smart nanomedicines. In this chapter, we employed a two-phase microfluidic reactor to produce DualM PNPs consisting of a glutathione (GSH)-responsive block copolymer with disulfide linkages at both the hydrophobic-hydrophilic junction and on pendant groups in the hydrophobic block and containing either the anticancer drug paclitaxel (PAX) or the fluorescent drug surrogate dye (DiI). We show that on-chip self-assembly at different flow rates yielded DualM PNPs with different flow-controlled sizes, structures, and drug delivery function. Sizes and morphologies of PAX-loaded and DiI-loaded PNPs were found to be similar to empty PNPs under the same flow conditions, providing opportunities for controlled loading of different therapeutics with different molecular structures. Using fluorescence imaging of the DiI probe dye, we show that microfluidic self-assembly improves encapsulation homogeneities within PNPs relative to bulk nanoprecipitation, with further improvements as the flow rate increases. PAX-loaded DualM PNPs were shown to be significantly more toxic to cancerous MCF-7 cells (lower EC_{50} values) than to healthy HaCaT cells, while free (not encapsulated) PAX showed similar toxicity to both cell lines, supporting the biological responsivity and selective nature of the nanocarriers. Interestingly, the specific drug delivery properties of the DualM PNP formulations were tunable with microfluidic flow rate, with several properties, including GSH-triggered release rate, MCF-7 cell uptake, cytotoxicity, and relative difference in MCF-7 and HaCaT cytotoxicity, increasing linearly as flow-directed PNP size decreased. These various linear size-property relations suggest that nanoparticle

hydrodynamic diameter, conveniently tunable via microfluidic flow rate, is a key structural factor influencing numerous important delivery properties for biologically responsive nanoparticles. These results highlight the potential of flow-directed shear processing in two-phase microfluidic reactors for providing controlled manufacturing routes to biological stimuli-responsive nanomedicines optimized for specific therapeutic applications.

3.5 Supporting Information

Bright-field and fluorescence images for *EH* determination; workflows for *EH* and RA_{compart} determination; TEM images of PAX-PNPs at different time points during PAX release experiments; $d_{\text{h,eff}}$ and RA_{compart} values of PAX-PNPs at different time points during PAX release experiments; cell viability raw data for EC_{50} determinations and associated controls; complete flow cytometry data and gating definitions; long-term stability test of PAX-PNPs; table of actual flow rates; and tables of statistical comparisons are included in *Appendix B*.

3.6 References

1. Huang, Y.; Moini Jazani, A.; Howell, E. P.; Reynolds, L. A.; Oh, J. K., Moffitt, M. G., Microfluidic shear processing control of biological reduction stimuli-responsive polymer nanoparticles for drug delivery. *ACS Biomater. Sci. Eng.* **2020**, *Article ASAP*.

2. Allen, C.; Maysinger, D.; Eisenberg, A., Nano-engineering block copolymer aggregates for drug delivery. *Colloids Surf., B* **1999**, *16*, 3-27.

3. Kataoka, K.; Harada, A.; Nagasaki, Y., Block copolymer micelles for drug delivery: design, characterization and biological significance. *Adv. Drug Delivery Rev.* **2001**, *47*, 113-131.

4. Rösler, A.; Vandermeulen, G. W. M.; Klok, H.-A., Advanced drug delivery devices via self-assembly of amphiphilic block bopolymers. *Adv. Drug Delivery Rev.* **2001**, *53*, 95-108.

5. Davis, M. E.; Chen, Z.; Shin, D. M., Nanoparticle therapeutics: an emerging treatment modality for cancer. *Nat. Rev. Drug Discov.* **2008**, *7*, 771-782.

6. Tyrrell, Z. L.; Shen, Y.; Radosz, M., Fabrication of micellar nanoparticles for drug delivery through the self-assembly of block copolymers. *Prog. Polym. Sci.* **2010**, *35*, 1128-1143.

7. Gong, J.; Chen, M.; Zheng, Y.; Wang, S.; Wang, Y., Polymeric micelles drug delivery system in oncology. *J. Controlled Release* **2012**, *159*, 312-323.

8. Sun, T.; Zhang, Y. S.; Pang, B.; Hyun, D. C.; Yang, M.; Xia, Y., Engineered nanoparticles for drug delivery in cancer therapy. *Angew. Chem. Int. Ed.* **2014**, *53*, 12320-12364.

9. Björnmalm, M.; Thurecht, K. J.; Michael, M.; Scott, A. M.; Caruso, F., Bridging bio–nano science and cancer nanomedicine. *ACS Nano* **2017**, *11*, 9594-9613.

10. Kakkar, A.; Traverso, G.; Farokhzad, O. C.; Weissleder, R.; Langer, R., Evolution of macromolecular complexity in drug delivery systems. *Nat. Rev. Chem.* **2017**, *1*, 0063.

11. Alexis, F.; Pridgen, E.; Molnar, L. K.; Farokhzad, O. C., Factors affecting the clearance and biodistribution of polymeric nanoparticles. *Mol. Pharmaceutics* **2008**, *5*, 505-515.

12. Elsabahy, M.; Wooley, K. L., Design of polymeric nanoparticles for biomedical delivery applications. *Chem. Soc. Rev.* **2012**, *41*, 2545-2561.

13. Maeda, H.; Wu, J.; Sawa, T.; Matsumura, Y.; Hori, K., Tumor vascular permeability and the EPR effect in macromolecular therapeutics: a review. *J. Controlled Release* **2000**, *65*, 271-284.

14. Maeda, H.; Nakamura, H.; Fang, J., The EPR effect for macromolecular drug delivery to solid tumors: Improvement of tumor uptake, lowering of systemic toxicity, and distinct tumor imaging in vivo. *Adv. Drug Delivery Rev.* **2013**, *65*, 71-79.

15. Perry, J. L.; Reuter, K. G.; Luft, J. C.; Pecot, C. V.; Zamboni, W.; DeSimone, J. M., Mediating passive tumor accumulation through particle size, tumor type, and location. *Nano Lett.* **2017**, *17*, 2879-2886.

16. Geng, Y.; Dalhaimer, P.; Cai, S.; Tsai, R.; Tewari, M.; Minko, T.; Discher, D. E., Shape effects of filaments versus spherical particles in flow and drug delivery. *Nat. Nanotechnol.* **2007**, *2*, 249-255.

17. Gaumet, M.; Vargas, A.; Gurny, R.; Delie, F., Nanoparticles for Drug Delivery: The need for precision in reporting particle size parameters. *Eur. J. Pharm. Biopharm.* **2008**, *69*, 1-9.

18. Fairley, N.; Hoang, B.; Allen, C., Morphological control of poly(ethylene glycol)-block-poly(ε-caprolactone) copolymer aggregates in aqueous solution. *Biomacromolecules* **2008**, *9*, 2283-2291.

19. Venkataraman, S.; Hedrick, J. L.; Ong, Z. Y.; Yang, C.; Ee, P. L. R.; Hammond, P. T.; Yang, Y. Y., The effects of polymeric nanostructure shape on drug delivery. *Adv. Drug Delivery Rev.* **2011**, *63*, 1228-1246.

20. Russo, A.; DeGraff, W.; Friedman, N.; Mitchell, J. B., Selective modulation of glutathione levels in human normal versus tumor cells and subsequent differential response to chemotherapy drugs. *Cancer Res.* **1986**, *46*, 2845.

21. Jiang, X. Q.; Yu, Y.; Chen, J. W.; Zhao, M. K.; Chen, H.; Song, X. Z.; Matzuk, A. J.; Carroll, S. L.; Tan, X.; Sizovs, A.; Cheng, N. H.; Wang, M. C.; Wang, J., Quantitative imaging of glutathione in live cells using a reversible reaction-based ratiometric fluorescent probe. *ACS Chem. Biol.* **2015**, *10*, 864-874.

22. Saito, G.; Swanson, J. A.; Lee, K.-D., Drug delivery strategy utilizing conjugation via reversible disulfide linkages: role and site of cellular reducing activities. *Adv. Drug Delivery Rev.* **2003**, *55*, 199-215.

23. Klaikherd, A.; Nagamani, C.; Thayumanavan, S., Multi-stimuli sensitive amphiphilic block copolymer assemblies. *J. Am. Chem. Soc.* **2009**, *131*, 4830-4838.

24. Tang, L.-Y.; Wang, Y.-C.; Li, Y.; Du, J.-Z.; Wang, J., Shell-detachable micelles based on disulfide-linked block copolymer as potential carrier for intracellular drug delivery. *Bioconjugate Chem.* **2009**, *20*, 1095-1099.

25. Khorsand, B.; Lapointe, G.; Brett, C.; Oh, J. K., Intracellular drug delivery nanocarriers of glutathione-responsive degradable block copolymers having pendant disulfide linkages. *Biomacromolecules* **2013**, *14*, 2103-2111.

26. Cunningham, A.; Oh, J. K., New design of thiol-responsive degradable polylactide-based block copolymer micelles. *Macromol. Rapid Commun.* **2013**, *34*, 163-168.

27. Oh, J. K., Disassembly and tumor-targeting drug delivery of reduction-responsive regradable rlock copolymer canoassemblies. *Polym. Chem.* **2019**, *10*, 1554-1568.

28. Biswas, D.; An, S. Y.; Li, Y.; Wang, X.; Oh, J. K., Intracellular delivery of colloidally stable core-cross-linked triblock copolymer micelles with glutathione-responsive enhanced drug release for cancer therapy. *Mol. Pharmaceutics* **2017**, *14*, 2518-2528.

29. Chan, N.; Khorsand, B.; Aleksanian, S.; Oh, J. K., A dual location stimuli-responsive degradation strategy of block copolymer nanocarriers for accelerated release. *Chem. Commun.* **2013**, *49*, 7534-7536.

30. Chen, W.; Yang, H.; Wang, R.; Cheng, R.; Meng, F.; Wei, W.; Zhong, Z., Versatile synthesis of functional biodegradable polymers by combining ring-opening polymerization and postpolymerization modification via michael-type addition reaction. *Macromolecules* **2010**, *43*, 201-207.

31. Liu, J.; Huang, W.; Pang, Y.; Zhu, X.; Zhou, Y.; Yan, D., Hyperbranched polyphosphates for drug delivery application: design, synthesis, and in vitro evaluation. *Biomacromolecules* **2010**, *11*, 1564-1570.

32. Zhang, Q.; Ko, N. R.; Oh, J. K., Recent advances in stimuli-responsive degradable block copolymer micelles: synthesis and controlled drug delivery applications. *Chem. Commun.* **2012**, *48*, 7542-7552.

33. Zhang, Q.; Ko, N. R. ; Oh, J. K., Modulated morphologies and tunable thiol-responsive shedding of aqueous block copolymer aggregates. *RSC Adv.* **2012**, *2*, 8079-8086.

34. Capretto, L.; Carugo, D.; Mazzitelli, S.; Nastruzzi, C.; Zhang, X., Microfluidic and lab-on-a-chip preparation routes for organic nanoparticles and vesicular systems for nanomedicine applications. *Adv. Drug Delivery Rev.* **2013**, *65*, 1496-1532.

35. Karnik, R.; Gu, F.; Basto, P.; Cannizzaro, C.; Dean, L.; Kyei-Manu, W.; Langer, R.; Farokhzad, O. C., Microfluidic platform for controlled synthesis of polymeric nanoparticles. *Nano Lett.* **2008**, *8*, 2906-2912.

36. Xu, Q.; Hashimoto, M.; Dang, T. T.; Hoare, T.; Kohane, D. S.; Whitesides, G. M.; Langer, R.; Anderson, D. G., Preparation of monodisperse biodegradable polymer microparticles using a microfluidic flow-focusing device for controlled drug delivery. *Small* **2009**, *5*, 1575-1581.

37. Zhang, Y.; Chan, H. F.; Leong, K. W., Advanced materials and processing for drug delivery: the past and the future. *Adv. Drug Delivery Rev.* **2013**, *65*, 104-120.

38. Schabas, G.; Wang, C.-W.; Oskooei, A.; Yusuf, H.; Moffitt, M. G.; Sinton, D., Formation and shear-induced processing of quantum dot colloidal assemblies in a multiphase microfluidic chip. *Langmuir* **2008**, *24*, 10596-10603.

39. Schabas, G.; Yusuf, H.; Moffitt, M. G.; Sinton, D., controlled self-assembly of quantum dots and block copolymers in a microfluidic device. *Langmuir* **2008**, *24*, 637-643.

40. Wang, C.-W.; Oskooei, A.; Sinton, D.; Moffitt, M. G., Controlled self-assembly of quantum dot−block copolymer colloids in multiphase microfluidic reactors. *Langmuir* **2010**, *26*, 716-723.

41. Wang, C.-W.; Sinton, D.; Moffitt, M. G., Flow-directed block copolymer micelle morphologies via microfluidic self-assembly. *J. Am. Chem. Soc.* **2011**, *133*, 18853-18864.

42. Wang, C.-W.; Bains, A.; Sinton, D.; Moffitt, M. G., Flow-directed assembly of block copolymer vesicles in the lab-on-a-chip. *Langmuir* **2012**, *28*, 15756-15761.

43. Wang, C.-W.; Bains, A.; Sinton, D.; Moffitt, M. G., Flow-directed loading of block copolymer micelles with hydrophobic probes in a gas–liquid microreactor. *Langmuir* **2013**, *29*, 8385-8394.

44. Wang, C.-W.; Sinton, D.; Moffitt, M. G., Morphological control via chemical and shear forces in block copolymer self-assembly in the lab-on-chip. *ACS Nano* **2013**, *7*, 1424-1436.

45. Bains, A.; Cao, Y.; Moffitt, M. G., Multiscale control of hierarchical structure in crystalline block copolymer nanoparticles using microfluidics. *Macromol. Rapid Commun.* **2015**, *36*, 2000-2005.

46. Xu, Z.; Yan, B.; Riordon, J.; Zhao, Y.; Sinton, D.; Moffitt, M. G., Microfluidic synthesis of photoresponsive spool-like block copolymer nanoparticles: flow-directed formation and light-triggered dissociation. *Chem. Mater.* **2015**, *27*, 8094-8104.

47. Bains, A.; Wulff, J. E.; Moffitt, M. G., Microfluidic synthesis of dye-loaded polycaprolactone-block-poly(ethylene oxide) nanoparticles: insights into flow-directed loading and in vitro release for drug delivery. *J. Colloid Interface Sci.* **2016**, *475*, 136-148.

48. Xu, Z.; Lu, C.; Riordon, J.; Sinton, D.; Moffitt, M. G., Microfluidic manufacturing of polymeric nanoparticles: comparing flow control of multiscale structure in single-phase staggered herringbone and two-phase reactors. *Langmuir* **2016**, *32*, 12781-12789.

49. Bains, A.; Cao, Y.; Kly, S.; Wulff, J. E.; Moffitt, M. G., Controlling structure and function of polymeric drug delivery nanoparticles using microfluidics. *Mol. Pharmaceutics* **2017**, *14*, 2595-2606.

50. Xu, Z.; Lu, C.; Lindenberger, C.; Cao, Y.; Wulff, J. E.; Moffitt, M. G., Synthesis, self-assembly, and drug delivery characteristics of poly(methyl caprolactone-co-caprolactone)-b-poly(ethylene oxide) copolymers with variable compositions of hydrophobic blocks: combining chemistry and microfluidic processing for polymeric nanomedicines. *ACS Omega* **2017**, *2*, 5289-5303.

51. Chen, R.; Wulff, J. E.; Moffitt, M. G., Microfluidic processing approach to controlling drug delivery properties of curcumin-loaded block copolymer nanoparticles. *Mol. Pharmaceutics* **2018**, *15*, 4517-4528.

52. Cao, Y.; Silverman, L.; Lu, C.; Hof, R.; Wulff, J. E.; Moffitt, M. G., Microfluidic manufacturing of SN-38-loaded polymer nanoparticles with shear processing control of drug delivery properties. *Mol. Pharmaceutics* **2019**, *16*, 96-107.

53. Huang, Y.; Moini Jazani, A.; Howell, E. P.; Oh, J. K.; Moffitt, M. G., Controlled microfluidic synthesis of biological stimuli-responsive polymer nanoparticles. *ACS Appl. Mater. Interfaces* **2020**, *12*, 177-190.

54. Hong, R.; Han, G.; Fernández, J. M.; Kim, B.-J.; Forbes, N. S.; Rotello, V. M., Glutathione-mediated delivery and release using monolayer protected nanoparticle carriers. *J. Am. Chem. Soc.* **2006**, *128*, 1078-1079.

Chapter 4 A Critical Literature Review of Biological Stimuli-Responsive Block Copolymer Nanoparticles for Drug Delivery

4.1 Introduction

Polymer nanoparticles (PNPs) self-assembled from amphiphilic block copolymers have been extensively investigated as drug delivery carriers due to their morphological variability, biocompatibility, and ease of functionalization.[1-10] A number of biocompatible block copolymers consisting of poly(ethylene oxide) (PEO) hydrophilic blocks and hydrophobic blocks comprised, for example, of polycaprolactone (PCL), poly(lactic acid) (PLA), or poly(lactic-*co*-glycolic acid) (PLGA), have been approved by the FDA as PNP-based drug delivery carriers.[8] For example, the self-assembly of PEO-*b*-PCL in aqueous media gives rise to PNPs consisting of hydrophilic PEO-forming coronae and hydrophobic PCL-forming cores. A wide range of hydrophobic drugs can be encapsulated within the PCL cores enhancing bioavailability,[9-11] while the PEO coronae protects the PNPs from the reticular endothelial system (RES) and renal clearance, improving circulation times and biodistribution.[12-14] PNPs that are not functionalized with specific biological ligands are generally passive delivery systems, meaning that PNP size and morphology plays a crucial role in drug delivery to the cancerous site. For example, it has been found that PNPs on colloidal length scales (~10 – 200 nm) are favorably retained in tumor tissues throughout the distribution.[12-14, 16-17] As well, longer *in vivo* circulation times have been for cylindrical PNPs compared to spherical PNPs, indicating PNP morphologies would also influence their biodistribution.[15] Finally, PNP sizes and morphologies are also shown to strongly affect the cellular uptake process.[6]

Although the design and manufacturing of PNPs with specific sizes and morphologies can increase passive localization at the tumor and uptake by target cells, it cannot eliminate

side effects caused by PNPs being taken up by healthy cells.[12-17] Therefore, along with passive or active targeting to increase localization (related to PNP size, morphology and external ligands), scientists have sought to add an additional level of specificity to PNPs by designing polymers that selectively release encapsulated drugs only within the target cells. Recently, stimuli-responsive degradation (SRD) strategies have been introduced in response to this challenge.[6, 19-23] SRD involves incorporation of covalent bonds within the copolymer chains which are cleavable in response to intracellular stimuli, thus causing PNP degradation and concomitant release of encapsulated drugs.[6, 19-23] For example, SRD applications in chemotherapeutic delivery systems generally considers the specific biological characteristics of cancerous tissues.[19, 22-23] The covalent bonds are cleavable only within the specific pathophysiological microenvironment, such that the selective PNP degradation and drug release occurs mainly within the cancerous cells.[19, 22-23]

An important feature of the microenvironment of cancerous cells is higher levels of oxidization-reduction reactions caused by faster metabolic cycles. This feature can be utilized as a stimulus for drug delivery PNPs through specific design of SRD polymers.[22-24] During the over-expression of oxidization-reduction reactions, glutathione (GSH, a cellular reducing agent) is found at elevated levels within cancer cells (> 10 mM) compared to most normal cells (1 – 2 mM) and compared to the extracellular environment (1 – 2 μM). Such differential concentrations shows GSH to be a promising stimulus agent for drug delivery PNPs comprised of SRD polymers.[24-26] Therefore, researchers have designed reduction-responsive block copolymers for producing PNPs with controlled intracellular release characteristics. The main strategy for reduction-responsive polymer design is disulfide chemistry.[23, 27-28] Disulfide bonds (-S-S-) are formed by covalent combination of

two thiol groups, while the presence of GSH can promote disulfide degradation to thiols. Thus, disulfide linkages introduced into the structure of a block copolymer provides a mechanism for GSH-triggered degradation.[23, 27-28]

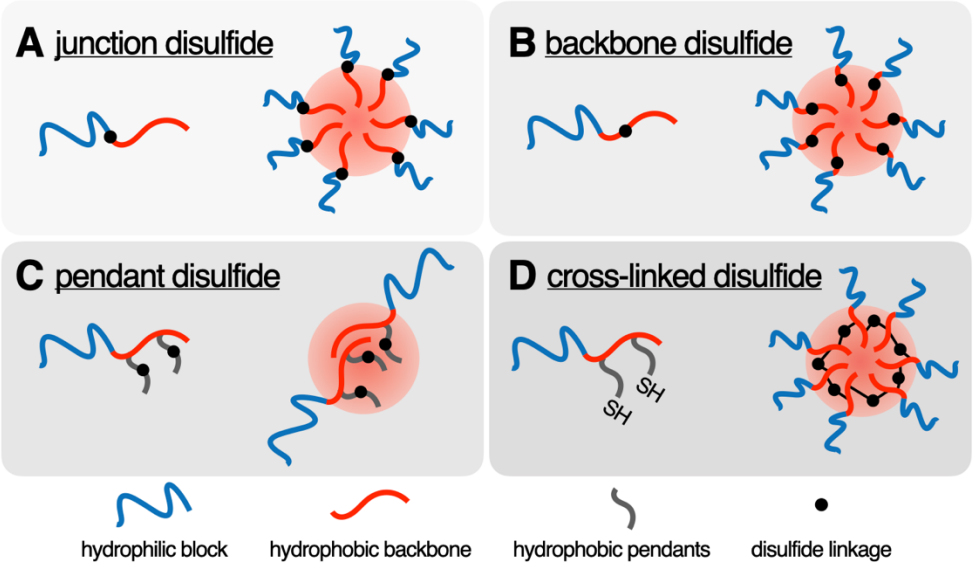

Figure 4-1. Schematics of (A) junction disulfide, (B) backbone disulfide, (C) pendant disulfide, and (D) cross-linked disulfide locations.

There are various locations available for disulfide linkages involved within the block copolymer structure. In this chapter, we will discussion four locations that are available for disulfide linkage insertion. First, disulfide linkages can be introduced at the junction between hydrophilic and hydrophobic blocks (*junction disulfides*, Figure 4-1A). GSH-triggered junction disulfide cleavage would cause the hydrophilic coronal chain detachment and thus PNP disassembly, providing a mechanism for enhanced drug release. Next, disulfide linkages can also be introduced within hydrophobic copolymer chains; they can be located on the block backbone (*backbone disulfide*s, Figure 4-1B), or on pendant chains (*pendant disulfides*, Figure 4-1C) in cases of hydrophobic blocks bearing branches. When disulfides are within PNP cores, core-forming polymer degradation would occur

upon GSH exposure. In addition, GSH would also trigger a change in the chemical nature of the core-forming polymer from hydrophobic to hydrophilic which induces dissociation of PNPs. Both of the mechanisms would trigger PNP core destabilization and lead to enhanced drug release. Finally, hydrophobic pendants chains bearing thiol groups can be designed for *in situ* formation of *cross-linked disulfides* (Figure 4-1D) within PNP cores. In such case, GSH-triggered decrosslinking would lead to PNP dissociation and enhanced drug release.

In this chapter, we summarize the various design strategies for reduction-responsive block copolymers and the PNP systems formed by their self-assembly. Various reduction-responsive PNP systems classified by the disulfide locations are discussed with a main focus on comparing their formation and redox-triggered degradation mechanisms. In addition, *reduction-responsivity* (i.e., rate of changes in multiscale structures, including copolymer chemical structure, PNP internal compartment volume, and PNP size) is an important parameter in the design of reduction-responsive PNPs since it significantly influences the colloidal stability during biodistribution and the rate of selective enhance release in targeted sites. Therefore, we have carried out some analysis of literature data aiming to provide new insight on the importance of PNP structures for PNP varying the reduction-responsivity. We further discuss the possibility of using various analytical techniques which could be used for tracking the degradation kinetics for different PNP systems. Through numerous examples, we show how established principles from copolymer design to PNP formation would open up vast possibilities for manufacturing smart nanomedicines with controllable responsivity.

4.2 Junction Disulfides at PNP Core-Corona Interfaces

A disulfide linkage that connects a hydrophilic copolymer block (PA) with a hydrophobic copolymer block (PB) is called a junction disulfide (PA-ss-PB). Following self-assembly of PA-ss-PB chains, the junction disulfides are located at the core/coronae interfaces of the PNPs. In response to elevated GSH concentrations, hydrophilic coronal chains will be shed from the hydrophobic cores upon junction disulfide cleavage, which causes enhanced drug release due to PNP core destabilization.

The simplest designs of block copolymers with junction disulfides are based on established commercial biocompatible polymers.[29-39] For example, Sun *et al.* reported the synthesis and characterization of PEO-ss-PCL and its assemblies.[30] PEO_{5k}-ss-PCL_{3k} (subscript number refers to M_n of the respective blocks) was synthesized *via* an exchange reaction between PEO orthopyridyl disulfide (PEO-ss-Py) and PCL bearing a thiol-end (PCL-SH). PEO_{5k}-ss-PCL_{3k} was self-assembled using the dialysis method, giving rise to PNPs that were prone to fast drug release (~100% within 12 h) in the presence of 10 mM GSH. In contrast, minimal drug release (<20%) was observed within 24 h for the same PNPs in the absence of GSH,[30] indicating selective and enhanced release in the presence of GSH.

Several flaws in PNPs involving junction disulfides are worth noting. Firstly, it has been reported that junction disulfides might encounter stability issues in the biodistribution process due to thiol-disulfide exchange with Cys-contained protein near PNP surfaces.[40-41] Secondly, the junction cleavage and resulting loss of PNP coronae leads to aggregation of the hydrophobic cores, which generally causes increases in measured size,[30-31, 33-39] which may lead to precipitation of copolymer and drug, resulting in toxicity effects and loss of

targeted drug.[33-34, 37-38] Thirdly, the addition of junction disulfide to the original copolymer backbone would cause difference in the resulting PNP structure compared to PNPs without disulfides.[30-32, 41] Thus it would be not practical to apply the established understanding of original PNP structures to their counterparts with improvements in GSH-responsivity. We take ref. 30 as an example, the self-assembly of PEO_{5k}-ss-PCL_{3k} formed spherical PNPs with an average hydrodynamic size of 240 nm, while a control sample of PEO_{5k}-*b*-PCL_{3k} without junction disulfides self-assembled into relatively smaller PNPs with size of 200 nm.[30]

Zhu *et al.* reported a Doxorubicin (DOX)-loaded cRGD-functionalized GSH-responsive PNP system treating U87MG glioblastoma cells in the xenografted Balb/c nude mice model.[41] The PNPs consisting of cRGD-PEO-*b*-PCL and PEO-ss-PCL block copolymers at a molar ratio of 20/80 (cRGD/PEO-ss-PCL, Figure 4-2A). cRGD peptide was selected as an active targeting ligand to U87MG tumorous cells. We observed GSH-responsivity of cRGD/PEO-ss-PCL PNPs in terms of enhanced DOX release; under 10 mM GSH incubation, a significant faster release (~80% in 24 h, red solid line, Figure 4-2B) was achieved by cRGD/PEO-ss-PCL PNPs compared to cRGD/PEO-PCL PNPs which did not contain disulfides (<20% in 24 h, blue solid line, Figure 4-2B).

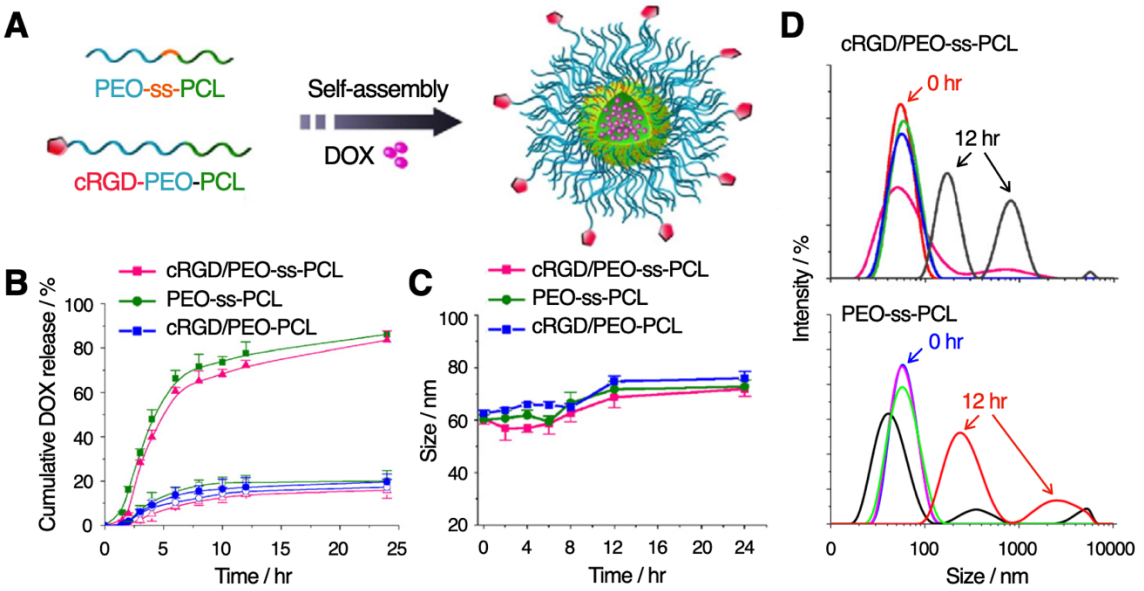

Figure 4-2. (A) Schematic of the self-assembly of DOX-loaded cRGD-functionalized GSH-responsive PNPs consisting of cRGD-PEO-*b*-PCL and PEO-ss-PCL block copolymers. (B) Release profiles of cRGD/PEO-ss-PCL, cRGD/PEO-PCL, and PEO-ss-PCL PNPs under various conditions. (C) Hydrodynamic sizes of cRGD/PEO-ss-PCL, cRGD/PEO-PCL, and PEO-ss-PCL PNPs in water at various time points measured by DLS. (D) Intensity-weighted CONTIN distribution of cRGD/PEO-ss-PCL and PEO-ss-PCL PNPs with 10 mM GSH incubation for 12 hr. Adapted from ref. 41. Copyright 2016 Elsevier B.V.

However, the study evaluated the critical roles of active-targeting and GSH-triggered release to enhanced tumor chemotherapy.[41] Tests on a series of control groups provide important insight into the effect of location and number of disulfides on PNP GSH-responsivity. Since junction disulfides are only located at the interfaces between hydrophilic coronae and hydrophobic cores, the surface disulfide density σ (which equals to chain density σ_{chain}) should play a curial role in tuning the PNP GSH-responsivity. We carried out some data analyses for ref. 41. The side effect of mixing PEO-ss-PCL with cRGD-decorated PEO- *b*-PCL copolymer is the dilution of junction disulfide at the PNP surface. In fact, cRGD/PEO-ss-PCL PNPs (Figure 4-2C, red line) showed similar hydrodynamic size with PEO-ss-PCL PNPs (Figure 4-2C, blue line). Thus σ of

cRGD/PEO-ss-PCL PNPs should be three forth of PNPs that only consists of PEO-ss-PCL assuming the mixing is statistical. In terms of size change, PEO-ss-PCL PNPs showed larger size increase upon 10 mM GSH incubation; intensity-weighted CONTIN analysis of PEO-ss-PCL PNPs showed bimodal distribution at ~200 nm and ~2 500 nm after 12 h incubation, while cRGD/PEO-ss-PCL PNPs showed bimodal distribution at ~200 nm and 800 nm (Figure 4-2C). Since PNP size increase in GSH-contained media is mainly caused by GSH-triggered disulfide cleavage and PNP aggregation, it is reasonable to conclude that cRGD/PEO-ss-PCL PNPs shows less GSH-responsivity.

Similarly, Zhong *et al.* reported the self-assembly and DOX encapsulation of PEO-ss-PCL and β-$_D$-galactose-PEO-PCL (Gal-PEO-PCL, where Gal shows high affinity to asialoglycoprotein receptor overexpressed in hepatocellular carcinoma cells) block copolymers.[42] The self-assembly of a mixture of PEO-ss-PCL and Gal-PEO-PCL (80/20 wt%) gave rise to PEO-ss-PCL/Gal20 PNPs with an average hydrodynamic size of 58.2 nm, similar to PNPs that only consists PEO-ss-PCL (47.9 nm). PEO-ss-PCL/Gal20 PNPs showed almost no change in terms of size under reductive environment for 10 h, while PEO-ss-PCL PNPs destabilized and formed large aggregates (d_h > 1 000 nm) under the same condition. The results point out that hybrid PEO-ss-PCL/Gal20 PNPs shedding off up to 80% of PEO shells could maintain aqueous colloidal stability.[42] In *in vitro* release experiments, PEO-ss-PCL/Gal20 PNPs showed constantly slower DOX release (release half time $t_{1/2}$ = 3.5 h) compared to PEO-ss-PCL PNPs ($t_{1/2}$ = 5 h) under reductive condition.[42]

We also carried out the calculation of surface disulfide density σ for systems in ref. 42. In such system, σ would depend on the fraction of Gal-PEO-PCL copolymers in the

mixture during PNP fabrication and the PNP size; $\sigma_{PEO\text{-}ss\text{-}PCL}$ is ~1.5-folder higher than $\sigma_{PEO\text{-}ss\text{-}PCL/Gal20}$ thus junction disulfide cleavage would occur more in PEO-ss-PCL PNPs. This analysis aligns with the experimental results in ref. 42 where PEO-ss-PCL showed larger size increase and faster DOX release, confirming GSH-responsivity of PNPs with junction disulfides can be regulated by σ.

We found that the surface disulfide density σ of PNPs would also depend the composition of individual copolymer chains. This is reasonable to conclude since hydrophobic block composition has been confirmed to have an effect on thermodynamics of PNP formation,[43-45] thus could further influence PNP morphology and surface disulfide distribution. Fan *et al.* synthesized a series of PEO-ss-PCL containing the same PEO block length but different PCL block length, and investigated the aggregation kinetics of self-assembled PNPs under GSH stimulus.[46] The hydrodynamic radius r_h and chain density σ_{chain} of PNPs showed linear correlation with PCL block length (Table 4-1).[46] The light scattering measurement of r_h changes versus GSH incubation time t was also performed and aggregation kinetics $r_h = f(t)$ for each sample was acquired. It was obvious that size showed greater increase in PEO_{113}-ss-PCL_{61} PNPs than other samples over the first 2 h of GSH incubation. Such fast aggregation processes might be due to the higher σ value and associated higher probability of disulfide-GSH interaction.[46]

Table 4-1. Light Scattering Characterization of Block Copolymers with Constant PEO Content and Various PCL Content[a]

Samples[b]	r_h / nm	σ_{chain} / nm^{-2}	Aggregation kinetics $r_h = f(t)$
PEO_{113}-ss-PCL_{61}	51.3	1.21	$54t^{0.19}$
PEO_{113}-ss-PCL_{39}	61.8	1.14	$57 + 4e^{t/86}$
PEO_{113}-ss-PCL_{22}	82.9	1.10	$79 + e^{t/183}$

[a]Adapted from ref. 46. Copyright 2017 American Chemical Society.
[b]Subscript number refers to number of repeat units.

4.3 Backbone Disulfides within PNP Cores

GSH-triggered PNP degradation and drug release can also be achieved by involving disulfide linkages within the hydrophobic cores. Disulfide cleavages would cause changes in both core hydrophobicity and core-forming chain conformation thus leading to PNP destabilization and enhanced drug release. The available locations of disulfide linkages within the cores include backbones and pendants of the hydrophobic chains. We will start the discussion on PNPs with disulfides on the hydrophobic backbone. Block copolymers bearing backbone disulfides are usually synthesized by step-growth polymerization of hydrophobic monomers with two thiol-ends onto a hydrophilic homopolymer with predetermined length, during which disulfides are located within the hydrophobic monomers.[47-52] The number of disulfides per chain can be determined by multiplying the polymerization degree of the hydrophobic blocks by number of disulfides within one repeat unit, and the number of disulfides in a PNP can be estimated by multiplying the aggregation number N_{agg} by the number of disulfides per chain.

Aleksanian *et al.* reported the synthesis of a polyester-based block copolymer containing backbone disulfide linkages by atom transfer radical polymerization (ATRP).[53] Briefly, a ssPES-*b*-POEOMA (Figure 4-3A) was synthesized by ATRP between an oligo(ethylene glycol) monomethyl ether methacrylate (OEOMA) and a polyester containing backbone disulfide linkages (ssPES) with the terminal bromine group (ssPES-Br). The copolymer consisting of hydrophobic ssPES block with disulfides on its backbone and hydrophilic POEOMA block thus could self-assemble into PNPs as drug delivery vehicles in the aqueous media. Since each repeat unit of ssPES contains two disulfide linkages, the number of disulfides per chain can be estimated as 6 given M_{ssPES} = 2 100 g

mol^{-1}.[53] The reduction-triggered PNP degradation was monitored by dynamic light scattering (DLS). The PNP hydrodynamic size was measured to be 68 nm and observed to be stable with a modal distribution by CONTIN analysis (Figure 4-3B). However, The CONTIN distribution of the PNPs became bimodal with the occurrence of a new smaller-sized population within 30 mins in the presence of 5 mM DTT (dithiothreitol, a reducing agent containing a disulfide substituting GSH[54]). The authors also noted that PNPs further aggregated to > 1 000 nm with the exposure to DTT after 5 h (Figure 4-3B). The drug release profiles are consistent with fast PNP degradation; a significant drop in fluorescence intensity of Nile Red (NR)-loaded PNPs was observed within 30 mins of DTT incubation compared to the control group (Figure 4-3C).

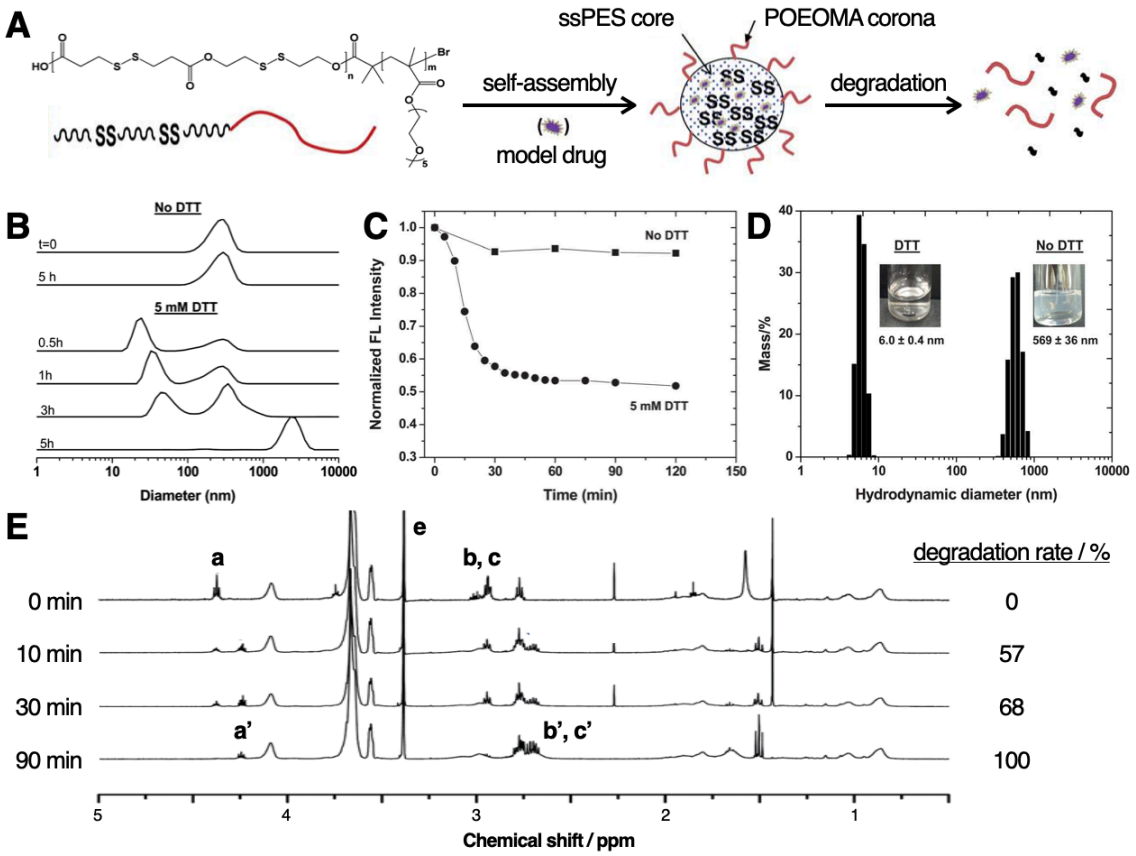

Figure 4-3. (A) Schematic of aqueous formation and reduction-triggered degradation of ssPES-POEOMA PNPs. (B) DLS CONTIN distributions of ssPES-POEOMA PNPs with or without DTT incubation at various time points. (C) Fluorescence intensities of NR-loaded ssPES-POEOMA PNP dispersion with or without DTT incubation at various time points. (D) DLS mass-weighted CONTIN distributions of ssPES-POEOMA PNPs self-assembled in a THF/water mixture with or without DTT incubation. Photographs of dispersions in different condition are shown as insets. (E) ^{1}H NMR spectra in $CDCl_3$ for the mixture of PNPs with DTT over incubation time. Water in samples has been removed before ^{1}H NMR characterization. Adapted from ref. 53. Copyright 2012 Royal Society of Chemistry.

In contrast with the observed degradation pattern (small bimodal to large modal size distribution) of PNPs formed in the aqueous condition, the PNP sample self-assembled in a water/THF mixture (40/60 wt%) showed nearly complete degradation with a significant size decrease from 569 nm to 6 nm in the presence of DTT for 5 h (Figure 4-3D). This is

explained by the hydrophobicity of the dithiol-deg species cleaved from ssPES blocks.[53] Dithiol-deg species would be stabilized by HS-POEOMA residues in water forming aggregates with a relatively large hydrodynamic size. However, dithiol-deg and HS-POEOMA species are both soluble in the THF/water mixture, which results in a observed transition of opaque dispersion to clear solution upon DTT incubation (Figure 4-3D, insets). These results could improve our understanding to reduction-triggered degradation mechanism of PNPs with backbone disulfides. We would expect to observe a size decrease when the degraded dithiol-deg species are more hydrophilic compared to the original hydrophobic backbone. This in contrast with the degradation of PNPs with junction disulfide which would always associate with PNP aggregation and size increase.[30-31, 33-37, 39]

The cleavage kinetics of backbone disulfide within PNP cores could not simply be correlated to the rate of size increase measured by DLS. Instead, proton nuclear magnetic resonance (^{1}H NMR)[47, 53] and gel permeation chromatography (GPC)[48-49, 53, 55] has been used to monitor the reduction-triggered degradation of the PNPs with backbone disulfides. For example, the authors of ref. 53 quantified the backbone disulfide cleavage kinetics by monitoring the ^{1}H NMR spectra evolution of the PNP samples with DTT exposure (Figure 4-3E). Without DTT incubation (t = 0), a peak (Figure 4-3E, a) at 4.4 ppm corresponds to methylene protons adjacent to ester linkages in the ssPES blocks. However, this peak disappears and a new peak at 4.2 ppm corresponding to the dithiol-deg species appears after the PNP exposure to DTT. In addition, peaks at 2.5–2.8 ppm (Figure 4-3E, b and c) corresponding to other methylene protons in ssPES has also changed after samples incubated with DTT. All peak evolution in the ^{1}H NMR spectra correlates to the reduction-

triggered core disulfide cleavage, and the disulfide cleavage kinetics can be linearly correlated to the evolution extent of thiol-related peaks. Specifically, quantitative analyses of disulfide cleavage kinetics can be performed by normalizing the integral ratio of peaks (a/e or a'/e, where e corresponds to $CDCl_3$) at time t with that at time t = 0 (no degradation).[51] However, the authors nicely established the correlation between integral ratio changes with the backbone disulfide cleavage, we note that such method might not be practical for the quantitative analyses in the GSH-exposure cases. GSH is a larger molecule ($M_{n,GSH}$ = 307 g mol^{-1} compared to $M_{n,DTT}$ = 154 g mol^{-1}) with a more complex molecular structure. Peak identification in ^{1}H NMR spectra of GSH/PNPs mixture and further integration would be difficult. Therefore, separation methods between thiol-contained PNP species and GSH needs to be developed prior to ^{1}H NMR analysis of GSH-triggered cleavage kinetics.

GSH-triggered drug release is often observed to be slower from PNPs with backbone disulfides than PNPs with junction disulfides. Yao *et al.* reported a comparison study between polyurethane PNPs with junction disulfides at the hydrophilic/hydrophobic interfaces (PU-ss-I) and PNPs with backbone disulfides within the hydrophobic cores (PU-ss-C).[56] The GSH-triggered release of PU-ss-I (~70%) was higher than PU-ss-C (~55%) within 24 h. To better evaluate the release rate for both PU-ss-I and PU-ss-C PNPs, we extracted the data from ref. 56 to calculate the slope k of release curves. Specifically, we determined k for PU-ss-I and PU-ss-C during the burst release period triggered by GSH (first 10 h): $k_{PU\text{-}ss\text{-}I,\ 10\ h}$ is 6.5 % h^{-1} while $k_{PU\text{-}ss\text{-}C,\ 10\ h}$ is 4 % h^{-1} which indicates backbone disulfide cleavage is more difficult to be triggered by GSH than junction disulfides. Such difference is understandable; hydrophilic GSH is more difficult to diffuse into the

hydrophobic core due to the hydrophilic/hydrophobic incompatibility, and thus is more difficult to initiate the GSH-triggered release. Therefore, the GSH-triggered release rate of PNPs containing backbone disulfides should depend on the diffusion rate of hydrophilic GSH into hydrophobic PNP cores (i.e., the hydrophobicity of PNP cores). Basak *et al.* investigated the effect of core hydrophobicity on the GSH-triggered PNP degradation and release kinetics using two copolymers with the same hydrophilic block length but different hydrophobic block length.[48] Authors showed that PNPs with relatively more hydrophobic interior would undergo slower disintegration of the backbone and drug release kinetics compared to PNPs with less hydrophobic character.[48] These results suggest the less core hydrophobicity would lead to faster backbone disulfide cleavages and therefore faster PNP degradation and drug release.

Along with the core hydrophobicity, the number of disulfides per chain also shows to influence the GSH-triggered PNP degradation and release kinetics; the release rate would be higher when the number of disulfides per chain increases, as Lin *et al.* demonstrated in a recent study.[57] A third parameter influencing GSH-triggered degradation and release kinetics of PNPs with backbone disulfides is the PNP morphology and locations of backbone disulfides within PNPs.[58-60] Along with the spheres with core-shell structure, amphiphilic block copolymers can also self-assemble into vesicles with bilayer structures under certain solvent environment, copolymer composition, and manufacturing method.[43-44] If block copolymers with backbone disulfides forms vesicles, backbone disulfides would locate in the hydrophobic internal part of the bilayer walls. Cerritelli *et al.* introduced the design of GSH-responsive vesicles containing backbone disulfides within the bilayer walls.[58] Specifically, a block copolymer consists hydrophilic PEO and hydrophobic

poly(propylene sulfide) (PPS), in which disulfides are located within the repeat units of the hydrophobic PPS blocks. The formed PEO-*b*-PPS vesicles showed relatively linear release profiles with k = ~0.9% min^{-1} for 80-min experiments under reductive condition.[58] This is in contrast with the observed redox-triggered burst release from the spherical PNPs with backbone disulfides, indicating the GSH-responsive degradation mechanism of vesicular PNPs could be different with spherical PNPs.

Another type of copolymers with disulfide on the backbone is triblock copolymers. The most typical structure of GSH-responsive triblock copolymers is that two identical amphiphilic block copolymers (PA-*b*-PB) conjugate through a disulfide linkage (PA-*b*-PB-ss-PB-*b*-PA), such that the disulfide linkage is located at the junction between two hydrophobic blocks B.[61-66] In such symmetric triblock copolymer having single disulfide linkage, the number of disulfides in a PNP equals to its N_{agg}. Behnoush *et al.* designed a symmetric triblock copolymer with single disulfide in the middle of the hydrophobic backbone ($ssABP_2$).[61] The triblock copolymer $ssABP_2$ was synthesized by ATRP between block copolymers consisting of hydrophilic polymethacrylate blocks with oligo(ethylene oxide) side chains (POEOMA) and hydrophobic polyacrylate blocks with oligo(propylene oxide) side chains and end-thiol group (PAP-SH) (Figure 4-4A). The triblock copolymer is still amphiphilic thus can self-assemble into PNPs in the aqueous media. In response to reductive environment, the backbone disulfides within PNP cores would cleavage and cause dissociation of the PNPs. Interestingly, both atom force microscopy (AFM) and DLS reveals that the backbone disulfide cleavage in such $ssABP_2$ system would cause PNP dissociation to smaller-sized self-assembled structure (Figure 4-4, B and C). Specifically, PNPs are spherical with an average size of 109.3 nm, while PNPs degraded to smaller

spheres with an average size of 70.4 nm upon DTT exposure. The decrease in size is because of the degradation of triblock copolymers to block copolymers; the backbone disulfide cleavage at the middle triblock copolymers would give rise to block copolymers which are still amphiphilic but with decrease in chain length to half, thus PNPs with smaller size would form in aqueous media.[61] Such process represents a new reduction-triggered degradation mechanism that is different with the case of diblock copolymer nanoparticles with backbone disulfides.

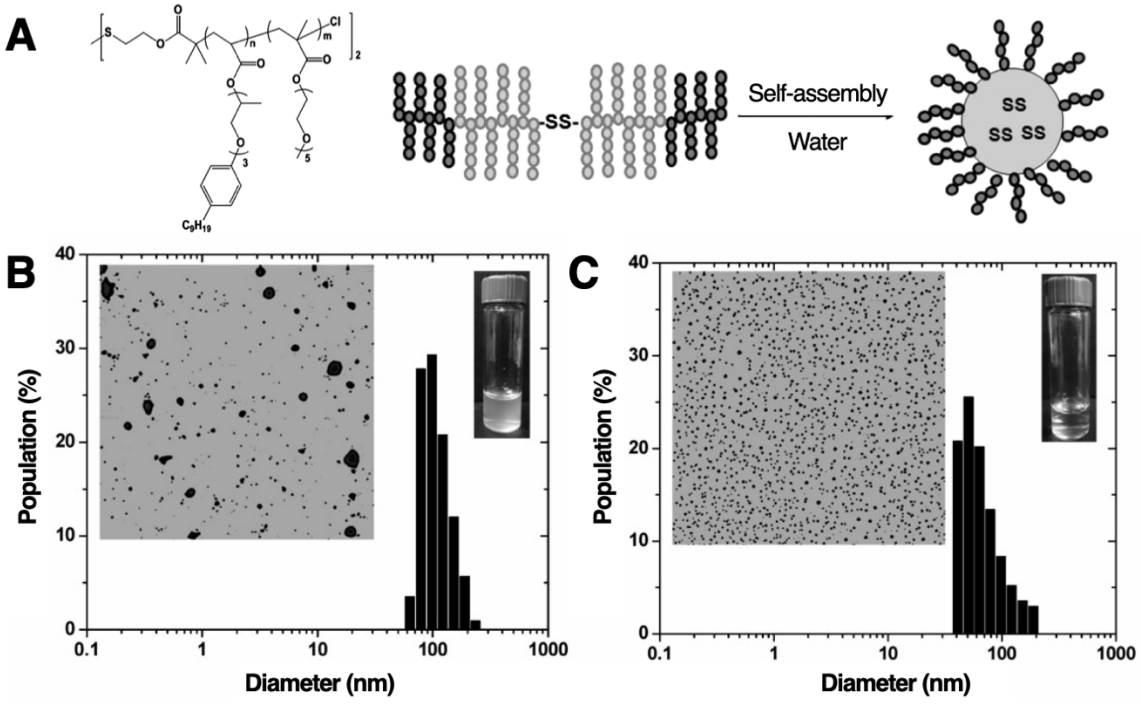

Figure 4-4. (A) Schematic of aqueous self-assembly of ss-ABP_2. DLS number-weighted CONTIN distributions of ss-ABP_2 PNPs before and after DTT incubation are shown in (B) and (C), respectively. Left and right insets in (B) and (C) shows AFM images with the size of 10 μm × 10 μm and photographs of the PNP dispersions, respectively. Adapted from ref. 61. Copyright 2011 WILEY-VCH Verlag GmbH & Co. KGaA, Weinheim.

However, there might be disadvantages of the triblock copolymer nanoparticles with backbone disulfides in terms of drug delivery. First, a complete drug release might not be observed upon GSH-trigger since the degradation-formed PNPs are not GSH-sensitive

anymore and drugs would be still stably encapsulated within the newly formed PNP cores in the reductive environment.[61-62, 64-65] Secondly, the degradation-formed PNPs could be larger *in vivo* and cause potential aggregation-induced toxicity, which is in contrast with the *in vitro* preliminary results that PNPs degrade to be smaller. This is because that the block copolymers would have thiol group at the end of the hydrophobic blocks after the backbone disulfide cleavage, and the thiol-ends could react with other thiol-contained biomacromolecules (e.g. GSH) in the body, forming biomacromolecule-conjugated copolymers and causing the sharp increase in the PNP hydrodynamic size.[40] In a study of triblock copolymer PEO-*b*-PLA-ss-PLA-*b*-PEO (ssBCP) with a backbone disulfide in the middle of hydrophobic block (Figure 4-5A),[65] we observed above drawbacks from the self-assembled PNPs from ssBCP. The GSH-triggered cumulative DOX release from ssBCP PNPs arrived at a plateau value at ~30% while the controlled sample (PNPs from PEO-*b*-PLA-*b*-PEO) showed ~20% release after the same incubation time (Figure 4-5B). Such low cumulative release from ssBCP PNPs upon GSH incubation suggests that ~70% of the drug might still be physically encapsulated in newly degradation-formed, non GSH-sensitive PNPs.[65] Moreover, significant difference in the PNP size change was observed upon incubation with different reducing agents.[65] PNP size showed decreasing trend with DTT incubation for 45 h (Figure 4-5C), indicating new PNPs with smaller size self-assembled from degradation-formed deblock copolymers. However, the main population of PNPs showed slightly increase and a new population of d_h > 500 nm occurred when PNPs were incubated with GSH for 45 h (Figure 4-5D). The proposed degraded product upon GSH incubation could be PEO-*b*-PLA-ss-GSH, and the presence of terminal GSH moiety could result in large hydrodynamic size measured by DLS. However, PNP sizes increase was not

observed in DTT incubated condition because that the end-thiol groups would keep unreacted with DTT (the degradation-formed copolymer would be PEO-*b*-PLA-SH).[65]

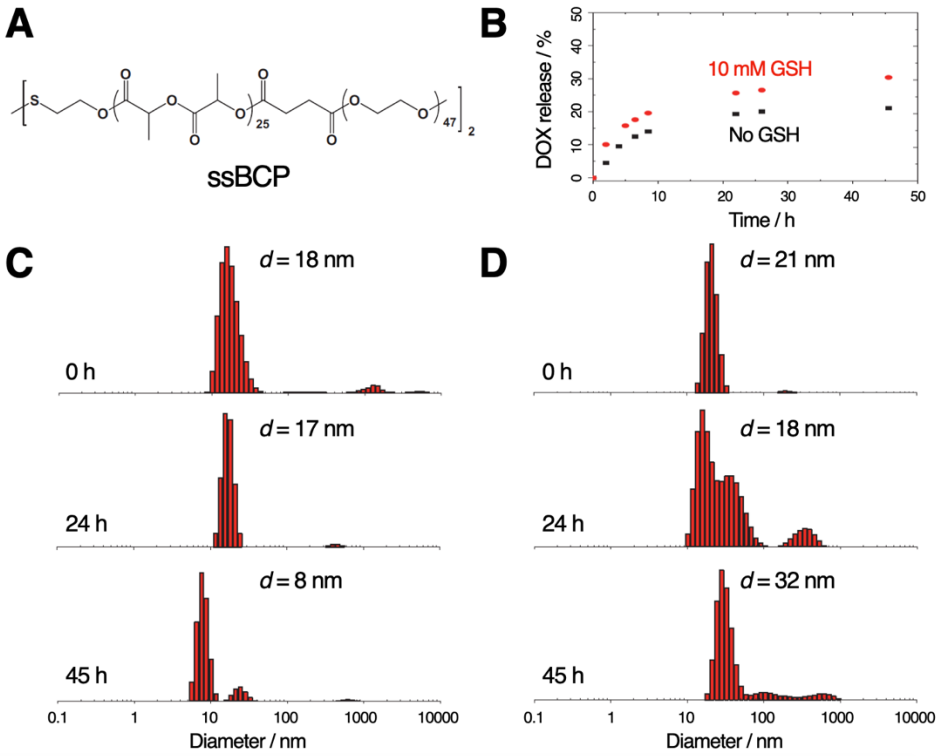

Figure 4-5. (A) Molecular structure of triblock copolymer ssBCP consisting of two PEO blocks, a PLA block, and single disulfide linkage in the middle of the PLA block. (B) Cumulative DOX release profiles of ssBCP PNPs under various conditions within 50 h. DLS number-weighted CONTIN distributions of ssBCP PNPs incubated with DTT and GSH at different time points are shown in (C) and (D), respectively. Numbers in (C) and (D) indicate sizes of the main peak in size distributions. Adapted from ref. 65. Copyright 2014 Elsevier B. V.

4.4 Pendant Disulfides within PNP Cores

Along with locations throughout the hydrophobic backbone, disulfide linkages can also be located within the pendant chains of the hydrophobic block such that they would be within the hydrophobic cores after the copolymers self-assembly. Similar with diblock copolymer nanoparticles with backbone disulfides, PNPs with pendant disulfides would undergo core-forming chain degradation and thus core destabilization upon GSH

incubation.[67-69] Further, pendant disulfide cleavages might cause generation of more hydrophilic species within the cores thus also leading to destabilization by hydrophilic/hydrophobic imbalance.[70] Syntheses of block copolymers with pendent disulfides usually utilize direct polyaddition of monomers bearing disulfide pendants to a hydrophilic chain with predetermined length.[71-74] The number of disulfides for a polymer chain can be calculated by multiplying number of disulfides per monomer by degree of polymerization of the hydrophobic block, and the number of disulfide in a PNP can be calculated by multiplying number of disulfides per chain by N_{agg}.

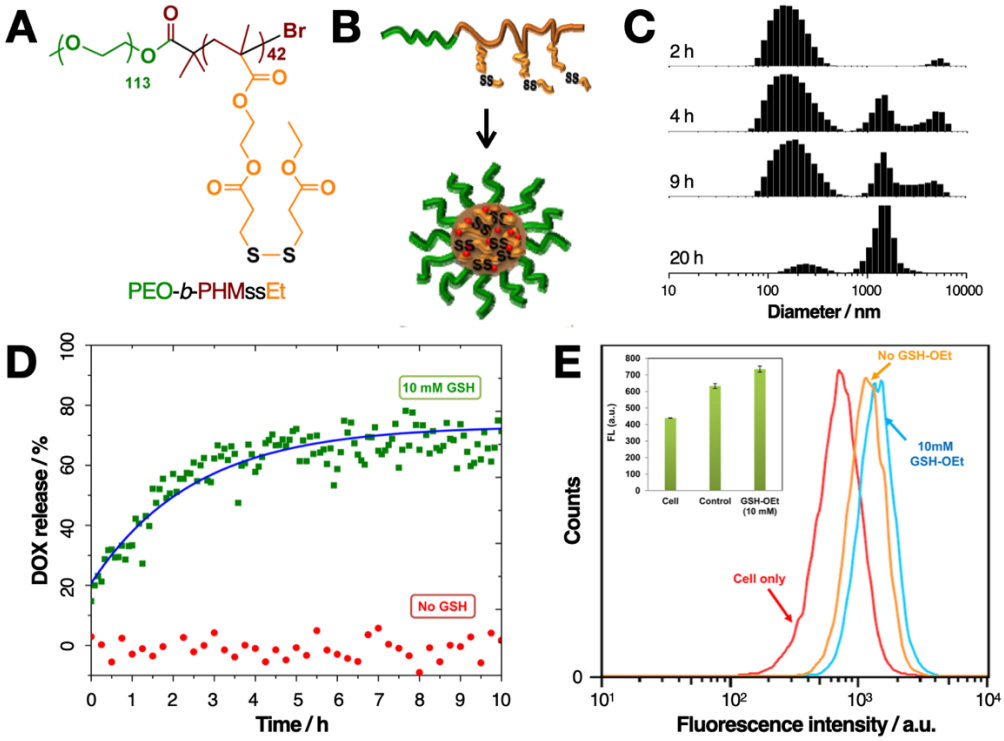

Figure 4-6. (A) Molecular structure of PEO-*b*-PHMssEt. (B) Schematic of PEO-*b*-PHMssEt copolymers self-assembly into PNPs with pendant disulfides. (C) DLS volume-weighted CONTIN distributions of PEO-*b*-PHMssEt PNPs under GSH incubation at different time points. (D) DOX release profiles of PEO-*b*-PHMssEt PNPs under GSH and no GSH incubation for 10 h. (E) Flow cytometric histograms of HeLa cells pretreated with or without GSH-OEt then incubated with PEO-*b*-PHMssEt PNPs. Inset shows mean fluorescence intensity for various cell groups. Adapted from ref. 68. Copyright 2013 American Chemical Society.

Khorsand *et al.* synthesized a block copolymer (PEO-*b*-PHMssEt) consisting of a hydrophilic PEO block and a hydrophobic methacrylate polymer block with disulfide-bearing pendants (PHMssEt) by ATRP approach (Figure 4-6A).[68] By dialysis method, amphiphilic PEO-*b*-PHMssEt can self-assemble into PNPs consisting of PEO corona and PHMssEt cores with pendant disulfides inside (Figure 4-6B), with single size distribution and an average hydrodynamic size of 145 nm. However, PEO-*b*-PHMssEt PNPs shows no significant change in size distribution over 20 h in aqueous condition. In response to GSH incubation, the size distribution of PEO-*b*-PHMssEt PNPs became bimodal and a population of large aggregates (d_h > 1 000 nm) occurred to increase over 20 h (Figure 4-6C). The PNP degradation and associated size increase was attributed to PNP hydrophilic/hydrophobic imbalance due to the GSH-triggered pendant disulfide cleavage. *In vitro* release also confirmed GSH-triggered PNP degradation. Compared to DOX-loaded PNPs without GSH incubation that did not release DOX over the incubation period, PNPs exposed to GSH showed enhanced DOX release to ~70% after 10 h (Figure 4-6D). In addition, flow cytometric PNP uptake experiments were performed for HeLa cells pretreated with or without GSH-OEt (which can manipulate intracellular GSH concentration[24]). A right shift of fluorescence intensity was observed for the HeLa cells with GSH-OEt and PNP treatments compared to cells with only PNP treatment (Figure 4-6E). Since static quenching and elimination of fluorescence would occur when DOX aggregates within PNP cores, such increase of fluorescence intensity detected within the cells indicates DOX was released from PNPs under high GSH concentration. These results further suggests the PNP degradation triggered by pendant disulfide cleavage would occur when exposed to high concentration of GSH.[68]

There are not yet reports to date on the quantitative analysis of the pendant disulfide cleavage kinetics. Such analysis could potentially be done by ^{1}H NMR, similarly with the analysis for backbone disulfide cleavage kinetics. However, separation methods between thiol-contained PNP species and GSH needs to be developed prior to ^{1}H NMR analysis. More recently, our group has attempted to scale the pendent disulfide cleavage kinetics with inner compartment volume change within the PNPs by transmission electron microscopy (TEM).[75] Specifically, degraded thiol-species with higher hydrophilicity would generate from the pendant disulfide cleavage. The hydrophobic/hydrophilic imbalance would cause microphase separation within the hydrophobic PNP cores, giving rise to hydrophilic inner compartment. By using negative staining agent such as uranyl acetate which specifically binding to hydrophilic compartment, the increase of inner compartment area could be visualized and thus measured on two-dimensional TEM images. The inner compartment area should increase with more pendant disulfides cleaved. However, there are disadvantages in this method as an initial attempt. Firstly, the area information could not truly reflect the three-dimensional volume information which represents inner compartment growth. Secondly, changes of inner compartment area over time also include other kinetic contributions from numerous process on different time scales, including polymer and particle diffusion, thus therefore do not directly provide cleavage kinetics.[75]

The control of GSH-responsive degradation of PNPs with pendant disulfides has been demonstrated by varying the number of disulfide per chain, which is specifically achieved by controlling the polymerization degree of the hydrophobic blocks with pendant disulfides.[74] However, the control of polymerization degree requires the optimization of

synthetic routes which is chemical in nature. Recently, our group applied a shear processing control over the GSH-responsivity of PNPs containing pendant disulfides using a two-phase gas-liquid microfluidic chip.[75] Without the change in chemical structures, shear-induced PNPs showed different pendant disulfide cleavage kinetics (i.e., GSH-responsivity) due to their differential excess Gibbs free energy G_{ex} which mainly described internal molecular configuration.[75]

Pendant disulfides within PNP cores could cleave to be thiols, and further convert to cross-linked disulfides within the cores through disulfide-thiol exchange reaction in the presence of a catalytic amount of reducing agent.[76-82] Compared to PNPs that physically encapsulate drugs within the cores, the core cross-linking would offer PNPs with enhanced colloidal stability for the encapsulated drugs.[3, 19-20, 22-23, 83-84] However, such preparation method for cross-linked disulfides is sometimes lack of practicality; PNP disintegration would also occur in the presence of reducing agent before crosslinking reactions.[21, 23]

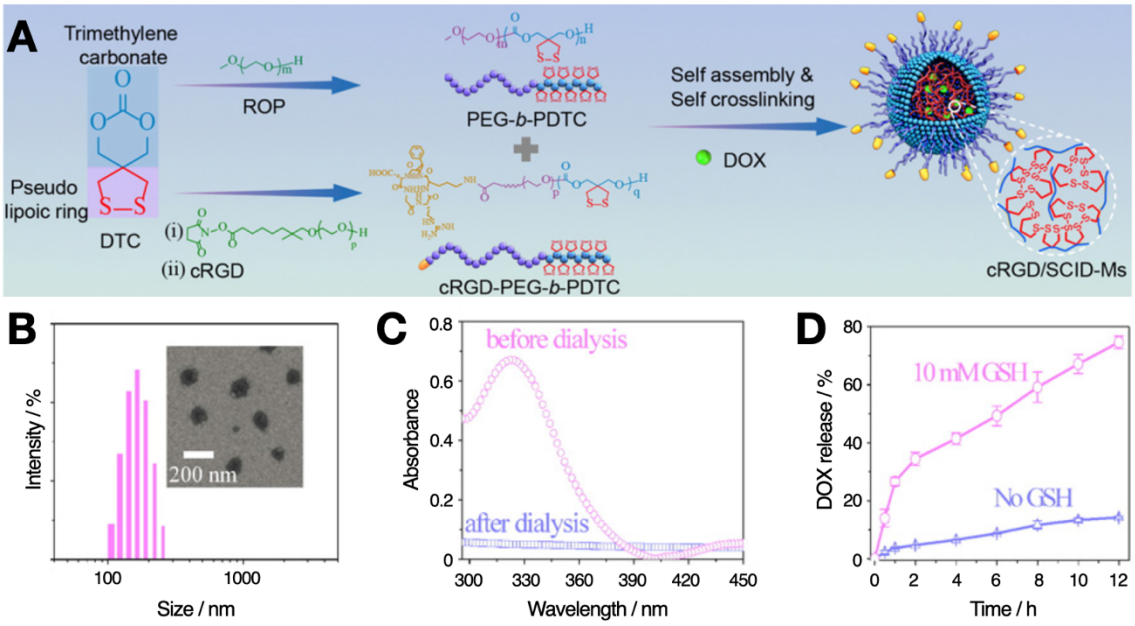

Figure 4-7. (A) Schematic of cRGD-decorated PNPs (cRGD/SCID-Ms) formation from cRGD-PEG-*b*-PDTC/PEG-*b*-PDTC PNPs with pendant disulfides cross-linking. (B) DLS intensity-weighted CONTIN distribution and TEM image of cRGD/SCID-Ms. (C) UV-Vis spectra of cRGD-PEG-*b*-PDTC /PEG-*b*-PDTC PNPs before and after pendant disulfides cross-linking (D) DOX release from cRGD/SCID-Ms under GSH or no GSH conditions over 12 h. Adapted from ref. 77. Copyright 2016 Elsevier B. V.

For instance, Zou *et al.* designed self-crosslinkable and intracellularly decrosslinkable PNPs (SCID-Ms) self-assembled from amphiphilic poly(ethylene glycol)-*b*-poly(dithiolane trimethylene carbonate) (PEG-*b*-PDTC), in which the hydrophobic PDTC blocks consist of poly(trimethylene carbonate) (PEMC) backbones and multiple dithiolane rings as pendants.[77] In addition, SCID-Ms corona was functionalized by cRGD such that cRGD/SCID-Ms were capable to actively deliver encapsulated drugs to tumor site (Figure 4-7A). In order to prepare cRGD/SCID-Ms, PEG-*b*-PDTC copolymers were firstly synthesized by ring-opening polymerization, and then cRGD was covalently attached to 10% of the PEG-ends. The cRGD-PEG-*b*-PDTC/PEG-*b*-PDTC copolymers self-assembled into cRGD/SCID-Ms by solvent evaporation method, and catalytic DTT was

added to induce the opening of dithiolane ring and formation of disulfides within the cores. The cRGD/SCID-Ms showed a modal distribution with an average size of 150 nm, and TEM revealed that the PNP morphology was sphere (Figure 4-7B). UV-Vis spectroscopy was used to investigate the cross-linking extent of the PNPs. Specifically, the absorbance at 330 nm completely disappeared after the catalytic DTT treatment, suggesting that all dithiolane rings had transformed to linear disulfide (Figure 4-7C). In *in vitro* release experiments, DOX-loaded cRGD/SCID-Ms showed significantly enhanced DOX release (~80% after 12 h) when GSH incubation was applied, indicating the decrosslinking within the cores accelerated the DOX release rate from PNPs (Figure 4-7D).[77]

Disulfide linkages require less space in terms of molecular configuration comparing to dithiolane rings, thus the cross-linking would cause the core volume compression and the decrease in PNP size due to less steric repulsion between hydrophobic blocks. On the contrary, decrosslinking of disulfides would usually cause the swelling of the PNPs and thus increase in size. Since the hydrophobicity of the core chains remains unchanged even when the pendent disulfides cleaved,[77] we would not observe the degradation of the PNPs into relatively small species due to the hydrophilic/hydrophobic imbalance, but the swelling of the PNPs instead due to the regeneration of dithiolane rings. In ref. 77, a quick swelling of PNPs from 150 nm to 338 nm was observed upon GSH incubation. However, no significant morphological change was observed and swelled PNPs remained spherical, indicating the decrosslinking would not cause PNP morphological degradation.

4.5 Disulfide Crosslinks within PNP Cores

As discussed in the previous section, the cross-linked disulfides can *in situ* form through thiol-disulfide exchange reactions between pendant disulfides within the

hydrophobic PNP cores. In addition, cross-linked disulfides can form through the oxidation of pendant thiol groups attached to copolymer side chains.[83, 85-89] In such case, a thiol group can conjugate with another thiol group on the ortho position, or on other polymer chains. The number of disulfides in a PNP could be estimated by monitoring the evolution of thiol-peaks in UV-Vis spectroscopy.[77] However, such method of conducting cross-linked disulfides requires the protection of thiol-groups throughout the copolymer synthesis until the PNP formation.[85-88]

Ding *et al.* synthesized a polypeptide block copolymer (PEG-$_D$-PC, $_D$ refers to a pH-sensitive dimethylmaleic anhydride derivative bond) which consists of a hydrophilic PEG block and a poly($_L$-cysteine) (PC) block bearing thiol-pendants by ring opening polymerization (Figure 4-8A).[89] The polypeptide copolymer nanoparticles with a pH-sheddable PEG corona and a core with cross-linked disulfides self-assembled in aqueous condition, offering pH/GSH dual-stimuli responsive properties. Cross-linked disulfides were formed by H_2O_2 oxidation of end-thiol groups within the PNP core. DLS revealed that the average hydrodynamic size of crosslinked PNPs was 135 nm (Figure 4-8B). However, the PNP size significantly decreased to ~75 nm upon DTT and neutral pH incubation of 24 h (Figure 4-8C), indicating the redox-triggered disulfide decrosslinking caused re-assembly of PNPs into smaller structures. The *in vitro* release experiments also showed the redox-triggered enhanced release of DOX-loaded PNPs (~50% in 84 h) upon DTT incubation with neutral pH (Figure 4-8D).

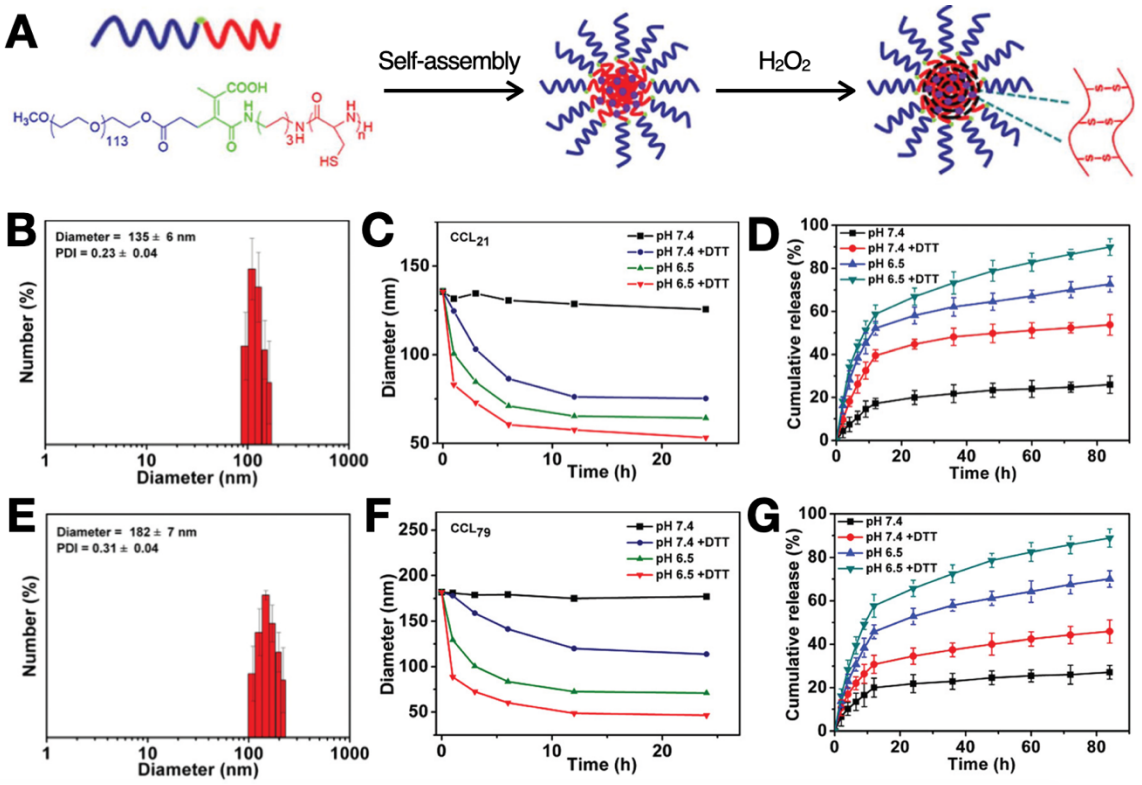

Figure 4-8. (A) Schematic of PEG-$_D$-PC block copolymers, their self-assembly and cross-linking procedure (B) DLS number-weighted CONTIN distribution of PEG-$_D$-PC_{21} PNPs. (C) DLS was used to monitor the size change of PEG-$_D$-PC_{21} PNPs under various incubation conditions for 24 h. (D) *In vitro* release profiles of PEG-$_D$-PC_{21} PNPs under various incubation conditions for 84 h. (E) DLS number-weighted CONTIN distribution of PEG-$_D$-PC_{79} PNPs. (F) DLS was used to monitor the size change of PEG-$_D$-PC_{79} PNPs under various incubation conditions for 24 h. (G) *In vitro* release profiles of PEG-$_D$-PC_{79} PNPs under various incubation conditions for 84 h Adapted from ref. 89. Copyright 2018 Royal Society of Chemistry.

We conclude that GSH-triggered degradation kinetics (i.e., rate of size decrease) of PNPs with cross-linked disulfides could be tuned by the number of disulfides formed within the core, which would rely on the cross-linking efficiency, and length of the hydrophobic block bearing thiol pendants. In ref. 89, two copolymers with different PC block length were synthesized. Compared to PNPs formed by PEG-$_D$-PC_{21} (subscript refers to the number of repeat unit), PEG-$_D$-PC_{79} self-assembly yielded PNPs with large size of

182 nm (Figure 4-8E). When incubated with the same amount of reducing agent and neutral pH, PEG-$_D$-PC$_{79}$ PNPs showed attenuated size decrease compared to PEG-$_D$-PC$_{21}$ PNPs (Figure 4-8F), suggesting PNPs with longer PC blocks would show slower degradation kinetics. Further release experiment confirmed such attenuating trend in PNP degradation; PEG-$_D$-PC$_{79}$ PNPs release only ~40% of DOX after 84 h upon reducing environment. Since longer PC block length would provide more thiol groups for cross-linking, PNPs with longer PC blocks would have more cross-linked disulfides within the core upon oxidation reactions and thus have higher threshold for GSH-triggered PNP degradation.

4.6 Conclusions

In this chapter, we summarized recent advances in the development of smart drug delivery polymer nanoparticles (PNPs) self-assembled from biological reduction-responsive degradable block copolymers. Such PNPs can undergo fast degradation and enhanced drug release upon reduction stimulus at target site (i.e. cancerous cells), providing promising "on-demand" therapeutic functions. We highlighted various design strategies that give rise to PNPs with disulfides at different locations. The disulfide linkages can be located at the hydrophilic corona/hydrophobic core interfaces for shell-sheddable PNPs, while disulfides can also be positioned within hydrophobic cores for backbone cleavable, pendant cleavable, or decrosslinkable PNPs. We further illustrated the redox-triggered degradation mechanisms of PNPs with disulfides at various locations by conducting retrospective data analysis of selected literatures. Briefly, reduction-responsivity of PNPs containing disulfides in terms of structural change (including size, morphology, and internal compartment volume) and release rates relies on the disulfide density σ, which is co-determined by polymerization degree (DP) of the copolymers, and

aggregation number (N_{agg}) of the PNPs. PNP Morphology might also affect the reduction-responsivity of PNPs. Reduction-responsivity for PNPs with junction, backbone, or pendant disulfides usually increases with disulfide density σ being higher, while PNPs with cross-linked disulfides show attenuated reduction-responsivity with increasing disulfide density σ. Finally, we provided suggestions on analytical techniques that could be potentially used for quantitative studies of the disulfide cleavage and PNP degradation kinetics. Junction-cleavage degradation kinetics could be scaled to the change in particle size, which can be monitored by DLS. While other types of disulfide cleavage did not follow linear trends in size change, other analytical techniques (including ^{1}H NMR, GPC, and TEM) can be used for tracking the cleavage kinetics. These new insights from the literature reanalysis should provide guidance on future studies of the manufacturing PNPs with controlled reduction-responsivity.

4.7 References

1. Allen, C.; Maysinger, D.; Eisenberg, A., Nano-engineering block copolymer aggregates for drug delivery. *Colloids Surf. B* **1999**, *16*, 3-27.

2. Kataoka, K.; Harada, A.; Nagasaki, Y., Block copolymer micelles for drug delivery: design, characterization and biological significance. *Adv. Drug Delivery Rev.* **2001**, *47*, 113-131.

3. Rösler, A.; Vandermeulen, G. W. M.; Klok, H.-A., Advanced drug delivery devices via self-assembly of amphiphilic block copolymers. *Adv. Drug Delivery Rev.* **2001**, *53*, 95-108.

4. Tyrrell, Z. L.; Shen, Y.; Radosz, M., Fabrication of micellar nanoparticles for drug delivery through the self-assembly of block copolymers. *Prog. Poly. Sci.* **2010**, *35*, 1128-1143.

5. Gong, J.; Chen, M.; Zheng, Y.; Wang, S.; Wang, Y., Polymeric micelles drug Delivery system in oncology. *J. Controlled Release* **2012**, *159*, 312-323.

6. Elsabahy, M.; Wooley, K. L., Design of polymeric nanoparticles for biomedical delivery applications. *Chem. Soc. Rev.* **2012**, *41*, 2545-2561.

7. Zhang, Y.; Chan, H. F.; Leong, K. W., Advanced materials and processing for drug delivery: the past and the future. *Adv. Drug Delivery Rev.* **2013**, *65*, 104-120.

8. Luk, B. T.; Zhang, L., Current advances in polymer-based nanotheranostics for cancer treatment and diagnosis. *ACS Appl. Mater. Interfaces* **2014**, *6*, 21859-21873.

9. Sun, T.; Zhang, Y. S.; Pang, B.; Hyun, D. C.; Yang, M.; Xia, Y., Engineered nanoparticles for drug delivery in cancer therapy. *Angew. Chem. Int. Ed.* **2014**, *53*, 12320-12364.

10. Björnmalm, M.; Thurecht, K. J.; Michael, M.; Scott, A. M.; Caruso, F., Bridging bio–nano science and cancer nanomedicine. *ACS Nano* **2017**, *11*, 9594-9613.

11. Owens III, D. E.; Peppas, N. A., Opsonization, biodistribution, and pharmacokinetics of polymeric nanoparticles. *Int. J. Pharm.* **2006**, *307*, 93-102.

12. Maeda, H.; Nakamura, H.; Fang, J., The EPR effect for macromolecular drug delivery to solid tumors: improvement of tumor uptake, lowering of systemic toxicity, and distinct tumor imaging in vivo. *Adv. Drug Delivery Rev.* **2013**, *65*, 71-79.

13. Maeda, H.; Wu, J.; Sawa, T.; Matsumura, Y.; Hori, K., Tumor vascular permeability and the EPR effect in macromolecular therapeutics: a review. *J. Controlled Release* **2000**, *65*, 271-284.

14. Perry, J. L.; Reuter, K. G.; Luft, J. C.; Pecot, C. V.; Zamboni, W.; DeSimone, J. M., Mediating passive tumor accumulation through particle Size, tumor type, and location. *Nano Lett.* **2017**, *17*, 2879-2886.

15. Geng, Y.; Dalhaimer, P.; Cai, S.; Tsai, R.; Tewari, M.; Minko, T.; Discher, D. E., Shape effects of filaments versus spherical particles in flow and drug delivery. *Nat. Nanotechnol.* **2007**, *2*, 249-255.

16. Gaumet, M.; Vargas, A.; Gurny, R.; Delie, F., Nanoparticles for drug delivery: the need for precision in reporting particle size parameters. *Eur. J. Pharm. Biopharm.* **2008**, *69*, 1-9.

17. Alexis, F.; Pridgen, E.; Molnar, L. K.; Farokhzad, O. C., Factors affecting the clearance and biodistribution of polymeric nanoparticles. *Mol. Pharmaceutics* **2008**, *5*, 505-515.

18. Bains, A.; Cao, Y.; Moffitt, M. G., Multiscale control of hierarchical structure in crystalline block copolymer nanoparticles using microfluidics. *Macromol. Rapid Commun.* **2015**, *36*, 2000-2005.

19. Ganta, S.; Devalapally, H.; Shahiwala, A.; Amiji, M., A review of stimuli-responsive nanocarriers for drug and gene delivery. *J. Controlled Release* **2008**, *126*, 187-204.

20. Stuart, M. A. C.; Huck, W. T.; Genzer, J.; Müller, M.; Ober, C.; Stamm, M.; Sukhorukov, G. B.; Szleifer, I.; Tsukruk, V. V.; Urban, M., Emerging applications of stimuli-responsive polymer materials. *Nat. Mater.* **2010**, *9*, 101-113.

21. Zhang, Q.; Ko, N. R.; Oh, J. K., Recent advances in stimuli-responsive degradable block copolymer micelles: synthesis and controlled drug delivery applications. *Chem. Commun.* **2012**, *48*, 7542-7552.

22. Mura, S.; Nicolas, J.; Couvreur, P., Stimuli-responsive nanocarriers for drug delivery. *Nat. Mater.* **2013**, *12*, 991-1003.

23. Oh, J. K., Disassembly and tumor-targeting drug delivery of reduction-responsive degradable block copolymer nanoassemblies. *Polym. Chem.* **2019**, *10*, 1554-1568.

24. Russo, A.; DeGraff, W.; Friedman, N.; Mitchell, J. B., Selective modulation of glutathione levels in human normal versus tumor cells and subsequent differential response to chemotherapy drugs. *Cancer Res.* **1986**, *46*, 2845.

25. Jones, D. P.; Carlson, J. L.; Samiec, P. S.; Sternberg, P.; Lou, A. S. B., Glutathione measurement in human plasma: evaluation of sample collection, storage and derivatization conditions for analysis of dansyl derivatives by HPLC. *Clin. Chim. Acta* **1998**, *275*, 175-184.

26. Jiang, X. Q.; Yu, Y.; Chen, J. W.; Zhao, M. K.; Chen, H.; Song, X. Z.; Matzuk, A. J.; Carroll, S. L.; Tan, X.; Sizovs, A.; Cheng, N. H.; Wang, M. C.; Wang, J. Quantitative imaging of glutathione in live cells using a reversible reaction-based ratiometric fluorescent probe. *ACS Chem. Biol.* **2015**, *10*, 864-874.

27. Hong, R.; Han, G.; Fernández, J. M.; Kim, B.-J.; Forbes, N. S.; Rotello, V. M., Glutathione-mediated delivery and release using monolayer protected nanoparticle carriers. *J. Am. Chem. Soc.* **2006**, *128*, 1078-1079.

28. Fleige, E.; Quadir, M. A.; Haag, R., Stimuli-responsive polymeric nanocarriers for the controlled transport of active compounds: concepts and applications. *Adv. Drug Delivery Rev.* **2012**, *64*, 866-884.

29. Klaikherd, A.; Ghosh, S.; Thayumanavan, S., A facile method for the synthesis of cleavable block copolymers from ATRP-based homopolymers. *Macromolecules* **2007**, *40*, 8518-8520.

30. Sun, H.; Guo, B.; Cheng, R.; Meng, F.; Liu, H.; Zhong, Z., Biodegradable micelles with sheddable poly(ethylene glycol) shells for triggered intracellular release of doxorubicin. *Biomaterials* **2009**, *30*, 6358-6366.

31. Tang, L. Y.; Wang, Y. C.; Li, Y.; Du, J. Z.; Wang, J., Shell-detachable micelles based on disulfide-linked block copolymer as potential carrier for intracellular drug delivery. *Bioconjugate Chem.* **2009**, *20*, 1095-1099.

32. Sun, H.; Guo, B.; Li, X.; Cheng, R.; Meng, F.; Liu, H.; Zhong, Z., Shell-sheddable micelles based on dextran-ss-poly(ε-caprolactone) diblock copolymer for efficient intracellular release of doxorubicin. *Biomacromolecules* **2010**, *11*, 848-854.

33. Wang, Y. C.; Wang, F.; Sun, T. M.; Wang, J., Redox-responsive nanoparticles from the single disulfide bond-bridged block copolymer as drug carriers for overcoming multidrug resistance in cancer cells. *Bioconjugate Chem.* **2011**, *22*, 1939-1945.

34. Wang, W.; Sun, H.; Meng, F.; Ma, S.; Liu, H.; Zhong, Z., Precise control of intracellular drug release and anti-tumor activity of biodegradable micellar drugs via reduction-sensitive shell-shedding. *Soft Matter* **2012**, *8*, 3949.

35. Wang, J.; Yang, G.; Guo, X.; Tang, Z.; Zhong, Z., Redox-responsive polyanhydride micelles for cancer therapy. *Biomaterials* **2014**.

36. Shi, C.; Guo, X.; Qu, Q.; Tang, Z.; Wang, Y.; Zhou, S., Actively targeted delivery of anticancer drug to tumor cells by redox-responsive star-shaped micelles. *Biomaterials* **2014**, *35*, 8711-8722.

37. Yang, Q.; Tan, L.; He, C.; Liu, B.; Xu, Y.; Zhu, Z.; Shao, Z.; Gong, B.; Shen, Y. M., Redox-responsive micelles self-assembled from dynamic covalent block copolymers for intracellular drug delivery. *Acta Biomaterialia* **2015**, *17*, 193-200.

38. Cui, C.; Yu, P.; Wu, M.; Zhang, Y.; Liu, L.; Wu, B.; Wang, C.-X.; Zhuo, R.-X.; Huang, S.-W., Reduction-sensitive micelles with sheddable PEG shells self-assembled from a Y-shaped amphiphilic polymer for intracellular doxorubicine release. *Colloids Surf. B* **2015**, *129*, 137-145.

39. Chen, C.; Zheng, P.; Cao, Z.; Ma, Y.; Li, J.; Qian, H.; Tao, W.; Yang, X., PEGylated hyperbranched polyphosphoester based nanocarriers for redox-responsive delivery of doxorubicin. *Biomater. Sci.* **2016**, *4*, 412-417.

40. Dong, H.; Tang, M.; Li, Y.; Li, Y.; Qian, D.; Shi, D., Disulfide-bridged cleavable PEGylation in polymeric nanomedicine for controlled therapeutic delivery. *Nanomedicine* **2015**, *10*, 1941-1958.

41. Zhu, Y.; Zhang, J.; Meng, F.; Deng, C.; Cheng, R.; Feijen, J.; Zhong, Z., cRGD-functionalized reduction-sensitive shell-sheddable biodegradable micelles mediate enhanced doxorubicin delivery to human glioma xenografts in vivo. *J. Controlled Release* **2016**, *233*, 29-38.

42. Zhong, Y.; Yang, W.; Sun, H.; Cheng, R.; Meng, F.; Deng, C.; Zhong, Z., Ligand-directed reduction-sensitive shell-sheddable biodegradable micelles actively deliver doxorubicin into the nuclei of target cancer cells. *Biomacromolecules* **2013**, *14*, 3723-3730.

43. Zhang, L.; Eisenberg, A., Multiple morphologies of "crew-cut" aggregates of polystyrene-b-poly(acrylic acid) block copolymers. *Science* **1995**, *268*, 1728-1731.

44. Zhang, L.; Eisenberg, A., Multiple morphologies andcCharacteristics of "crew-cut" micelle-like aggregates of polystyrene-b-poly(acrylic acid) diblock copolymers in aqueous solutions. *J. Am. Chem. Soc.* **1996**, *118*, 3168-3181.

45. Zhang, L.; Eisenberg, A., Thermodynamic vs kinetic aspects in the formation and morphological transitions of crew-cut aggregates produced by self-assembly of polystyrene-b-poly(acrylic acid) block copolymers in dilute solution. *Macromolecules* **1999**, *32*, 2239-2249.

46. Fan, H.; Li, Y.; Yang, J.; Ye, X., Effect of hydrophobic chain length on the stability and guest exchange behavior of shell-sheddable micelles formed by disulfide-linked diblock copolymers. *J. Phy. Chem. B* **2017**, *121*, 9708-9717.

47. Fan, H.; Jin, H.; Li, Y.; Yu, J.; Chen, J., Fabrication of reduction-degradable micelle based on disulfide-linked graft copolymer-camptothecin conjugate for enhancing solubility and stability of camptothecin. *Polymer* **2010**, *51*, 5107-5114.

48. Basak, D.; Bej, R.; Ghosh, S., Amphiphilic poly(disulfide) micelle and remarkable impact of the core hydrophobicity on redox responsive disassembly. *Polym. Chem.* **2015**, *6*, 6465-6474.

49. Li, D.; Bu, Y.; Zhang, L.; Wang, X.; Yang, Y., Facile construction of pH- and redox-responsive micelles from a biodegradable poly($_D$-hydroxyl amine) for drug delivery. *Biomacromolecules* **2016**.

50. Zhuang, Y.; Deng, H.; Su, Y.; He, L.; Wang, R.; Tong, G.; He, D.; Zhu, X., Aptamer-functionalized and backbone redox-responsive hyperbranched polymer for targeted drug delivery in cancer therapy. *Biomacromolecules* **2016**, *17*, 2050-2062.

51. Behrendt, F. N.; Schlaad, H., Metathesis polymerization of cystine-based macrocycles. *Polym. Chem.* **2017**, *8*, 366-369.

52. Behrendt, F. N.; Schlaad, H., Entropy-driven ring-opening disulfide metathesis polymerization for the synthesis of functional poly(disulfide)s. *Macromol. Rapid Commun.* **2018**, *39*, 1700735.

53. Aleksanian, S.; Khorsand, B.; Schmidt, R.; Oh, J. K., Rapidly thiol-responsive degradable block copolymer nanocarriers with facile bioconjugation. *Polym. Chem.* **2012**, *3*, 2138-2147.

54. Yang, D.; Chen, W.; Hu, J., Design of controlled drug delivery system based on disulfide cleavage trigger. *J. Phys. Chem. B* **2014**, *118*, 12311-12317.

55. Liu, J.; Pang, Y.; Huang, W.; Zhu, Z.; Zhu, X.; Zhou, Y.; Yan, D., Redox-responsive polyphosphate nanosized assemblies: a smart drug delivery platform for cancer therapy. *Biomacromolecules* **2011**, *12*, 2407-2415.

56. Yao, Y.; Xu, H.; Liu, C.; Guan, Y.; Xu, D.; Zhang, J.; Su, Y.; Zhao, L.; Luo, J., biodegradable multi-blocked polyurethane micelles for intracellular drug delivery: the effect of disulfide location on the drug release profile. *RSC Adv.* **2016**, *6*, 9082-9089.

57. Lin, C.; Lou, B.; Zhao, J.; Jin, R.; Zhao, P.; Li, J.; Ren, J., Self-assembled micelles of PEG–poly(disulfide carbamate amine) copolymers for intracellular dual-responsive drug delivery. *J. Mater. Chem. B* **2016**, *4*, 902-909.

58. Cerritelli, S.; Velluto, D.; Hubbell, J. A., PEG-ss-PPS: reduction-sensitive disulfide block copolymer vesicles for intracellular drug delivery. *Biomacromolecules* **2007**, *8*, 1966-1972.

59. Jain, J. P.; Kumar, N., Self-assembly of amphiphilic $(PEG)_3$-PLA copolymer as polymersomes: preparation, characterization, and their evaluation as drug carrier. *Biomacromolecules* **2010**, *11*, 1027-35.

60. Tao, Y.; Zhao, H., Synthesis and self-assembly of amphiphilic tadpole-shaped block copolymer with disulfides at the junction points between cyclic PEG and linear PS. *Polymer* **2017**, *122*, 52-59.

61. Khorsand, B.; Schmidt, R.; Oh, J. K., New thiol-responsive mono-cleavable block copolymer micelles labeled with single disulfides. *Macromol. Rapid Commun.* **2011**, *32*, 1652-1657.

62. Sun, L.; Liu, W.; Dong, C.-M., Bioreducible micelles and hydrogels with tunable properties from multi-armed biodegradable copolymers. *Chem. Commun.* **2011**, *47*, 11282-11284.

63. Li, S.; Ye, C.; Zhao, G.; Zhang, M.; Zhao, Y., Synthesis and properties of monocleavable amphiphilic comblike copolymers with alternating PEG and PCL grafts. *J. Polym. Sci. A: Polym. Chem.* **2012**, *50*, 3135-3148.

64. Liu, D. L.; Chang, X.; Dong, C. M., Reduction- and thermo-sensitive star polypeptide micelles and hydrogels for on-demand drug delivery. *Chem. Commun.* **2013**, *49*, 1229-1231.

65. Cunningham, A.; Ko, N. R.; Oh, J. K., Synthesis and reduction-responsive disassembly of PLA-based mono-cleavable micelles. *Colloids Surf. B* **2014**, *122*, 693-700.

66. Wu, W.; Dai, W.; Zhao, X.; Zhang, J.; Zhao, Y., Synthesis, self-assembly and drug release behaviors of reduction-labile multi-responsive block miktobrush quaterpolymers with linear and V-shaped grafts. *Polym. Chem.* **2018**, *9*, 1947-1960.

67. Jackson, A. W.; Fulton, D. A., Triggering polymeric nanoparticle disassembly through the simultaneous application of two different stimuli. *Macromolecules* **2012**, *45*, 2699-2708.

68. Khorsand, B.; Lapointe, G.; Brett, C.; Oh, J. K., Intracellular drug delivery nanocarriers of glutathione-responsive degradable block copolymers having pendant disulfide linkages. *Biomacromolecules* **2013**, *14*, 2103-2111.

69. Chan, N.; An, S. Y.; Yee, N.; Oh, J. K., Dual redox and thermoresponsive double hydrophilic block copolymers with tunable thermoresponsive properties and self-assembly behavior. *Macromol. Rapid Commun.* **2014**, *35*, 752-757.

70. Chan, N.; Khorsand, B.; Aleksanian, S.; Oh, J. K., A dual location stimuli-responsive degradation strategy of block copolymer nanocarriers for accelerated release. *Chem. Commun.* **2013**, *49*, 7534-7536.

71. Yang, J.; Wu, K.; Konak, C.; Kopecek, J., Dynamic light scattering study of self-assembly of HPMA hybrid graft copolymers. *Biomacromolecules* **2008**, *9*, 510-517.

72. Ryu, J.-H.; Jiwpanich, S.; Chacko, R.; Bickerton, S.; Thayumanavan, S., Surface-functionalizable polymer nanogels with facile hydrophobic guest encapsulation capabilities. *J. Am. Chem. Soc.* **2010**, *132*, 8246-8247.

73. Novo, L.; Takeda, K. M.; Petteta, T.; Dakwar, G. R.; Van, d. D., Joep B; Remaut, K.; Braeckmans, K.; Van Nostrum, C. F.; Mastrobattista, E.; Hennink, W. E., Targeted decationized polyplexes for siRNA delivery. *Mol. Pharmaceutics* **2015**, *12*, 150-161.

74. Deng, Z.; Yuan, S.; Xu, R. X.; Liang, H.; Liu, S., Reduction-triggered transformation of disulfide-containing micelles at chemically tunable rates. *Angew. Chem. Int. Ed.* **2018**, *57*, 8896-8900.

75. Huang, Y.; Moini Jazani, A.; Howell, E. P.; Oh, J. K.; Moffitt, M. G., Controlled microfluidic synthesis of biological stimuli-responsive polymer nanoparticles. *ACS Appl. Mater. Interfaces* **2020**, *12*, 177-190.

76. Cheng, R.; Meng, F.; Deng, C.; Klok, H.-A.; Zhong, Z., Dual and multi-stimuli responsive polymeric nanoparticles for programmed site-specific drug delivery. *Biomaterials* **2013**, *34*, 3647-3657.

77. Zou, Y.; Fang, Y.; Meng, H.; Meng, F.; Deng, C.; Zhang, J.; Zhong, Z., Self-crosslinkable and intracellularly decrosslinkable biodegradable micellar nanoparticles: a robust, simple and multifunctional nanoplatform for high-efficiency targeted cancer chemotherapy. *J. Controlled Release* **2016**, *244*, 326-335.

78. How, S.-C.; Chen, Y.-F.; Hsieh, P.-L.; Wang, S. S. S.; Jan, J.-S., Cell-targeted, dual reduction- and pH-responsive saccharide/lipoic acid-modified poly(L-lysine) and poly(acrylic acid) polyionic complex nanogels for drug delivery. *Colloids Surf. B* **2017**, *153*, 244-252.

79. Zou, Y.; Meng, F.; Zhang, J.; Zhong, Z., Highly efficacious and targeted chemotherapy of human lung cancer by $A_3\beta_1$ integrin specific, redox-responsive and reversibly crosslinked polymersomes. *J. Controlled Release* **2017**, *259*, e164.

80. Meng, H.; Zou, Y.; Zhong, P.; Meng, F.; Zhang, J.; Cheng, R.; Zhong, Z., A smart nano-prodrug platform with reactive drug loading, superb stability, and fast responsive drug release for targeted cancer therapy. *Macromol. Biosci.* **2017**, *17*, 1600518.

81. Song-Qing, Z.; Guiju, H.; Xun-Hui, X.; Shu-Ming, K.; Na, L.; Zong-Quan, W., Synthesis of redox-responsive core cross-linked micelles carrying optically active helical poly(phenyl isocyanide) arms and their applications in drug delivery. *ACS Macro Lett.* **2018**, 1073-1079.

82. Zou, Y.; Wei, Y.; Sun, Y.; Bao, J.; Yao, F.; Li, Z.; Meng, F.; Hu, C.; Storm, G.; Zhong, Z., Cyclic RGD-functionalized and disulfide-crosslinked iodine-rich polymersomes as a robust and smart theranostic agent for targeted CT imaging and chemotherapy of tumor. *Theranostics* **2019**, *9*, 8061-8072.

83. Li, Y.; Xiao, K.; Zhu, W.; Deng, W.; Lam, K. S., Stimuli-responsive cross-linked micelles for on-demand drug delivery against cancers. *Adv. Drug Delivery Rev.* **2014**, *66*, 58-73.

84. Zhang, Q.; Na, R. K.; Oh, J. K., Recent advances in stimuli-responsive degradable block copolymer micelles: synthesis and controlled drug delivery applications. *Chem. Commun.* **2012**, *48*, 7542-7552.

85. Shu, X. Z.; Liu, Y.; Luo, Y.; Roberts, M. C.; Prestwich, G. D., Disulfide cross-linked hyaluronan hydrogels. *Biomacromolecules* **2002**, *3*, 1304-1311.

86. Li, Y.; Lokitz, B. S.; Armes, S. P.; McCormick, C. L., Synthesis of reversible shell cross-linked micelles for controlled release of bioactive agents. *Macromolecules* **2006**, *39*, 2726-2728.

87. Yan, L.; Wu, W.; Zhao, W.; Qi, R.; Cui, D.; Xie, Z.; Huang, Y.; Tong, T.; Jing, X., Reduction-sensitive core-cross-linked mPEG–poly(ester-carbonate) micelles for glutathione-triggered intracellular drug release. *Polym. Chem.* **2012**, *3*, 2403-2412.

88. Lin, W.; Ma, G.; Kampf, N.; Yuan, Z.; Chen, S., Development of long-circulating zwitterionic cross-linked micelles for active-targeted drug delivery. *Biomacromolecules* **2016**, *17*, 2010-2018.

89. Ding, Y.; Du, C.; Qian, J.; Zhou, L.; Su, Y.; Zhang, R.; Dong, C.-M., Tumor pH and intracellular reduction responsive polypeptide nanomedicine with a sheddable PEG corona and a disulfide-cross-linked core. *Polym. Chem.* **2018**, *9*, 3488-3498.

Chapter 5 Conclusions and Future Outlooks

5.1 Conclusions

In this thesis, we demonstrate a microfluidic approach to manufacturing biological stimuli-responsive polymer nanoparticles (PNPs) with flow-tunable physicochemical and pharmacological characteristics. Compared to conventional self-assembly methods, microfluidics has shown added advantages of fast mixing and high-shear processing control over PNP structure and functions.[1] The effect of high shear on block copolymer self-assembly has been investigated previously in our group, including medically relevant formulations that physically encapsulate therapeutic agents.[2-6] However, these previously investigated formulations were not chemical-responsive in nature; the drug release depends solely on PNP size and crystallinity and thus is non-specific to cells. Stimuli-responsive degradation (SRD) strategy has been applied in polymer synthesis for assembling PNPs with on-demand drug release profiles.[7] In this thesis, we have investigated the effect of microfluidic high-shear processing on the formation and functions of PNPs involving SRD design.

The proof-of-concept stimuli-responsive copolymer investigated in this thesis forms "DualM" PNPs consisting of a hydrophilic poly(ethylene oxide) (PEO) block, a hydrophobic polymethacrylate block having disulfide pendants (PHMssEt), and a disulfide linkage as junction between hydrophilic and hydrophobic blocks (PEO-ss-PHMssEt). DualM PNPs exhibit biological glutathione (GSH)-responsivity since disulfide linkages within hydrophobic cores and at hydrophilic/hydrophobic interfaces are cleavable upon elevated GSH concentrations in tumor microenvironments. The PEO-ss-PHMssEt copolymer samples were provided by Arman Moini Jazani in the group of our collaborator

Prof. John Oh (Department of Chemistry and Biochemistry, Concordia University), and its self-assembly by conventional bulk methods has been previously investigated.[8]

We firstly investigated the effect of microfluidic flow rate on physicochemical properties of DualM PNPs that did not encapsulate drugs. By adjusting flow rate, we obtained various PNPs with sizes that are distinct with their self-assembly counterparts by bulk nanoprecipitation. Specifically, hydrodynamic sizes $d_{h,eff}$ of microfluidic PNPs are all larger than bulk PNPs and followed a trend that increased and then decreased with the manufacturing flow rate increased. Such nonmonotonic trend was attributed to the interplay of shear-induced coalescence and shear-induced breakup. Manufacturing flow rate also show strong effects on PNP morphologies and internal structures; we observed various shear-induced morphologies, including cylinders and multicompartment vesicles with complex internal structures. By quantitative analyses of the electron microscopic images of numerous shear-dependent morphologies, we obtained the most detailed mechanism to date of microfluidic PNP formation in the presence of flow-variable high shear. Based on the proposed mechanism, the morphological and internal structural varieties were attributed to the interplay of shear-induced coalescence, shear-induced breakup, and intraparticle rearrangement. The mechanism also revealed the inverse relationship between excess Gibbs free energy states G_{ex} to PNP internal structures (described by relative inner compartment area $RA_{compart}$). We further investigated the effect of flow rate on GSH-triggered degradation kinetics of DualM PNPs without drug encapsulation. We showed for the first time the location of chemically responsive groups within flow-directed PNPs determined the relative roles of size and internal structures in the resulting reaction kinetics. We monitored rates of PNP $d_{h,eff}$ and $RA_{compart}$ increase as

scales of junction and pendant disulfide cleavage kinetics, respectively. We showed that microfluidic high-shear processing control of size and internal structure could be applied to tune GSH responsivities of DualM PNPs. Specifically, flow-directed PNPs with smaller average sizes showed faster $d_{h,eff}$ increase, attributed to junction disulfide cleavage, and those with higher G_{ex} showered faster $RA_{compart}$ growth, attributed to pendant disulfide cleavage.

Next, we expanded our mechanistic study on the microfluidic formation and physicochemical properties of the PNPs without encapsulated drug to a new focus on microfluidic control of the pharmacological properties of the PNPs containing either an anticancer drug (paclitaxel, PAX) or a florescent drug surrogate (DiI). We firstly investigated the effect of encapsulated molecules on physicochemical properties of flow-directed DualM PNPs. PAX-loaded and DiI-loaded PNPs showed similar sizes, polydispersities, and morphologies with their non-drug-loaded counterparts under the same flow conditions, suggesting the rationale of applying the obtained process-structure relationships to PAX-PNPs and DiI-PNPs. We then investigated the effect of flow rate on pharmacological properties of DualM PNPs, including encapsulation efficiency, GSH-triggered release rate, MCF-7 cell uptake, cytotoxicity against MCF-7 (cancerous) and HaCaT (healthy), and relative difference in MCF-7 and HaCaT cytotoxicity. We found all of these properties increased linearly as flow-directed PNP size decreased, providing remarkably simple process-structure-property relationships. In addition, we showed the first time that microfluidic manufacturing improved encapsulation homogeneities within PNPs relative to bulk nanoprecipitation, with further improvements as the flow rate increases.

Finally, we summarized various design strategies of biological stimuli-responsive PNPs by reviewing recent literatures. We showed that the location and density of disulfide linkages within PNPs determined stimulus-triggered degradation pattern and kinetics, respectively. In addition, we showed various bottom-up approaches to tune PNP responsivities involving chemical processing, including formulation chemistry (copolymer composition) and intramolecular forces (preparation method). Along with the top-down microfluidic approach that had been demonstrated experimentally, we provided a more comprehensive understanding of process-structure-property relationships opening up vast possibilities for manufacturing smarter nanomedicines with controllable responsivities.

This thesis provides important insight of the role of high shear processing in stimuli-responsive PNP formation and its effect on functions; we demonstrate a remarkably simple process-structure-function relationship in which various important pharmacological properties linearly correlate to flow-tunable PNP hydrodynamic size. These results highlight the potential of flow-directed shear processing in microfluidics for providing controlled manufacturing routes to smart nanomedicines optimized for specific therapeutic application. Moreover, unlike the conventional manufacturing approaches for stimuli-responsive PNPs in which formulation optimization depends on the redesign of copolymer synthesis and processing conditions, the microfluidic approach provides a convenient handle for PNP structure-function manipulation simply by tuning manufacturing flow rate. Such convenience allows preparation of smart nanomedicine with high time efficiency, high reproducibility, and ease of high throughput optimization of specific functions, which is of great importance in the future translational research towards clinical trials.

5.2 Future Outlooks

The current stage of *in vitro* evaluation of DualM PNPs provides a complete study from molecular-level drug diffusion to cell propagation and death on the micron scale. A future step in developing microfluidic formulations is extending the study to animal tests in the macroscale, which will be important for moving the microfluidic strategy closer to clinical trials. A series of pharmacological properties, including biodistribution, pharmacokinetics, and antitumor efficacy, should be investigated in xenograft models to better evaluate the *in vivo* performances of microfluidic formulations. However, a challenge that needs to be overcome before actual *in vivo* studies is the polydisperse size distribution and morphology composition presented in our current microfluidic formulations. Morphologies with large size, such as multicompartment vesicles (d > 1 000 nm) formed at Q = 200 μL/min, would not be suitable for *in vivo* experiments since they would be rapidly cleared by reticuloendothelial system. To overcome such problem, morphology purification and size filtration procedures prior to *in vivo* experiments should be developed. On the other hand, we could further optimize various chemical parameters (water content, copolymer composition, and solvent type, etc.) and processing parameters (flow rate, and microfluidic reactor design) of the manufacturing condition to precisely tune PNP structure towards modal size distribution and pure morphology. For example, an intermediate flow rate between Q = 100 μL/min and Q = 200 μL/min could be tested to manufacture PNPs with a pure morphology of spheres and the smallest hydrodynamic size, which should also show optimized therapeutics functions based on the linear size-property relations.

In the perspective of fundamental mechanistic studies, GSH-triggered disulfide cleavage kinetics within DualM PNPs is worth investigating further. However, we attributed increases in $d_{h,eff}$ and $RA_{compart}$ to junction and pendant disulfide cleavages, respectively. We could not deny that increases in $d_{h,eff}$ and $RA_{compart}$ also include other kinetic contributions from numerous processes on different time scales, including polymer and particle diffusion, phase separation, and particle coalescence. Therefore, current DLS and TEM analyses on $d_{h,eff}$ and $RA_{compart}$ do not directly provide reaction kinetics for the junction and pendant cleavage reactions, respectively. To quantitatively monitor the cleavage of junction and pendant disulfide linkages as a function of incubation time with GSH, analytical techniques such as GPC and ^{1}H NMR that allow for the characterization of degraded products can be used.[9] Evolution of characteristic peaks belong to degraded products should quantitatively reveal the disulfide cleavage kinetics.[9] However, purification procedures of the degraded products should be established prior to chemical analysis.

The effect of responsive disulfide location on microfluidic PNP degradation kinetics is also of interest. A mechanistic study based on block copolymers with similar composition with PEO-ss-PHMssEt but have single disulfide location will address the question. PEO-*b*-PHMssEt copolymer with junction disulfides alone has been synthesized in our collaborator Prof. John Oh's group, and its self-assembly by bulk method and stimulus-triggered degradation has been demonstrated,[10] which gives us preliminary understanding on the degradation kinetics of bulk sample. The synthesis of PEO-ss-PHMEt copolymers with pendant disulfides alone should be studied first, and then microfluidic formation of PEO-*b*-PHMssEt and PEO-ss-PHMEt PNPs can be carried out. Similar

methodology of DLS and TEM analyses can be applied to monitor $d_{h,eff}$ and $RA_{compart}$ changes of microfluidic PNPs. Thus it becomes possible to identify the $d_{h,eff}$ increase due to junction cleavages and the $RA_{compart}$ increase due to pendant cleavages, and these results should improve our understanding of degradation kinetics of microfluidic DualM PNPs with dual locations of disulfides. We should have conducted such study by visiting Prof. John Oh's lab and preparing the copolymer materials there. However, the trip has to be cancelled due to the COVID-19 travel restrictions and social distancing policies.

5.3 References

1. Karnik, R.; Gu, F.; Basto, P.; Cannizzaro, C.; Dean, L.; Kyei-Manu, W.; Langer, R.; Farokhzad, O. C., Microfluidic platform for controlled synthesis of polymeric nanoparticles. *Nano Lett.* **2008**, *8*, 2906-2912.

2. Wang, C.-W.; Sinton, D.; Moffitt, M. G., Flow-directed block copolymer micelle morphologies via microfluidic self-assembly. *J. Am. Chem. Soc.* **2011**, *133*, 18853-18864.

3. Xu, Z.; Lu, C.; Lindenberger, C.; Cao, Y.; Wulff, J. E.; Moffitt, M. G., Synthesis, self-assembly, and drug delivery characteristics of poly(methyl caprolactone-co-caprolactone)-b-poly(ethylene oxide) copolymers with variable compositions of hydrophobic blocks: combining chemistry and microfluidic processing for polymeric nanomedicines. *ACS Omega* **2017**, *2*, 5289-5303.

4. Bains, A.; Cao, Y.; Kly, S.; Wulff, J. E.; Moffitt, M. G., Controlling structure and function of polymeric drug delivery nanoparticles using microfluidics. *Mol. Pharmaceutics* **2017**, *14*, 2595-2606.

5. Chen, R.; Wulff, J. E.; Moffitt, M. G., Microfluidic processing approach to controlling drug delivery properties of curcumin-loaded block copolymer nanoparticles. *Mol. Pharmaceutics* **2018**, *15*, 4517-4528.

6. Cao, Y.; Silverman, L.; Lu, C.; Hof, R.; Wulff, J. E.; Moffitt, M. G., Microfluidic manufacturing of SN-38-loaded polymer nanoparticles with shear processing control of drug delivery properties. *Mol. Pharmaceutics* **2019**, *16*, 96-107.

7. Oh, J. K., Disassembly and tumor-targeting drug delivery of reduction-responsive degradable block copolymer nanoassemblies. *Polym. Chem.* **2019**, *10*, 1554-1568.

8. Chan, N.; Khorsand, B.; Aleksanian, S.; Oh, J. K., A dual location stimuli-responsive degradation strategy of block copolymer nanocarriers for accelerated release. *Chem. Commun.* **2013**, *49*, 7534-7536.

9. Aleksanian, S.; Khorsand, B.; Schmidt, R.; Oh, J. K., Rapidly thiol-responsive degradable block copolymer nanocarriers with facile bioconjugation. *Polym. Chem.* **2012**, *3*, 2138-2147.

10. Khorsand, B.; Lapointe, G.; Brett, C.; Oh, J. K., Intracellular drug delivery nanocarriers of glutathione-responsive degradable block copolymers having pendant disulfide linkages. *Biomacromolecules* **2013**, *14*, 2103-2111.

Appendix

Appendix A. Supporting Information for Chapter 2

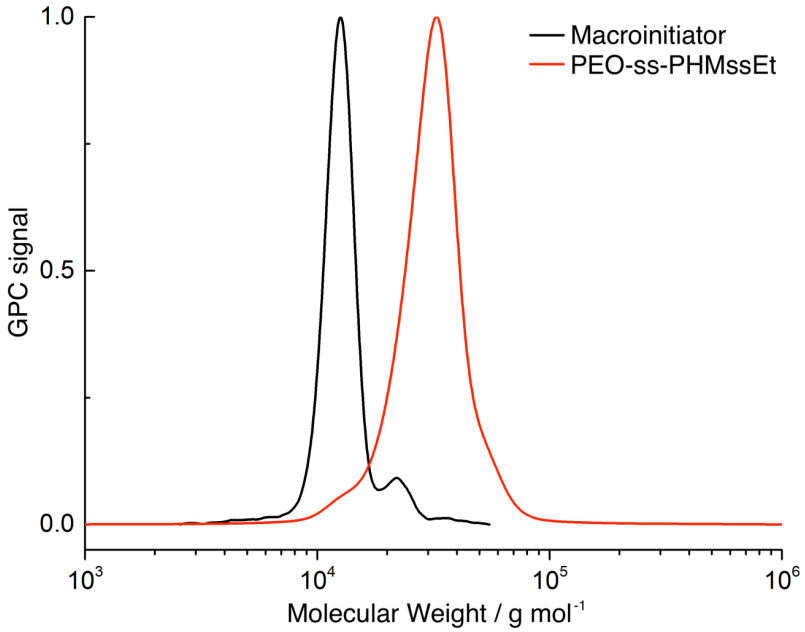

Figure A-1. GPC chromatograms of PEO-ss-PHMssEt block copolymers and PEO-ss-Br macroinitiators in DMF solutions, which was further used to determine the molecular weight distribution (M_w/M_n) of the resulting block copolymers.

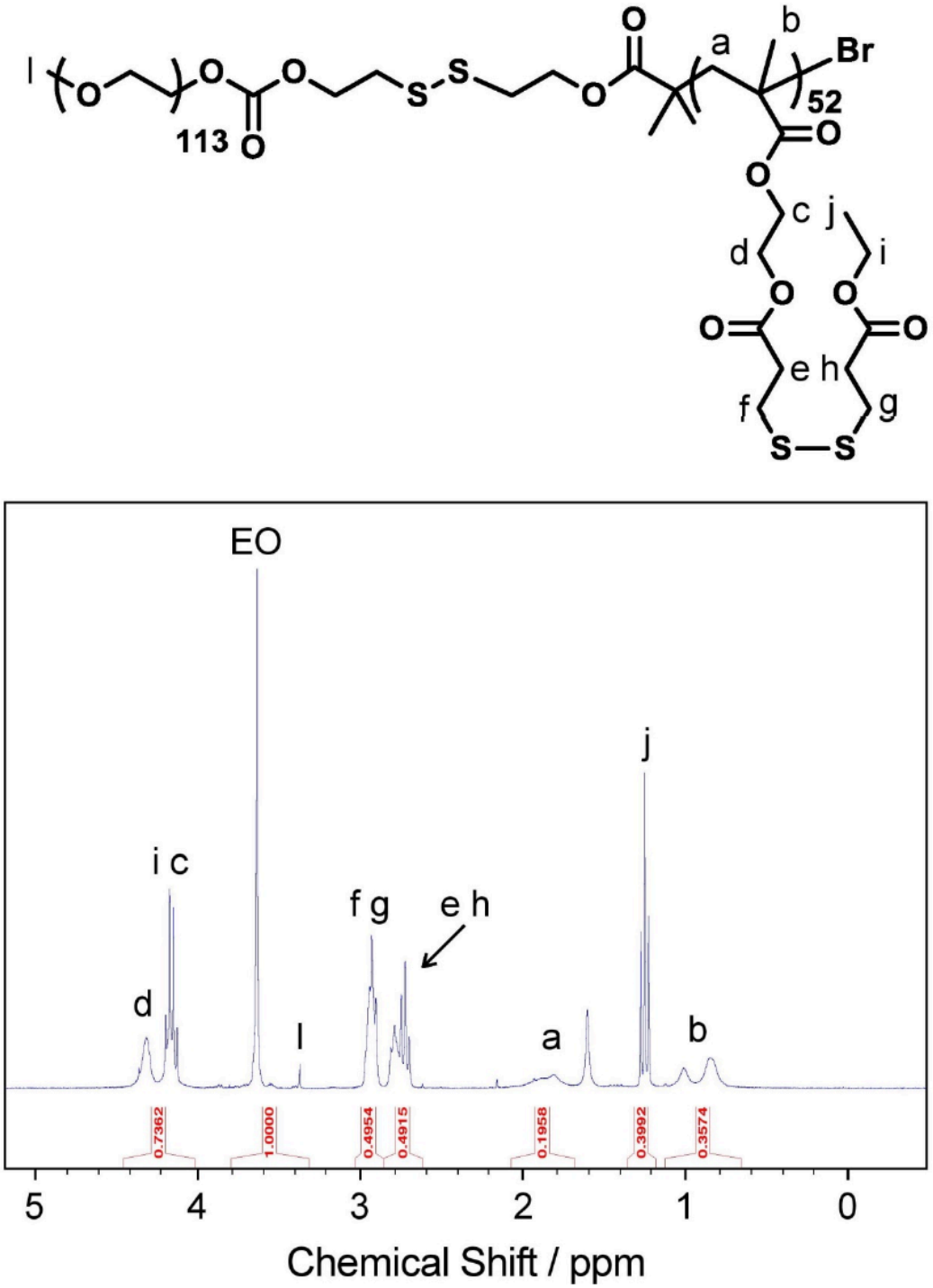

Figure A-2. ^{1}H NMR spectrum of PEO-ss-PHMssEt copolymers in $CDCl_3$ solution. The degree of polymerization (DP) was determined by the ratio between integration values of PEO and PHMssEt blocks.

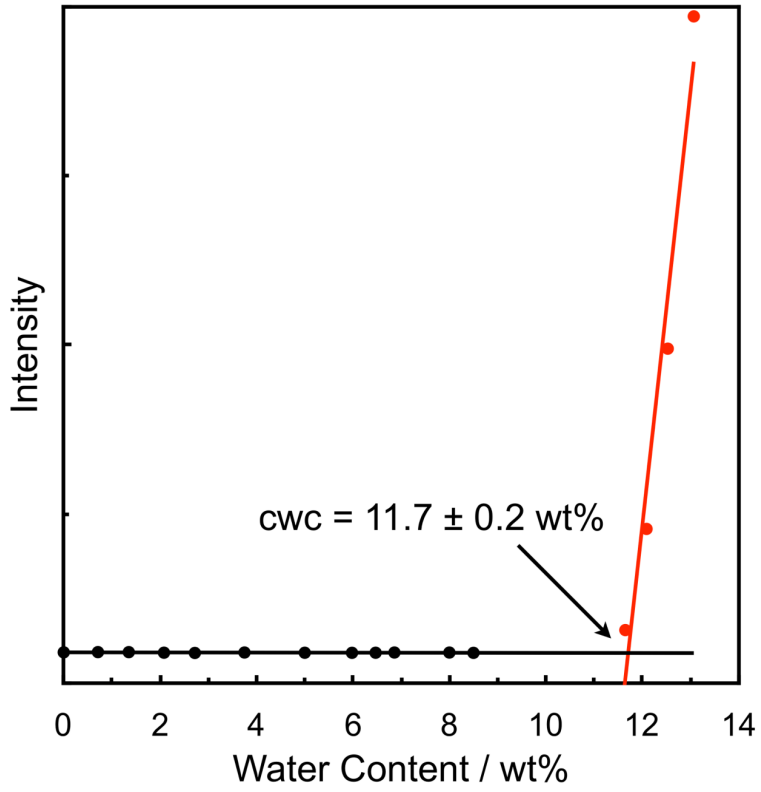

Figure A-3. SLS was performed to determine the critical water concentration (cwc) of 0.33 wt% PEO-ss-PHMssEt in DMF solution, which was further used for the determination of the water content for on-chip DualM PNP preparations (cwc + 10 wt%).

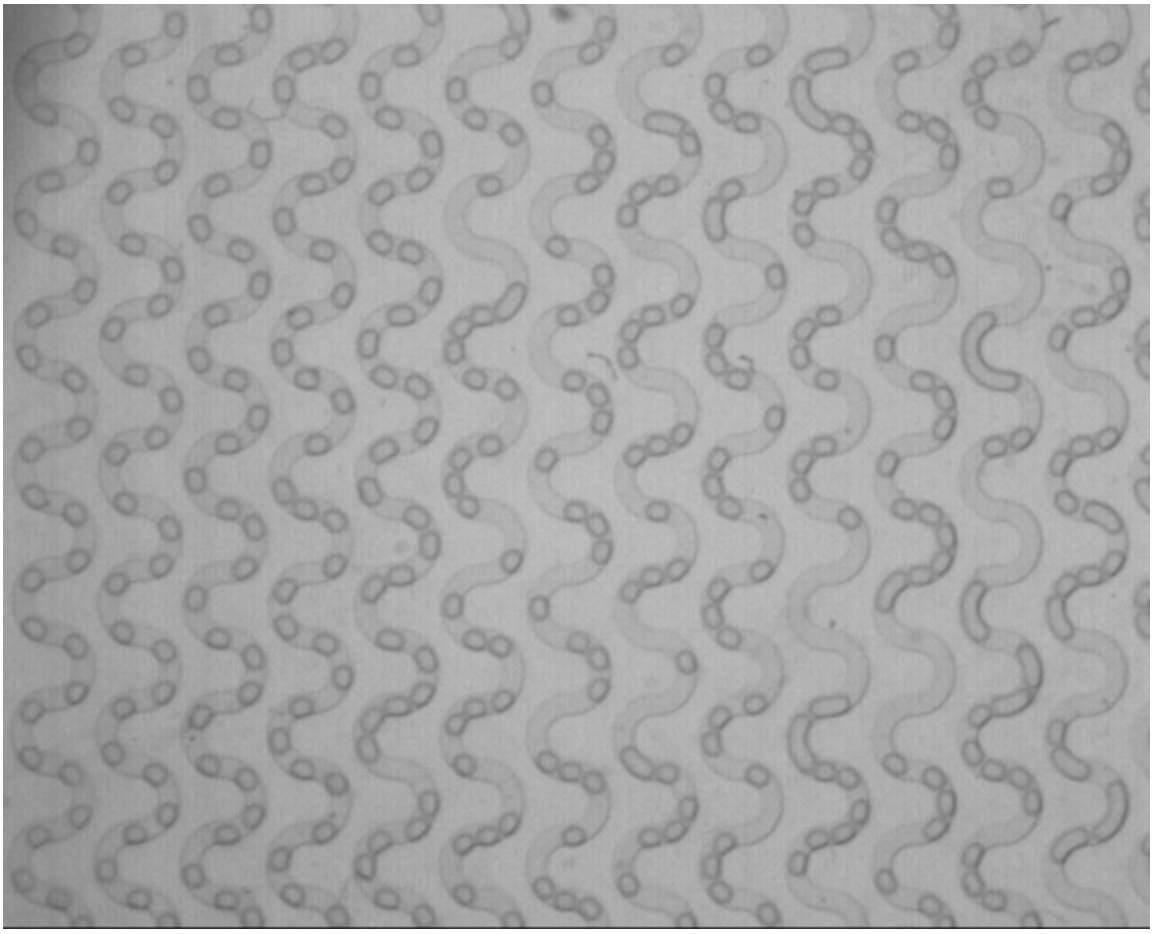

Figure A-4. Typical optical microscope image of the stable two-phase segmented flow within the microfluidic reactor, in which plugs with black edges are Ar bubbles.

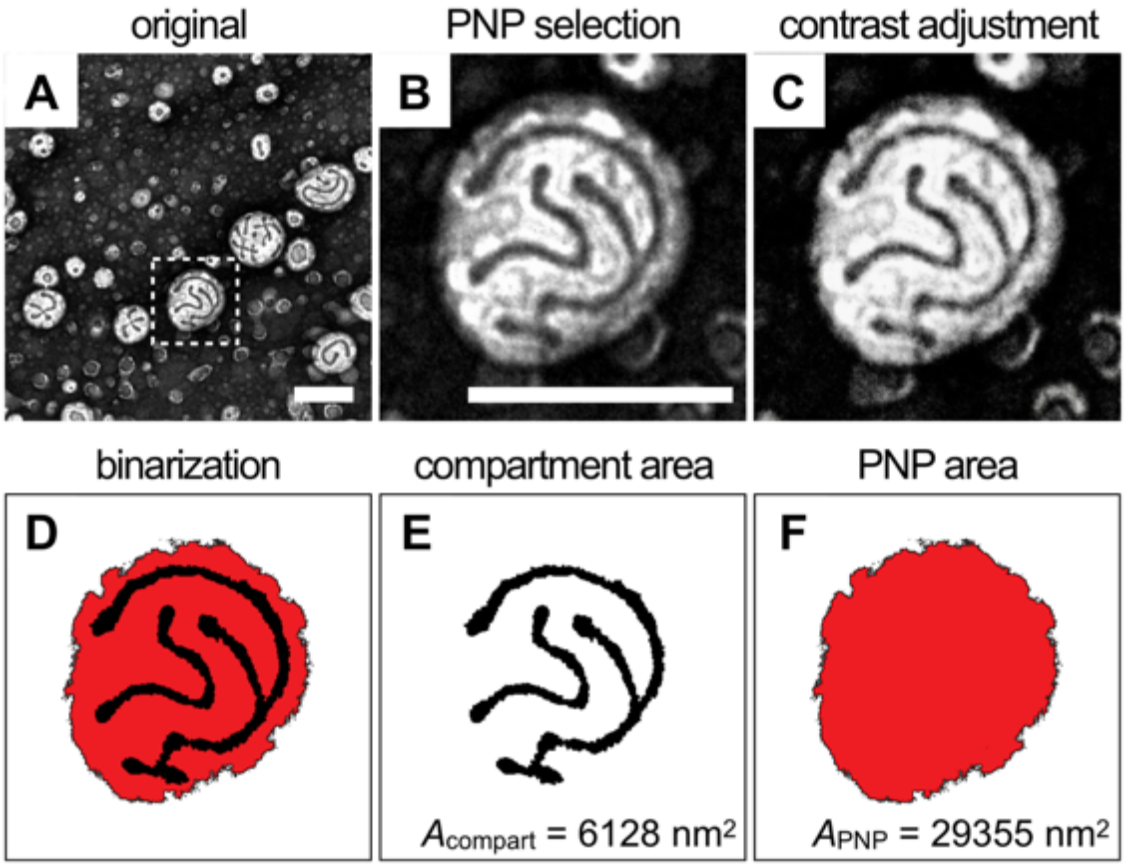

Figure A-5. Work flow of PNP relative compartment area determination by TEM image analysis. First, (A-B) a single PNP containing inner compartments was cropped from the main image; (C) contrast was then adjusted, and (D) the boundaries of the PNP and its internal compartments were defined using the ImageJ binarization function. Next, the areas of the inner compartment (E, $A_{compart}$) and the PNP (F, A_{PNP}) were determined using the measurement function in ImageJ. The value of $RA_{compart}$ for the individual PNP was calculated as $RA_{compart}$ (%) = $A_{compart}/A_{PNP}$ = 6128 nm^2 / 29355 nm^2 × 100% = 20.88%. Reported $RA_{compart}$ values represent averages calculated from $N \geqslant$ 50 PNPs containing compartments selected from at least 3 images taken in different regions of the TEM grid. Scale bar is 200 nm..

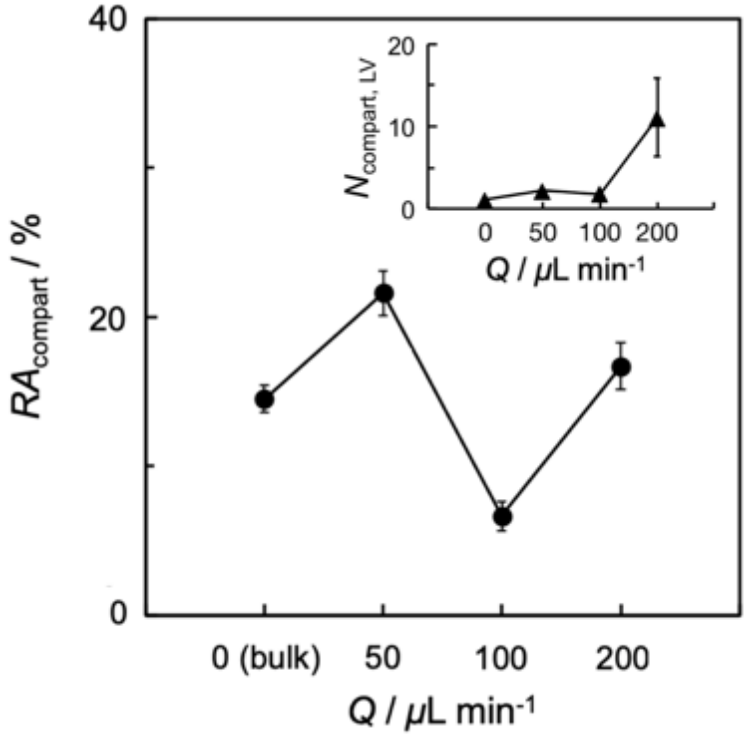

Figure A-6. Effect of preparation method and microfluidic flow rate on (main) the relative compartment area of DualM PNPs, and (inset) average number of compartments in LVs.

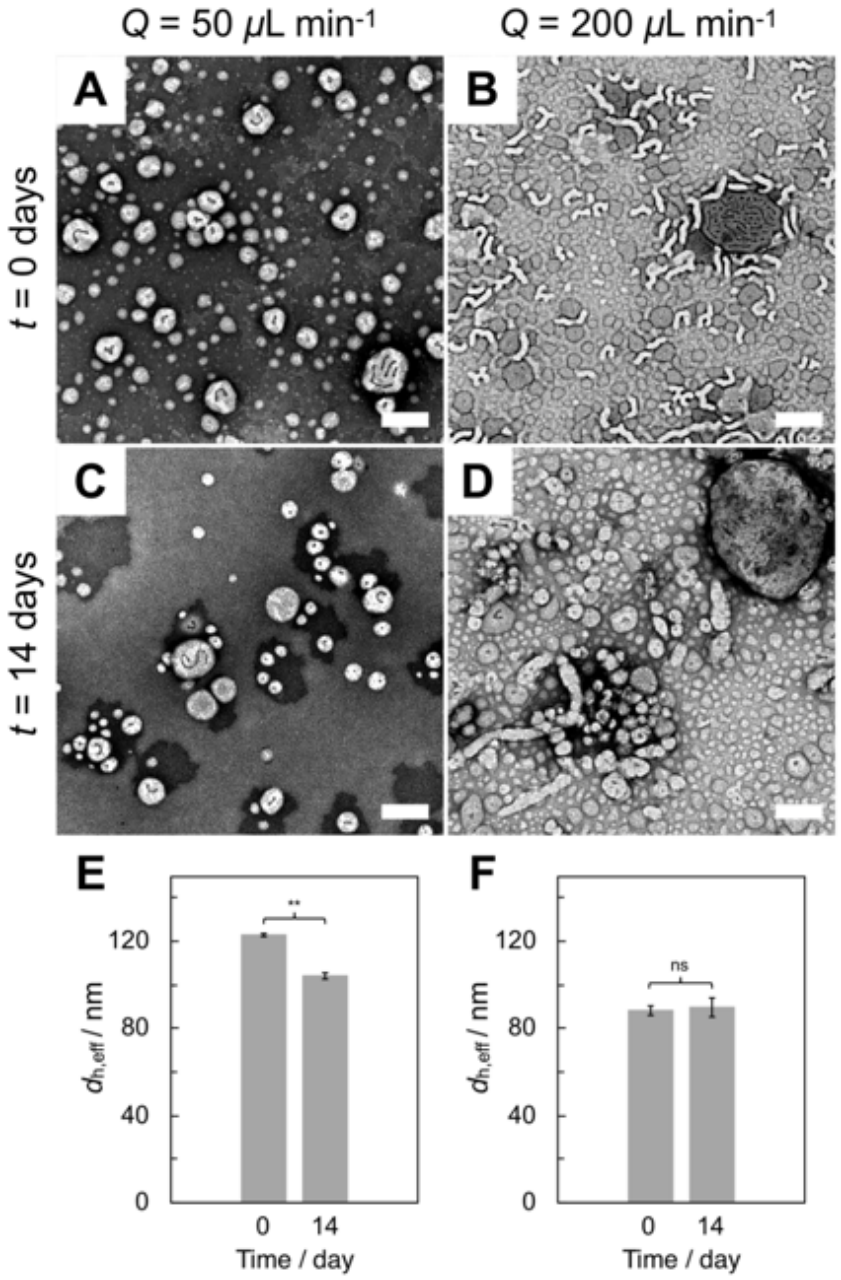

Figure A-7. Stability test of quenched DualM PNPs manufactured at the Q = 50 μL/min and Q = 200 μL/min flow rates. TEM images (A–D) were taken immediately after dialysis (t = 0 days) and two weeks after dialysis (t = 14 days) for the two samples. Corresponding hydrodynamic effective diameters ($d_{h,eff}$, E–F) were also measured from DLS cumulant analysis for the comparison. Statistical comparison between $d_{h,eff}$ at different time points are indicated ** (p<0.005), or ns (p>0.05). Experimental errors were calculated from three measurements for each sample. Scale bars are 200 nm in the TEM images.

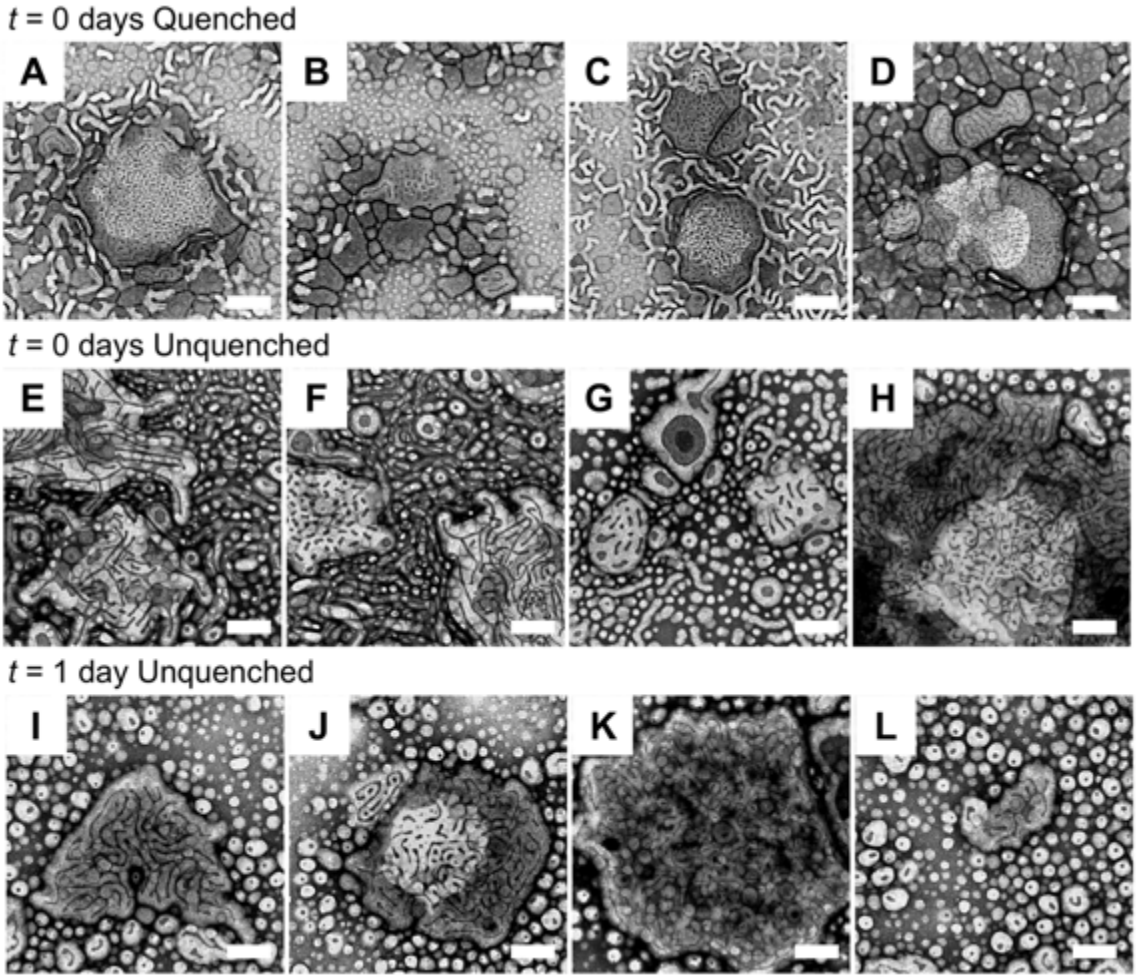

Figure A-8. Additional TEM images shown progression of LVs from discrete spherical (A–D) to discrete cylindrical (E–H) to highly interconnected cylindrical compartments (I–L). Scale bars are 200 nm in the TEM images.

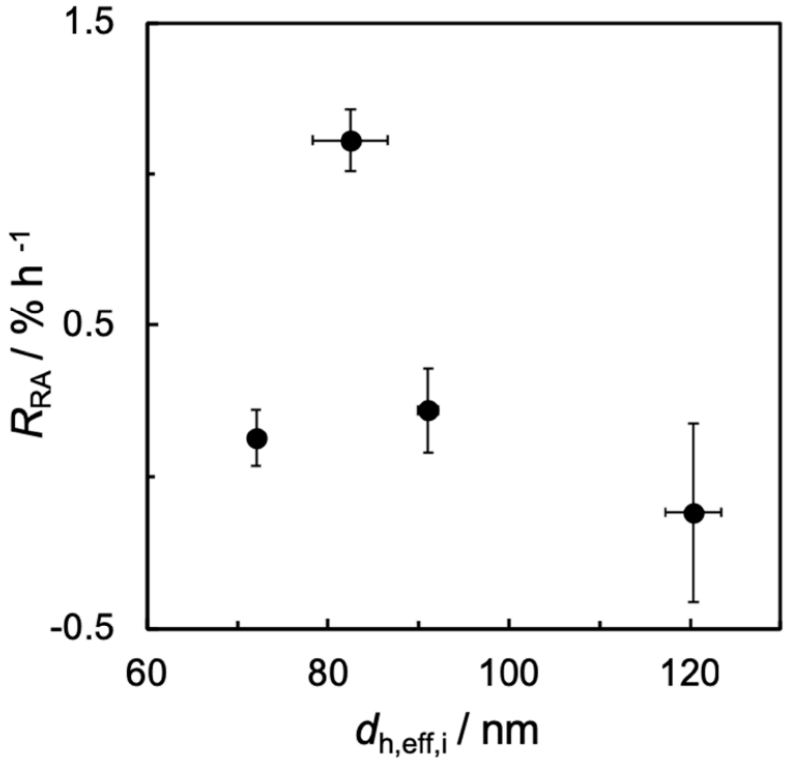

Figure A-9. Average GSH-triggered growth rate of relative compartment area, R_{RA} vs. initial effective hydrodynamic diameter, $d_{h,eff,i}$. Unlike the linear plot of negative slope for R_{RA} vs. $RA_{compart,i}$ (Figure 11B), no obvious trend is found in the above plot.

Table A-1. Actual Flow Rates of Various Preparations of PEO-ss-PHMssEt PNPs within the Two-Phase Segmented Microfluidic Reactor Described in the Main Text

Nominal flow rate	Q_{gas} **(**μ**L/min)**	Q_{liq} [a] **(**μ**L/min)**	Q_{gas}/Q_{liq}	Q_{total} **(**μ**L/min)**
50 μL/min				
Prep #1	25	25	1.00	50
Prep #2	27	25	1.08	52
Prep #3	24	25	0.96	49
100 μL/min				
Prep #1	51	50	1.02	101
Prep #2	52	50	1.04	102
Prep #3	55	50	1.10	105
200 μL/min				
Prep #1	88	100	0.88	188
Prep #2	93	100	0.93	193
Prep #3	114	100	1.14	214

[a] The liquid flow rate was assumed to be the sum of three flow-rate readings shown on the syringe pumps.

Table A-2. Statistical Comparisons between Polydispersity Data in Figure 2-3A

Comparison pair		***p*-value**	**Result**[a]
Bulk	Q = 50 μL/min	0.011304	*
Q = 50 μL/min	Q = 100 μL/min	0.42273	ns
Q = 50 μL/min	Q = 200 μL/min	0.33470	ns
Q = 100 μL/min	Q = 200 μL/min	0.20508	ns

[a] * indicates $p < 0.05$ and ns indicates $p > 0.05$.

Table A-3. Time-Dependent Morphologies[a] and Mean Dimensions[b] for Quenched DualM PNPs Manufactured On-Chip at Q = 50 μL/min and Q = 200 μL/min

Q (μL/min)	Morphology	t = 0 days		t = 14 days	
		Dimension / nm	Number Percentage / %	Dimension / nm	Number Percentage / %
50	S	62 ± 4	77 ± 2	63 ± 6	65 ± 5
	SV	71 ± 3	14.1 ± 0.6	69 ± 4	22 ± 3
	LV	143 ± 2	9 ± 3	120 ± 27	13 ± 7
200	S	49 ± 2	61 ± 5	47 ± 2	60 ± 4
	SV	67 ± 4	1.4 ± 0.2	61 ± 3	8 ± 2
	LV	249 ± 36	4.2 ± 0.5	231 ± 18	7.1 ± 0.9
	C	34 ± 2	35 ± 4	40 ± 4	25 ± 4

[a]Morphologies are indicated as S (spheres), SV (small vesicles), LV (large vesicles), or C (cylinders). [b]Dimensions refer to sphere and small vesicle diameters and cylinder widths determined from TEM images. For non-spherical large vesicles, dimensions refer to the longest measurable internal distance. Standard errors are reported to represent the uncertainty of mean dimensions determined from triplicate images in different regions of the TEM grid.

Table A-4. Statistical Comparisons between $d_{h,eff}$ Data in Figure 2-11A

Comparison pair		***p*-value**	**Result**[a]
Bulk			
t = 0 h	t = 4 h	0.0000010586	**
t = 4 h	t = 24 h	0.029273	*
***Q* = 50 μL/min**			
t = 0 h	t = 4 h	0.83924	ns
t = 4 h	t = 24 h	0.89779	ns
***Q* = 100 μL/min**			
t = 0 h	t = 4 h	0.00042115	**
t = 4 h	t = 24 h	0.0000049091	**
***Q* = 200 μL/min**			
t = 0 h	t = 4 h	0.0073183	*
t = 4 h	t = 24 h	0.37961	ns

[a] * indicates $p < 0.05$, ** indicates $p < 0.005$, and ns indicates $p > 0.05$.

Appendix B. Supporting Information for Chapter 3

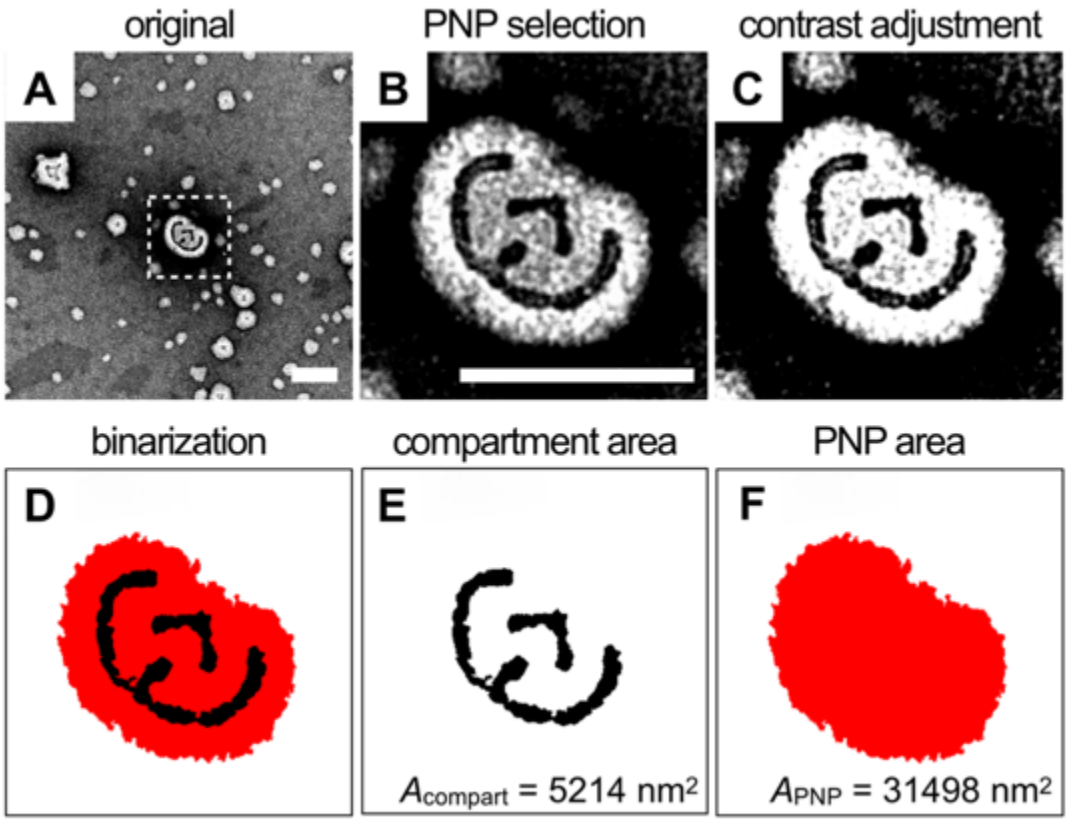

Figure B-1. Work flow of PNP relative compartment area determination by TEM image analysis, in which (A–B) single PNP containing inner compartments was cropped from the main image, (C) contrast was then adjusted, and (D) the binaries of the PNP and its internal compartments were defined using imageJ binarization function. The areas of the inner compartment ($A_{compart}$, E) and the PNP (A_{PNP}, F) were measured using measurement function in imageJ. The final value of $RA_{compart}$ was calculated as $RA_{compart}$ (%) = $A_{compart}/A_{PNP}$ = 5214 nm^2 / 41498 nm^2 × 100% = 16.55%. Reported $RA_{compart}$ values represent averages calculated from $N \geqslant 50$ PNPs containing compartments selected from at least 3 images taken in different regions of the TEM grid. Scale bar is 200 nm.

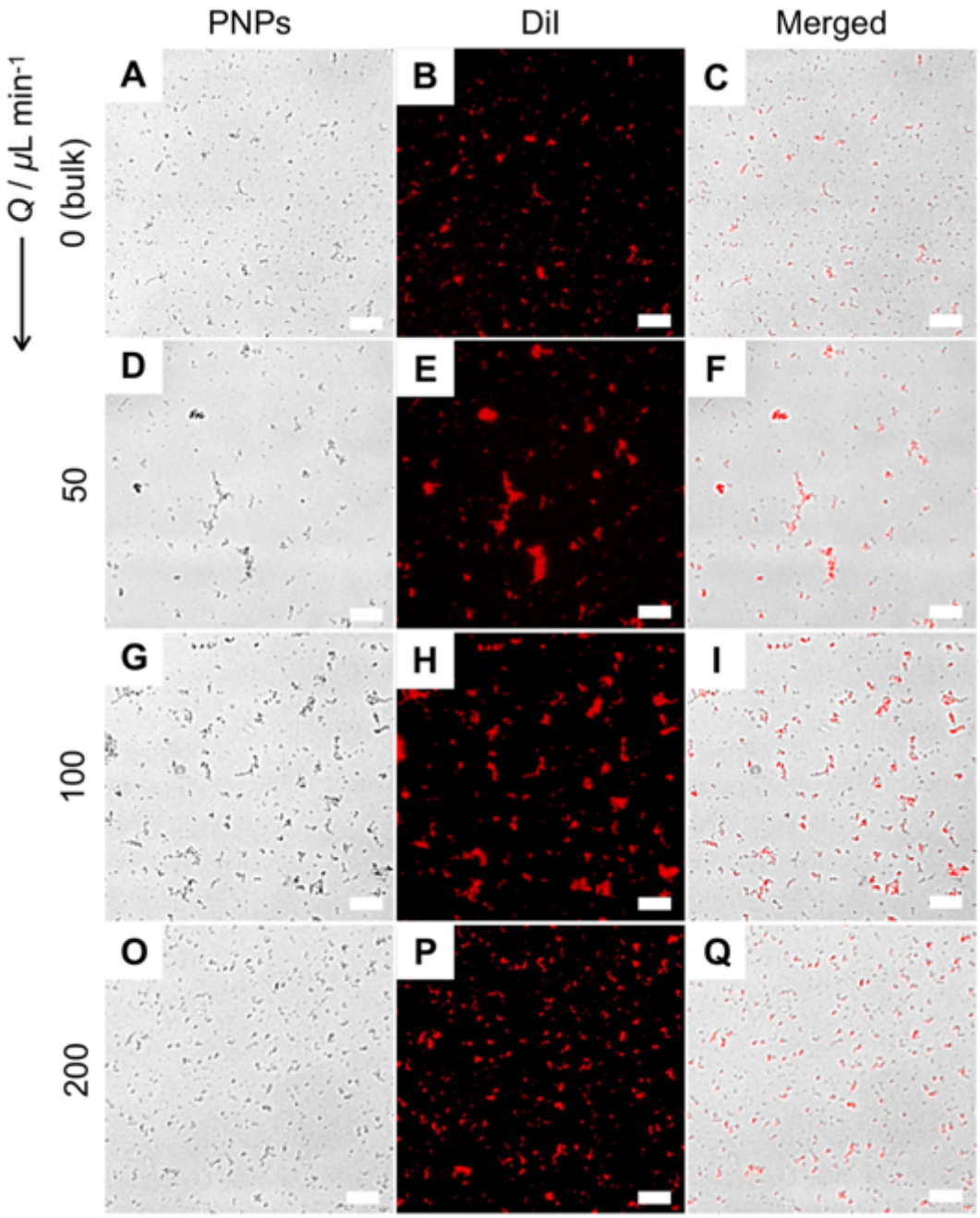

Figure B-2. Original data for Figure 7A-D. Optical microscopy images of DiI-PNPs manufactured using microfluidics various flow rates or bulk nanoprecipitation are shown in the first panel (A, D, G, O). Associated fluorescence images are shown in the second panel (B, E, H, P), where DiI emission is shown in red. The overlap between red regions of DiI emission and dark regions of PNPs processed by the imaging software is shown in the third panel (C, F, I, Q). Scale bars are 20 μm.

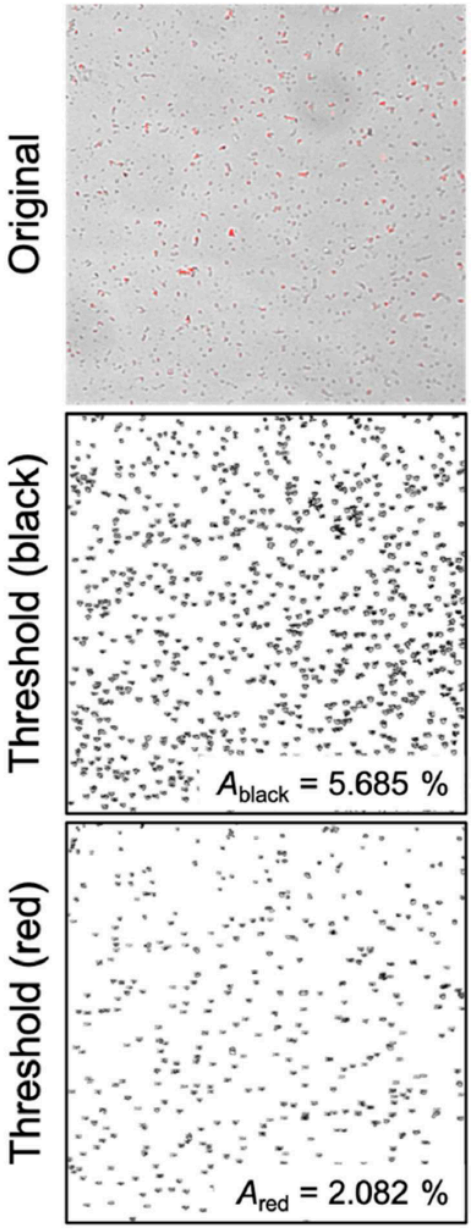

Figure B-3. Work flow of *EH* determination using ImageJ. Color threshold function was used to define the dark and red regions of the merged images, while measurement function was used to measure the areal percentage of the above regions. The final value of *EH* was calculated as $EH = A_{red}/A_{black}$ = 2.082% / 5.685% × 100% = 36.62%.

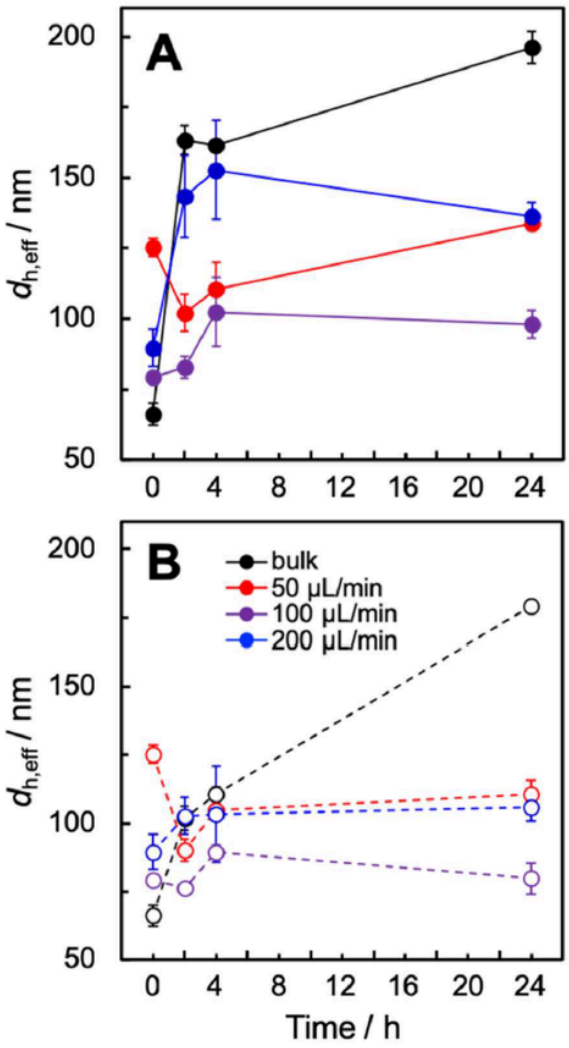

Figure B-4. Changes in hydrodynamic effective diameters ($d_{h,eff}$) of various PAX-PNP formulations during first 24 h of PAX release experiments under perfect sink conditions at 37ºC using release media consisting of (A) PBS + 10 mM GSH and (B) PBS without GSH.

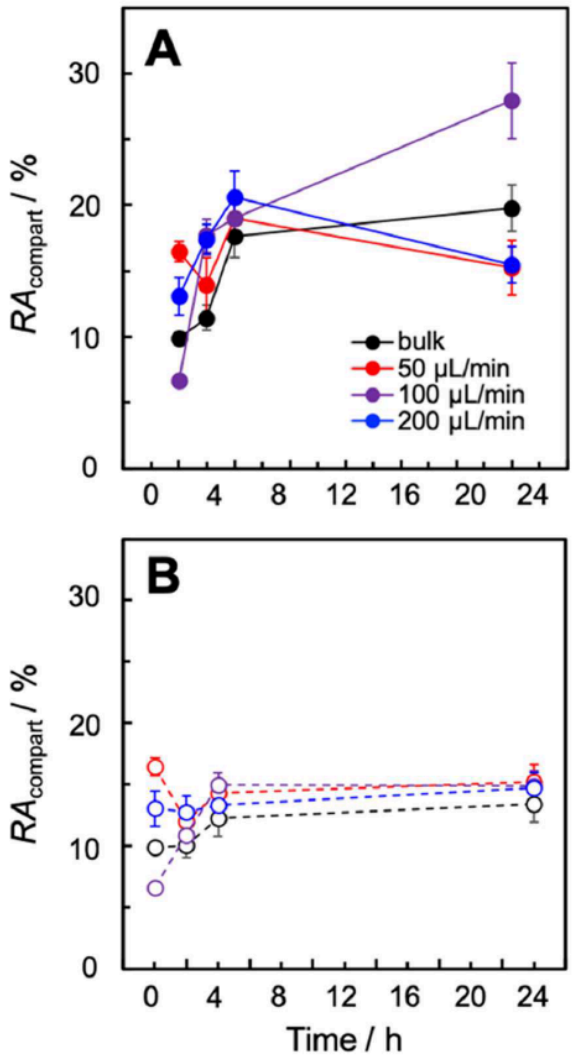

Figure B-5. Changes in hydrodynamic effective diameters ($RA_{compart}$) of various PAX-PNP formulations during first 24 h of PAX release experiments under perfect sink conditions at 37ºC using release media consisting of (A) PBS + 10 mM GSH and (B) PBS without GSH.

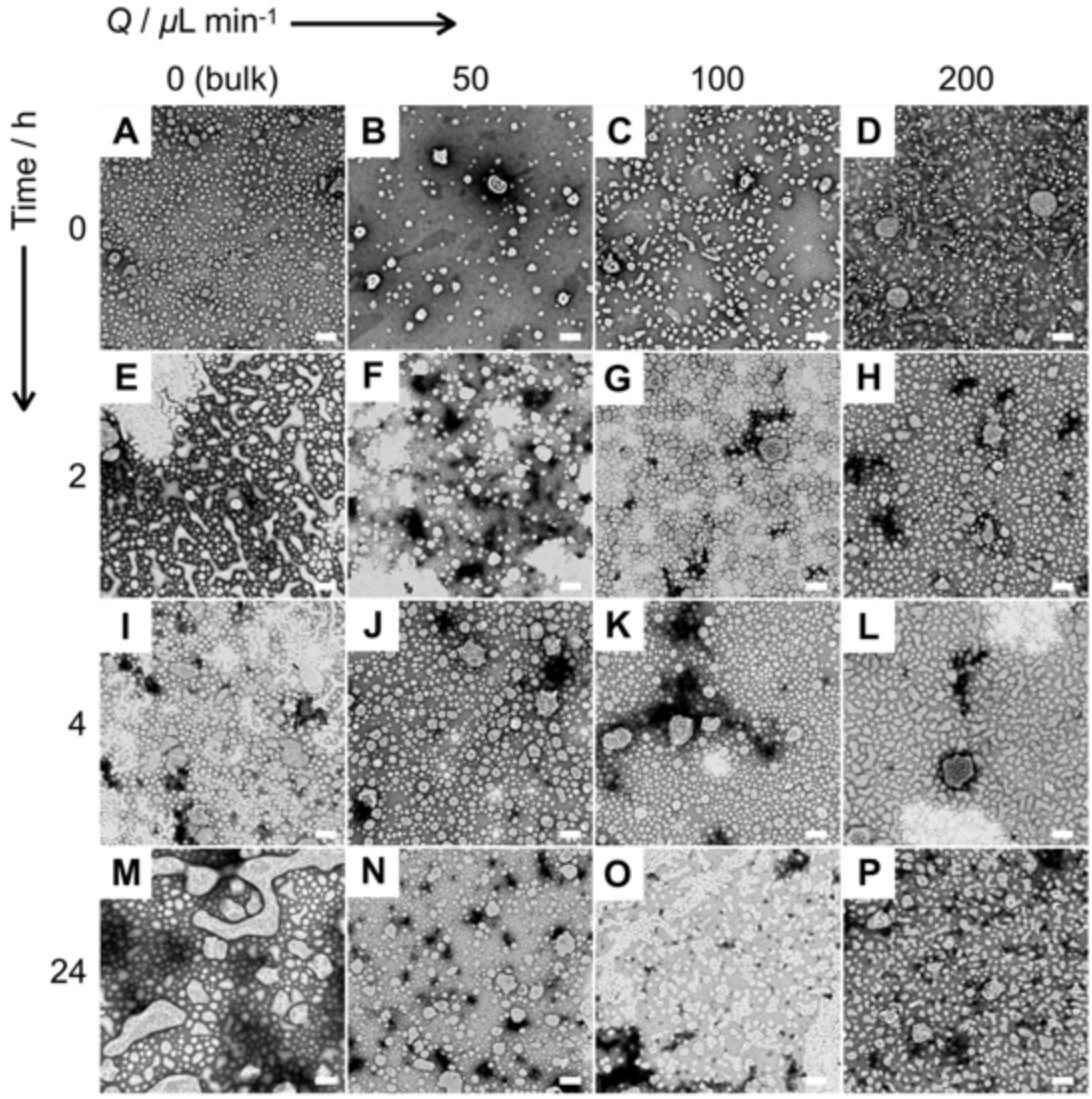

Figure B-6. TEM of PAX-PNPs during first 24 h of PAX release experiments under perfect sink conditions at 37ºC using release media consisting of PBS + 10 mM only (no GSH). Representative images of initial (t = 0) PAX-PNPs formed at (A) Q = 0 μL/min (bulk), (B) Q = 50 μL/min, (C) Q = 100 μL/min, and (D) Q = 200 μL/min and PAX-PNPs at three other time points of PAX release: (B−H) 2 h, (I−L) 4 h, and (M−P) 24 h. Scale bars are 200 nm.

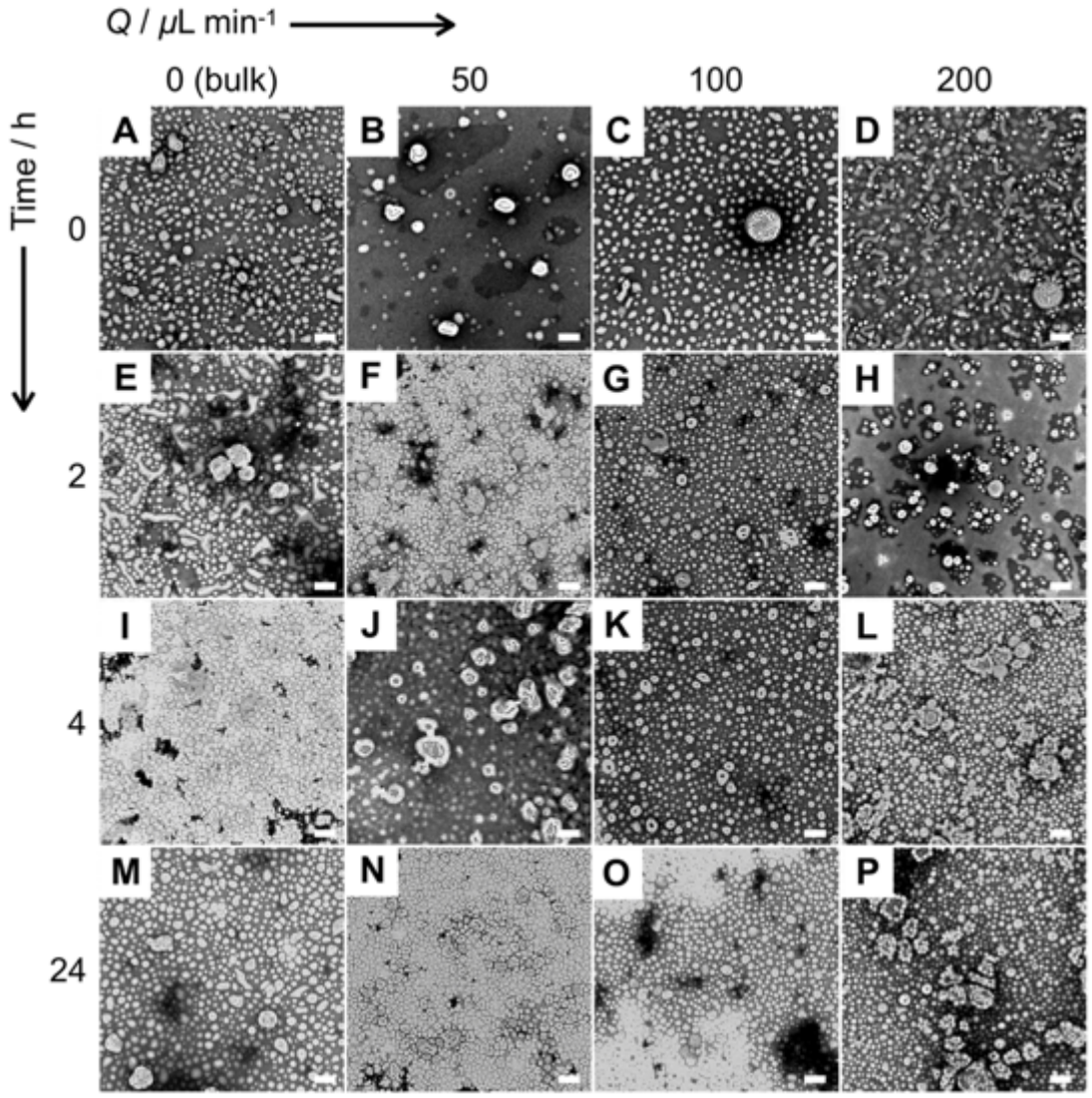

Figure B-7. TEM of PAX-PNPs during first 24 h of PAX release experiments under perfect sink conditions at 37ºC using release media consisting of PBS + 10 mM only (no GSH). Representative images of initial (t = 0) PAX-PNPs formed at (A) Q = 0 μL/min (bulk), (B) Q = 50 μL/min, (C) Q = 100 μL/min, and (D) Q = 200 μL/min and PAX-PNPs at three other time points of PAX release: (B−H) 2 h, (I−L) 4 h, and (M−P) 24 h. Scale bars are 200 nm.

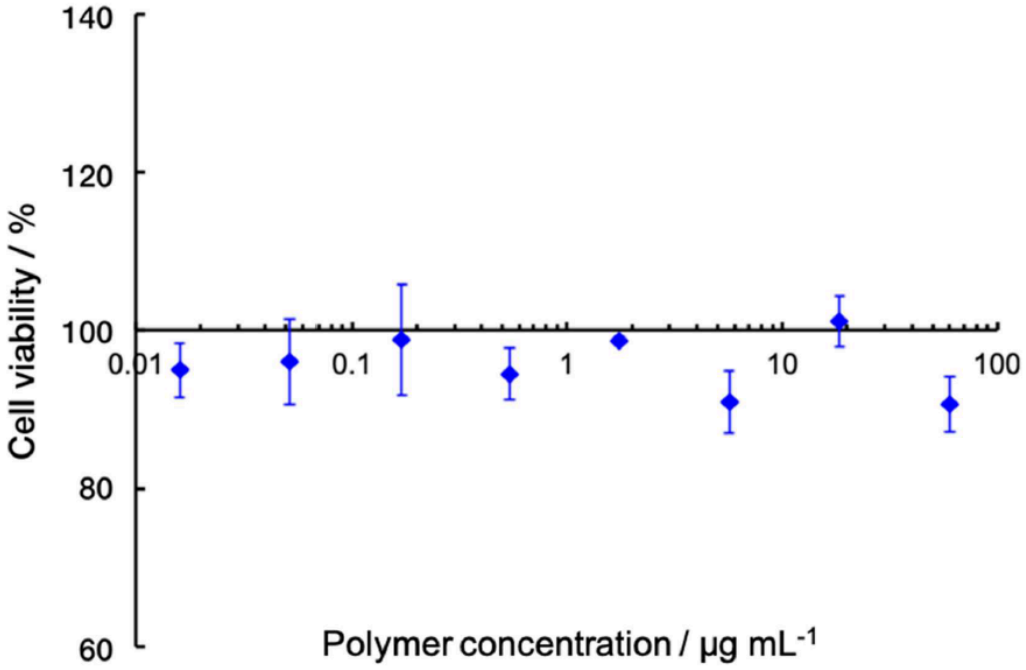

Figure B-8. HaCaT cell viability with various concentrations of empty PNPs (48 h incubation). Error bars were determined from triplicate PNP preparations.

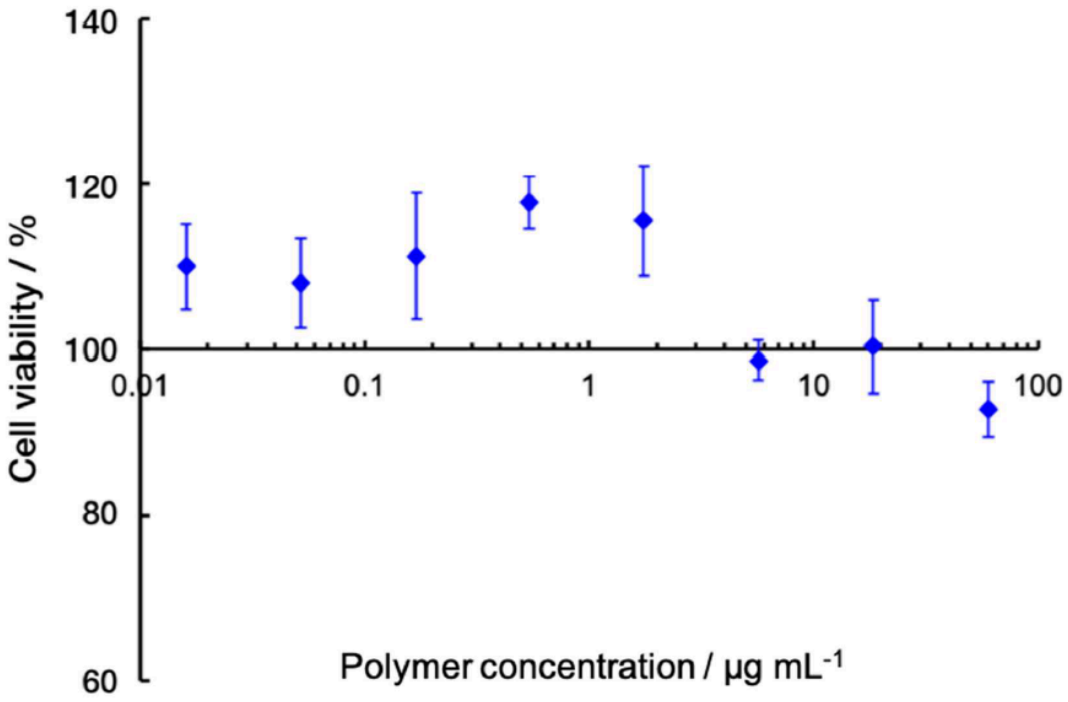

Figure B-9. MCF-7 cell viability with various concentrations of empty PNPs (48 h incubation). Error bars were determined from triplicate PNP preparations.

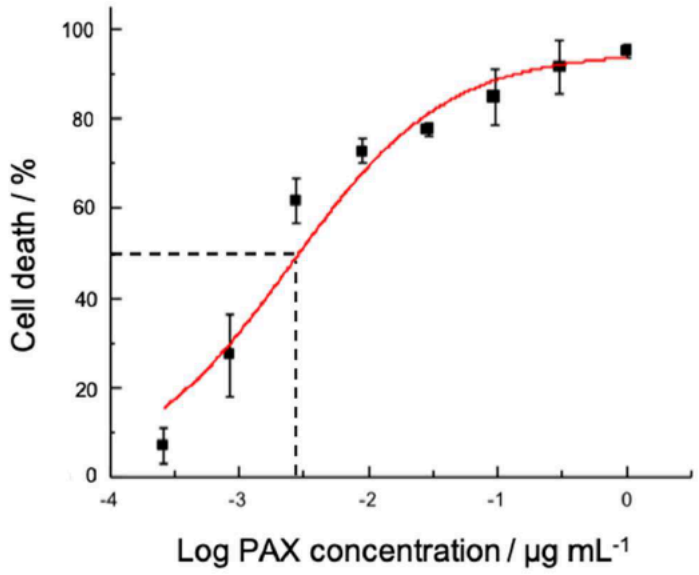

Figure B-10. HaCaT cell death vs. PAX concentration for free (unencapsulated) PAX. Data points represent mean data from triplicate PAX solution preparations. Solid line represents the best fit curve and dashed horizontal line indicates EC_{50} value.

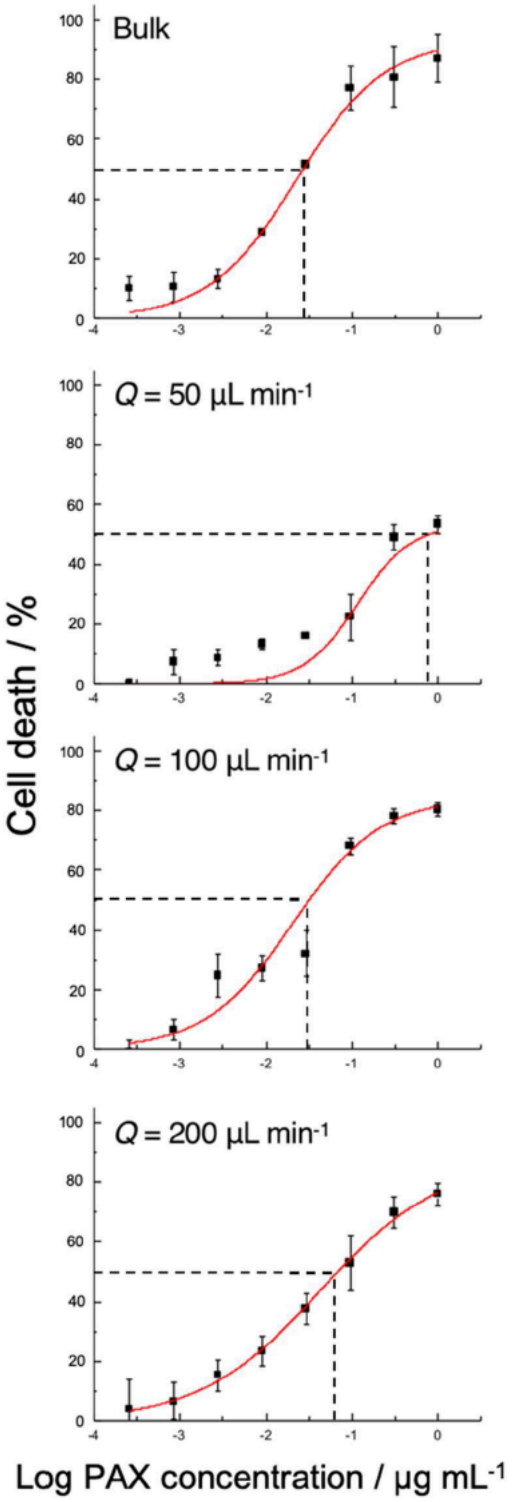

Figure B-11. HaCaT cell death vs. PAX concentration for various PAX-PNP formulations. Data points represent mean data from triplicate PAX-PNP preparations. Solid lines represent the best fit curves and dashed horizontal lines indicates EC_{50} values.

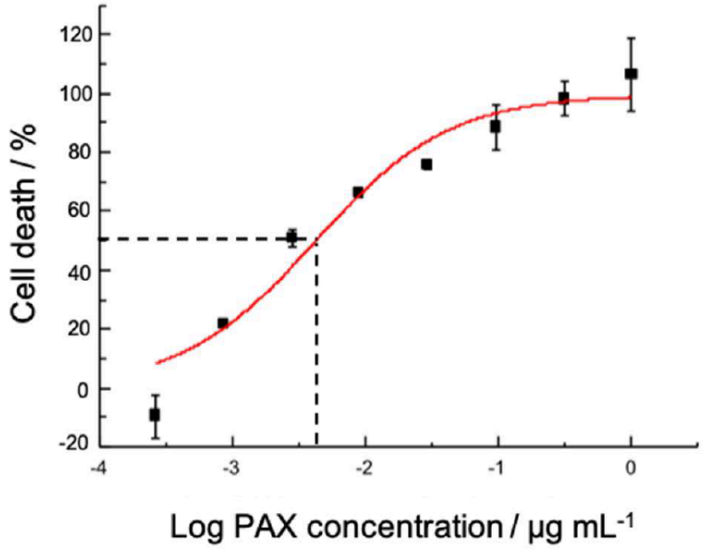

Figure B-12. MCF-7 cell death vs. PAX concentration for free (unencapsulated) PAX. Data points represent mean data from triplicate PAX solution preparations. Solid line represents the best fit curve and dashed horizontal line indicates EC_{50} value.

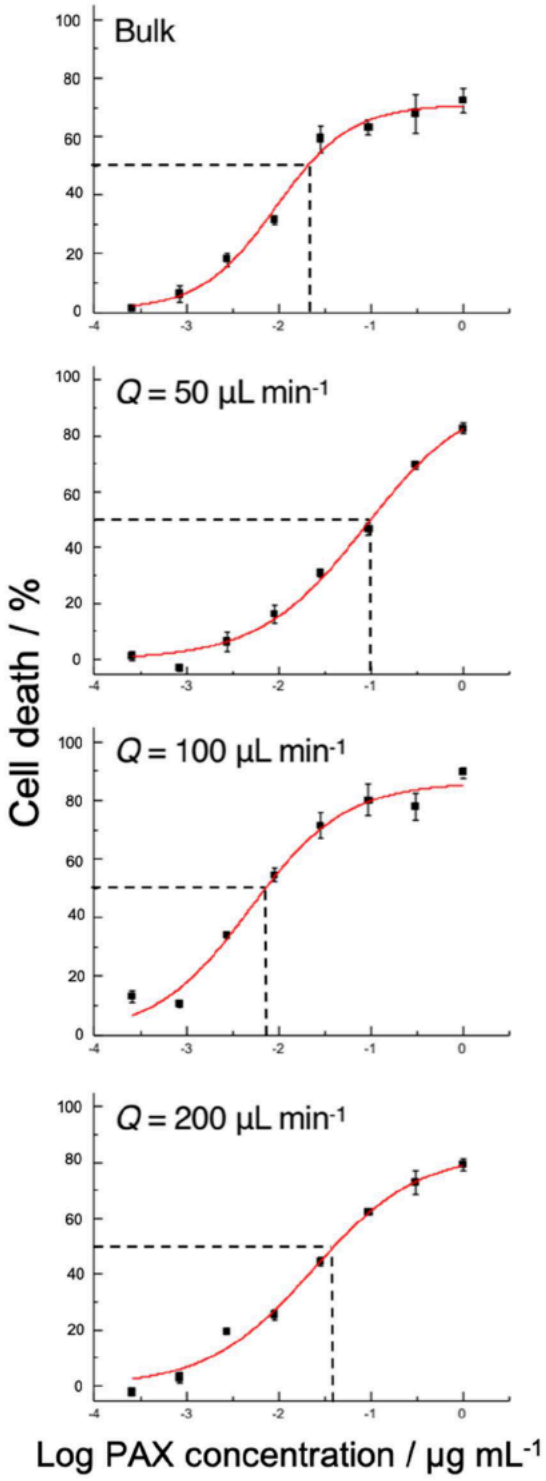

Figure B-13. MCF-7 cell death vs. PAX concentration for various PAX-PNP formulations. Data points represent mean data from triplicate PAX-PNP preparations. Solid lines represent the best fit curves and dashed horizontal lines indicates EC_{50} values.

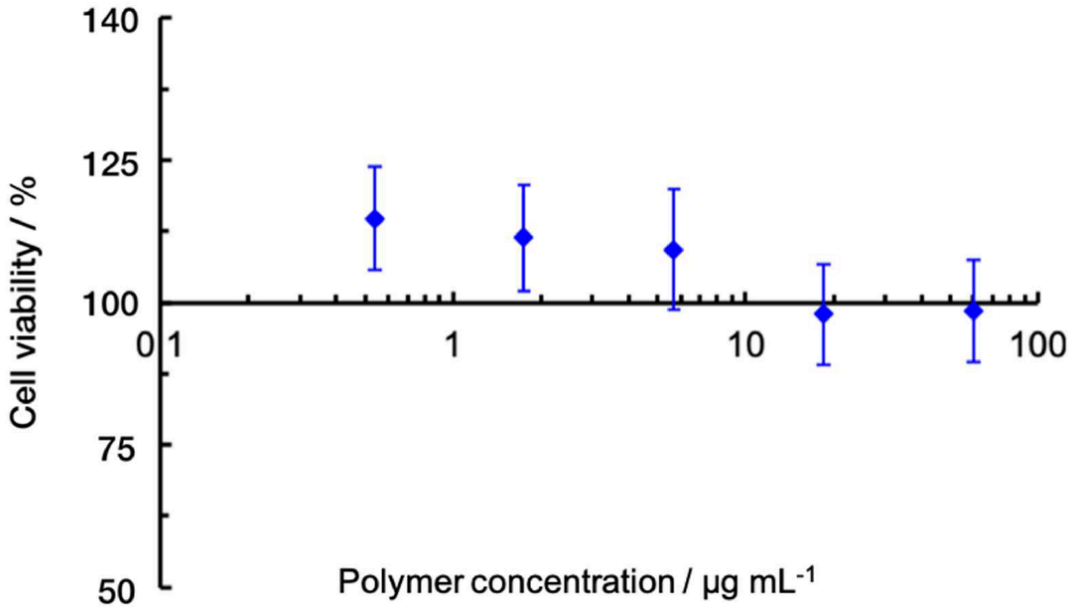

Figure B-14. MCF-7 + 10 mM GSH-OEt cell viability with various concentrations of empty PNPs (48 h incubation). Error bars were determined from triplicate PNP preparations.

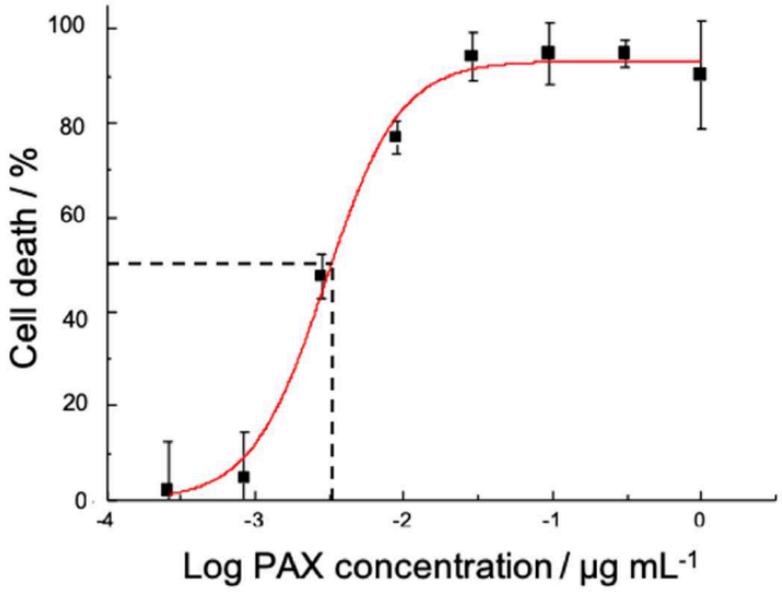

Figure B-15. MCF-7 + 10 mM GSH-OEt cell death vs. PAX concentration for free (unencapsulated) PAX. Data points represent mean data from triplicate PAX solution preparations. Solid line represents the best fit curve and dashed horizontal line indicates EC_{50} value.

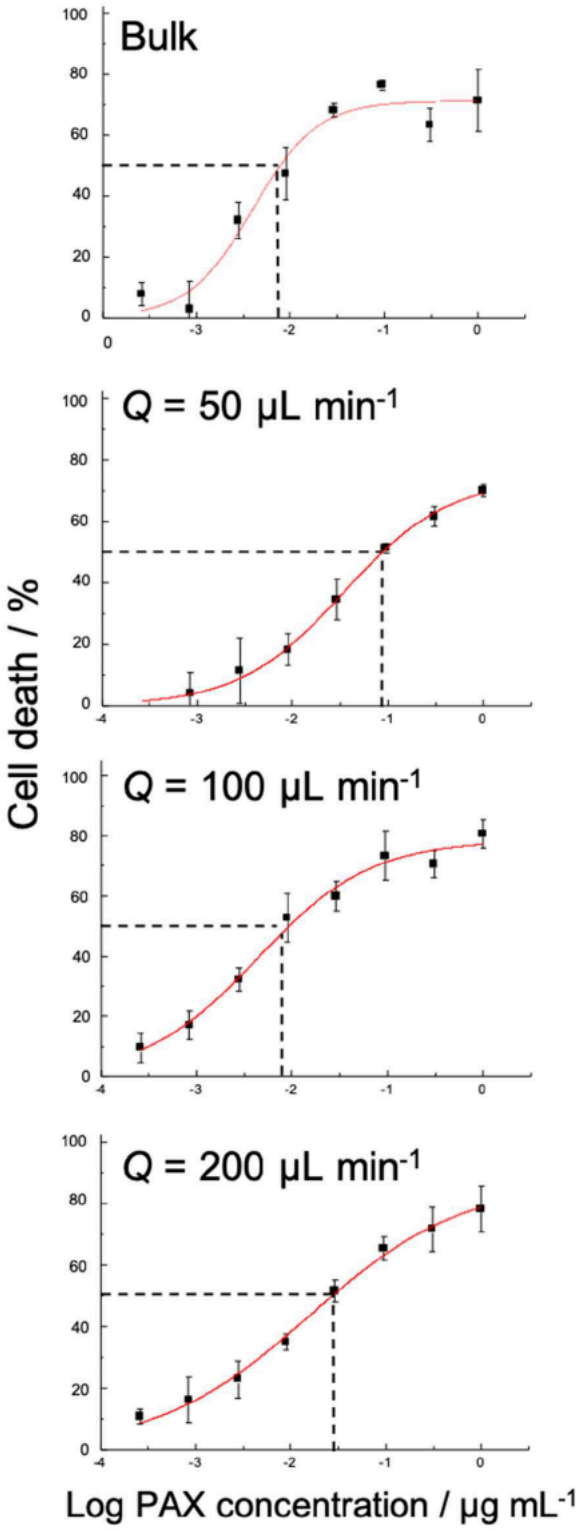

Figure B-16. MCF-7 + 10 mM GSH-OEt cell death vs. PAX concentration for various PAX-PNP formulations. Data points represent mean data from triplicate PAX-PNP preparations. Solid lines represents the best fit curves and dashed horizontal lines indicates EC_{50} values.

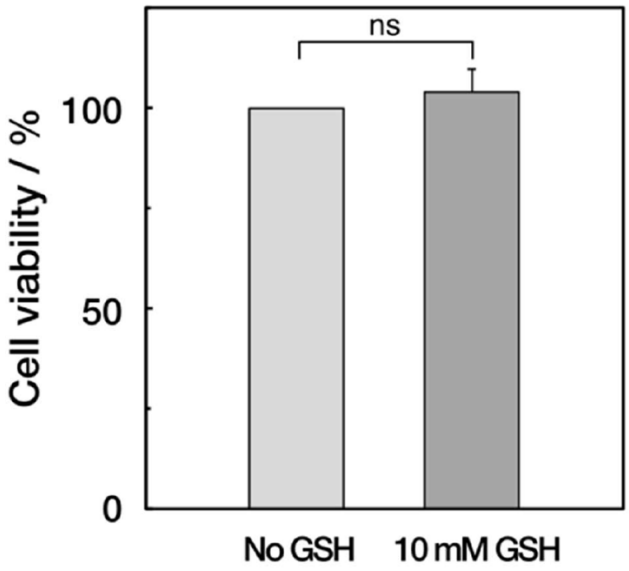

Figure B-17. MCF-7 cell viability in DMEM with no GSH and DMEM with 10 mM GSH-OEt (48 h incubation), showing no statistical difference in the two conditions. 100 % viability was defined based on the average plate reading from cells with no GSH-OEt treatment such that the viability without GSH is exactly 100% (no error bar). Error bar on viability with 10mM GSH was determined from 6 replicate measurements.

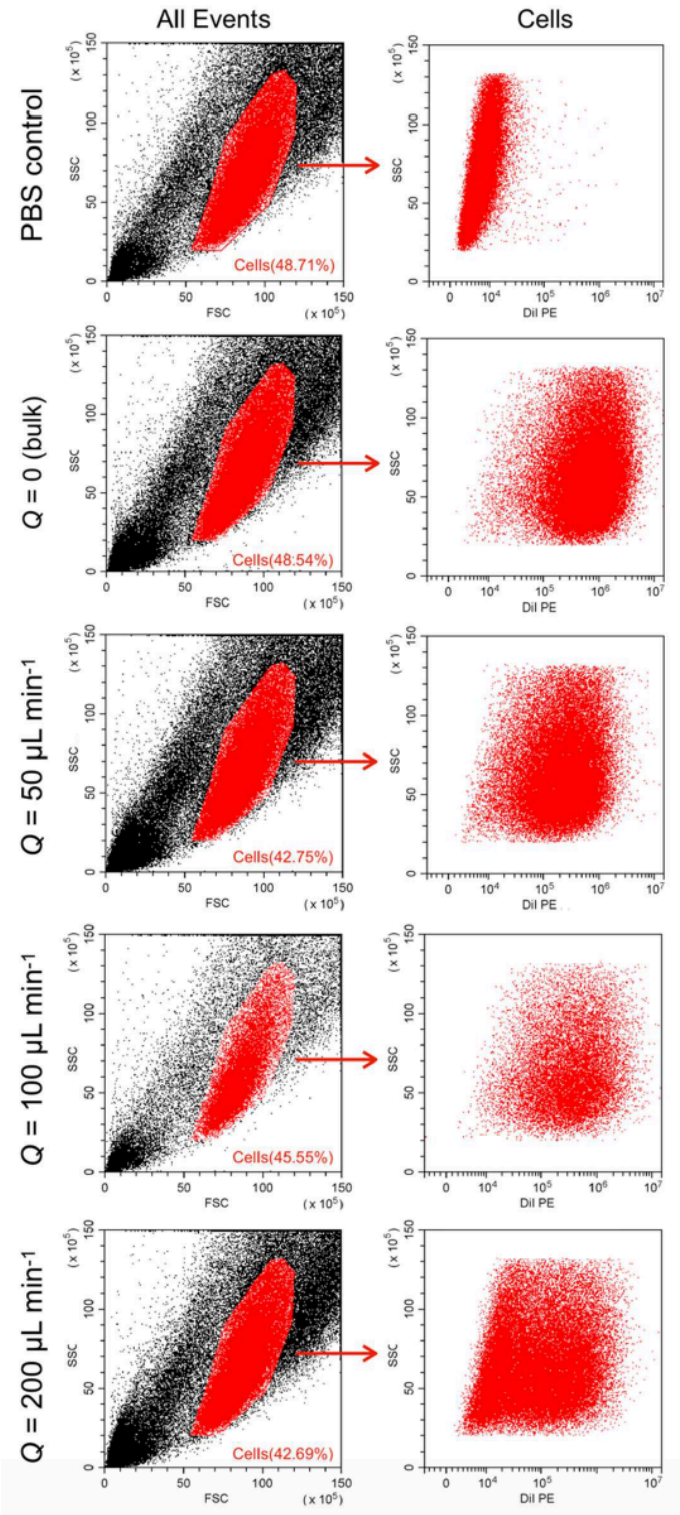

Figure B-18. Flow cytometry dot plots for MCF-7 cells with either PBS + 10% FBS treatment (negative control) or following treatment with various DiI-PNP formulations for 2 h. Cells for conducting histograms and mean DiI fluorescence intensity measurements were selected based on size and granularity (shown in red gates).

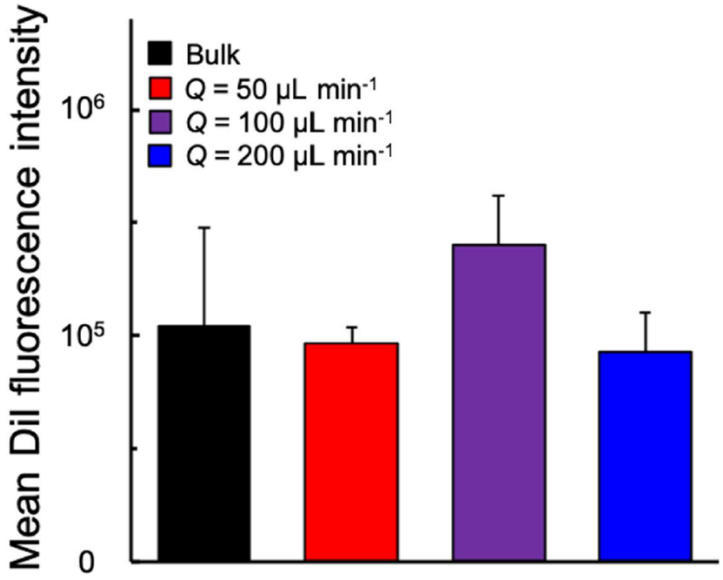

Figure B-19. Mean DiI fluorescence intensities of gated MCF-7 cells with various DiI-PNPs treatment. These values were further normalized to consider the factor of dye loading (*DL*) levels, and the resulting data is shown in Figure 12B.

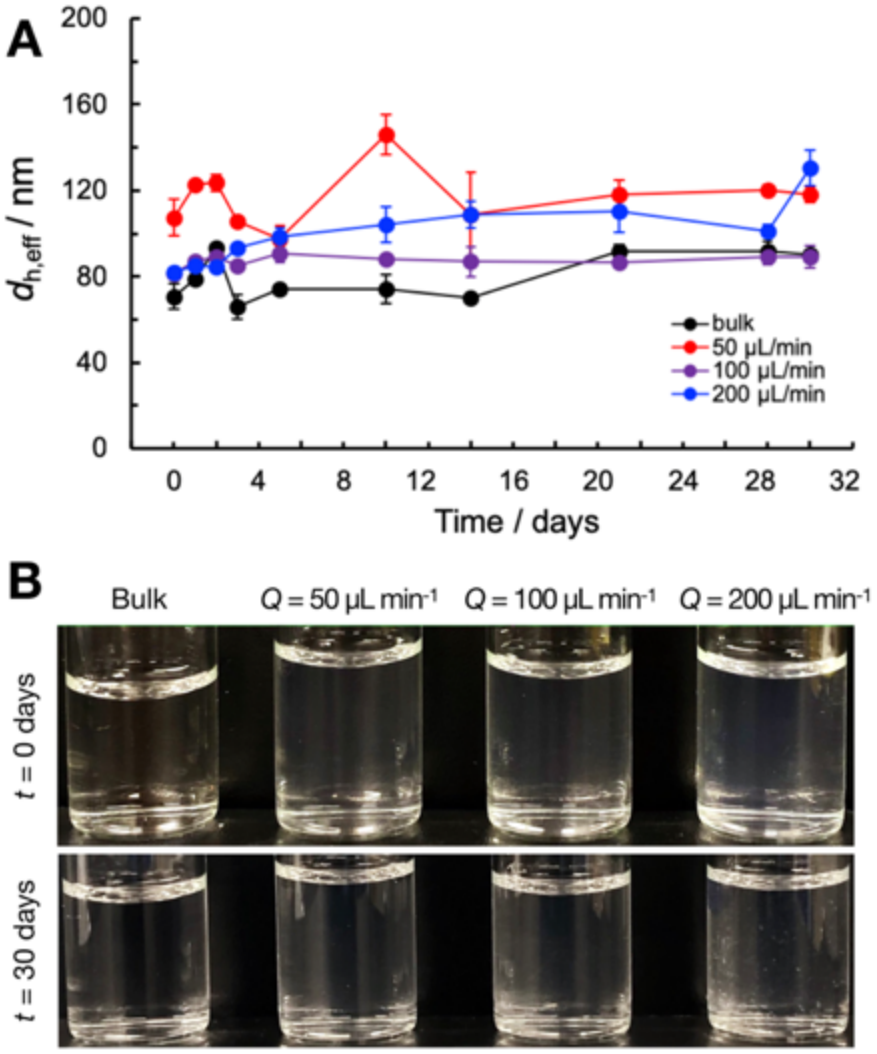

Figure B-20. Storage stability test of various PAX-PNP formulations. PNP dispersions in deionized water were stored in the dark at 22 °C immediately after preparation and dialysis. (A) Aliquots were taken from each sample and hydrodynamic effective diameters ($d_{h,eff}$) were periodically measured from DLS cumulant analysis. Experimental errors were calculated from three measurements for each sample. (B) Photographs of various PAX-PNP dispersions at $t = 0$ and $t = 30$ days. No significant differences in $d_{h,eff}$ values or dispersion clarity were found after 30-day storage of all PAX-PNP formulations.

Table B-1. Actual Flow Rates of Various Preparations of PAX-PNPs within the Two-Phase Segmented Microfluidic Reactor Described in the Main Text

Nominal flow rate	Q_{gas} **(**μ**L/min)**	Q_{liq} **(**μ**L/min)** [a]	Q_{gas}/Q_{liq}	Q_{total} **(**μ**L/min)**
50 μL/min				
Prep #1	25	25	1.00	50
Prep #2	24	25	0.96	49
Prep #3	27	25	1.08	52
100 μL/min				
Prep #1	46	50	0.92	96
Prep #2	53	50	1.06	103
Prep #3	55	50	1.10	105
200 μL/min				
Prep #1	118	100	1.18	218
Prep #2	112	100	1.12	212
Prep #3	103	100	1.03	203

[a] The liquid flow rate was assumed to be the sum of three flow-rate readings shown on the syringe pumps.

Table B-2. Actual Flow Rates of Various Preparations of DiI-PNPs within the Two-Phase Segmented Microfluidic Reactor Described in the Main Text

Nominal flow rate	Q_{gas} (μL/min)	Q_{liq} (μL/min) [a]	Q_{gas}/Q_{liq}	Q_{total} (μL/min)
50 μL/min				
Prep #1	23	25	0.92	48
Prep #2	23	25	0.92	48
Prep #3	25	25	1.00	50
100 μL/min				
Prep #1	57	50	1.14	107
Prep #2	52	50	1.04	102
Prep #3	51	50	1.02	101
200 μL/min				
Prep #1	109	100	1.09	209
Prep #2	113	100	1.13	213
Prep #3	102	100	1.02	202

[a] The liquid flow rate was assumed to be the sum of three flow-rate readings shown on the syringe pumps.

Table B-3. Statistical Comparisons between $d_{h,eff}$ Data in Figure 3-3A

Comparison pair		***p*-value**	**Result**[a]
Bulk			
Empty-PNPs	PAX-PNPs	0.36004	ns
Empty-PNPs	DiI-PNPs	0.54347	ns
PAX-PNPs	DiI-PNPs	0.84409	ns
***Q* = 50 *μ*L/min**			
Empty-PNPs	PAX-PNPs	0.51045	ns
Empty-PNPs	DiI-PNPs	0.51167	ns
PAX-PNPs	DiI-PNPs	0.14185	ns
***Q* = 100 *μ*L/min**			
Empty-PNPs	PAX-PNPs	0.48916	ns
Empty-PNPs	DiI-PNPs	0.81633	ns
PAX-PNPs	DiI-PNPs	0.05665	ns
***Q* = 200 *μ*L/min**			
Empty-PNPs	PAX-PNPs	0.83337	ns
Empty-PNPs	DiI-PNPs	0.46944	ns
PAX-PNPs	DiI-PNPs	0.65376	ns

[a] ns indicates $p > 0.05$.

Table B-4. Statistical Comparisons between Polydispersity Data of Various PNPs Manufactured at $Q = 0$ μL/min and $Q = 50$ μL/min in Figure 3-3B

Encapsulated probe	***p*-value**	**Result**[a]
Empty	0.011304	*
PAX	0.022224	*
DiI	0.013250	*

[a] * indicates $p < 0.05$.

Table B-5. Statistical Comparisons between $RA_{compart}$ Data in Figure 3-5

Comparison pair		***p*-value**	**Result**[a]
Bulk			
Empty-PNPs	PAX-PNPs	0.0099564	**
PAX-PNPs	DiI-PNPs	0.00050261	**
***Q* = 50 *μ*L/min**			
Empty-PNPs	PAX-PNPs	0.03681	*
PAX-PNPs	DiI-PNPs	0.0098547	*
***Q* = 100 *μ*L/min**			
Empty-PNPs	PAX-PNPs	0.99663	ns
PAX-PNPs	DiI-PNPs	0.17437	ns
***Q* = 200 *μ*L/min**			
Empty-PNPs	PAX-PNPs	0.16005	ns
PAX-PNPs	DiI-PNPs	0.06942	ns

[a] * indicates $p < 0.05$, ** indicates $p < 0.005$, and ns indicates $p > 0.05$.

Table B-6. Statistical Comparisons between *EE* and *DL* Data of Various PNPs Manufactured at Q = 0 μL/min and Q = 50 μL/min in Figure 3-6

Comparison pair	***p*-value**	**Result**[a]
EE		
PAX-PNPs	0.02065	*
DiI-PNPs	0.00022213	**
DL		
PAX-PNPs	0.12984	ns
DiI-PNPs	0.11681	ns

[a] * indicates $p < 0.05$, ** indicates $p < 0.005$, and ns indicates $p > 0.05$.

Table B-7. Statistical Comparisons between EC_{50} Data of Various PNPs against HaCaT and MCF-7 Cell Lines in Figure 3-10B

Comparison pair		***p*-value**	**Result**[a]
HaCaT			
Free PAX	Bulk	0.0021361	**
Bulk	Q = 50 μL/min	0.0048654	**
Q = 50 μL/min	Q = 100 μL/min	0.0041245	**
Q = 100 μL/min	Q = 200 μL/min	0.041597	*
Bulk	Q = 100 μL/min	0.75714	ns
MCF-7			
Free PAX	Bulk	0.0099196	*
Bulk	Q = 50 μL/min	0.000010884	**
Q = 50 μL/min	Q = 100 μL/min	0.000053162	**
Q = 100 μL/min	Q = 200 μL/min	0.0011766	**
Bulk	Q = 100 μL/min	0.054843	ns

[a] * indicates $p < 0.05$, ** indicates $p < 0.005$, and ns indicates $p > 0.05$.

Table B-8. Statistical Comparisons between EC_{50} Data of Various PNPs against HaCaT, MCF-7, and MCF-7 + GSH Cell Lines in Figure 3-10C

Comparison pair		***p*-value**	**Result**[a]
Free PAX			
HaCaT	MCF-7	0.27647	ns
MCF-7	MCF-7 + GSH	0.89915	ns
Bulk			
HaCaT	MCF-7	0.031486	*
MCF-7	MCF-7 + GSH	0.030277	*
***Q* = 50 *μ*L/min**			
HaCaT	MCF-7	0.35888	ns
MCF-7	MCF-7 + GSH	0.018235	*
HaCaT	MCF-7 + GSH	0.015937	*
***Q* = 100 *μ*L/min**			
HaCaT	MCF-7	0.015294	*
MCF-7	MCF-7 + GSH	0.748531	ns
***Q* = 200 *μ*L/min**			
HaCaT	MCF-7	0.061067	ns
MCF-7	MCF-7 + GSH	0.45485	ns
HaCaT	MCF-7 + GSH	0.045874	*

[a] * indicates $p < 0.05$, ** indicates $p < 0.005$, and ns indicates $p > 0.05$.

Table B-9. Statistical Comparisons between Normalized DiI Intensity Data of MCF-7 Cells Treated with Various PNPs in Figure 3-12

Comparison pair		***p*-value**	**Result**[a]
Bulk	Q = 50 μL/min	0.13952	ns
Q = 50 μL/min	Q = 100 μL/min	0.00049611	**
Q = 50 μL/min	Q = 200 μL/min	0.027076	*
Q = 100 μL/min	Q = 200 μL/min	0.0088461	*

[a] * indicates $p < 0.05$, ** indicates $p < 0.005$, and ns indicates $p > 0.05$.